A study of the effect of perturbations in spin ice systems: site dilution, weak exchange, quantum and finite-size effects

by

Taoran Lin

A thesis
presented to the University of Waterloo
in fulfillment of the
thesis requirement for the degree of
Doctor of Philosophy
in
Physics

Waterloo, Ontario, Canada, 2014

Author's Declaration

I hereby declare that I am the sole author of this thesis. This is a true copy of the thesis, including any required final revisions, as accepted by my examiners.

I understand that my thesis may be made electronically available to the public.

Abstract

In this thesis we investigate a range of properties for spin ice under various perturbations theoretically. Diluted spin ices, $Dy_{2-x}Y_xTi_2O_7$ and $Ho_{2-x}Y_xTi_2O_7$, where the magnetic rare-earth ions Dy^{3+} and Ho^{3+} are replaced by the non-magnetic Y^{3+} ions, are modeled by the random-site diluted dipolar spin ice Hamiltonians. It is found that the Monte Carlo simulation results for the specific heat of the model Hamiltonians describe the experimental measurements accurately up to $x = 1.7$ for a large temperature range. The experimentally observed, and simulation-confirmed, non-monotonicities in the specific heat broad peak and residual entropy are then rationalized theoretically by a numerical linked cluster expansion to the first order, *i.e.*, a single-tetrahedron approximation. The broad peak of the specific heat of spin ice is shown to be related to the thermal defect monopole density. For a nearest-neighbour spin ice, the paramagnetic phase is shown to be stable for all dilution levels at finite temperatures through a random site-diluted Husimi tree Bethe-Peierls argument. The loss of the projective equivalence in the presence of dilution is commented for the problem.

Thin film spin ices, are studied for a film surface normal to the [001] direction. Corrections to the Pauling's residual entropy are derived for different surface states, and are confirmed by Monte Carlo study. An important geometrical object on the [001] surface, the orphan bond, is identified. By tuning the strength of the orphan bond, various surface states emerge in the simulations. Most notably, in the dipolar spin ice thin film with an antiferromagnetic orphan bond, a novel phenomenon of surface magnetic freezing is found in the simulations. The transition to long-range order for the surface freezing is found to be continuous. The mechanism for surface freezing is argued to be induced by a self-screening of the dipolar interactions due to the pyrochlore structure below the surface.

The microscopic model of $Dy_2Ti_2O_7$, is scrutinized for further neighbour exchange interactions. A dimensionality reduction [112] field experiment is considered, which allows for unambiguous determination for the constraints for the exchange interactions. With such constraints we attempt to fit the microscopic model of $Dy_2Ti_2O_7$, to three sets of experiments. First is the specific heat measurement from the work of Pomaranski *et al.* [1], second is the specific heat measurement from the work of Ke *et al.* [2], and third is the neutron scattering measurement by Fennell *et al.* [3]. The second set of data is in quantitative agreement with the majority of specific heat measurements for $Dy_2Ti_2O_7$, where a residual entropy plateau of Pauling's value [4] is found. The first set of data,

however, shows an absence of Pauling's entropy, but it is believed to be better equilibrated [1]. In this work, we show by fitting our model to the three sets of data, that the second and third sets of data can be simultaneously fitted but not for the first and third sets of data. Therefore our analysis exposes further inconsistencies in the measurements for the compound $Dy_2Ti_2O_7$, by relating specific heat and neutron scattering measurements through the microscopic model.

We examine the pinch point singularity in the neutron scattering data of spin ice through Monte Carlo simulations. It is found in simulations that pinch points exist up to high temperatures in dipolar spin ice, where local ice-rule no longer applies. Such observation is crucial in understanding experimental observed pinch points in spin ice materials, such as in $Ho_2Ti_2O_7$ [5], that the pinch point seen in neutron scattering may be a deceptive signal when the system possesses large dipolar interaction. The thermal broadening of the pinch points for a nearest-neighbour spin ice model is also considered. The correlation length from fitting the broadening of the pinch point is compared with the average thermal defect monopole distances.

The quantum spin ice candidate material $Yb_2Ti_2O_7$ is regarded as a rare candidate for spin liquid with a well parameterized Hamiltonian [6]. In the presence of a quantum microscopic model, numerical methods are needed in calculating its properties with controllable errors. For the Hamiltonian of the quantum spin ice $Yb_2Ti_2O_7$, we demonstrate the capability of the numerical linked cluster method in calculating the neutron scattering intensity patterns. These results open avenues for future works on the study of the quantum spin ices.

Acknowledgements

I would like to express my sincere gratitude to my supervisor Prof. Michel J. P. Gingras of the department of Physics and Astronomy at University of Waterloo. His enthusiasm, hard work and patience made this project possible. He provided guidance and encouragement during the course of this work.

I would like to thank my Ph.D. advisory committee Prof. Roger Melko, Prof. Rob Hill, Prof. Jan Kycia, and Prof. Pierre-Nicholas Roy for their guidance during my studies.

I would like to thank Prof. Cristian Batista of Los Alamos National Laboratory for agreeing to be my external examiner and offering many constructive comments to the thesis.

I would like to acknowledge collaborations with Prof. Xianglin Ke, Mischa Thesberg, Prof. Peter Schiffer and Prof. Roger Melko on the diluted spin ice projects, Tuba Shafqat, Prof. Ludovic Jaubert, Prof. Peter Holdsworth on the spin ice thin film project, Prof. Patrik Henelius, Prof. Matthew Enjalran, Zhihao Hao, Felix Flicker, Taras Yavors'kii, Jaan Altosaar on the project of ground state properties of $Dy_2Ti_2O_7$, Zhihao Hao and Felix Flicker on the spin ice pinch point project, and Prof. Rajiv Singh on the numerical linked cluster study of quantum spin ices. In particular I would like to thank Prof. Rajiv Singh for his hospitality in inviting me for a one-month visit to UC Davis.

I would like to thank my colleagues in the condensed matter group at University of Waterloo for many interesting discussions and collaborations: Alexandre Day, Zhihao Hao, Stephen Inglis, Behnam Javanparast, Zijian Long, Andrew MacDonald, Paul McClarty, David Pomaranski, Pawel Stasiak, Yu-Cheng Su, Ka-Ming Tam, Jordan Thompson, William Toews, Anson Wong, Brian Yee, and Wuyang Zhang.

I would like to thank Kexin Ji for her support and editing many typos in the thesis.

At last I want to thank my parents for their support and patience during my Ph.D. studies.

Dedication

To my parents

Table of Contents

List of Figures

List of Tables

Chapter 1

Introduction

1.1 Geometrical frustration

Frustration in magnetism refers to the situation where not all the interactions can be simultaneously satisfied. Consider the following example of an Ising antiferromagnet on a triangular lattice, of which a triangular plaquette is shown in Fig. 1.1. It is clearly not possible to satisfy all the pairwise interactions on a triangular plaquette.

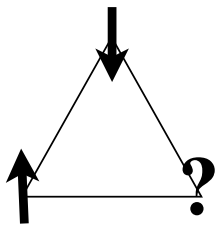

Figure 1.1: Ising antiferromagnet on a triangular plaquette

An important consequence from frustration, as seen in this example, is the degeneracy of the ground state, as there are different ways to choose which bond is frustrated. In the thermodynamic limit, the degenerate ground states are *not* symmetry related, and the number of them is macroscopic. Note that eventually the degeneracy will be lifted by weak

perturbations in experimental systems, leading to a long range order transition or even a glass transition [8] at a temperature much lower than the frustrated interaction energy scale. In experiment, frustration is often characterized by the frustration index [9]

$$f \equiv \frac{|\theta_{\mathrm{CW}}|}{T^*} \tag{1.1}$$

where θ_{CW} is the Curie-Weiss temperature, which reflects the dominant interaction energy scales in the problem and is determined from the inverse susceptibility at high temperatures. T^* is the critical temperature where the system eventually develops long-range order or, in the case of a thermodynamic spin-glass transition, the freezing temperature.

1.2 Rare earth pyrochlores

Spin ice materials, the subject of this thesis, belong to the cubic pyrochlore oxide family, $A_2B_2O_7$, where A and B represent two species of ions. Either or both of them can be magnetic and they independently occupy two separate pyrochlore lattices [8]. Canonical spin ice materials, $Dy_2Ti_2O_7$ and $Ho_2Ti_2O_7$, are the cases where the A site is a $4f$ rare-earth trivalent ion (Dy^{3+} or Ho^{3+}), which is magnetic, whereas the B site is a transition metal, which is non-magnetic.

1.2.1 Pyrochlore lattice

The pyrochlore lattice consists of an FCC Bravais lattice, with a basis of four ions. It is a network of corner-sharing tetrahedra, which makes the pyrochlore lattice an ideal structure for geometrical frustration, as each tetrahedron consists of four triangular plaquette faces. Fig. 1.2 shows the pyrochlore lattice in a conventional cubic unit cell.

1.2.2 Crystal field and single ion properties

For rare-earth ions, the spin-orbit interaction is large and $\mathbf{J} = \mathbf{L} + \mathbf{S}$ is a good quantum number, with Hund's rules determining the electronic ground state of an isolated ion [8]. For Dy^{3+}, since the outer electronic configuration is $4f^9$, we have $S = 5/2$ in maximizing S

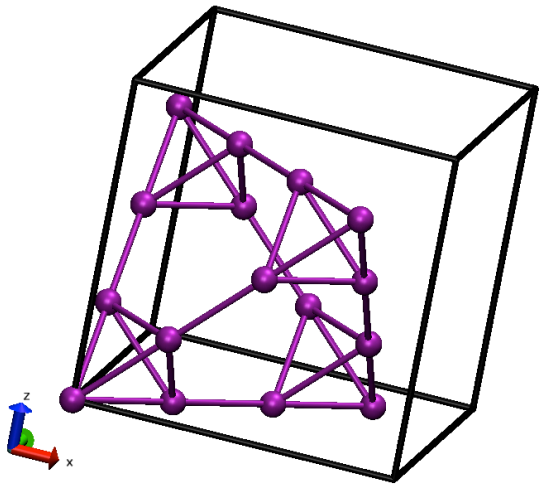

Figure 1.2: Pyrochlore lattice in a cubic unit cell

and $L = 5$ in maximizing L from Hund's rules, thus $J = 15/2$ for Dy^{3+}. For Ho^{3+}, its outer electronic configuration is $4f^{10}$, thus we have $S = 2$ and $L = 6$ from Hund's rules, leading to $J = 8$ for Ho^{3+}. For an isolated ion all the $2J + 1$ states are degenerate.

The $2J + 1$ degeneracy is lifted by the crystal field (CF) Hamiltonian resulting from the electrostatic and covalent bonding from the local environment of the rare-earth ions. In terms of Steven's operators [10], the CF Hamiltonian can be written as

$$\mathbf{H}_{\mathrm{CF}} = \sum_i \sum_{l,m} B_l^m O_l^m(\mathbf{J}_i) \tag{1.2}$$

The Steven's operators for some given symmetries can be found in existing tables [11].

For the pyrochlore structure, the immediate environment for the rare-earth ions are the eight oxygens surrounding each of them. Two of the oxygens are in the center of the two tetrahedra the rare-earth ion connects, therefore these two oxygens and the rare-earth ion form a line in the direction of the local [111] axis of the rare earth ion. The other six oxygen ions form a "puckered six-member ring" [8] in a plane normal to the local [111] direction. Therefore for the A site rare-earth ion, its local [111] direction is special from the crystal

field Hamiltonian. Depending on the details of the crystal fields, the magnetic anisotropy for the rare-earth ground state can be either easy plane or easy axis with respect to the local [111] direction.

It turns out that for $Dy_2Ti_2O_7$ and $Ho_2Ti_2O_7$, their respective crystal field Hamiltonians select ground state doublets for both rare-earth ions. The ground state doublets are characterize by an easy-axis local susceptibility with respect to the local [111] directions dictated by the symmetry of the surrounding oxygen atoms. Furthermore, these ground state doublets are separated from their higher crystal field levels by an energy scale of the order of hundred Kelvin [12, 13]. Therefore, at temperatures below tens of Kelvin, they form an effective Hilbert space for the rare-earth ions, and the magnetic moments for $Dy_2Ti_2O_7$ and $Ho_2Ti_2O_7$ can be described by classical Ising spins confined to point along their local [111] direction.

1.3 Spin ice and residual entropy

1.3.1 Residual entropy and mapping to water ice

As we discussed in Section 1.2 the magnetic moments in spin ice have easy axes along their local [111] direction. The neighbouring interactions between two spins on the same tetrahedron are determined to be ferromagnetic [14]. Considering a spin pointing into a tetrahedron, to satisfy the ferromagnetic interaction between this spin and the three other spins, the three other spins need to be pointing out. However it is impossible to satisfy all these interactions between the four spins on a tetrahedron. Thus spin ice is frustrated, and the lowest energy configuration for a tetrahedron is that two of the spins point in and the other two point out of each tetrahedron, as shown in Fig. 1.3. This is the so-called *ice rule*, as the two-in-two-out spin constraint can be mapped to the Bernal-Fowler ice rule in the hexagonal and cubic water ice for the proton disorder [4].

Shown in Fig. 1.3, the oxygen atoms (red circle) in water ice are located on a diamond lattice, which are the centers of the tetrahedra of the pyrochlore lattice. Between two neighbouring oxygens, there is exactly one proton (blue circles) in between and the proton is closer to one oxygen than the other. The ice rule requires that there are exactly two protons closer to an oxygen atom and the other two farther away [4]. Thus the proton displacements can be mapped to the two-in-two-out spin configuration in spin ice.

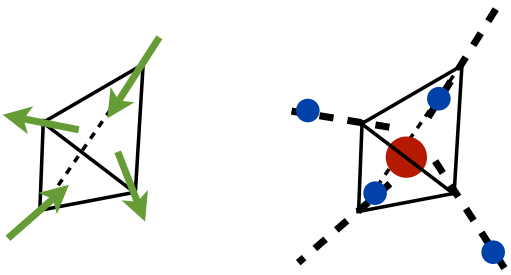

Figure 1.3: Left: ice rule on a tetrahedra; Right: ice rule for the proton displacement

In the work by Pauling [4], the residual entropy per proton is estimated to be $(k_B/2)\ln(3/2)$. The similar argument for spin ice goes as follows: Suppose we have N spins under consideration, and the number of tetrahedra is thus $N/2$. If there is no ice rules, the total number of spin configurations is 2^N. However, out of the 16 spin configurations for a given tetrahedron, only 6 of them satisfy the ice rule, thus the total number of ice-rule configurations is $2^N(6/16)^{N/2}$ Thus we have the entropy of $(k_B/2)\ln(3/2)$ per spin in spin ice. The approximation made here is that we take the probability to satisfy the ice rule given a random spin configuration to be independent among tetrahedra.

1.3.2 Spin ice materials

Besides the canonical spin ice materials $Dy_2Ti_2O_7$ and $Ho_2Ti_2O_7$ [15], recent years have seen new compounds being synthesized and studied under this category. Some examples include $Dy_2Sn_2O_7$ [16], $Ho_2Sn_2O_7$ [17]. Also high pressure has allowed researchers to make the $Dy_2Ge_2O_7$ and $Ho_2Ge_2O_7$ compounds, and thermodynamic measurements have indicated that these materials also belong to the spin ice class [18, 19, 20, 21].

1.4 Spin ice Hamiltonians

There are two types of spin ice models of interest in this thesis.

The minimal model that describes the geometrical frustration in spin ices reads

$$\mathcal{H}_{\rm nn} = J_{\rm nn} \sum_{\langle i,j \rangle} \sigma_i \sigma_j, \tag{1.3}$$

where σ_i and σ_j are the Ising variables and $J_{\rm nn} > 0$ is the effective antiferromagnetic interaction. The sum is over all nearest neighbours rare-earth ions in the pyrochlore lattice. Such a model, as originally suggested for spin ice compound $Ho_2Ti_2O_7$ [22], enforces the ice-rule at zero temperature, and therefore possesses the Pauling's residual entropy.

It turns out that the spins in the spin ice compounds $Dy_2Ti_2O_7$ and $Ho_2Ti_2O_7$ possess large magnetic moment of $\sim 10\mu_B$ which can not be ignored [23, 24]. Thus, with the long range dipolar interaction, the dipolar spin ice model (DSIM) Hamiltonian reads

$$\mathcal{H}_{\rm DSIM} = \sum_{i>j} \sigma_i \sigma_j \{ J_{i,j} \hat{z}_i \cdot \hat{z}_j + D(r_{nn}/r_{ij})^3 [\hat{z}_i \cdot \hat{z}_j - 3(\hat{z}_i \cdot \hat{r}_{ij})(\hat{z}_j \cdot \hat{r}_{ij})] \}, \tag{1.4}$$

where $\sigma_i = \pm 1$ are the Ising spin variables. The first term describes the Ising exchange interaction between neighbouring spins up to third neighbouring distances, with J_1, J_2, and J_3 the exchange parameters for the first, second and third nearest neighbours. There are two types of third neighbours which we consider later in Chapter 5, one type shares a common nearest neighbour and the other type doesn't. The sign convention here for the neighbouring interactions is such that a positive J value indicates antiferromagnetic interaction and a negative J value indicates ferromagnetic interaction. The second term is the long-range magnetic dipole-dipole interaction, where $r_{\rm nn}$ is the nearest neighbour distance in the pyrochlore lattice. $\hat{z}_i$ and $\hat{z}_j$ are the local $\langle 111 \rangle$ directions of the spins. Such a model forms the backbone of the discussions about experimental spin ice compounds [23, 25, 26, 24]. The issue of consistency between experimental measurements within the framework of this model is part of the discussion in Chapter 5 of this thesis.

1.5 Dipolar interaction in spin ice

An important aspect of this thesis, is the explanation of the properties of the dipolar interaction on a pyrochlore lattice. One of the most important properties, the *projective equivalence* [27] or *self-screening* [28], is the backbone of many discussions throughout the thesis. We introduce these interesting concepts what follows.

Between two spins, $\mathbf{s}_i$ and $\mathbf{s}_j$, at positions $\mathbf{r}_i$ and $\mathbf{r}_j$, the form of the dipolar interaction reads

$$\mathcal{H}_{\text{dip}} = \frac{\mathbf{s}_i \cdot \mathbf{s}_j}{{r_{ij}}^3} - \frac{3(\mathbf{s}_i \cdot \mathbf{r}_{ij})(\mathbf{s}_j \cdot \mathbf{r}_{ij})}{{r_{ij}}^5}. \tag{1.5}$$

Thus the interaction between two spins, depends not only on the relative orientation of the two spins, but also on the relative displacement between the two spins. Furthermore, the dipolar interaction is long ranged, such that in a lattice system every spin is interacting with every other spin. With all these complexity, the question is how the dipolar effects can be efficiently understood.

It has been noted in previous works [23, 28] that the dipolar Hamiltonian Eq. (1.4) for $Dy_2Ti_2O_7$ and $Ho_2Ti_2O_7$ has the same qualitative properties as the nearest-neighbour Hamiltonian Eq. (1.3). From a mean-field perspective by Gingras *et al.* [28], the energy spectrum for the largest eigenvalue for the nearest-neighbour model is found to be flat, indicating zero-energy excitation modes in real space, which corresponds to the highly degenerate ice-rule ground states. For the dipolar Hamiltonian restricted to only nearest-neighbour and dipolar interactions, Eq. (1.4), the energy spectrum is found to be almost flat, as the truncations of the dipolar interaction go to infinity [28]. This work shows that the selection of a particular ordering due to the dipolar interaction is very week in the ice-rule manifold.

Later, Isakov *et al.* [27] further show that by a "model" dipole interaction, the energy spectrum in the $\mathbf{q}$-space is completely flat, as in the nearest neighbour model, and the correction from the true dipolar interaction to the "model" dipole interaction is of order $O(r^{-5})$. Isakov *et al.* termed the equivalence between the dipolar interaction and the nearest-neighbour interaction "*projective equivalence*".

Intuitively, projective equivalence can be understood by the dumbbell model of spin ice introduced in Castelnovo *et al.* [29]. In the dumbbell model, the point dipole of a spin is replaced by two monopoles of opposite charges at the centers of the two tetrahedra linking the spin. Normally in the problem of electrostatics, we expand the charge distribution in the far field in terms of multipole expansions. Now in the dumbbell model, the process is reversed and we replace the point dipole by a distribution of two point charges. The corrections from such a replacement is small when viewed from a long distance away, as it only consists of higher multipole moments. Once the replacement is done, it follows from the ice-rule on a tetrahedron that these charges cancel each other at the center of the

tetrahedron. Thus we have the projective equivalence, or we say the dipolar interactions are *self-screened*.

Thus the key to understand the dipolar interaction in Eq. (1.5) on a pyrochlore lattice with Ising spins in their local $\langle 111 \rangle$ easy axes, is to approximate the dipole by a pair of monopoles. The dominant physics at play is the cancellation of the monopole charges due to the ice rule.

Note that the dumbbell model has found applications in other systems, such as dipolar spin ice on a kagome ice, where a two-stage ordering is found for the monopole charges and the spins, respectively [30].

1.6 Magnetic monopoles in spin ice

In this section we discuss the recent idea of magnetic monopoles in spin ice [29, 31, 32, 33].

The monopoles are defined as the ice-rule breaking excitations above the ice state. Consider a lattice of ice-rule fulfilling tetrahedra, flipping a spin breaks the two-in-two-out ice rules for the two tetrahedra connecting to that spin, and thus creates two tetrahedra which are in the three-in-one-out and three-out-one-in configurations. In a coarse-grained field description of the spins, these three-in-one-out or three-out-one-in configurations are the "sinks" and "sources" of the coarse-grained field [31, 32], thus they are referred to as the *magnetic monopoles* (of opposite signs) [29] in spin ice. The monopoles may diffuse by further flipping spins on the ice-rule defected tetrahedra, which restores the ice-rule along the path of the monopole diffusion [33].

The interaction between the monopoles turns out to be of the form of the Coulomb interaction, with two origins. The first origin is the entropic force between the monopoles when the underlying spin ice configurations are summed in the partition function. In the nearest neighbour spin ice model, Eq. (1.3), the diffusion of the monopoles, once created, does not cost energy. However, the number of ice-rule configurations underlying two closer monopoles is larger than the number for two farther away monopoles, thus inducing the entropic Coulomb potential between the two monopoles [32]. The second origin is the energetic interaction between the monopoles in the dipolar spin ice [29]. In the dumbbell model, as mentioned in Section 1.5, the three-in-one-out or three-out-one-in configurations on a tetrahedron can be approximated by a monopole charge at the center of

the tetrahedron. Thus the potential energy between these monopoles are of the Coulombic form [29].

The monopole concept has motivated recent search of such exotic excitations in previous experimental works [5, 34, 35]. In essence, the monopole concept provides an economic language in describing excitations in the background of the ice-rule 'vacuum' states, where the dipolar coupled spins are self-screened due to the monopole charge cancellation by the ice rules.

1.7 Spin liquid and quantum spin ice

In an ideal frustrated magnet with no extra perturbations, there may be no transition to long range order, implying a frustrated index, as defined in Section 1.1, to be $f = \infty$. The constituent spins remain disordered but are highly correlated down to zero temperature, *i.e.*, they are in a *spin liquid* state [36].

For spin ices, $Dy_2Ti_2O_7$ and $Ho_2Ti_2O_7$ can be viewed as examples of such spin liquids [36], or in the context of the work by Villain [37], cooperative paramagnets. More precisely, they should be called "classical spin liquid", since quantum dynamics have been quenched due to the strong Ising nature of the crystal-field ground state doublets for Dy^{3+} and Ho^{3+}. They are, however, "liquid" with extremely slow dynamics below $T \sim 1$ K, due to the high temperature barrier in breaking the ice rule in these materials [33].

On the other hand, we may have a *quantum* spin liquid state, where large zero-point quantum mechanical spin fluctuations prevent the system from developing long range order. Since the spin ice models already have a classical spin liquid state, one might ask whether the addition of quantum dynamics can result in a quantum spin liquid phase. In the works by Hermele *et al.* [38] and by Castro Neto *et al.* [39], it is found that within the constrained ice-rule manifold, the addition of quantum dynamics may lead to a $U(1)$ quantum spin liquid.

On the material side, the search for quantum spin liquids seems most promising in the Yb- based pyrochlores, as their microscopic Hamiltonians may be described by an effective quantum pseudospin-1/2 model [40, 41]. For example, the $Yb_2Ti_2O_7$ compound seems to be the first quantum spin liquid candidate with a known Hamiltonian fitted with high field inelastic neutron scattering experiments [6], however, with still unsolved complications in

the highly sensitive sample dependence of the specific heat at low temperatures [42, 43]. The model was later confirmed through numerical linked cluster studies finding results in agreement with bulk measurements [44, 45]. In Chapter 7, we further explore the numerical linked cluster method in calculations of the neutron scatterings.

1.8 Outline of the thesis

In this thesis, we study different kinds of perturbations in spin ice, including random dilution, finite-size surface effects, further exchanges, and the addition of quantum dynamics.

In Chapter 2, we review the main methods we use in this thesis.

In Chapter 3, we study the effect of random site dilution on dipolar spin ice and nearest neighbour spin ice. The microscopic models for $Dy_{2-x}Y_xTi_2O_7$ and $Ho_{2-x}Y_xTi_2O_7$ are validated through Monte Carlo simulation studies. In the study of the diluted nearest-neighbour model, we comment on the meaning of the broad peak of specific heat generic in spin ice material, *i.e.*, its relation to thermal monopole excitation populations. A simple, yet extremely accurate approximation is presented and analyzed, which gives an explanation for the observed non-monotonicities in the calorimetric measurements. Stability of the paramagnetic phase in the presence of site dilution is explored through the perspective of a Bethe-Peierls calculation. A comment is offered on the breakdown of the projective equivalence in the presence of dilution.

In Chapter 4, we study spin ice in the form o a thin film. Surface corrections to the Pauling's residual entropy are derived due to the different conditions at the free surface. For dipolar spin ice films, we find a surface freezing resulting by the tuning of surface conditions. The reason for such surface freezing, as we argue in the chapter, arises from a different screening property of the dipolar interaction than that found with the projective equivalence considered in previous works.

In Chapter 5, we study the microscopic aspect of the dipolar spin ice model by trying to examine both the calorimetric and neutron scattering experimental measurements. We demonstrate, through parametric constraints provided by in-field experiments, bulk measurements of the specific heat and correlation measurements of the neutron scattering can be compared through the microscopic model.

In Chapter 6, we turn to the study of pinch point singularities in the neutron scattering intensity pattern in spin ice. Our Monte Carlo results show that the pinch point singularities, viewed as a signature for the emergent gauge structures, can be deceptive in the case for a system with long range dipolar interaction. We also study through Monte Carlo simulations, how the pinch point singularities evolve as a function of temperature.

In Chapter 7, we investigate the capability of the numerical linked cluster (NLC) method in the study of neutron scatterings for quantum spin ices. As a demonstration of the method, neutron scatterings for $Yb_2Ti_2O_7$ are calculated to various orders of the cluster expansion.

Chapter 8 concludes the thesis.

Chapter 2

Methods

In this chapter we review the main methods used in this thesis.

2.1 Monte Carlo method

In this section we give a brief summary of the Metropolis Monte Carlo method. Since such a method has been one of the most commonly used in condensed matter physics, numerous books and reviews can be found on the subject. The interested reader may refer to the book by Binder and Heerman [46], or the one by Neumann [47] for a more detailed account.

In statistical mechanics, our goal is to calculate the thermal average of some quantity

$$\langle Q \rangle = \frac{\sum_\mu Q_\mu e^{-E_\mu/k_B T}}{\sum_\mu e^{-E_\mu/k_B T}}, \tag{2.1}$$

where the summation is over all possible states, μ, of the system.

However, the summation is usually impossible to carry out exactly. For example, for an Ising model with N spins, the number of all possible states equals 2^N, which is a huge number even for a modest number of spins. Thus the best we can do is to sample only a subset of all the possible states. Suppose we choose a subset of states, $\{\mu_1, \mu_2, ..., \mu_M\}$, with a probability distribution $p(\mu)$, then our best estimate for the quantity $\langle Q \rangle$ is given by

$$Q_E = \frac{\sum_i^M Q_{\mu_i} p(\mu_i)^{-1} e^{-E_{\mu_i}/k_B T}}{\sum_j^M p(\mu_j)^{-1} e^{-E_{\mu_j}/k_B T}} \tag{2.2}$$

Still another problem remains that, in Eq. (2.1), not all the states contribute the same to the sum of the thermal average. In fact, for a typical thermal system, only a small fraction of all possible states contribute significantly. Therefore, if we choose our subset of states uniformly, chances are we might never "hit" the right states in that small fraction which contribute to Eq. (2.1), and we end up summing over nearly zero values from our choice of subsets. Thus we need the concept of *importance sampling*. One way of doing so is to choose the probability distribution

$$p(\mu) = \frac{e^{-E_\mu/k_B T}}{Z}. \tag{2.3}$$

By doing so, our estimator Eq. (2.2) becomes

$$Q_E = \frac{1}{M}\sum_i^M Q_{\mu_i}. \tag{2.4}$$

The problem then becomes how the Boltzmann distribution, Eq. (2.3), can be realized. The answer is to make use a Markov process to generate a random set of states according to the distribution.

Suppose at time n the system is in state μ, then there is a fix probability, $P(\mu \to \nu)$, that at time $n+1$ the system is in state ν. A Markov process means the transition probability from state μ to state ν, $P(\mu \to \nu)$, only depends on the state μ, but not on any previous states. It also requires

$$\sum_\nu P(\mu \to \nu) = 1 \tag{2.5}$$

for all possible states, ν, the Markov process can travel to.

For the generated states to acquire a Boltzmann probability distribution after equilibrium, two additional conditions need to be imposed on the Markov process: the ergodicity condition and the detailed balanced condition.

The ergodicity condition requires that, starting from any state, the Markov process can access any other state. In other words, all the phase space can eventually be visited by the Markov process given the process is run long enough.

The detailed balanced condition requires

$$p(\mu)P(\mu \to \nu) = p(\nu)P(\nu \to \mu) \tag{2.6}$$

where $p(\mu)$ is the probability distribution.

Therefore, from the detailed balanced condition, to generate the Boltzmann distribution Eq. (2.3), the transition probabilities must satisfy

$$\frac{P(\mu \to \nu)}{P(\nu \to \mu)} = \frac{p(\nu)}{p(\mu)} = e^{-(E_\nu - E_\mu)/k_B T}. \tag{2.7}$$

In practice, the transition probability consists of the selection probability, $g(\mu \to \nu)$, and the acceptance probability, $A(\mu \to \nu)$, such that

$$P(\mu \to \nu) = g(\mu \to \nu) A(\mu \to \nu). \tag{2.8}$$

In a usual Monte Carlo algorithm, the selection probability is often the same for $g(\mu \to \nu)$ and $g(\nu \to \mu)$. For example, in the "single-spin-flip" algorithm for an Ising model, they both equal to $1/N$, where N is the number of spins in the system.

The Metropolis algorithm is one which chooses

$$A(\mu \to \nu) = \begin{cases} e^{-(E_\nu - E_\mu)/k_B T} & \text{if } E_\nu - E_\mu < 0 \\ 1 & \text{otherwise.} \end{cases} \tag{2.9}$$

2.2 Closed and open loop updates

2.2.1 Closed loop algorithm

For spin ice at low temperatures, where the ice rule is enforced on each tetrahedron, single spin flip updates are inefficient in maintaining ergodicity, as such updates violate the ice rule and thus raise the energy of the system. For a nearest-neighbour spin ice with nearest-neighbour interaction J, the raise in energy is $\Delta E = 4J$ for a single spin flip in the ice rule state, and the acceptance rate drops as $e^{-4J/k_B T}$ at low temperatures. On the other hand, all the ice rule states, which have the same energy for the nearest-neighbour model, ought to be sampled in a Monte Carlo simulation at equilibrium.

Therefore, we need an update to "tunnel" between different ice rule states. One way to do so is to use the loop update algorithm developed for square ice models [47] and for spin ices [48]. Here is a summary of the algorithm.

The algorithm consists of first finding a loop of spins that is "flippable" and then flip the spins that form the loop according to the Metropolis algorithm.

We depict the flow chart of the closed loop algorithm in Fig. 2.1. The algorithm randomly chooses a loop that goes through two-in-two-out ice rule tetrahedra. Thus in the step to determine whether the tetrahedron is defected, we reject thermally excited (not two-in-two-out) tetrahedra, or in the presence of dilution, a diluted tetrahedron.

The loop algorithm closes on itself, which corresponds to the *short loop* algorithm in Melko *et al.* [48]. Also, we refer to it as a *closed* loop algorithm to differentiate the *open* loop algorithm discussed later.

2.2.2 Ergodicity of the closed loop algorithm

For spin ice in states satisfying the ice rules, the closed loop update is ergodic within the ice manifold. This means starting with any ice-rule state, the loop updates can reach any other ice-rule state within a finite number of steps.

The key to the proof relies on an important observation of the ice rule. In Fig. 2.2 we plot the six possible ice rule states for a tetrahedron. By inspection it can be shown that any two of six ice rule states differ each other by an even number of spins, and among those spins that are different there are the same number of spins in and out of the tetrahedron.

Therefore, suppose we have two ice-rule states on a pyrochlore lattice and we consider only the spins that are different between the two states, these spins have to form loops, possibly intersecting at some tetrahedron, since by the property of the ice-rule the "chain" of arrows can not end at any tetrahedron.

Thus, to get from one ice-rule state to another, we need to reverse the direction of the different spins, which form loops, and there are only a finite number of loops. Therefore our loop updates can reach any other ice-rule state starting from any ice-rule state. Equivalently speaking, the loop update is ergodic within the ice-rule manifold.

Note 1

Notice that the proof only depends on the property of the ice rule, thus for 2D square ice, the same argument holds.

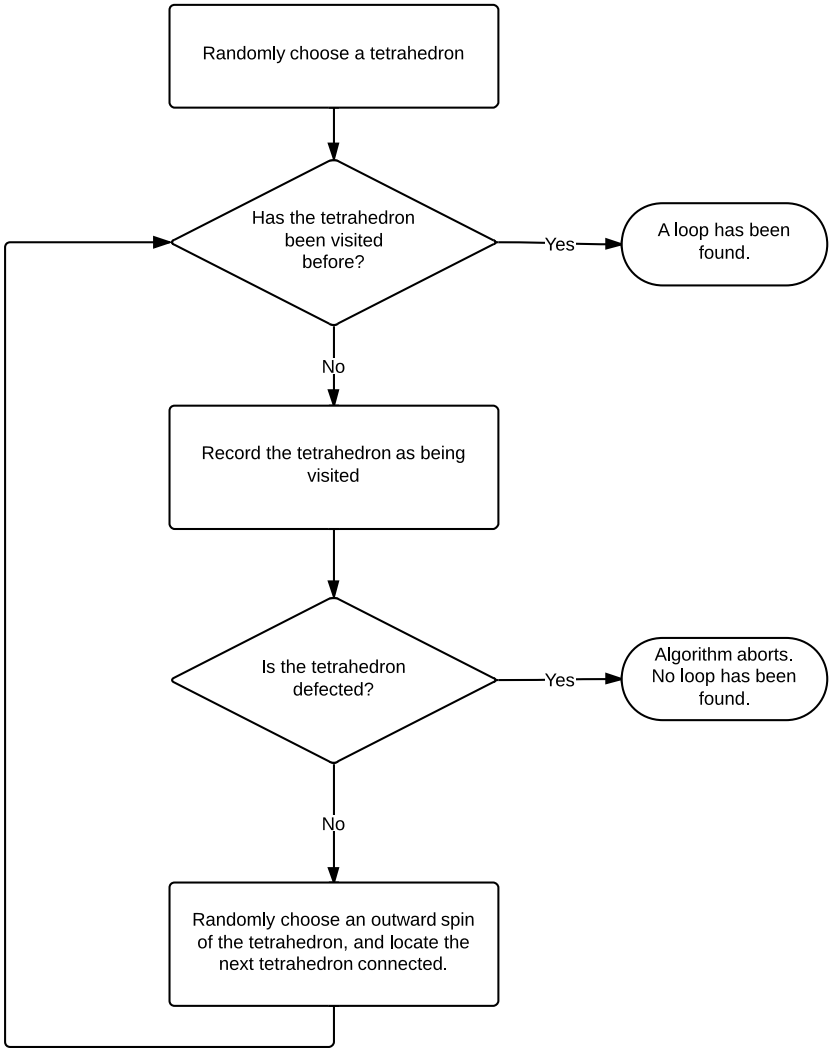

Figure 2.1: Flow chart for the closed loop algorithm.

Note 2

Note also that to achieve ergodicity, the loops need to be able to wrap around the system (with periodic boundary condition), since any local loops do not change the total mag-

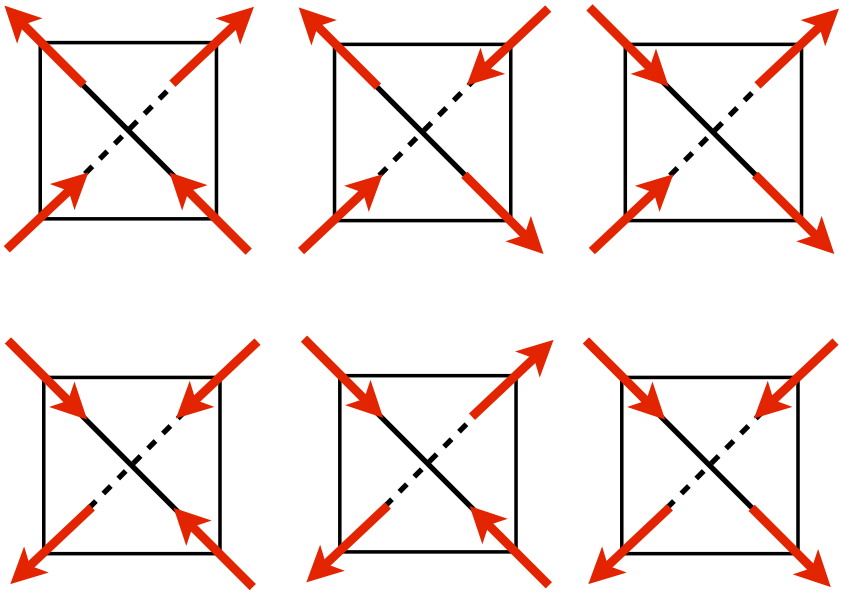

Figure 2.2: Six possible ice rule states for a tetrahedron.

netization of the system. The loops that wrap around the system are referred to as a *topological fluctuation* [49].

Note 3

The smallest loop consists of six spins on a hexagon. Clearly, these hexagon loops are not ergodic as noted in Note 2. But it is still an interesting question to ask whether these hexagon loops are ergodic within a *topological sector*, as defined by the constant magnetization. This question is of particular interest to the recent study of possible spin liquid states for quantum spin ices, where the hexagonal flippable loops serve as the quantum tunnelling among ice states. [38, 50]

In general the answer is no. For example, we consider the two states both in the topological sector of zero magnetization. In Fig. 2.3, we plot two zero total magnetization ice-rule states. One of the shown states is the magnetic ground state found in a previous

Monte Carlo study of the dipolar spin ice, [48] and there is no flippable hexagon loops in such a state. The other one, which we will encounter in later chapters, possesses a zero total magnetization, and has within the state flippable hexagon loops, as shown by the shaded green plaquettes. Therefore, it is impossible to connect the two states with only hexagon loops even though they are of the same topological sector defined by zero magnetization.

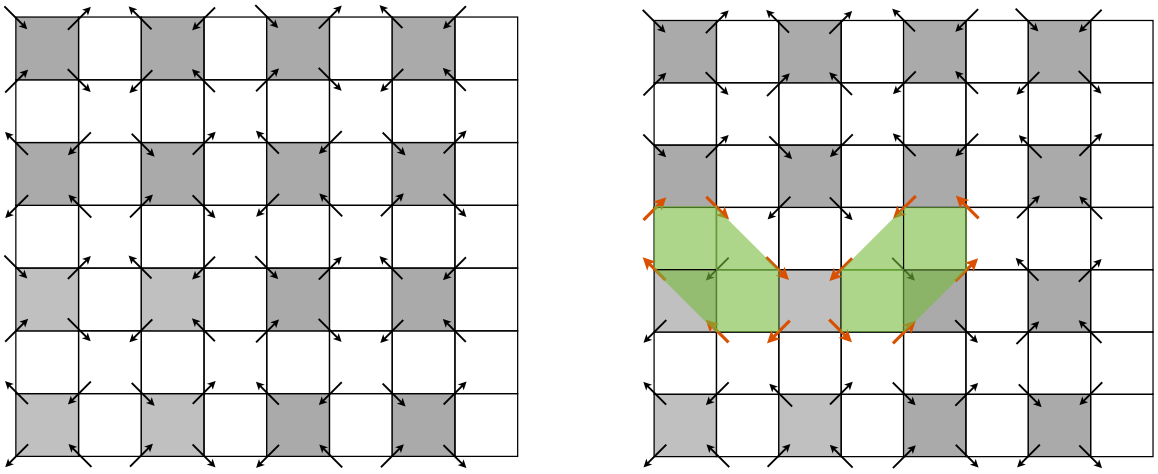

Figure 2.3: Single chain vs. double chain. The green plaquette: six spins on a hexagon forming a flippable loop.

2.2.3 Open loop algorithm

For the diluted spin ice problem, we also use an open loop algorithm to restore ergodicity at low temperatures.

Dilution, as we will discuss further in Chapter 3 on diluted spin ices, "removes" the Ising spins from the pyrochlore lattice. This creates tetrahedra in the lattice possibly with three, two and one spins left.

Consider the case for a tetrahedron with three spins left. With only nearest-neighbour interaction present, the lowest energy states for the three-spin tetrahedron are the two-in-one-out or two-out-one-in configurations. For convenience, we now refer to the two-in-one-out configuration as charge +1 and the two-out-one-in configuration as charge −1. In Fig. 2.4 we depict a scenario with two spins diluted, thus with four three-spin tetrahedron. Also it happens that the charges ±1 form two dipoles about the two diluted sites. However, the energy of the system would be exactly the same regardless of the sign of the charges on the three-spin tetrahedra.

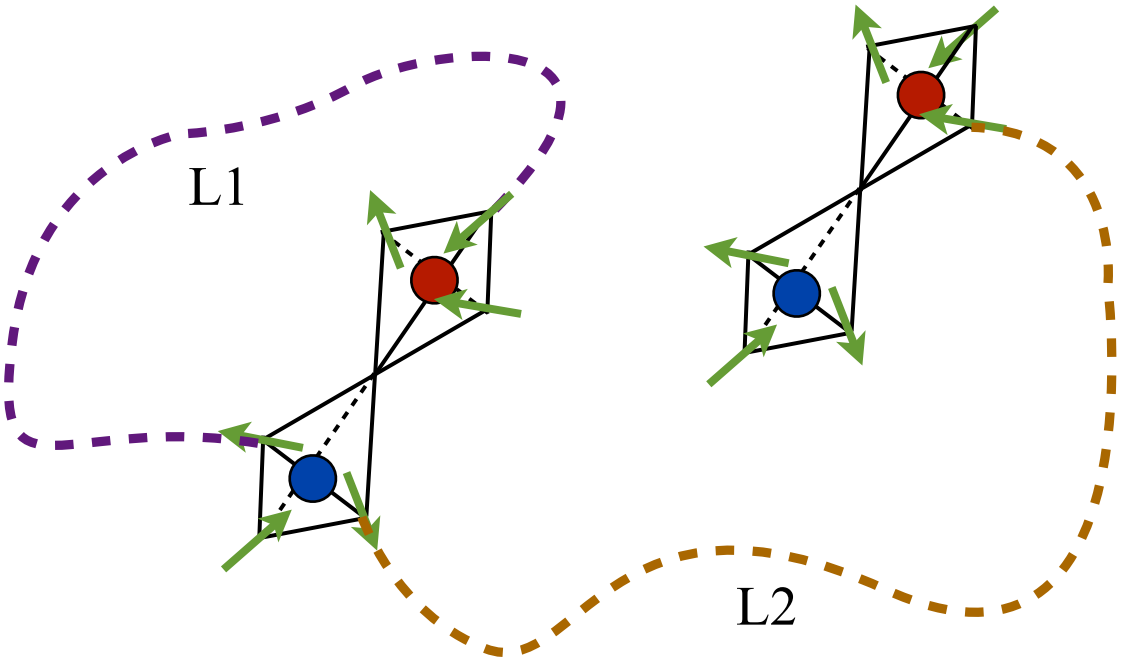

Figure 2.4: Open loop schematic

For example, the ±1 charges on the left charge dipole object can be swapped by flipping a chain of spins along path $L1$. Or two +1 charges can both appear on the left dipole and two −1 charges can both appear on the right dipole by flipping a chain of spins along path

$L2$. (The ice rule conditions along paths $L1$ and $L2$ are always satisfied.) To maintain the ergodicity of the system, we require that all these degenerate states are sampled in the Markov process even at low temperatures.

Clearly single spin flip updates suffer the same problem as we discussed in the closed loop algorithm subsection. By creating a gapped excitation in the system, the acceptance rate is doomed to vanish at low temperatures. The closed loop algorithms on the other hand, do not change the sign of the above defined charges, even if we modify the algorithm to allow trespassing defected tetrahedra.

Thus to restore the ergodicity of the diluted system at low temperatures, we implement the *open loop algorithm*, which is exactly the same as the *closed loop algorithm* discussed previously, except that the loop, by construct, starts and ends at charges of opposite signs.

2.3 Measurements in Monte Carlo simulations

In this section we discuss some of the quantities we can measure in a Monte Carlo simulation.

Specific heat and residual entropy

One of the foremost quantities of interest in this thesis is the specific heat, C. It is measured in Monte Carlo simulation by recording the fluctuations in the total energy E of the system

$$C = \frac{\langle E^2 \rangle - \langle E \rangle^2}{k_{\mathrm{B}} T^2}. \tag{2.10}$$

Through the measurement of the specific heat, we can determine the entropy, S, of the system by doing a numerical integration of the specific heat

$$S(T_2) - S(T_1) = \int_{T_1}^{T_2} \frac{C(T)}{T} dT. \tag{2.11}$$

To calculate the absolute entropy for a given temperature, one of the temperatures in the above equation is taken to be infinite. For example, in an Ising system of N spins, we

know that $S(T=\infty) = k_{\mathrm{B}}\ln(2)$, therefore the entropy at T_1 is given by

$$S(T_1) = k_{\mathrm{B}}\ln(2) - \int_{T_1}^{\infty} \frac{C(T)}{T} dT \tag{2.12}$$

The integration to infinity is achieved by first making a measurement to sufficiently high temperatures, where the specific heat is expected to take the form

$$C(T) = A/T^2 + B/T^3 \tag{2.13}$$

from the perspective of a high temperature expansion. Then the parameters A and B of the above form can be fitted. The integration is then separated into two parts:

$$\int_{T_1}^{\infty} \frac{C(T)}{T} dT = \int_{T_1}^{T_{\max}} \frac{C(T)}{T} dT + \int_{T_{\max}}^{\infty} \frac{C(T)}{T} dT \tag{2.14}$$

where the second part can be analytically calculated using the A and B parameters fitted above.

Structure factors

Another quantity that we calculate throughout the thesis is the structure factor of various quantities, for example, the spin-spin correlation function and the neutron scattering. In general we need to calculate quantities of the form

$$S(\vec{q}) = (1/N)\sum_{i,j} \sigma_i \sigma_j e^{i\vec{q}\cdot\vec{r}_{ij}} \tag{2.15}$$

With periodic boundary conditions for a cubic simulation box of linear size L, we have

$$e^{iqL} = 1 \tag{2.16}$$

thus

$$q = 2\pi n/L \tag{2.17}$$

where n is an integer. Therefore the smallest interval in **q**-space for a system of linear size L is

$$\Delta q = 2\pi/L \tag{2.18}$$

We see that the resolution in the **q**-space is restricted by the size of the simulation box.

Bootstrapping for error analysis

In order to evaluate the error bar for various quantities measured, we employ the bootstrapping method [47]. The procedure of the method is the following.

Suppose we want to measure the error for the specific heat, C. Normally we would use Eq. (2.10) for a set of n samplings of the energy from the Monte Carlo simulation $\{E_1, E_2, ..., E_n\}$.

However, in the bootstrap method, we choose randomly from the n samplings n elements within. Note that the same element can be repeated. Thus we get a new set of n samplings of the energy $\{E_1^{(1)}, E_2^{(1)}, ..., E_n^{(1)}\}$. From this new set of sampling we can calculate the specific heat using Eq. (2.10) to get $C^{(1)}$.

The process is then repeated and we get a series of specific heats from the generated sets of samplings, $C^{(1)}$, $C^{(2)}$, $C^{(3)}$, ...

The estimate of the specific heat, is given by the average of these series of specific heats, $\bar{C}$.

The estimate of the error on the specific heat, is given by the standard deviation of the above average value

$$\sigma = \sqrt{\bar{C}^2 - \bar{C}^2} \tag{2.19}$$

For other quantities, the same procedure can be used.

2.4 Bethe tree calculation

In this Section, we summarize the procedure employed in the Bethe tree calculations. The Husimi tree calculation, which we generalize to the case with random site dilution, is in essence a Bethe tree calculation, but with the basic units of the tree structure replaced by tetrahedra. The central idea of the Bethe tree calculation is the derivation of the recursive relations between different layers of the tree structure, thus making the problem exactly solvable. For more details of the method, the reader can refer to the book by Baxter. [51]

Consider the tree structure in Fig. 2.5. Starting from the central site 0, q (in the case of the figure, $q = 3$) branches of sites are grown from shell 1. Then, at each site on shell 1,

$q-1$ branches of lattice sites are grown to form shell 2, and so on for shell 3. The number of sites on each shell r is therefore

$$N_r = q(q-1)^{r-1} \tag{2.20}$$

Such a tree structure is referred to as the Cayley tree.

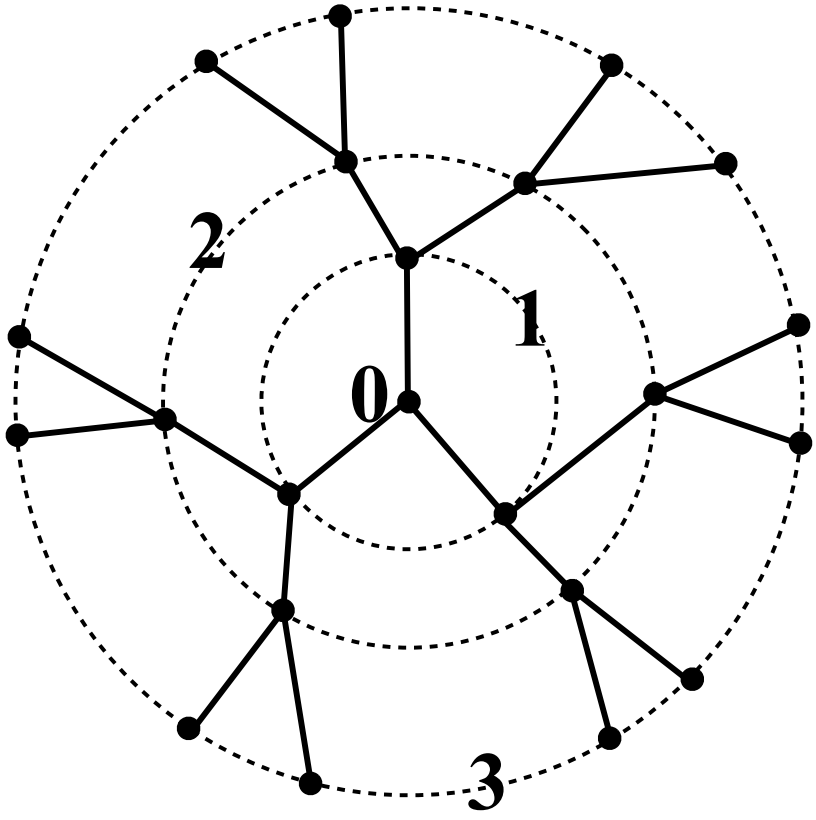

Figure 2.5: Cayley tree structure – numbers indicates the shell each site is on.

Internally for each site of the Cayley tree, there are q sites connected to it, and this is taken as an approximation to a lattice structure with the coordination number q. In an

ordinary lattice, the ratio between the number of sites on the boundary and the number of sites in the interior approaches zero as the size of the system increases. On the Cayley tree, however, as can be seen from Eq. (2.20), this ratio does not go to zero. To avoid the discussion of the boundaries, we consider the case where the number of shells defined above goes to *infinity*. In this case, the Cayley tree becomes the Bethe tree. As noted in the book by Baxter [51], the dimensionality of the Bethe tree (lattice) is infinite.

One important property of the Bethe tree is that its partition function can be calculated exactly. The key idea is in the factoring of the partition function between neighbouring shells. Here we show an example of an Ising Hamiltonian only with exchange interaction on neighbouring sites on the Bethe tree, where the partition function can be written as

$$Z = \sum_{\{\sigma\}} e^{K \sum_{<i,j>} \sigma_i \sigma_j}. \tag{2.21}$$

For simplicity, consider the branch depicted in Fig. 2.6, where σ_0 forms shell 1, σ_1 and σ_2 form shell 2, σ_3 to σ_6 form shell 3, and the rest of the shells (to infinity) attached to sites on shell 3 are omitted in the figure.

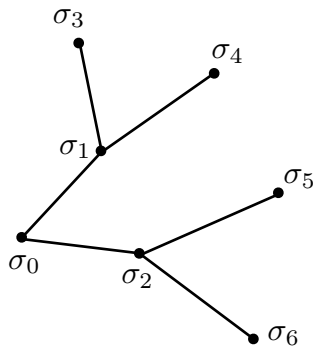

Figure 2.6: Branch of the Cayley tree structure.

The partition function can be written as

$$Z = \sum_{\sigma_0} \sum_{\sigma_1,\sigma_2} \sum_{\{\sigma\}-\{\sigma_0,\sigma_1,\sigma_2\}} e^{K\sigma_0\sigma_1 + K\sigma_0\sigma_2} e^{K\sigma_1\sigma_3 + K\sigma_1\sigma_4} e^{K\sigma_2\sigma_5 + K\sigma_2\sigma_6} e^{K \sum_{<i,j>'} \sigma_i \sigma_j} \tag{2.22}$$

where $\{\sigma\} - \{\sigma_0, \sigma_1, \sigma_2\}$ means the spin configurations without σ_0, σ_1, and σ_2.

Now writing

$$Z_0^{\sigma_0} = \sum_{\sigma_1,\sigma_2} \sum_{\{\sigma\}'} e^{K\sigma_0\sigma_1 + K\sigma_0\sigma_2} e^{K\sigma_1\sigma_3 + K\sigma_1\sigma_4} e^{K\sigma_2\sigma_5 + K\sigma_2\sigma_6} e^{K\sum_{<i,j>'}\sigma_i\sigma_j} \tag{2.23}$$

and

$$Z_1^{\sigma_1} = \sum_{\{\sigma\}-\{\sigma_0,\sigma_1,\sigma_2\}} e^{K\sigma_1\sigma_3 + K\sigma_1\sigma_4} e^{K\sum_{<i,j>'}\sigma_i\sigma_j} \tag{2.24}$$

and

$$Z_1^{\sigma_2} = \sum_{\{\sigma\}-\{\sigma_0,\sigma_1,\sigma_2\}} e^{K\sigma_2\sigma_5 + K\sigma_2\sigma_6} e^{K\sum_{<i,j>'}\sigma_i\sigma_j} \tag{2.25}$$

the partition function can be written as

$$Z = \sum_{\sigma_0} Z_0^{\sigma_0} \tag{2.26}$$

with

$$Z_0 = \sum_{\sigma_1,\sigma_2} e^{K\sigma_0\sigma_1 + K\sigma_0\sigma_2} Z_1^{\sigma_1} Z_1^{\sigma_2}. \tag{2.27}$$

The last equation is in general true, *i.e.*,

$$Z_{n+1}^{\sigma_{n+1}} = \sum_{\sigma_{n1}\sigma_{n2}} e^{-H(\sigma_{n1},\sigma_{n2}|\sigma_{n+1})/k_BT} Z_n^{\sigma_{n1}} Z_n^{\sigma_{n2}} \tag{2.28}$$

where we have deliberately reversed the labeling of the shells, and σ_{n1} and σ_{n2} refer to the two spins on the outer shell.

The magnetization on shell n is

$$m_n = \frac{Z_n^+ - Z_n^-}{Z_n^+ + Z_n^-} \tag{2.29}$$

From Eq. (2.29) and Eq. (2.28), we have the recursive relation for the magnetization

$$m_{n+1} = f(m_n) \tag{2.30}$$

where the fixed point solution is defined by

$$m^* = f(m^*) \tag{2.31}$$

as the solution for the magnetization on the Bethe tree.

In Section 3.3, we extend the above recursive calculation to the problem of spin ice with random site dilution.

2.5 Numerical linked cluster expansion

In this section we review the numerical linked cluster (NLC) expansion [52, 53, 54, 55], which is used in Chapter 7 to study the neutron scattering of the quantum spin ice candidate $Yb_2Ti_2O_7$. For the same material, the numerical linked cluster expansion method has been applied to study the specific heat and magnetization [44, 45].

The basic scheme for the method is to write the extensive quantity to be calculated, P, in the from of

$$P/N = \sum_c L(c) \times W(c) \tag{2.32}$$

where $L(c)$ is the lattice constant and $W(c)$ is the weight of the cluster c. The lattice constant is defined as the number of ways cluster c can be embedded into the lattice, divided by the number of sites in the lattice.

For the weight of a cluster, it is defined as

$$W(c) = P(c) - \sum_s W(s) \tag{2.33}$$

where s is the "sub-clusters" that can be embedded in a cluster c.

Here we provide a simple example for the calculation of the weights. Suppose we want to expand the quantity P in terms of the clusters listed in Fig. 2.7

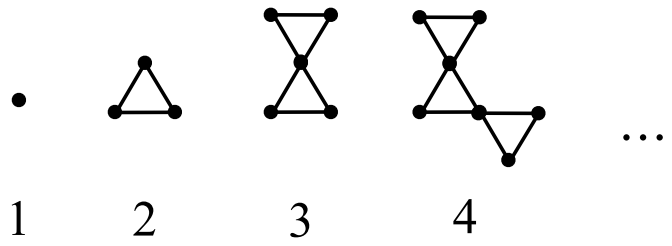

Figure 2.7: Orders of linked clusters in a kagome lattice.

The weight for cluster 1 is just

$$W_1 = P_1. \tag{2.34}$$

To calculate the weight for cluster 2, we need to subtract the weight of cluster 1 from the property of a cluster 2, *i.e.*,

$$W_2 = P_2 - 3W_1. \tag{2.35}$$

Carrying with the program, we have for cluster 3

$$W_3 = P_3 - 2W_2 - 5W_1, \tag{2.36}$$

and for cluster 4

$$W_4 = P_4 - 2W_3 - 3W_2 - 7W_1, \tag{2.37}$$

and so on for higher order clusters.

The extensive properties of each cluster, P, can be calculated, from which weights for each order of cluster can be obtained through the above program. Then, using the lattice constants, through Eq. (2.32), we can obtain any property of the lattice systematically to any order we want.

However, in most practical calculations, two technical difficulties prevent us from achieving very high order of cluster calculation. First is that the calculation of the properties of a high order cluster becomes difficult. Suppose we want to calculate through exact diagonalization for the cluster properties, the computer memory requirement grows exponentially as a function of the number of sites in the cluster. Second is that the bookkeeping of the lattice constants and the embedding of sub-clusters quickly becomes tediously complicated as we reach for higher order clusters. Separate computer codes have to be written to facilitate such bookkeeping. Some details of such computer codes can be found in the book by Oitmaa *et. al.* [55]

Chapter 3

Diluted Dipolar Spin Ice

Water ice, as discussed in Chapter 1, possesses Pauling's residual entropy $k_B/2\ln(3/2)$, which can be estimated from the proton (H^+) disorder in a crystalized oxygen diamond structure.[4] Interestingly it was found that as water ice is doped with alkali hydroxides, K(Rb)OH, the residual entropy is eliminated through the latent heat associated with a first order transition to a long-range proton-ordered ice state [56], *i.e.*, the third law of thermodynamics is recovered with added impurities in water ice. Such experiment suggests that the proton disorder in the ice state is unstable against impurities. Yet it remains unclear what is the precise mechanism via which alkali hydroxides in the water ice system promotes the development of long-range order [57].

Such a phenomenon in water ice relates to one of the main questions in this thesis: how perturbations (in water ice, doped impurities) affect the cooperative paramagnetic state of a frustrated system. Particularly, how does the residual entropy of a frustrated ground state depend on the added perturbations. It is interesting to ask whether the magnetic spin ice analogue of water ice could also display some interesting behaviour when subjected to the addition of random impurities.

In this chapter, we study the perturbation of magnetic site dilution of spin ice. Experimentally, site dilution can be achieved in $Dy_2Ti_2O_7$ and $Ho_2Ti_2O_7$ through the replacement of the rare earth ions Dy^{3+} and Ho^{3+} by non-magnetic Y^{3+} ions [2], with the general chemical formulae for both materials being $Dy_{2-x}Y_xTi_2O_7$ and $Ho_{2-x}Y_xTi_2O_7$, respectively. The close ionic radius of Y^{3+} with that of Dy^{3+} and Ho^{3+} allows for a substitution that causes negligible local lattice deformation and strain. As a first approximation, the dilution of

Dy^{3+}/Ho^{3+} by Y^{3+} can thus be viewed as the mere replacement of the Dy^{3+}/Ho^{3+} magnetic species by a magnetically inert substitute. This is the view that we shall confirm in Section 3.1.

A recent neutron scattering experiment [58] shows no sign of long-range ordering in $Ho_{2-x}Y_xTi_2O_7$ down to 30 mK for x = 0.3 and x = 1.0. On the other hand, specific heat measurements have found that the low-temperature residual entropy, $S_{\rm res}$, of diluted $Dy_{2-x}Y_xTi_2O_7$ and $Ho_{2-x}Y_xTi_2O_7$ spin ices display a non-monotonic dependence on the level of dilution [2]. A calculation generalizing Pauling's argument [4] to the case of site dilution of a nearest-neighbour spin ice model [22] was able to qualitatively account for such a non-monotonic behaviour [2]. However, the apparent systematic departures between the generalized Pauling's argument and the experimental results as well as the differences between Dy− and Ho− based materials [2] have so far remained unaddressed. It was suggested in the previous work [2] that the residual entropy may be material-dependent and have a more drastic non-monotonic dependence on the levels of dilution than the analytic generalized Pauling's argument does. The reason for these differences might be caused, for example, by the extra complexities of the long-range dipolar interactions compared with the nearest-neighbour model. These are the questions we attempt to answer in this chapter of the thesis. Specifically, we address and rationalize quantitatively the origin of the difference in residual low temperature entropy between $Dy_{2-x}Y_xTi_2O_7$ and $Ho_{2-x}Y_xTi_2O_7$ as well as with the generalized Pauling's argument as originally presented by Ke *et al.* [2].

Besides these questions directly related to experimental observations, the theoretical motivations for this work are the following. Firstly we find in our attempt to model the diluted spin ices $Dy_{2-x}Y_xTi_2O_7$ and $Ho_{2-x}Y_xTi_2O_7$ that not only the residual entropy, but also the magnetic specific heat, $C_m(T)$, exhibits non-monotonic behaviours. The non-monotonicity of $C_m(T)$ was already present in the originally reported experimental results [2] and is closely related to the non-monotonicity in the residual entropy. Thus we ask why is there such a non-monotonicity of $C_m(T)$? In the pursuit of this question one may ask a further underlying question: what causes the Schottky specific heat broad peaks in spin ices, and how it relates to the microscopic quantities in the system? These are the questions we will also address in this chapter.

It turns out that the physics involved in the problem of diluted spin ices is very rich. In this chapter we revisit the concept of *projective equivalence* [27] or the *self screening* [28] in diluted spin ice.

The rest of the chapter is organized as follows:

In Section 3.1 of this chapter, we investigate the microscopic models of the diluted spin ices $Dy_{2-x}Y_xTi_2O_7$ and $Ho_{2-x}Y_xTi_2O_7$, which lay the foundations for the subsequent two sections devoted to problems regarding the interplay between dilution and frustration. The model we study involves dipolar interaction and we subsequently refer it as the dipolar spin ice model. Non-monotonicities in the specific heat and residual entropy are observed as numerical facts, in good agreement with experiments by Ke *et al.* [2]. The open loop algorithm is used in the Monte Carlo simulations.

In Section 3.2, we discuss in the simplest frustrated spin ice model, the one with solely nearest-neighbour interactions, how the site dilution affects the calorimetric (specific heat or entropy) observables. A simple approximation, the single tetrahedron approximation (STA), or numerical linked cluster to the first order, is offered in the calculation of the specific heat for all dilution levels. Such an approximation was found to be very accurate in comparison with the Monte Carlo simulations of the corresponding site-diluted nearest-neighbour spin ice model. We investigate the meaning of the broad specific heat peak observed in spin ice $C(T)$ measurements and how it relates to the monopole defect densities. Non-monotonicities observed numerically in Section 3.1 and in experiments are thus physically explained through the STA.

For the nearest-neighbour spin ice model, we also study the stability of the paramagnetic solution through the Husimi cactus method in Section 3.3, which offers insight into why the STA works and sheds light on the problem of absence of a spin glass phase in the model.

In Section 3.4, we return to the discussion of the diluted dipolar spin ice model validated in Section 3.1. One of the most important properties of dipolar spin ice, the self-screening of the dipolar interaction, or projective equivalence, plays a central role in the understanding of diluted dipolar spin ice. Deviations in calorimetric measurements from the dipolar spin ice to the nearest-neighbour spin ice can be understood elegantly through the *un-screening* of the dipolar interactions at the defect sites.

Section 3.5 concludes the chapter.

3.1 Diluted dipolar spin ice

For the canonical spin ice materials $Dy_2Ti_2O_7$ and $Ho_2Ti_2O_7$, the experimental means to achieve dilution is to replace the rare earth ions Dy^{3+} and Ho^{3+} by non-magnetic Y^{3+} ions. The resulting chemical formulae are $Dy_{2-x}Y_xTi_2O_7$ and $Ho_{2-x}Y_xTi_2O_7$. On average, the probability of a site being diluted, μ, relates to x as

$$\mu = x/2. \tag{3.1}$$

One of the first questions to be asked for the diluted chemical compounds $Dy_{2-x}Y_xTi_2O_7$ and $Ho_{2-x}Y_xTi_2O_7$ is whether the Ising nature of the rare earth ions Dy^{3+} and Ho^{3+} still holds once they are replaced by the non-magnetic ion Y^{3+}. Slight difference in the ionic radius between the magnetic ions and the non-magnetic ion may result in local distortions of the lattice, which leads to different crystal field environment at the side of the remaining magnetic ions. An even worse possibility is whether the pyrochlore structure for the rare earth ions endures the change of the chemical composition. In Ke *et al.* [2], the pyrochlore structure was confirmed experimentally through X-ray diffraction, where the diluted samples were found to be in a single phase of the pyrochlore structure for all $x \geq 0$. Without resorting to *ab initio* calculations of the crystal fields for a diluted compound, one can assert the Ising nature of the magnetic moment through measuring the saturated magnetic moments, as reported in Ke *et al.* [2], where *polycrystalline* samples of $Dy_{2-x}Y_xTi_2O_7$ and $Ho_{2-x}Y_xTi_2O_7$ were obtained for measurements. For high enough external magnetic fields in which all the magnetic moments are polarized along the field to the maximum capacity allowed by the ion's anisotropy, one can theoretically calculate the average saturation moment in the poly-crystal as

$$\begin{aligned} < m > &= \int_0^{2\pi} \int_0^{\pi/2} |\vec{m} \cdot \hat{h}| \sin(\theta) d\theta d\psi / (4\pi) \\ &= m/2, \end{aligned} \tag{3.2}$$

where m is the magnetic moment of the rare-earth ion and makes an angle, θ, with the external field with a uniform distribution over the 4π sphere. From crystal field calculations [24] and field experiments, [7] we know that for non-diluted $Dy_2Ti_2O_7$ and $Ho_2Ti_2O_7$ compounds, the magnetic moment $m \sim 10\mu_B$, with easy-axis direction along the local [111] direction. Therefore, if the Ising nature of the rare-earth ions remains for the diluted compounds, one would measure a saturated moment of about $5\mu_B$ per moment Dy^{3+} or

Ho^{3+} ion for a poly-crystal according to Eq. (3.2). Experimentally, in Ke *et al.* [2], the saturation magnetization was found to be $5\mu_B$ at 1.8 K in a magnetic field of 5.5 T. Therefore the Ising nature of the spins was confirmed.

With the Ising nature of the spins intact, the question that follows is whether the model for non-diluted spin ices $Dy_2Ti_2O_7$ and $Ho_2Ti_2O_7$, fitted in previous works [14, 22, 23, 24, 25, 26, 59, 60], can account for the diluted compounds $Dy_{2-x}Y_xTi_2O_7$ and $Ho_{2-x}Y_xTi_2O_7$, respectively, with a mere random site dilution in the Hamiltonian. This is the question we address in the rest of this Section. We approach this problem by performing Monte Carlo simulations of the random site diluted dipolar spin ice models and compare simulated $C(T)$ curves with the ones obtained in the Ke *et al.* [2] experiment. Remarkable agreements are found in the temperature-dependence of the magnetic specific heats, thus validating the simple random site dilution models.

With the model validated, we can readily answer the following experimental question posed by the previous works [2] as numerical facts. Experimentally [2] a significant material dependence of the non-monotonicity of the residual entropy was found, and we find at the end of this Section that the dependence can be traced to the differences of the relative exchange energy scales compared to dipolar energy scale between the $Ho_2Ti_2O_7$ and $Dy_2Ti_2O_7$ in the Hamiltonian.

As a reminder to the reader, this section serves as establishing numerical facts against experimental observations. The development of an understanding of the various physical mechanisms involved are postponed to the latter sections of this chapter.

3.1.1 Microscopic models of diluted dipolar spin ice

In Dy and Ho based spin ice materials, the Dy^{3+} and Ho^{3+} ions carry a large magnetic moment ($\sim 10\mu_B$) [7, 24] and the long-range dipolar interactions cannot be ignored [23, 27, 28]. Given the symmetry of the crystal field ground state [13, 22], the magnetic moments can be well described by vector spins constrained by the single-ion anisotropy to point along their respective local [111] direction (*i.e.*, along the line from the corners to the center of each tetrahedron.) Taking the dipolar interaction and the essentially infinite local Ising anisotropy into consideration, the dipolar spin ice model is defined by the Hamiltonian

[24]:

$$\mathcal{H}_{\text{DSIM}} = \sum_{i>j} \sigma_i \sigma_j \{ \sum_{\upsilon=1}^{3} J_\upsilon \delta_{r_{ij},r_\upsilon} \hat{z}_i \cdot \hat{z}_j + D(r_{\text{nn}}/r_{ij})^3 [\hat{z}_i \cdot \hat{z}_j - 3(\hat{z}_i \cdot \hat{r}_{ij})(\hat{z}_j \cdot \hat{r}_{ij})] \} \tag{3.3}$$

where $\sigma_i = \pm 1$ are Ising spin variables; $\nu = 1, 2$ or 3 refers to first, second or third nearest-neighbours respectively. In the pyrochlore lattice, there are two distinct types of third nearest-neighbours: one type of third-neighbours share a common (first) nearest-neighbour, while the other type of third-neighbours do not. In this chapter, we do not differentiate the two types of third-neighbours, as in the previous work of Yavors'kii *et al.* [24]. J_ν is the exchange interaction couplings for neighbouring spins and r_ν is distance between them. r_{nn} is the distance between nearest-neighbours. $\hat{z}_i$ and $\hat{z}_j$ are the local [111] directions of the respective Ising spins. D is the strength of the dipolar interactions at nearest-neighbour distance. Under such definition of the dipolar term, we have

$$D = \mu_0 (\langle J^z \rangle g \mu_B)^2 / 4\pi r_{\text{nn}}^3 \tag{3.4}$$

where μ_0 is the vacuum permeability, $g\langle J^z \rangle \mu_B$ is the magnetic moment of the spin, and μ_B is the Bohr magneton.

Using the most up-to-date values for J_ν and D that we are aware of, we have with our sign convention of the J_ν's ($J_\nu > 0$ is antiferromagnetic; $J_\nu < 0$ is ferromagnetic): $J_1 \simeq 3.41$ K, $J_2 \simeq -0.14$ K, $J_3 \simeq 0.025$ K and $D \simeq 1.32$ K for $Dy_{2-x}Y_xTi_2O_7$ [24], and $J_1 \simeq 1.56$ K, $J_2 \simeq 0$ K, $J_3 \simeq 0$ K and $D \simeq 1.41$ K for $Ho_{2-x}Y_xTi_2O_7$ [25] For details of the fitting procedures, the reader should refer to the references given. Unfortunately, because of the complexity introduced by the large hyperfine coupling interactions in the Ho-based materials [25], much less systematic calorimetric measurements, which provide many of the constraints used to determine J_1 and J_2, have been carried out on $Ho_2Ti_2O_7$ compared to $Dy_2Ti_2O_7$. Consequently, the J_2 and J_3 values for $Ho_2Ti_2O_7$ have not yet been determined [25] and we therefore set $J_2 = J_3 = 0$ for this compound. As we shall see below, it turns out that this ($J_2 = J_3 = 0$) model describes reasonably well the magnetic specific heat of $Ho_{2-x}Y_xTi_2O_7$ for the $x = 0, 0.4, 0.8$ and 1.2 values considered in this work.

For the diluted samples, we assume that the non-magnetic diluting Y^{3+} ions are introduced randomly while *all* other parameters of the material, and therefore those of the model in Eq. (3.3), are assumed to be unchanged. This means that, until more accurate microscopic ab-initio modeling of the effect of diamagnetic site-dilution in spin ice

compounds becomes available, we ignore local lattice strain effects that may result from the substitution of Dy^{3+} or Ho^{3+} by Y^{3+}. In practice, we thus ignore any changes that may occur in the J_ν exchange couplings and the rare-earth ion magnetic moment μ that would result from variation of the single-ion crystal field ground state wavefunctions. This would seem a reasonable first approximation given the close ionic radius of Y^{3+} with Dy^{3+} and Ho^{3+}. We note in passing that such an approximation has been shown to describe quantitatively quite well the variation of the critical ferromagnetic temperature in Ho^{3+} substituted by Y^{3+} in $LiHo_{1-x}Y_xF_4$ all the way to, [61, 62] and perhaps even including, the dipolar spin glass regime [63, 64]. In practice, the microscopic J_ν's and D in Eq. 3.3 are kept to their pure $Dy_2Ti_2O_7$ and $Ho_2Ti_2O_7$ values while the Ising variables are redefined as $\sigma_i \to \theta_i\sigma_i$, with $\theta_i = 0$ if site i is occupied by non-magnetic Y^{3+} ion or $\theta_i = 1$ if occupied by a magnetic rare-earth ion. Thus, for $[Dy,Ho]_{2-x}Y_xTi_2O_7$, the site-random probability distribution of θ_i, $P(\theta_i)$, is given by $P(\theta_i) = (x/2)\delta(\theta_i) + (1-x/2)\delta(\theta_i - 1)$, where $\delta(u)$ is the Dirac delta function.

The final Hamiltonian reads

$$\mathcal{H}_{\rm DSIM} = \sum_{i>j} \theta_i\theta_j\sigma_i\sigma_j\{\sum_{\upsilon=1}^{3} J_\upsilon \delta_{r_{ij},r_\upsilon}\hat{z}_i\cdot\hat{z}_j + D(r_{\rm nn}/r_{ij})^3[\hat{z}_i\cdot\hat{z}_j - 3(\hat{z}_i\cdot\hat{r}_{ij})(\hat{z}_j\cdot\hat{r}_{ij})]\} \qquad (3.5)$$

3.1.2 Monte Carlo methods for the dilution problem

We carried out Monte Carlo simulations for the above dipolar spin ice model for $Dy_{2-x}Y_xTi_2O_7$ and $Ho_{2-x}Y_xTi_2O_7$ at various Y^{3+} concentrations x. We used a conventional cubic unit cell containing 16 spins, with the system of linear size L having $16L^3$ spins. Dilution is treated by randomly taking spins out of the system, and a disorder average over at least 50 different random dilution configurations was performed for each dilution level x. Periodic boundary conditions are used, and we implement the infinite range dipole interactions using the Ewald summation technique [65]. Most of the data production was done with $L = 4$ while, for higher dilutions ($x \geq 1.5$), we used $L = 5$ to have a reasonably large number of spins remaining in the system. For most, if not all, of the results presented below, very little system size dependence for the magnetic specific heat, $C_{\rm m}(T)$, data was observed.

A conventional single spin-flip Metropolis algorithm was employed for the Monte Carlo simulation. In addition, non-local *close loop* and *open loop* updates are used as well to maintain ergodicity of the ice states, as discussed in Chapter 2. In order to further facilitate

the equilibrium of the system, we have also employed the parallel tempering technique which is commonly used in the study of spin glass models [66].

The magnetic specific heat was determined by performing a disorder average of the energy fluctuations:

$$C_{\rm m}(T) = \frac{[\langle E^2\rangle - \langle E\rangle^2]}{k_{\rm B}T^2} \tag{3.6}$$

where $\langle ...\rangle$ and $[...]$ are thermal and disorder averages, respectively.

There are two sources of errors in our simulations. One is from the Monte Carlo statistics for each disorder realization. The other is from the sample-to-sample fluctuations for different realizations of the sample dilution level, since in the simulations we are dealing with a finite-sized system. We checked that the error bars from the Monte Carlo statistics are generally very small (less than one percent for all cases we checked). So we ignore this type of error and only consider the error from sample-to-sample fluctuations. Therefore our error bars are given by

$$\sigma = \sqrt{\frac{1}{n-1}([C^2] - [C]^2)} \tag{3.7}$$

where $n = 50$ is the number of disorder realizations.

3.1.3 Specific heat for $Dy_{2-x}Y_xTi_2O_7$ and $Ho_{2-x}Y_xTi_2O_7$

We plot in Fig. 3.1 the magnetic specific heat versus temperature, $C_{\rm m}(T)$, obtained from Monte Carlo simulations of Eq. (3.5) (solid lines) for various levels of dilution in comparison with experimental data (open black circles for $Dy_{2-x}Y_xTi_2O_7$, open red squares for $Ho_{2-x}Y_xTi_2O_7$).

The agreement between our Monte Carlo simulation and the previous experiment [2] is strikingly good for most dilution levels (up to and including $x = 1.7$ for $Dy_{2-x}Y_xTi_2O_7$) and over a rather wide temperature range $T \sim [0.4\text{ K} - 5\text{ K}]$. This is particularly noteworthy given that there is *no* adjustment of the microscopic parameters of the dipolar spin ice Hamiltonian of Eq. (3.5), except for the dilution of spins in the system. From these results, we can immediately conclude that a simple site-diluted version of the DSIM of Eq. (3.5) does capture the dilution physics of *both* materials at a quantitative level. This constitutes the main conclusion of this section.

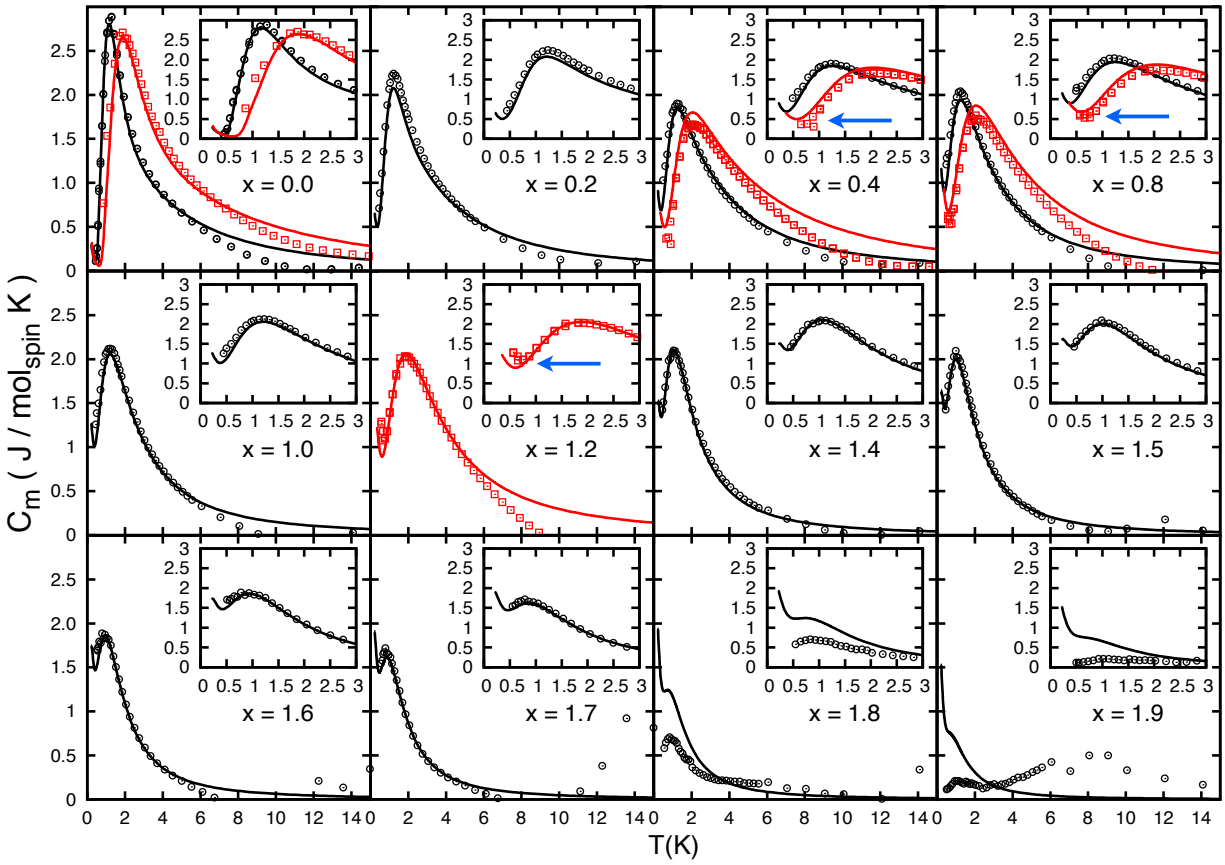

Figure 3.1: Comparison of the magnetic specific heat, $C_{\rm m}(T)$, between Monte Carlo simulations and experiments. Black open circles are for $Dy_{2-x}Y_xTi_2O_7$ experiment, solid black curves are for $Dy_{2-x}Y_xTi_2O_7$ simulations. Red open squares are for $Ho_{2-x}Y_xTi_2O_7$ experiment, and solid red curves are for $Ho_{2-x}Y_xTi_2O_7$ simulations. Insets show an enlargement around the Schottky peak at $T_{\rm p}$, arising from the formation of the spin ice state. The horizontal blue arrows indicate location of $C_{\rm m}(T)$ minima that may be occuring in $Ho_{2-x}Y_xTi_2O_7$. Error bars on the Monte Carlo data are included and for most cases smaller than the width of the lines.

Close inspection of Fig. 3.1 shows that there is a discrepancy in $C_{\rm m}(T)$ between simulation and experimental results for $T \gtrsim 5$ K. Also, the simulation results show a rise of $C_{\rm m}(T)$ as T decreases below a temperature of approximately 0.4 K and 0.6 K for $Dy_{2-x}Y_xTi_2O_7$ and $Ho_{2-x}Y_xTi_2O_7$, respectively, while this behaviour is barely noticeable in the experimental results. We address these two points in further detail in the following discussion, mostly at the phenomenological level, postponing the discussion of the physical implications of these results for the determination of the residual entropy in Section 3.1.4.

High temperature regime

In the "high-temperature regime", typically above 4 K ~ 5 K, we observe that our simulation results for $C_{\rm m}(T)$ depart from the experimental results. Such a discrepancy needs clarification since (i) a demonstration of the validity of the microscopic models considered depends on achieving a good degree of agreement between experimental and Monte Carlo $C_{\rm m}(T)$ curves and since, (ii) as we shall see when discussing the residual entropy in the next subsection, $C_{\rm m}(T)$ for $T \gtrsim 5$ K contributes up to about 10% of the full $\mathrm{R}\ln(2)$ magnetic entropy.

From a high-temperature expansion perspective, the magnetic specific heat is expected to follow a $C_{\rm m}(T) \sim 1/T^2$ form at temperatures large compared to the typical temperature scale T_p, the temperature at which the specific heat peaks, set by the interactions. This form was indeed verified in all our simulation results. In contrast, all the experimental $C_{\rm m}(T)$ data decrease at $T \gtrsim 5$ K significantly faster and are obviously not in agreement with this necessary $1/T^2$ high-temperature form.

We believe this fast drop-off in experiment is likely due to an over-subtraction of the lattice contribution to the total specific heat at these temperatures. The usual method for carrying out such a subtraction relies on an estimated Debye contribution for the acoustic phonons. For example, by considering the temperature range of 10 K $\leq T \leq$ 20 K, one might try to fit the total specific heat to the form $C_{\rm total}(T) = A/T^2 + BT^3$, where the $1/T^2$ part comes from the aforementioned magnetic contribution while the T^3 part is the Debye phonon contribution. Unfortunately, for $T \gtrsim 10$ K, background contributions from other "components" of the experimental setup become significant. In particular, we note that in order to facilitate thermal conduction in the measurements, Ag powder was mixed into the spin ice powder. At these higher temperatures, the specific heat contribution from the

Ag powder component becomes larger than the magnetic component that we are trying to isolate. Fitting the phonon contribution with all these high temperature background contributions embeds errors in the A and B fitting parameters, which then causes an over-subtraction for the magnetic specific heat $C_m(T)$ for $T \geq 5$ K.

Low temperature regime

We now turn to the low temperature regime of the $C_{\rm m}(T)$ curves, below the prominent peak at $T = T_p$, with $T_p \sim 1$ K for $Dy_{2-x}Y_xTi_2O_7$ and $T_p \sim 1.9$ K for $Ho_{2-x}Y_xTi_2O_7$. In particular, we discuss the minima found in the simulation results for all dilution levels (including $x = 0$, although in this case the minimum is more subtle [48, 67]) in both the Dy and Ho spin ices (see solid curves in insets of Fig. 3.1). As we shall discuss in Section 3.1.4 below, the integrated entropy is highly dependent on the $C_{\rm m}(T)$ results at low temperatures since $dS = \frac{C_{\rm m}(T)}{T} dT$.

It is known that in simulations of the non-diluted dipolar spin ice model [48, 67], a $C_{\rm m}(T)$ minimum arises from the development of extra correlations within the spin ice state caused by the dipolar interactions, with the system eventually undergoing a transition to long-range order at $T_c \sim 0.13D$ ($T_c \sim 0.18$ K, for the J_1, D parameters appropriate for $Ho_2Ti_2O_7$ [48, 67].) For such minima to be found in non-diluted spin ice simulations, collective spin update algorithms such as the closed loop updates have to be included. On the other hand, it is very difficult for experiments to display such a $C_{\rm m}(T)$ minimum and the long-range order transition, due to the freezing of spins below a temperature $T \sim 0.5$ K [1, 68].

For the diluted systems, the existence of the minima in our simulation suggests that a dynamical arrest similar to the one in the non-diluted systems does occur. Indeed, as discussed in Section 2.4, equilibrium in simulations cannot be achieved without using collective update algorithms, further supplemented by parallel tempering. For $Dy_{2-x}Y_xTi_2O_7$, having used a ^{3}He cryostat in Ke *et al.* [2], the experiments stop at temperatures just above the simulation-predicted minima. For $Ho_{2-x}Y_xTi_2O_7$, the $C_{\rm m}(T)$ minima are perhaps experimentally observed (see horizontal blue arrows in the insets of Fig. 3.1), although the experimental data points below the minima do not agree very well with the simulation results. In this case, one should be warned that there is a large nuclear contribution at $T \lesssim 0.5$ K for $Hi_2Ti_2O_7$ [25] Even though this nuclear component has been subtracted, [2]

its existence nevertheless complicates the possible experimental observation of the minima in the magnetic-only part, $C_{\rm m}(T)$, of the total specific heat $C(T)$.

While the present experimental data do not allow for a convincing observation of the minima in $C_{\rm m}(T)$, we unquestionably find them in the Monte Carlo simulations of the microscopic dipolar spin ice models, Eq. 5.1. The minima observed in the specific heat simulations of the diluted DSIMs acquires a significant value, as seen in Fig. 3.1, as opposed to the very small values in the non-diluted variants [24, 48, 67]. Furthermore, the broad specific heat peak at $T_p(x)$, which signals the development of ice rule correlations as in the non-diluted Dy and Ho spin ices, is less well defined in the diluted sample. For example, for $x = 1.7$, the peak is more of a feature resulting from a slight drop at about 0.4 K on the rising $C_{\rm m}(T)$ curve as T approaches zero, rather than a well-defined peak. Indeed, at such a high dilution, the ice rules are marginally enforced and the $C_{\rm m}(T)$ peak associated with the development of ice rules fulfilling tetrahedra is not very prominent. As discussed further in Section 3.1.4 regarding the determination of the residual entropy, $S_{\rm res}(T_0)$, at a low temperature T_0, the behaviour of the $C_{\rm m}(T)$ curves suggests that the residual entropy concept employed for non-diluted spin ices *cannot* be readily discussed without a specification of the lowest temperature T_0 at which (equilibrated) experimental data are obtained.

To sum up, there exist significant systematic experimental difficulties in determining the magnetic-only contribution to the specific heat, $C_{\rm m}(T)$, in the high temperature regime ($T \gtrsim 5$ K). For the low temperature regime ($T \lesssim 0.5$ K), in contrast to the non-diluted case, the $C_{\rm m}(T)$ curves from our simulations display clear minima with significant $C_{\rm m}(T)$ values. On the experimental front, these minima may be marginally observed in $Ho_{2-x}Y_xTi_2O_7$ ($x = 0.4, 0.8, 1.2$), but are not observed in $Dy_{2-x}Y_xTi_2O_7$. At the same time, the very good agreement between the experimental and Monte Carlo $C_{\rm m}(T)$ for both materials (for x up to $x = 1.8$ for $Dy_{2-x}Y_xTi_2O_7$) and for 0.5 K $\lesssim T \lesssim$ 5 K seemingly vindicates the applicability of a simple site-diluted version of the dipolar spin ice model to describe $Dy_{2-x}Y_xTi_2O_7$ and $Ho_{2-x}Y_xTi_2O_7$. We thus take the following approach. Having demonstrated good agreement between experiments and models in the temperature range $T \sim$ [0.4 K – 5 K] for both $Dy_{2-x}Y_xTi_2O_7$ and $Ho_{2-x}Y_xTi_2O_7$, in order to remedy the aforementioned experimental caveats, we henceforth only consider the simulation data of Eq. (3.5) to expose accurately what is the x dependence of the low-temperature residual entropy, $S_{\rm res}(T_0)$ of the $Dy_{2-x}Y_xTi_2O_7$ and $Ho_{2-x}Y_xTi_2O_7$ diluted dipolar spin ice materials.

3.1.4 Non-monotonic residual entropy

Since Eq. 3.5 describes an Ising model, the entropy at infinite temperature per mole of spin is $\mathrm{R}\ln 2$. Thus the residual entropy at a given temperature T_0 can be written as

$$S_{\mathrm{res}}(T_0) = \mathrm{R}\ln 2 - \int_{T_0}^{\infty} \frac{C_{\mathrm{m}}(T)}{T} dT \tag{3.8}$$

We plot $S_{\mathrm{res}}(T_0)$ obtained from the Monte Carlo simulations for different choices of T_0, where the integration up to infinite temperature is done by fitting the $C_{\mathrm{m}}(T)$ curves at high temperatures (> 10 K) to the $1/T^2$ form.

The results from these Monte Carlo determinations of the residual entropy, $S_{\mathrm{res}}(T_0)$ are shown in Fig. 3.2 for both $Dy_{2-x}Y_xTi_2O_7$ and $Ho_{2-x}Y_xTi_2O_7$. We confirm the previous observation made by Ke *et al.* [2] that there does exist (i) a systematic non-monotonic x dependence of $S_{\mathrm{res}}(T_0)$ and (ii) that there is a difference in $S_{\mathrm{res}}(T_0)$ between the two materials. The main new result here is that, thanks to the ability of the Monte Carlo simulations to provide accurate $C_{\mathrm{m}}(T)$ data for $T \lesssim 0.5$ K and $T \gtrsim 10$ K ranges, we can now *robustly* expose both the x dependence and the specific material dependence of S_{res}. Supplementing the previous report [2], we are now also uncovering the importance of specifying the base temperature T_0 used in the determination of $S_{\mathrm{res}}(T_0)$. Such a need to specify T_0 does not arise in previous work on non-diluted $Dy_2Ti_2O_7$ and $Ho_2Ti_2O_7$ because $C_{\mathrm{m}}(T)$ practically drops to zero near $T \sim 0.4$ K and S_{res} remains close to the Pauling value for $C_{\mathrm{m}}(T)/T$ integrated upward anywhere from 0.4 K $\pm$ 0.1 K. In particular, as a final and crucial observation, we note that for all values of x and for a given T_0, $S_{\mathrm{res}}(x)$ is *lower* for $Ho_{2-x}Y_xTi_2O_7$ than for $Dy_{2-x}Y_xTi_2O_7$, in *contrast* to the conclusion that was reached in Ke et al. [2]. However, as a remark on the status of research of non-diluted $Dy_2Ti_2O_7$, a recent experiment [1] found non-vanishing $C_{\mathrm{m}}(T)$ values near $T \sim 0.4$ K, a point we shall pick up in Chapter 5.

To reiterate, as seen in Fig. 3.2, the results of the residual entropy for the diluted ($x > 0$) dipolar spin ice model depend strongly on the choice of T_0, in contrast to the non-diluted case ($x = 0$), in which the $S_{\mathrm{res}}(T_0)$ for different T_0 almost collapse onto the calculation of the Pauling's entropy, $(\mathrm{R}/2)\ln(3/2)$. For $x = 0$, the collapse of the $S_{\mathrm{res}}(T_0)$ for different T_0's is the manifestation of the *projective equivalence* [27], which states that the quasi-ground state properties of the dipolar spin ice model can be described by an effective nearest-neighbour spin ice model up to corrections falling off as $1/r^5$. But for $x > 0$, the T_0 dependence suggests the failure of the projective equivalence upon dilution.

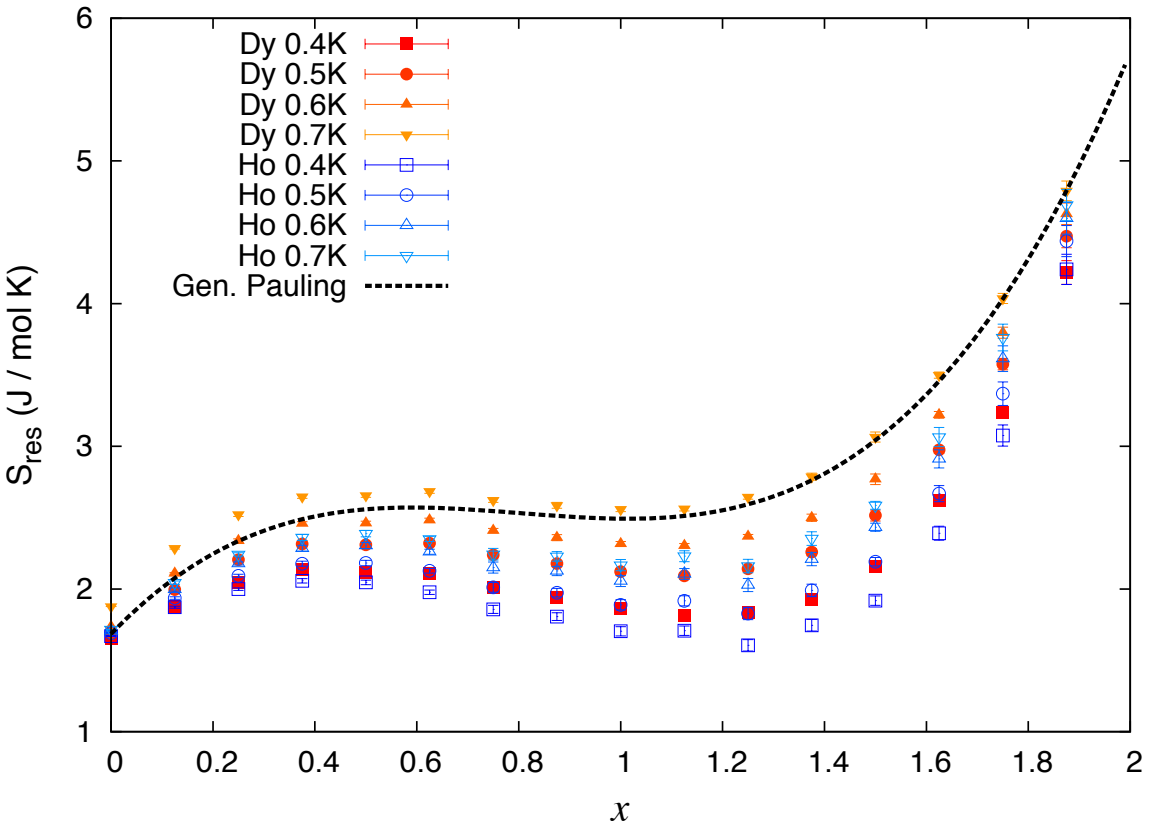

Figure 3.2: Residual entropy determined from Monte Carlo simulations for both $Dy_{2-x}Y_xTi_2O_7$ and $Ho_{2-x}Y_xTi_2O_7$ with different low temperature limits T_0. The dotted black curve shows $S_{\rm res}$ given by the generalized Pauling's argument [2].

The overall non-monotonic trend of the entropy from the generalized Pauling's argument being in rough qualitative agreement with the results for the real materials suggests a remnant of the diluted nearest-neighbour spin ice model physics in the diluted dipolar spin ice model. Yet, the two materials, because of their different magnetic interactions, display distinct $S_{\rm res}(x, T_0)$. Specifically, the two materials possess different energy scales for their nearest-neighbour energy scale, J_1, relative to the dipolar interactions, D (see Eq. (3.5)). Thus, the higher overall temperature scale for the formation of the spin ice state in $Ho_{2-x}Y_xTi_2O_7$ compared to $Dy_{2-x}Y_xTi_2O_7$ results in a residual entropy $S_{\rm res}(T_0, x)$ for $Ho_{2-x}Y_xTi_2O_7$ lower than for $Dy_{2-x}Y_xTi_2O_7$ for all x and *for a given* T_0. However, a

choice of T_0 that varies for different values of x for a given compound will lead to a less smooth $S_{\rm res}(T_0, x)$ evolution than the one seen in Fig. 3.2.

Revisiting the task of comparing $S_{\rm res}$ from Monte Carlo and from the previous experimental work [2], we offer a two-point summary of the above discussions for the origin of the discrepancy between them. Firstly, the discrepancy arises from the experimental uncertainties associated with high and low temperature regimes, as we discussed in the Section 3.1.3. Secondly and more conceptually, it is the low temperature rising of the specific heat in diluted samples, which carries an indication of the physics induced by dipolar interactions beyond nearest-neighbour spin ice upon dilution, and which is omitted in the experimental work by Ke *et. al.*. The merit of this work is to quantitatively expose this physics as far as the accuracy of the microscopic model goes.

3.1.5 Large level of dilution

It is perhaps remarkable that the nice agreement found between Monte Carlo simulations and experiments shown in Fig. 3.1 for $Dy_{2-x}Y_xTi_2O_7$ for $0 < x \leq 1.7$ disappears rather abruptly and essentially completely going from $x = 1.7$ to $x = 1.8$ and $x = 1.9$ (see Fig. 3.1). The only similarity left is that both Monte Carlo and experimental $C_{\rm m}(T)$ data show a small low-temperature hump at a temperature $T \sim 0.8$ K that somewhat agrees between Monte Carlo and experiments (see insets of Fig. 3.1 for $x = 1.8$ and $x = 1.9$, which are further reproduced in Fig. 3.3). Figure 3.3 further illustrates that, despite the large dilution of magnetic ions for $x = 1.8$ and $x = 1.9$, finite size effects remain negligible. We are thus rather confident that the discrepancy between simulation and experimental results does not arise from computational pitfalls, but is a genuine physical difference.

Presently, we do not have a good suggestion as to what may cause such a sudden (in terms of "just" going from $x = 1.7$ to $x = 1.8$) and large discrepancy between experiments and Monte Carlo data. A possible mechanism includes the development of a dipolar Ising spin glass state [63, 64] inhibiting thermal equilibrium in the experiments, though that should not be at play at temperatures as high as 1 K. Another possibility includes a significant random local lattice distortion developing upon reaching large levels of dilution. This would affect the J_ν couplings and the crystal field, hence the magnetic moment μ and the coupling D compared to the values determined for $x = 0$. A third possibility is that of a highly uneven distribution of the magnetic ions as $x \to 2$. These last two possibilities

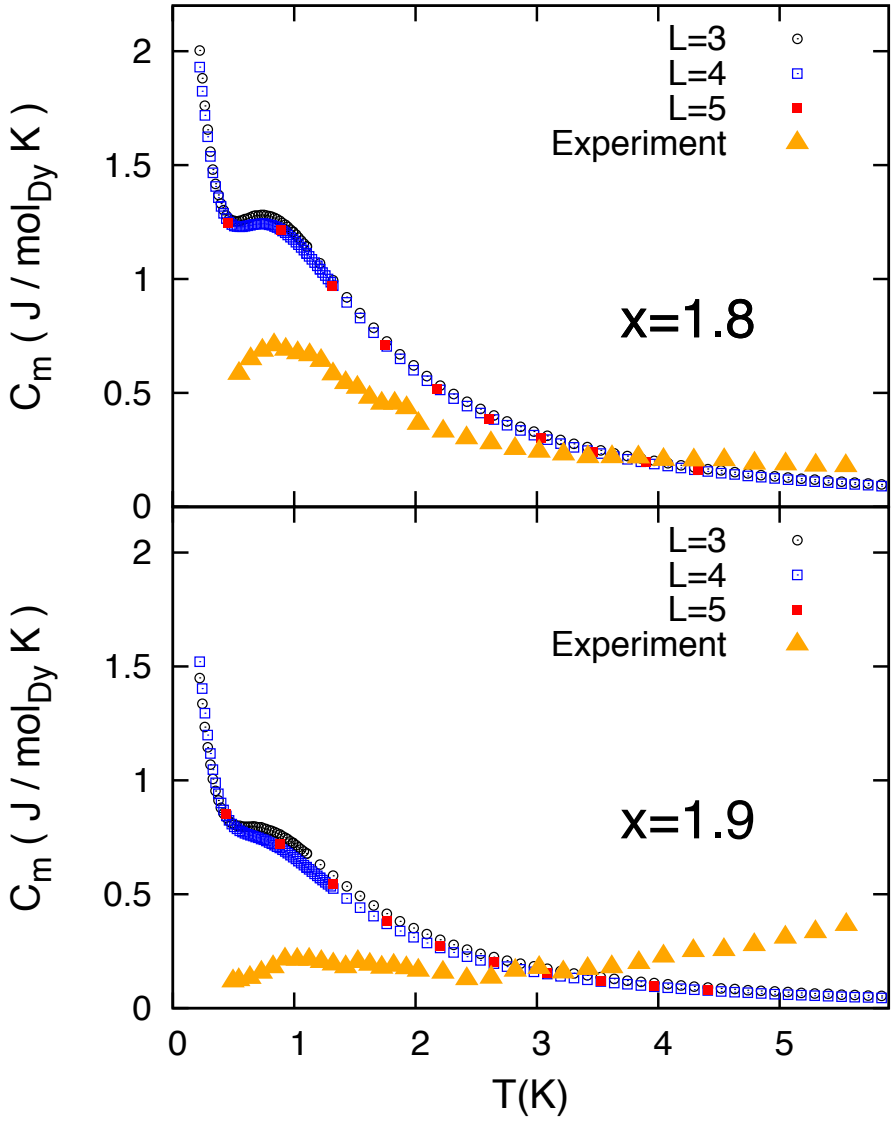

Figure 3.3: Comparison of Monte Carlo specific heat with experimental results for $Dy_{2-x}Y_xTi_2O_7$ for sizes $L = 3, 4, 5$ for $x = 1.8$ (top panel) and $x = 1.9$ (bottom panel).

seem rather unlikely given the close ionic radius of Y^{3+} with Dy^{3+} and Ho^{3+} and the solid solution that exist in the whole $x \in [0, 2]$ range. More experiments are definitely required to understand the $x \to 2$ behaviour of diluted spin ice materials.

3.1.6 Error analysis

As shown in Section 3.1.5, there is a clear disagreement between the Monte Carlo results and the experiments for the highly diluted samples of $Dy_{2-x}Y_xTi_2O_7$ for $x = 1.8$ and $x = 1.9$. One of the concerns about the Monte Carlo methods is that at such highly diluted samples, we might not have enough disorder samples to achieve a good sample average. Throughout our simulations, typically 40~50 samples are used for the disorder average. To address the concern of on insufficient number of disordered samples, we increased the number of samples by 2500%, *i.e.*, with 1000 disordered samples for the $x = 1.8$ and $x = 1.9$ dilution levels.

Some of the results from averaging over the 40 samples and averaging from the 1000 samples are listed in Table 3.1

Dil(x)	T(K)	$L = 5$, $N_s = 40$	$L = 5$, $N_s = 1000$	relative difference	$L = 4$, $N_s = 50$
1.8	0.4408	1.265042	1.286582	1.67 %	1.265877
1.8	1.3224	0.983148	0.963335	2.06 %	0.970326
1.8	2.2040	0.516152	0.499696	3.29 %	0.512963
1.9	0.4408	0.851199	0.865990	1.71 %	0.844197
1.9	1.3224	0.543663	0.550485	1.24 %	0.525173
1.9	2.2040	0.272823	0.273045	0.08 %	0.264252

Table 3.1: Magnetic specific heat results, $C_m(T)$, from different number of samples for $L = 5$. The relative differences are also calculated for $L = 5$. As a reference, $C_m(T)$ values for the $L = 4$ are also listed.

It can be seen from the table that with 25 times more samples, the differences in the specific heat are averages only a few percents. On the other hand, the discrepancy between experimental $C_m(T)$ and Monte Carlo $C_m(T)$ is much more significant.

In addition, we plot the histogram of the specific heat from the 1000-sample simulations in Fig. 3.4. The histograms show that the specific heat results for different realizations of dilution disorder approximately follow a normal distribution.

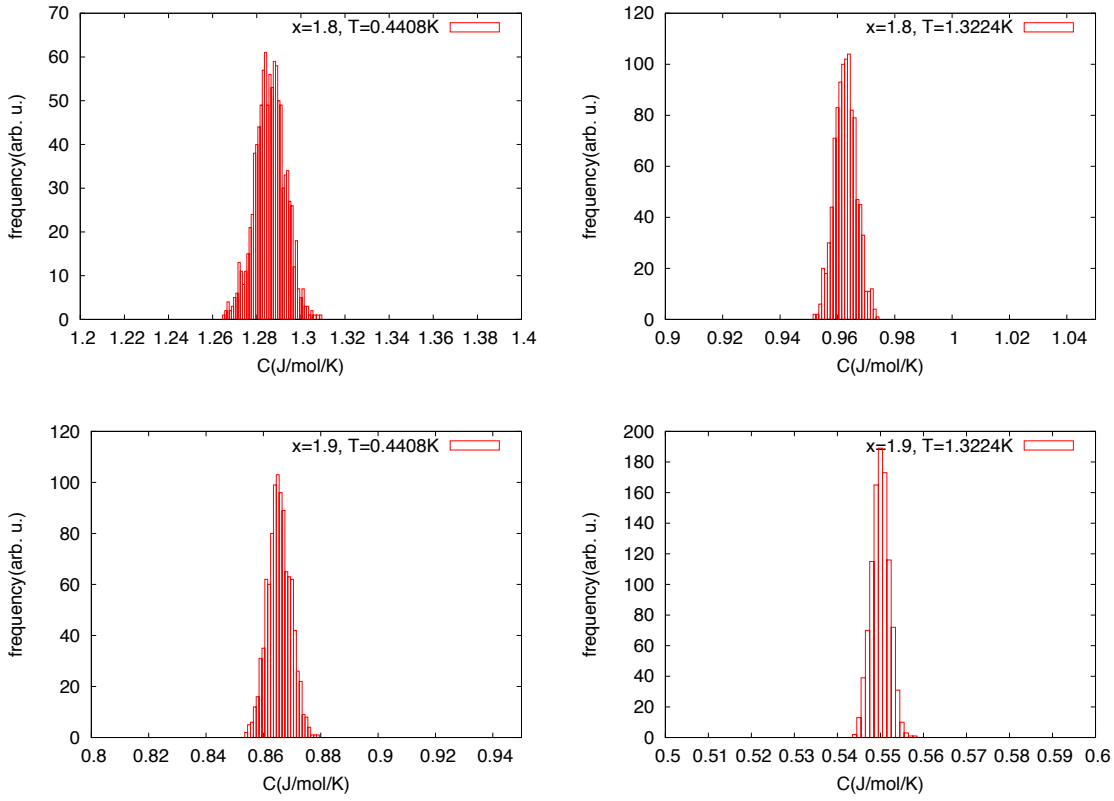

Figure 3.4: Specific heat histogram for different realizations of dilution disorder at large dopings of $x = 1.8$ and $x = 1.9$

Error bars

There are two sources of errors in our simulations. One is from the Monte Carlo statistics for each disorder realization. The other is from the sample-to-sample fluctuations for different realizations of the sample dilution level, since in simulation we are dealing with a finite-sized system.

We checked that the error bars from the Monte Carlo statistics are generally very small. Such error bars can be calculated from the bootstrap method presented in Section 2.3. Here we consider a few examples (for one realization of each dilution level at various

temperatures) for $Dy_{2-x}Y_xTi_2O_7$ with a system size $L = 4$:

Dilution level(x)	Temperature(K)	Specific heat (C)	Bootstrap error (σ)
0.2	0.5	0.657478	0.002475
0.2	1.0	1.941898	0.007017
0.2	1.5	1.950690	0.007584
0.2	2.0	1.581808	0.005756
0.2	2.5	1.320090	0.004446
1.0	0.5	1.100804	0.003977
1.0	1.0	2.019855	0.007193
1.0	1.5	1.988720	0.006108
1.0	2.0	1.657819	0.006050
1.0	2.5	1.318661	0.004542
1.7	0.5	1.462010	0.005824
1.7	1.0	1.683816	0.007273
1.7	1.5	1.320184	0.005308
1.7	2.0	0.914419	0.003614
1.7	2.5	0.636502	0.002418

Table 3.2: Monte Carlo specific heat and bootstrap errors for $Dy_{2-x}Y_xTi_2O_7$, and for a simulation box of size $L = 4$.

As illustrated in Table 3.2, the statistical errors from the Monte Carlo are very small for the cases we checked. We therefore ignore this type of error and only consider the sample-to-sample fluctuation error.

The sample-to-sample fluctuation error is given by

$$\sigma = \sqrt{\frac{1}{n-1}([C^2] - [C]^2)} \tag{3.9}$$

over an ensemble of 50 samples for a given dilution level.

Generally, this type of error turns out to be small. In Table 3.3 we show some numerical examples for $Dy_{2-x}Y_xTi_2O_7$ for a simulation box size of $L = 4$.

Dilution level(x)	Temperature(K)	Specific heat (C)	Sample fluctuation error (σ)
0.2	0.2204	0.654985	0.004210
0.2	1.1020	2.044120	0.004781
0.2	2.2040	1.473623	0.001712
1.0	0.2204	1.266760	0.012628
1.0	1.1020	2.039623	0.011120
1.0	2.2040	1.494663	0.004633
1.7	0.2204	1.898602	0.027357
1.7	1.1020	1.534690	0.016225
1.7	2.2040	0.752040	0.008782

Table 3.3: Sample-to-sample fluctuation for $Dy_{2-x}Y_xTi_2O_7$, with a simulation box of $L = 4$. 50 samples are considered.

We have therefore only considered sample-to-sample fluctuations in the specific heat plots against experimental results in Fig. 3.1. In general, they are smaller than the size of the line symbol used.

3.1.7 Conclusion

Spin ice is at the present time one of the best understood highly frustrated magnetic systems, both from a microscopic model perspective [24] as well as from a field theory one [31, 32, 69, 70]. Spin ices would thus appear to be an ideal system to investigate quantitatively the effects of random disorder in a highly frustrated magnetic setting [69, 70]. The broad goal of this project was to perform such a quantitative comparison between theoretical modeling and experimental measurements in a specific class of disordered highly frustrated magnetic materials. As a first step, in this section we reported results from Monte Carlo simulations of a site-diluted version of the dipolar spin ice model (DSIM) given by Eq. 5.1 for $Dy_{2-x}Y_xTi_2O_7$ and $Ho_{2-x}Y_xTi_2O_7$. A close match between simulation results and experiments in the temperature range 0.5 K $\lesssim T \lesssim$ 5 K was found up to, and including, $x = 1.7$ (85% magnetic ions diluted) for $Dy_{2-x}Y_xTi_2O_7$. This good agreement between simulations and experiments validates further the underlying dipolar spin ice models for these two compounds [24, 25]

The non-monotonicity of the residual entropy as a function of dilution levels, $S_{\rm res}(T_0, x)$, is confirmed to originate from the material-specific spin-spin interactions themselves, namely the relative strength of (mostly) the nearest-neighbour exchange coupling J_1 with respect to the dipolar interactions. Furthermore, despite the importance of specifying the base temperature, T_0, from which thermodynamic integration of the magnetic specific heat $C_{\rm m}(T)/T$ is carried out, $S_{\rm res}(T_0, x)$ is nevertheless found to be roughly qualitatively described by the generalized Pauling's estimate, as shown by Ref. [2]. In summary, the difference in the residual entropy $S_{\rm res}$ between $Dy_{2-x}Y_xTi_2O_7$ and $Ho_{2-x}Y_xTi_2O_7$, as well as with the generalized Pauling's argument, have been resolved in this Section.

3.2 Diluted nearest-neighbour spin ice

In the previous section, we explored the material versus microscopic model aspect of the diluted spin ice problem. The validity of the random site diluted dipolar spin ice models was demonstrated through the detailed comparison of the specific heat measurements between Monte Carlo simulations and the experiment. Some salient features of the numerical and experimental facts found so far await physical explanations that we address the following in this chapter:

- origin of the specific heat broad peak observed for all dilution levels
- origin of the non-monotonicity of the residual entropy
- origin of the non-monotonicity of the specific heat peaks

Indeed, one of the most important signatures for identifying spin ice materials is the observation of the broad specific heat peak and its integration yielding a Pauling entropy [59]. In this Section, we offer a new insight into the meaning of the broad peaks in terms of thermal defect populations in the system.

Features of the calorimetric measurements are readily explained through the approximation developed and detailed Monte Carlo simulations in this Section. Stability of the nearest neighbour model Hamiltonian is also discussed in Section 3.3, which can be understood through a Bethe-Peierls calculation.

3.2.1 Model Hamiltonians

In this subsection, we consider two microscopic models for diluted spin ices. The first model is the diluted nearest-neighbour spin ice model (NNSIM), defined by the Hamiltonian

$$\mathcal{H}_{\text{NNSIM}} = -\sum_{\langle i,j \rangle} J\sigma_i\sigma_j\theta_i\theta_j \tag{3.10}$$

where the $\sigma_{i,j} = \pm 1$ are the Ising variables and the $\theta_{i,j}$ indicates whether a magnetic site has been diluted, with $\theta_i = 0$ when site i is diluted and $\theta_i = 1$ otherwise. The probability distribution of θ_i, therefore satisfies

$$p(\theta_i) = \mu\delta(\theta_i) + (1-\mu)\delta(\theta_i - 1) \tag{3.11}$$

where μ is the probability of a site being diluted with $\mu = x/2$ for x in the chemical formulae $Dy_{2-x}Y_xTi_2O_7$ and $Ho_{2-x}Y_xTi_2O_7$. J is the coupling between the Ising variables with $J < 0$ for spin ice. The sum is carried over spins that are nearest-neighbours. The spins represented by the Ising variables are on a pyrochlore lattice with corner-sharing tetrahedra, where the combination of triangular plaquettes and the effective antiferromagnetic interactions leads to geometrical frustration in the undiluted case and random frustration when diluted ($\mu \neq 0$).

The second model that we consider is the diluted dipolar spin ice model (DSIM), defined in Eq. 3.5.

For the non-diluted spin ices, it first came as a puzzle why the dipolar model displays similar spin ice behaviour as the nearest-neighbour model[22, 23, 67]. The resolution was found in a later work [27] that the Ising pyrochlore system possesses the remarkable property of *projective equivalence*, so that the long range parts of the dipolar interactions are *self-screened* [28]. The eventual long-range order transition from the dipolar interaction was shown numerically [48, 67] to happen at a much lower temperature compared to $J_{\text{eff}} = (5D - J_1)/3$, the nearest-neighbour energy scale of Eq. 3.5.

For diluted spin ices, we showed in Section 3.1 that for $Dy_{2-x}Y_xTi_2O_7$ and $Ho_{2-x}Y_xTi_2O_7$ [2], their specific heat can be accurately described by the dipolar spin ice model (DSIM) with parameters fitted in the pure cases [24, 25].

In this section, we will largely focus on the NNSIM due to its simplicity as a natural theoretical starting point. Yet, its physical relationship to the DSIM and experiments will also be discussed.

3.2.2 Single tetrahedron approximation

To understand the diluted NNSIM, we consider approximating the NNSIM by a collection of non-interacting tetrahedra, where we term such an approach the *single tetrahedron approximation* (STA). We will show later in this section that the STA is very accurate for the diluted NNSIM, and provides new insights into the broad specific heat peak of the spin ices. The rest of this subsection is a detailed account of the calculation.

The STA calculation consists of two parts. One part is to calculate the probabilities for the occurence of each type of tetrahedron. The other part is to calculate the physical properties associated with each type of diluted tetrahedron.

A tetrahedron can be diluted in different ways. In zero field, dilution on a single tetrahedron can be characterized by the number of sites remaining. In this section we only consider the zero field problem. Thus there are five dilution level on a tetrahedron, from tetrahedron with zero sites remaining to tetrahedron with all four sites remaining.

The probabilities for each way of diluting a tetrahedron are given by

$$P_i(\mu) = \frac{C_4^i (1-\mu)^i \mu^{4-i}}{2(1-\mu)} \tag{3.12}$$

where $i = 0, 1, 2, 3, 4$ indicates the number of spins remaining, and μ, as defined before, is the probability of a site being diluted. Note that we have inserted the $1/2(1-\mu)$ factor such that our weighting factors are for properties per undiluted spin, where the factor 2 here reflects the sharing of a spin between two tetrehdra.

With the probabilities for each type of dilution calculated, we can proceed to calculate the physical observables from the STA as

$$O_{\mathrm{STA}}(T, \mu) = \sum_{i \in \{0,1,2,3,4\}} P_i(\mu) O_i(T) \tag{3.13}$$

where O_i is the physical observable associated with the tetrahedron with i sites remaining.

We are particularly interested in two observables, the specific heat, $C(T, \mu)$, which is a macroscopic quantity, and the charge densities, $n_{\pm i}(T, \mu)$, which is a microscopic quantity. Here the charges are defined as the sums of the Ising variables on each tetrahedron, with the sum indicated by the subscript $\pm i$. In particular, the ± 2 charges defined here are the *magnetic monopoles* defined in previous works [29, 33, 71].

The energy spectrum for each type of dilution for a single tetrahedron is given in Table 3.4, along with the degeneracy of each energy level. From this table, the observables for the specific heat and the charge densities can be calculated.

Charge	4-spin tetra.	3-spin tetra.	2-spin tetra.	1-spin tetra.
±4	2, $-8J$	-	-	-
±3	-	2, $-4J$	-	-
±2	8, $-2J$	-	2, $-2J$	-
±1	-	6, GS	-	2, -
±0	6, GS	-	2, GS	-

Table 3.4: Degeneracy and energy above the ground state (GS) for each type of single tetrahedron under dilution. The charge is defined as the sum of all Ising variables of the tetrahedron. Note that for the nearest-neighbour spin ice model (NNSIM) of Eq. (3.10), $J < 0$.

3.2.3 Single tetrahedron approximation compared with Monte Carlo simulation

To test the validity of the STA, we compared the specific heat and the charge densities with Monte Carlo simulations of the site-diluted NNSIM. The Monte Carlo algorithm we use here is the same as in the previous section of the chapter, where besides the conventional single spin flip updates, collective updates of spins on closed and open loops are performed. The loops are designed to tunnel the system among spin ice states with no charge excitations as explained in Section 2.4. For the data presented here, a system of 8192 ($L = 8$) sites is used, with an average up to 200 samples considered for different realizations for a given dilution level μ. Up to 200,000 MC sweeps along with the collective updates are used in equilibration and data production. The error bars are produced from the sample-to-sample fluctuations, where the MC error from each sample is checked to be very small and therefore ignored.

In Fig. 3.5, we plot the specific heat $C(T)$ results obtained from Monte Carlo simulations and from the STA calculations. Notice that for all diluted levels the STA calculation agrees very well with the Monte Carlo simulation over the *whole* temperature range. Note that there are no adjustable fitting parameters here.

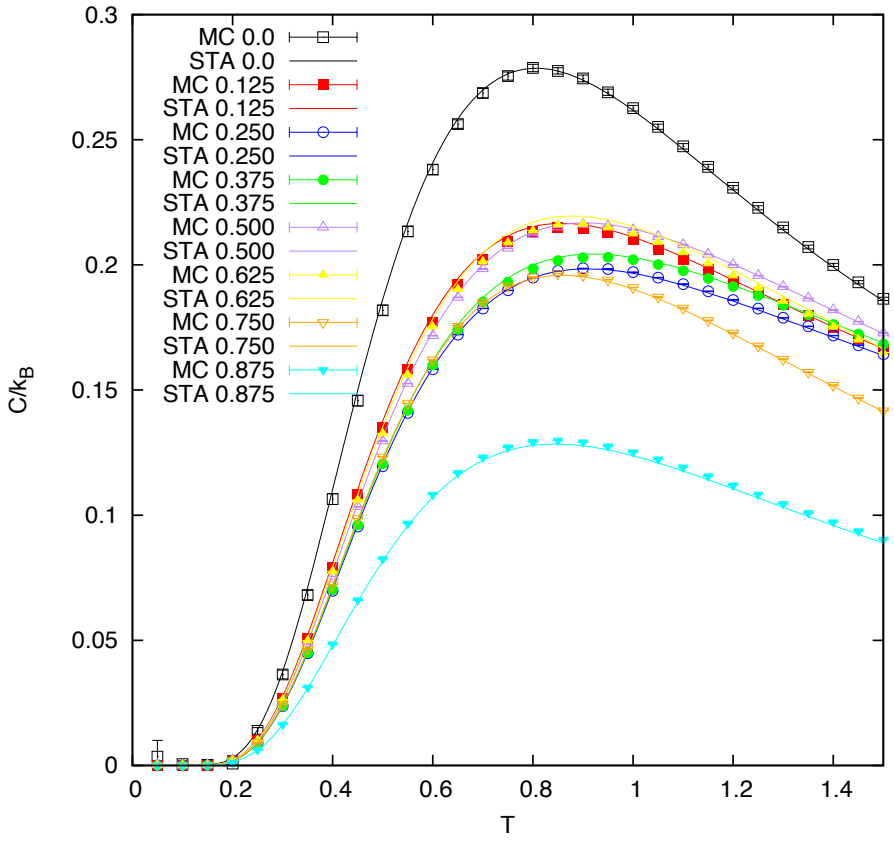

Figure 3.5: Comparison between specific heat from Monte Carlo simulations of the nearest-neighbour spin ice model (NNSIM) (dots) and single-tetrahedron approximation (STA) (lines). Monte Carlo simulations are performed using a simulation box of size $L = 8$. Temperature is in unit of $|J|$. "MC" and "STA" indicates whether the results are from a Monte Carlo simulation or from a STA calculation, respectively. The numerical values beside the "MC" or "STA" labels indicates the percentages of missing spins, *i.e.*, μ.

For the NNSIM, the $C(T)$ curves do not develop a sharp first order transition peak

below the specific heat broad peak, as opposed to the DSIM [48]. Therefore, from the specific heat calculations, it seems that dilution defects in the NNSIM do not introduce a long range order transition or a freezing into a spin glass state, which would be accompanied by a specific heat peak. Later in this section, we will comment on the absence of magnetic long range or spin glass order from the perspective of a Bethe-Peierls calculation method discussed in Section 2.4.

For the charge densities, we also found an excellent agreement between the STA calculation and the Monte Carlo simulation for all dilution levels and the whole temperature range. For example, we plot in Fig. 3.6 $n_{\pm 4}(T)$, $n_{\pm 3}(T)$, and $n_{\pm 2}(T)$ for $\mu = 0$, $\mu = 1/8$, $\mu = 1/2$, and $\mu = 7/8$. Note that for $\mu = 0.0$ there is no charge ± 3 since no tetrahedron is diluted.

Therefore through direct comparison, we have shown that the STA calculation describes the diluted NNSIM quantitatively, this is one of the main conclusions of this section.

3.2.4 Interpretation of the broad specific heat peak in spin ice

Having shown that the STA describes accurately the specific heat and the charge densities for the diluted NNSIM, we point out in this subsection an interpretation of the dilution dependence of the specific heat in diluted NNSIM, *i.e.*, the following relation holds true for all dilution levels μ and the whole temperature range

$$C(T,\mu) = -8J\frac{dn_4(T,\mu)}{dT} - 4J\frac{dn_3(T,\mu)}{dT} - 2J\frac{dn_2(T,\mu)}{dT} \tag{3.14}$$

The coefficients of Eq. (3.14) can be read from Table 3.4 with the assumption that the excitation energy of the system equates the sum of energies of the non-interacting charges. This equation relates a thermodynamic quantity, the specific heat, directly to the microscopic charge densities in a many body system. For the pure spin ice, n_3 is zero and at low temperatures the n_4 term is small compared with the n_2 term. Therefore for pure spin ice the specific heat at low temperatures can be interpreted as the temperature derivative for the *magnetic monopole* [29] (charge ± 2 objects) densities. With dilution and for the whole temperature range, all three charge defect densities contribute to the specific heat.

We believe that this result provides an interesting new insight into the physical interpretation of the broad specific heat peak of spin ices.

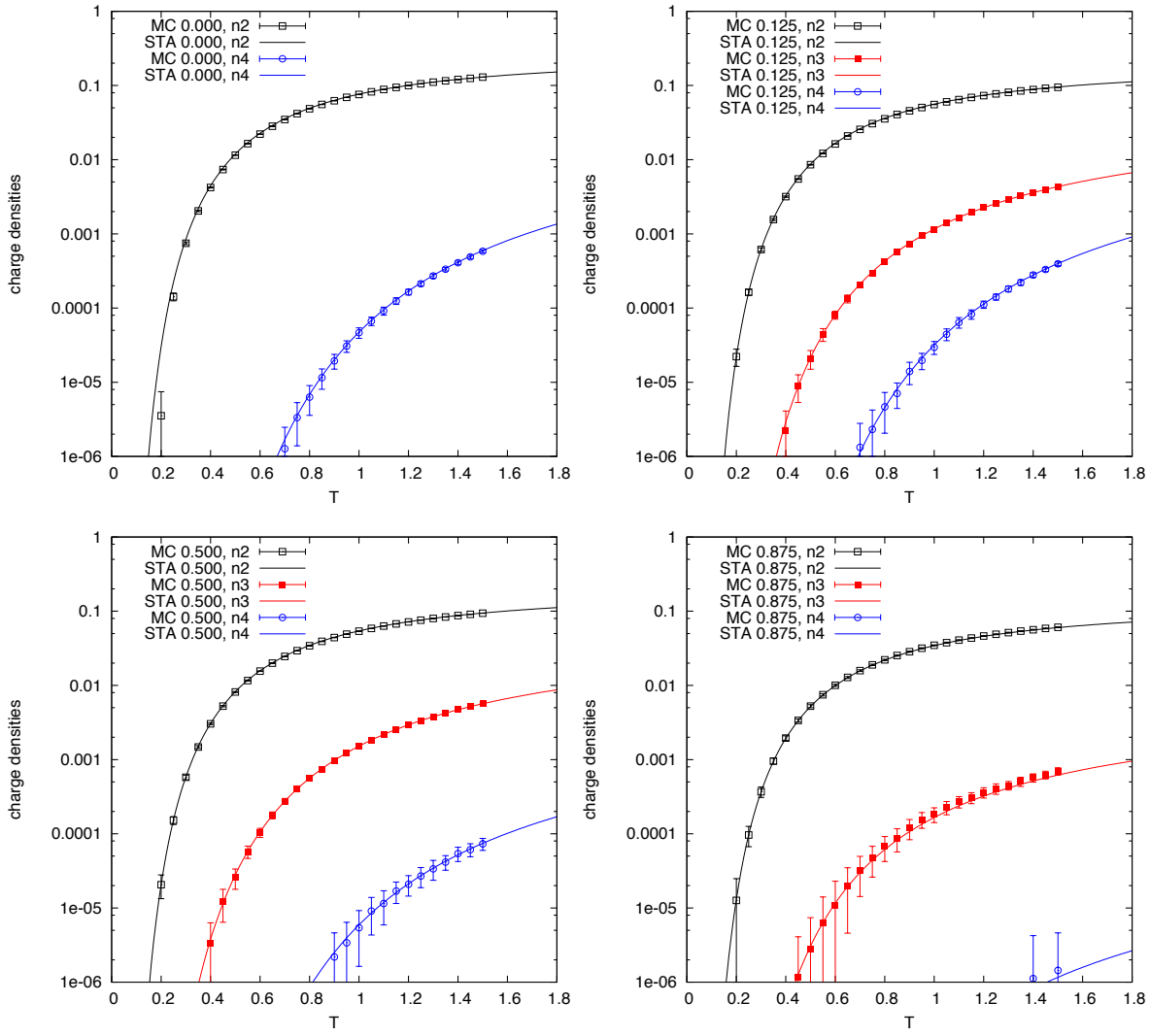

Figure 3.6: The average numbers of the thermally excited defects from Monte Carlo simulations (symbols) and from the STA calculations (lines) for the site-diluted NNSIM. Temperature is in unit of $|J|$. "MC" and "STA" indicates whether the results are from a Monte Carlo simulation or from a STA calculation, respectively. The numerical values beside the "MC" or "STA" labels indicates the percentages of missing spins, *i.e.*, μ.

3.2.5 Application: non-monotonicity of the specific heat

As an application of the STA interpretation for spin ices, we discuss in this subsection the non-monotonicity in height and temperature location of the specific heat broad peak and how the STA can explain it.

For diluted spin ices, we observe that the $C(T,\mu)$ curves evolve in a non-monotonic manner as a function of μ in both their peak heights and their peak positions for $Dy_{2-x}Y_xTi_2O_7$. This is the case for the NNSIM, as can be seen from Fig. 3.5, and is also the case for the DSIM and the experiments, as can be seen in Fig. 3.7. This non-monotonicity can be explained as the shifting of the occurance probabilities and the differences in the specific heat contributions from the three types of the single tetrahedron.

As discussed previously, the STA treats each tetrahedron independently and the final result is given by Eq. 3.13, where the $P_i(\mu)$'s are given by Eq. 3.12. Specifically, for specific heat only the 4-spin, 3-spin and 2-spin tetrahedra contribute to the final result, which can be written as

$$C(\mu,T) = \sum_{i=2}^{4} P_i(\mu) C_i(T) \tag{3.15}$$

To explain the non-monotonicity, we plot in Fig. 3.8 the $C_i(T)$'s and $P_i(\mu)$'s. As can be seen, the $C_3(T)$ curve is much lower in peak height and occurs at higher temperature than $C_4(T)$ and $C_2(T)$. Therefore as μ increases from zero the dominance of the weighting factor $P_i(\mu)$'s shifts from $i = 4$ to $i = 3$, and thus the resultant peak height decreases and the peak position of $C(T)$ moves to higher temperatures. At larger μ, as the dominance shifts to $i = 2$, the resultant peak height increases and the peak position occurs at lower temperatures again due to the higher $C_2(T)$ curve relative to the $C_3(T)$ curve.

In this way we show that the STA can be used to explain an observed experimental phenomenon.

3.3 Discussion: stability of the paramagnetic solution from a Bethe-Peierls calculation

The question we ask in this section is whether the diluted NNSIM, there is a phase transition out of the paramagnetic phase at some region of the $T-\mu$ phase diagram, into either

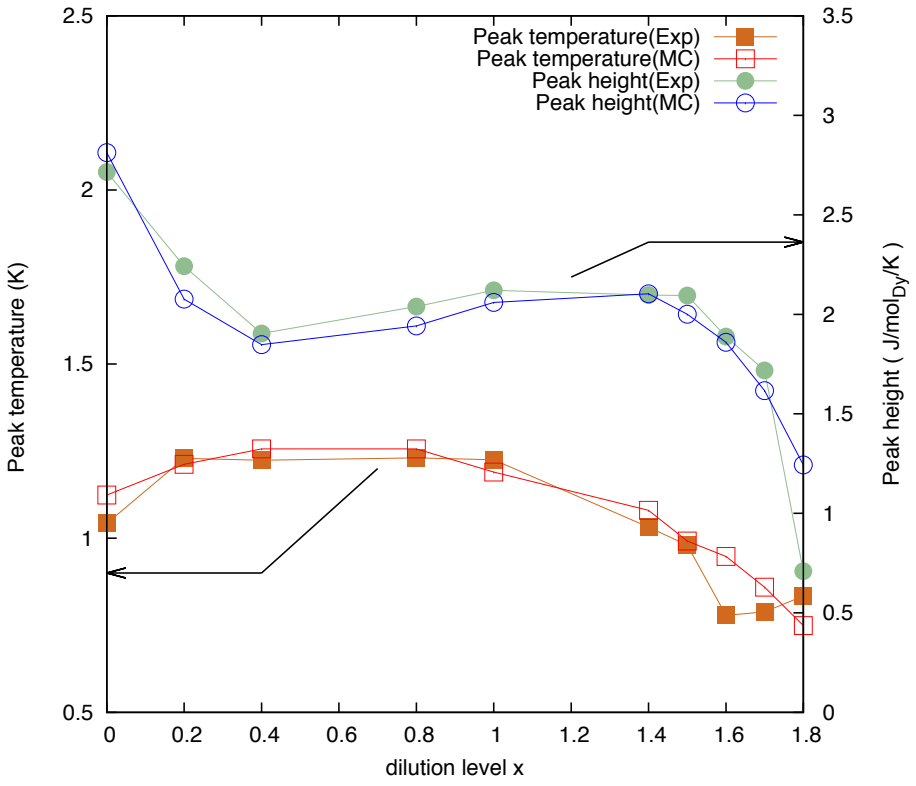

Figure 3.7: Magnetic heat capacity of $Dy_{2-x}Y_xTi_2O_7$ from experiment and Monte Carlo simulation of the *dipolar* spin ice model. Non-monotonic trends of the C_{peak} heights and temperature location can be seen.

longe-range ordered state or spin-glass phase. We employ a Bethe-Peierls approximation to explore this question. From this calculation we find that the diluted NNSIM remains a paramagnet for all finite temperatures and dilution levels.

In this work, we adapt the same method as in the work by Mélin *et al.* [72] to our site-diluted pyrochlore problem. The general idea of a Bethe-Peierls calculation is to replace

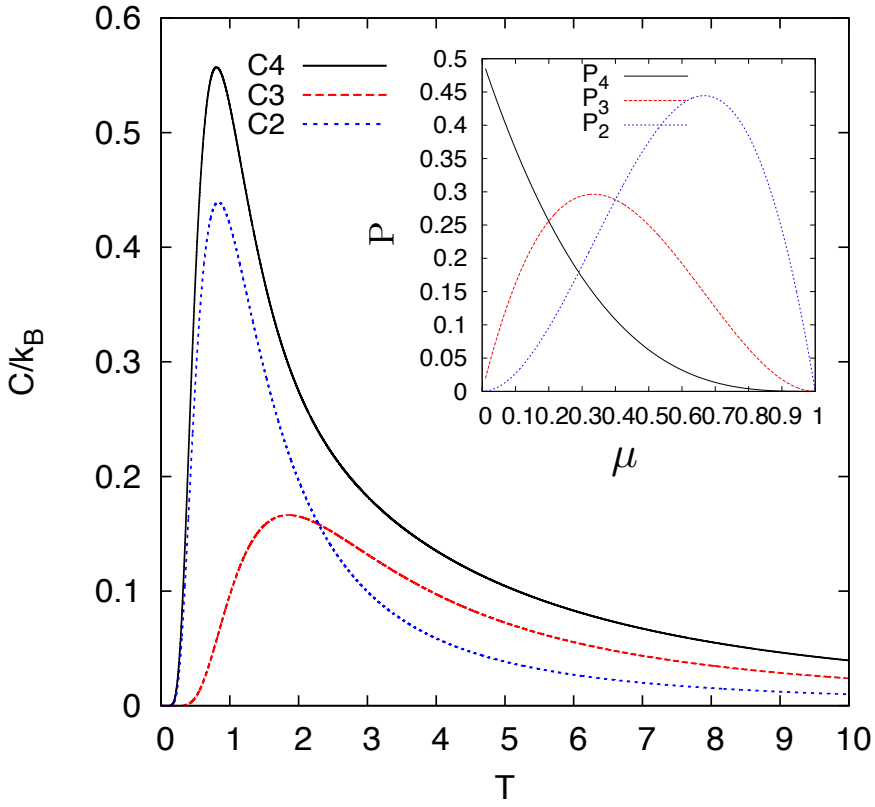

Figure 3.8: Rationalization of the non-monotonic treands of C_{peak} and T_{peak}. Black (solid), red (dashed), and blue (dotted) curves are for 4-spin, 3-spin, and 2-spin tetrahedra respectively. Inset is a comparison between the weighting factors for different dilution levels of the central tetrahedron.

the pyrochlore lattice by a Husimi cactus-like structure (Fig. 3.9). This enables an analytic solution to the recursive relations for the physical properties of the spins on adjacent layers of the tree structure. The thermodynamic limit is then taken by extending the recursive relation to infinity and we are interested in the resultant *fixed points* in the probability distribution of the physical properties. Usually, the physical property that we are interested in is the magnetization m. Depending on the different *fixed points* in the probability distribution of m, $P^*(m)$, we have a paramagnetic solution if $P(m) = \delta(m)$, ferromagntic solution if $P^*(m)$ has a finite first moment, and a spin-glass solution if $P^*(m)$ is even. In

the following, we show in detail that for our problem, the paramagnetic solution, $P(m) = \delta(m)$, remains stable with respect to the first and second moment of the magnetization.

3.3.1 Model

The Hamiltonian that we study is the diluted NNSIM, defined by Eq. (3.10).

The pyrochlore lattice is now replaced by a Husimi cactus, as depicted in Fig. 3.9, which is a tree structure of tetrahedra. Note that the outward tetrahedra from different branches never re-connect.

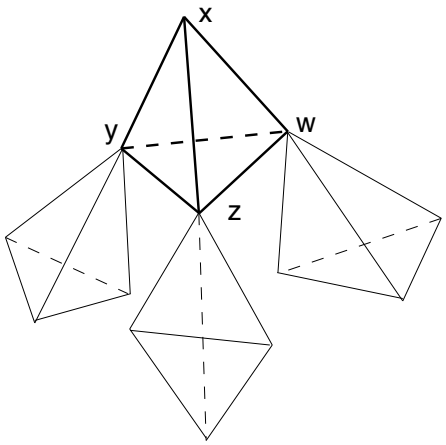

Figure 3.9: The Husimi cactus of diluted magnet spin ice. The top spin x is attached to the next layer's spins y, z, and w. The spins are diluted with probability μ.

3.3.2 Recursive relation for the magnetization

Our first goal is to derive the recursive relation for the magnetization between two adjacent layers (connecting tetrahedra). In Fig. 3.9, the "inner" layer (later subscripted with $n+1$) is labeled by x, and the "outer" layer (later subscripted with n) are labeled by y, z, and w. We are interested in how the magnetization m_x is dependent on m_y, m_z and m_w,

conditional on θ_x, θ_y, θ_z, and θ_w, *i.e.*, the function

$$m_x = f(m_y, m_z, m_w|\theta_x, \theta_y, \theta_z, \theta_w) \tag{3.16}$$

Consider the conditional partition function for the x layer spin having value of σ_x

$$Z_x^{\sigma_x} = \sum_{\theta_y,\theta_z,\theta_w} W^B_{\theta_y,\theta_z,\theta_w}(\sigma_y, \sigma_z, \sigma_w|\sigma_x) Z_y^{\sigma_y} Z_z^{\sigma_z} Z_w^{\sigma_w} \tag{3.17}$$

where $W^B_{\theta_y,\theta_z,\theta_w}(\sigma_y, \sigma_z, \sigma_w|\sigma_x)$ is the Boltzmann factor defined as

$$\begin{aligned} &W^B_{\theta_y,\theta_z,\theta_w}(\sigma_y, \sigma_z, \sigma_w|\sigma_x) = \\ &e^{(\beta\sigma_x\sigma_y\theta_x\theta_y + \beta\sigma_x\sigma_z\theta_x\theta_z + \beta\sigma_x\sigma_w\theta_x\theta_w)} \times \\ &e^{(\beta\sigma_y\sigma_z\theta_y\theta_z + \beta\sigma_y\sigma_w\theta_y\theta_w + \beta\sigma_z\sigma_w\theta_z\theta_w)} \end{aligned} \tag{3.18}$$

with $\beta \equiv J/k_{\mathrm{B}}T$.

Using the relation

$$m_\gamma = \frac{Z_\gamma^+ - Z_\gamma^-}{Z_\gamma^+ + Z_\gamma^-} \tag{3.19}$$

for $\gamma = x, y, z, w$, we have

$$m_x = \frac{\begin{array}{c}\sum_{\sigma_y,\sigma_z,\sigma_w=\pm1}(1+\sigma_y m_y)(1+\sigma_z m_z)(1+\sigma_w m_w)\times \\ \sinh(\beta(\theta_x\sigma_y\theta_y + \theta_x\sigma_z\theta_z + \theta_x\sigma_w\theta_w))e^{\beta(\sigma_y\sigma_z\theta_y\theta_z + \sigma_y\sigma_w\theta_y\theta_w + \sigma_z\sigma_w\theta_z\theta_w)}\end{array}}{\begin{array}{c}\sum_{\sigma_y,\sigma_z,\sigma_w=\pm1}(1+\sigma_y m_y)(1+\sigma_z m_z)(1+\sigma_w m_w)\times \\ \cosh(\beta(\theta_x\sigma_y\theta_y + \theta_x\sigma_z\theta_z + \theta_x\sigma_w\theta_w))e^{\beta(\sigma_y\sigma_z\theta_y\theta_z + \sigma_y\sigma_w\theta_y\theta_w + \sigma_z\sigma_w\theta_z\theta_w)}\end{array}} \tag{3.20}$$

Note that $\tanh(K\sigma) = \tanh(K)\sigma$ for $\sigma = 0, \pm1$, we have the recursion relation for the magnetization

$$
\begin{aligned}
m_x = & \\
& [p\theta_x\theta_w + p^2\theta_x\theta_w(\theta_y^2+\theta_z^2) + 2p^3\theta_x\theta_w\theta_y^2\theta_z^2 + p^4\theta_x\theta_w\theta_y^2\theta_z^2(\theta_w^2+\theta_x^2) + p^5\theta_x^3\theta_w^3\theta_y^2\theta_z^2]m_w \\
& \quad [p\theta_x\theta_y + p^2\theta_x\theta_y(\theta_w^2+\theta_z^2) + 2p^3\theta_x\theta_y\theta_w^2\theta_z^2 + p^4\theta_x\theta_y\theta_w^2\theta_z^2(\theta_y^2+\theta_x^2) + p^5\theta_x^3\theta_y^3\theta_w^2\theta_z^2]m_y + \\
& \quad\quad [p\theta_x\theta_z + p^2\theta_x\theta_z(\theta_w^2+\theta_y^2) + 2p^3\theta_x\theta_z\theta_w^2\theta_y^2 + p^4\theta_x\theta_z\theta_w^2\theta_y^2(\theta_z^2+\theta_x^2) + p^5\theta_x^3\theta_z^3\theta_w^2\theta_y^2]m_z + \\
& \quad\quad\quad [3p^2\theta_w\theta_x\theta_y\theta_z + p^3\theta_x\theta_w\theta_y\theta_z(\theta_x^2+\theta_y^2+\theta_z^2+\theta_w^2) + p^6\theta_x^3\theta_w^3\theta_y^3\theta_z^3]m_w m_y m_z \\
& \hline \\
& 1 + p^3\theta_x^2(\theta_w^2\theta_y^2+\theta_w^2\theta_z^2+\theta_y^2\theta_z^2) + p^3\theta_w^2\theta_y^2\theta_z^2 + 3p^4\theta_x^2\theta_w^2\theta_y^2\theta_z^2 \\
& \quad [p\theta_w\theta_y + p^2\theta_w\theta_y(\theta_x^2+\theta_z^2) + 2p^3\theta_x^2\theta_w^2\theta_y\theta_z^2 + p^4\theta_w\theta_x^2\theta_y\theta_z^2(\theta_w^2+\theta_y^2) + p^5\theta_x^2\theta_w^3\theta_y^3\theta_z^2]m_w m_y \\
& \quad\quad [p\theta_w\theta_z + p^2\theta_w\theta_z(\theta_x^2+\theta_y^2) + 2p^3\theta_x^2\theta_w\theta_z\theta_y^2 + p^4\theta_w\theta_z\theta_x^2\theta_y^2(\theta_w^2+\theta_w^2) + p^5\theta_x^2\theta_w^3\theta_z^3\theta_y^2]m_w m_z \\
& \quad\quad\quad [p\theta_y\theta_z + p^2\theta_y\theta_z(\theta_x^2+\theta_w^2) + 2p^3\theta_x^2\theta_y\theta_z\theta_w^2 + p^4\theta_y\theta_z\theta_x^2\theta_w^2(\theta_y^2+\theta_z^2) + p^5\theta_x^2\theta_y^3\theta_z^3\theta_w^2]m_y m_z \\
& \equiv f(m_y, m_z, m_w|\theta_x, \theta_y, \theta_z, \theta_w)
\end{aligned}
\tag{3.21}
$$

where $p \equiv \tanh(\beta)$.

3.3.3 Statibility of the paramagnetic solution

With the magnetization recursion relation Eq. (3.21), we can study the stability of the paramagnetic solution for the first and second moment of the magnetization.

For the first moment, we have

$$
\begin{aligned}
& \langle\!\langle m \rangle\!\rangle_{n+1} \equiv \int dm_x P_{n+1}(m_x) m_x \\
& = \int dm_x \int dm_y dm_z dm_w \sum_{\theta_x,\theta_y,\theta_z,\theta_w} p(\theta_z)p(\theta_y)p(\theta_z)p(\theta_w) \times \\
& P_n(m_x)P_n(m_z)P_n(m_w) \times \\
& \delta(m_x - f(m_y, m_z, m_w|\theta_x, \theta_y, \theta_z, \theta_w)) m_x
\end{aligned}
\tag{3.22}
$$

To the lowest order in m, we have

$$\begin{aligned}
&\langle\!\langle m_x \rangle\!\rangle_{n+1} \approx \\
&\sum_{\theta_x,\theta_y,\theta_z,\theta_w} p(\theta_z)p(\theta_y)p(\theta_z)p(\theta_w)\times \\
&\frac{\begin{array}{c} p\theta_x\theta_w + p^2\theta_x\theta_w(\theta_y^2+\theta_z^2) + 2p^3\theta_x\theta_w\theta_y^2\theta_z^2 + \\ p^4\theta_x\theta_w\theta_y^2\theta_z^2(\theta_w^2+\theta_x^2) + p^5\theta_x^3\theta_w^3\theta_y^2\theta_z^2 \end{array}}{\begin{array}{c} 1 + p^3\theta_x^2(\theta_w^2\theta_y^2 + \theta_w^2\theta_z^2 + \theta_y^2\theta_z^2) + \\ p^3\theta_w^2\theta_y^2\theta_z^2 + 3p^4\theta_x^2\theta_w^2\theta_y^2\theta_z^2 \end{array}}\times \\
&\langle\!\langle m_w \rangle\!\rangle_n \times 3 \\
&= 3\langle\!\langle G_{wyz}(\theta_x,\theta_y,\theta_z,\theta_w,p)\rangle\!\rangle\langle\!\langle m_w \rangle\!\rangle_n \qquad (3.23) \\
&\equiv C_1\langle\!\langle m_w \rangle\!\rangle_n \qquad (3.24)
\end{aligned}$$

where

$$\begin{aligned}
&G_{wyz}(\theta_x,\theta_y,\theta_z,\theta_w,p) \equiv \\
&\frac{\begin{array}{c} p\theta_x\theta_w + p^2\theta_x\theta_w(\theta_y^2+\theta_z^2) + 2p^3\theta_x\theta_w\theta_y^2\theta_z^2 + \\ p^4\theta_x\theta_w\theta_y^2\theta_z^2(\theta_w^2+\theta_x^2) + p^5\theta_x^3\theta_w^3\theta_y^2\theta_z^2 \end{array}}{\begin{array}{c} 1 + p^3\theta_x^2(\theta_w^2\theta_y^2 + \theta_w^2\theta_z^2 + \theta_y^2\theta_z^2) + \\ p^3\theta_w^2\theta_y^2\theta_z^2 + 3p^4\theta_x^2\theta_w^2\theta_y^2\theta_z^2 \end{array}}
\end{aligned} \qquad (3.25)$$

and we have defined

$$\begin{aligned}
&\langle\!\langle G^n_{wyz}(\theta_x,\theta_y,\theta_z,\theta_w,p)\rangle\!\rangle \equiv \\
&\sum_{\theta_x,\theta_y,\theta_z,\theta_w} p(\theta_x)p(\theta_y)p(\theta_z)p(\theta_w)G^n_{wyz}(\theta_x,\theta_y,\theta_z,\theta_w,p)
\end{aligned} \qquad (3.26)$$

Similarly, for the second moment, to lowest order in the phase diagram where the first moment vanishes, we have

$$\begin{aligned}
\langle\!\langle m_x^2 \rangle\!\rangle_{n+1} &= 3\langle\!\langle G^2_{wyz}(\theta_x,\theta_y,\theta_z,\theta_w,p)\rangle\!\rangle\langle\!\langle m_w^2 \rangle\!\rangle_n \qquad (3.27) \\
&\equiv C_2\langle\!\langle m_w^2 \rangle\!\rangle_n \qquad (3.28)
\end{aligned}$$

The paramagnetic phase is stable with respect to perturbations in the first and second moment if

$$|C_1| < 1 \text{ and } |C_2| < 1. \qquad (3.29)$$

We plot C_1 and C_2 as functions of μ and p in Fig. 3.10. As can be seen from the figure, Eq. (3.29) is always satisfied at any nonzero temperature and all dilution levels. Therefore, the paramagnetic solution is shown to be stable with respect to the first and second moment of the magnetization.

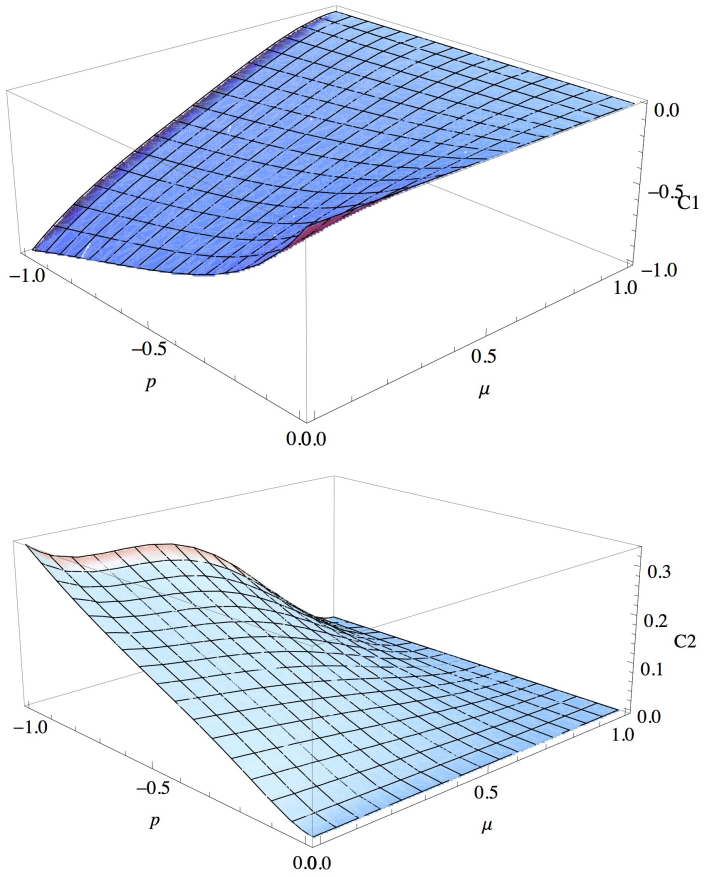

Figure 3.10: The C_1 and C_2 as functions of $p(\equiv tanh(\beta))$ and dilution level μ. $|C_1| < 1$ and $|C_2| < 1$ are always satisfied at any nonzero temperature and all dilution levels.

From Eq. (3.19), the conditional partition function in the paramagnetic region is unity. Then, from Eq. (3.17) the properties of the "inner" spin do not depend on the properties of the "outer" spin, or the *effective field* [51] on the "inner" spin is zero. Therefore, we can consider only the innermost object of the Husimi cactus, which is just a single tetrahe-

dron, in calculating the physical properties of the whole structure. The presence of dilution allows for the possibility of having four spins to zero spin on a tetrahedron, and the thermodynamic properties should then be calculated for each possibility and weighted according to the probabilities of find each of them. Thus the single tetrahedron approximation in Section 3.2 is justified through the Bethe-Peierls calculation.

In summary, we have shown using Bethe-Peierls calculation that the diluted NNSIM remains paramagnetic, and consequently such calculation reduces to the calculation of a single tetrahedron of the pyrochlore.

3.4 Lost of the projective equivalence in diluted spin ice

In Section 3.2, we demonstrated that for the nearest-neighbour spin ice model, the broad peak of the specific heat can be directly mapped to the changes of the thermal defect densities via Eq. (3.14), with the mapping holding true at all dilution levels.

In this chapter, by applying Eq. (3.14) to the dipolar spin ice model, we provide a concrete physical picture of how the *projective equivalence* works for the non-diluted spin ices, while it fails in the presence of site dilution.

In Fig. 3.11, we plot the specific heat as a function of temperature as well as the "STA specific heat" from the change of the thermal defect densities via Eq. (3.14). The STA specific heat is rescaled by an overall factor for each dilution level x separately to match the "real" specific heat at $T = 3.5$ K.

Consider the case of the non-diluted spin ice ($x = 0.0$). First, we face the problem of the value of J_{eff} in Eq. (3.14). For a nearest-neighbour model, the energy spectrum of the thermal excited defects has no ambiguities in units of exchange interaction. However, in the dipolar spin ice model, the excitation energy has contributions not just from the nearest-neighbours, but also from the texture of the "vacuum", (magnetic charge neutral space) and other monopole charge excitations present in the system. The last of the contributions is part of the interesting topic of the Debye-Huckle theory of the magnetic charges in spin ice [29, 71], which is the subject of Chapter 6. For the moment we are satisfied with just a scale factor between the STA specific heat and the real specific heat, keeping in mind

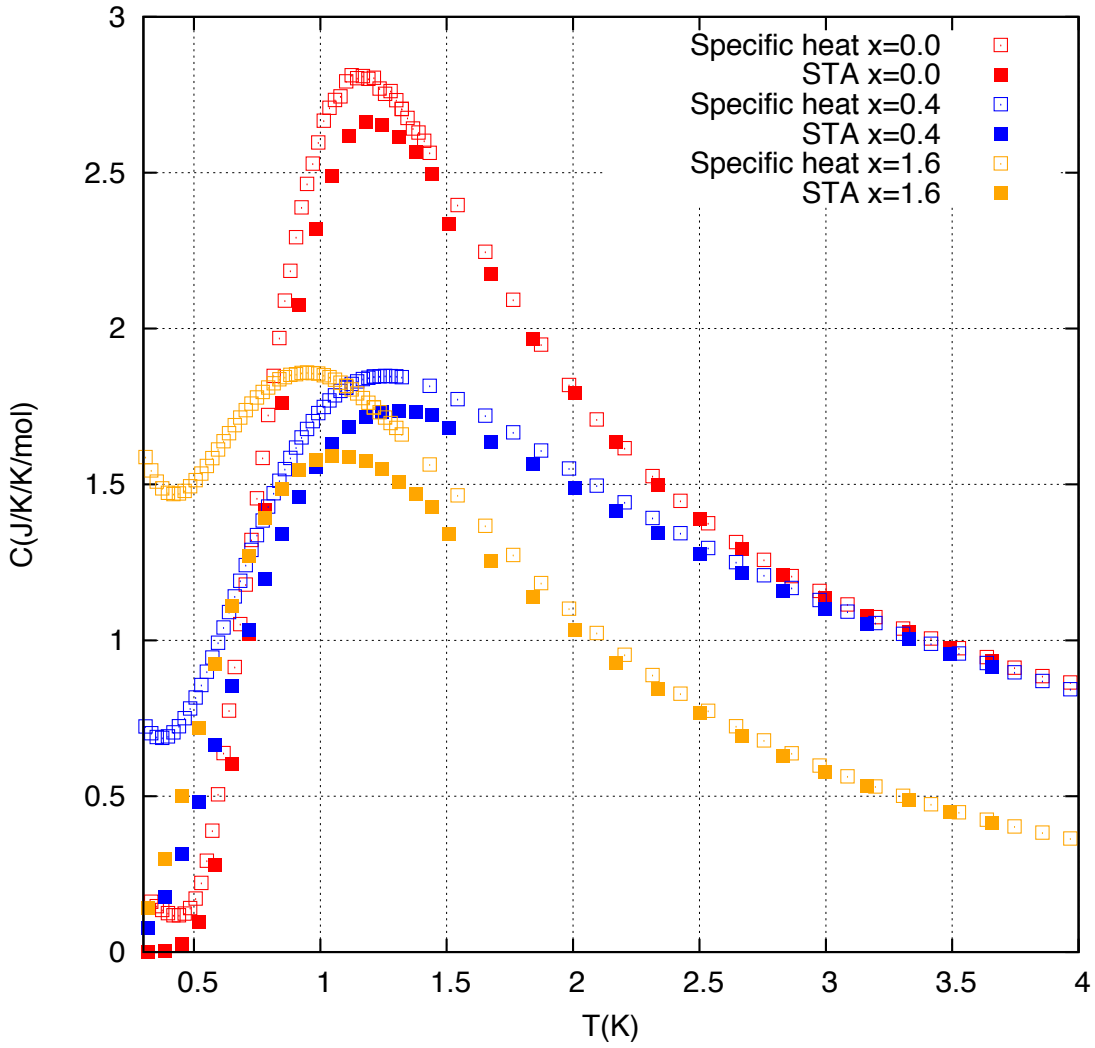

Figure 3.11: An attempt to map the defect densities to the specific heat via Eq. 3.14. Monte Carlo simulations for $Dy_{2-x}Y_xTi_2O_7$ at three dilution levels. The density results are marked by "STA" in the label and is scaled at $T = 3.5$ K to match the specific heat.

the scaling constant (if one scalar is at all sufficient) incorporates physics we have not understood completely.

As shown in Fig. 3.11, for the non-diluted spin ice, Eq. (3.14) works reasonably well, and the small difference below the broad peak of the specific heat is most likely due to the aforementioned neglects. Thus, this result provides a microscopic interpretation of the specific heat broad peak of spin ice, in terms of the thermal defects (magnetic monopoles in the language of the work by Castelnovo *et al.* [29]). The projective equivalence, or the self-screening of the charges, is illustrated as the close match between the STA results and the true specific heat results.

Next we consider the case for the diluted spin ices (x = 0.4 and x = 1.6 in Fig. 3.11). As shown in the figure, the STA specific heat curves depart from the true specific heat *below* the broad peak (while we suffer the same problem with the scaling factor). The departure can be understood by an argument of the breakdown of the projective equivalence. One way to understand the projective equivalence is through the dumbbell model of the magnetic spins [29], where the dipole moment of the spins is replaced by two opposite charges at the centres of the two tetrahedra linked by the spins. In the presence of the dilution, some of the tetrahedra are no longer surrounded by four spins. Therefore, there is a surplus of charges at the centres of these diluted tetrahedra. These unscreened charges interact among themselves as well as with the "vacuum fluctuations" of the ice-rule states by the magnetic field they generate. Therefore we have a much richer energy landscape than that described by the STA. We thus have departures between the STA specific heat and the true specific heat.

In this chapter, we have illustrated a breakdown of the projective equivalence in the diluted dipolar spin ice. Relate back to Section 3.1, it is because of this breakdown in the self-screening that there is no well defined residual entropy plateau at the Pauling's value. Only a remnant of the diluted nearest-neighbour spin ice persists in the dipolar spin ice, notably the non-monotonic peak of the specific heat curves, as discussed in Section 3.2.

3.5 Conclusion and future works

In conclusion, in this chapter we studied the compounds of diluted spin ices $Dy_{2-x}Y_xTi_2O_7$ and $Ho_{2-x}Y_xTi_2O_7$. We found that the site-diluted dipolar spin ice model describes the experimental observables very well. The meaning of the broad peak in specific heat, as we discussed in Section 3.2, can be ascribed to the change of the thermal defect populations in the nearest-neighbour spin ice. The single-tetrahedron approximation, which we use to

describe the nearest-neighbour model, successfully describes the non-monotonicity of the specific heat broad peak. The paramagnetic phase, as we argued in Section 3.3, survives random site dilution in the nearest-neighbour model. We show in Section 3.4 that for dipolar spin ice model, the breakdown of projective equivalence happens at finite dilutions.

3.5.1 Future work

Consider the low dilution limit, where magnetic site vacancies are sparse and well separated. Due to the dumbbell description of spin ice, at the two tetrahedra linked to the magnetic spin vacancy site, two magnetic charges appear. Due to their proximity they will form dipoles at low temperatures. Therefore, at not so low a temperature where magnetic ordering sets in for the charge "vacuum" (ice-rule fulfilling) spins, we have a dilute dipole model. For a similar dilute dipolar model $LiHo_xY_{1-x}F_4$ [64, 73, 74], glass transition remains a controversial topic. Future directions of work would include the exploration of a possible glass phase arising from these effective dipole moments.

Chapter 4

Spin Ice Thin Films

Spin ice thin films constitute an emerging field of study. Several interesting questions contribute to the surge of interest.

First is the question of restoration of the third law of thermodynamics. The defining feature of spin ice is its residual entropy of $(k_{\mathrm{B}}/2)\ln(3/2)$, due to the degeneracy of the exponentially numbered (in the volume of the system) ice-rule fulfilling states. With dipolar interaction, this degeneracy is slightly lifted, and the transition to long-range order was predicted to be 0.18 K in a previous simulation study [48] but has never been observed in experiment. In fact, for dipolar spin ice, the appearance of a quasi-degenerate low temperature state is due to a remarkable property of the dipolar interaction on the pyrochlore lattice. The dipolar interactions are self-screened [28] and, as studied by Isakov *et al.* [27], they are *projective equivalent* to the nearest-neighbour interactions on the pyrochlore. Therefore, for a dipolar spin ice thin film, we may ask if such an equivalence, or self-screening of the dipolar interaction, still remains, thus allowing a quasi-degenerate ground state, or if the opposite is true and eliminate all the residual entropy to restore the third law of thermodynamics. On the other hand, since experimentally spin ice films are usually grown on substrates of other chemical compounds [75], we may have a geometrically distorted system, and maybe the strains induced by the surface can restore the third law.

Second, is the prospect of realizing a magnetic equivalence of a spintronic device in a thin film. Emergent magnetic monopoles and magnetricity have been proposed for spin ice materials [29, 76]. Furthermore, it was noted by Khomskii [77] that for a magnetic

monopole in spin ice, an electric dipole can be associated with it. Thus we have a complete analogue between electrons and magnetic monopoles, and between spins of electrons and electric dipole moments of the magnetic monopoles. Possibly, wisdom gained in the study of spintronics may be eventually applied to spin ice film devices with reversed electric-magnetic relations.

Third, is the question of surface freezing versus surface melting. For water ice, surface melting, or premelting occurs and it has huge consequences in earth and planetary sciences. An everyday example of why the concept of surface melting is important is that it is one of the explanations why skating is possible (there is alway a thin film of water on ice due to premelting). On the other hand, surface freezing is much rarer in nature, and one example is in molten normal alkanes [78]. Therefore we ask if for spin ice thin films whether a magnetic surface freezing or surface melting occurs

Experimentally, a couple studies of spin ice thin films have been reported. [75, 79] Fabrication of $Ho_2Ti_2O_7$ using pulsed laser deposition showing high quality of crystalization is possible [79]. In the work of Bovo *et al.* [75], a restoration of the third law in spin ice $Dy_2Ti_2O_7$ was observed and was attributed to strain-induced ordering.

In this chapter, we will be studying dipolar spin ice thin films with the [001] surface. The reason we only use a [001] surface as opposed to the other experimental reported surfaces of [110] [75] and [111] [79] is mainly due to theoretical convenience. The conventional cubic unit cell for the FCC lattice has the [001] surface when stacked periodically in the x and y directions. In general an orthorhombic unit cell is needed, therefore the conventional Ewald Eq. [65] has to be re-derived for such geometry. Eventually all these subtleties should be considered and addressed. But for the scope of this work, we found the [001] surface of spin ice thin film to already contain rich and fascinating physics that we are presenting in what follows.

The microscopic Hamiltonians we are considering in this chapter are the following two. The first one is the dipolar spin ice model, with the Hamiltonian

$$\mathcal{H}_{\text{DSIM}} = \sum_{i>j} \sigma_i \sigma_j \{ J_{i,j} \hat{z}_i \cdot \hat{z}_j + D(r_{nn}/r_{ij})^3 [\hat{z}_i \cdot \hat{z}_j - 3(\hat{z}_i \cdot \hat{r}_{ij})(\hat{z}_j \cdot \hat{r}_{ij})] \} \tag{4.1}$$

where the σ_i and σ_j are the Ising variables, $\hat{z}_i$ and $\hat{z}_j$ are the local $\langle 111 \rangle$ directions of the rare-earth magnetic moments. r_{nn} is the distance between nearest-neighbour ions. $J_{i,j}$ is the exchange interaction and $J_{i,j} = J_1$ only when i and j are nearest-neighbours. D is

the strength of the dipolar interaction. In this "thin film" study we take $J_1 = 3.72$ K and $D = 2.35$ K, corresponding to the parameters used for $Dy_2Ti_2O_7$ by den Hertog *et al.* [23]. Such a choice of parameter is mainly for theoretical simplicity, since in a previous work by Melko *et al.* [48] the ground state of this model is known through Monte Carlo simulations.

The second model we consider is the nearest-neighbour spin ice model with the Hamiltonian

$$\mathcal{H}_{\rm nn} = J \sum_{<i,j>} \sigma_i \sigma_j \tag{4.2}$$

where $J > 0$ for interactions between neighbouring spins.

We start the chapter by considering the corrections to the Pauling's residual entropy due to constraints at the surface. As in Pauling's original work on water ice [4], we assume paramagnetic phases for different surface conditions. The significance of a geometrical object pertinent to pyrochlore films along [001], the *orphan bonds*, is described in this section.

Then, in Section 4.2, we present results for Monte Carlo simulations for the thin film problem. We discuss especially how the film geometry is represented in Monte Carlo studies using Ewald summations for the dipolar interactions.

In Section 4.3, we examine the specific heat results from the Monte Carlo simulations. Specifically, we study how different surface conditions and long-range dipolar interactions affect the residual entropy. Schemes developed in Section 4.1 to estimate the surface corrections to the Pauling's entropy are compared with the simulation results.

Next, in Section 4.4, we present the most important results of this Chapter. By tuning the strength of the orphan bonds defined in Section 4.1, we can achieve a surface ordering of the free (magnetic) charges while the bulk of the spins inside the film remain disordered. Structure factors for the surface charges are presented. The ordering of the surface charges is found to be second order, in the two-dimensional Ising universality class.

In Section 4.5, we explain why a surface ordering can be achieved.

4.1 Surface corrections to the Pauling's residual entropy

4.1.1 Orphan bonds at the [001] surface

When a crystal of spin ice is cut to expose the [001] surface, one important structure of the surface requires particular attention. As shown in Fig. 4.1 and Fig. 4.2, on the [001] surface of the pyrochlore slab, a bond, which is defined as the line segment connecting two nearest-neighbours, appears on the surface linking two neighbouring tetrahedra. Since these bonds are not part of any tetrahedra, they are hereafter referred to as the *orphan bonds*.

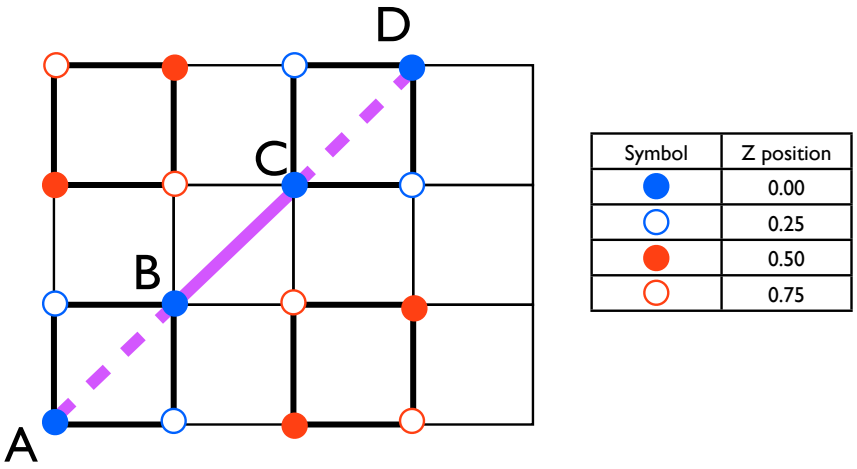

Figure 4.1: A conventional cubic unit cell viewed along the $\hat{z}$ ([001]) direction. Sites A, B, C, D are on the "bottom" surface. Bonds AB and CD are on the surface and still part of tetrahedra. Bond BC is on the surface but no longer part of any tetrahedron. Bond BC is referred to as the *orphan bond*.

The exchange interactions between neighbouring spins in spin ice ultimately depend on the chemical environment which the rare-earth magnetic ions dwell in, especially the oxygen atoms immediately surrounding the ions. On the surface, for the two neighbouring ions that

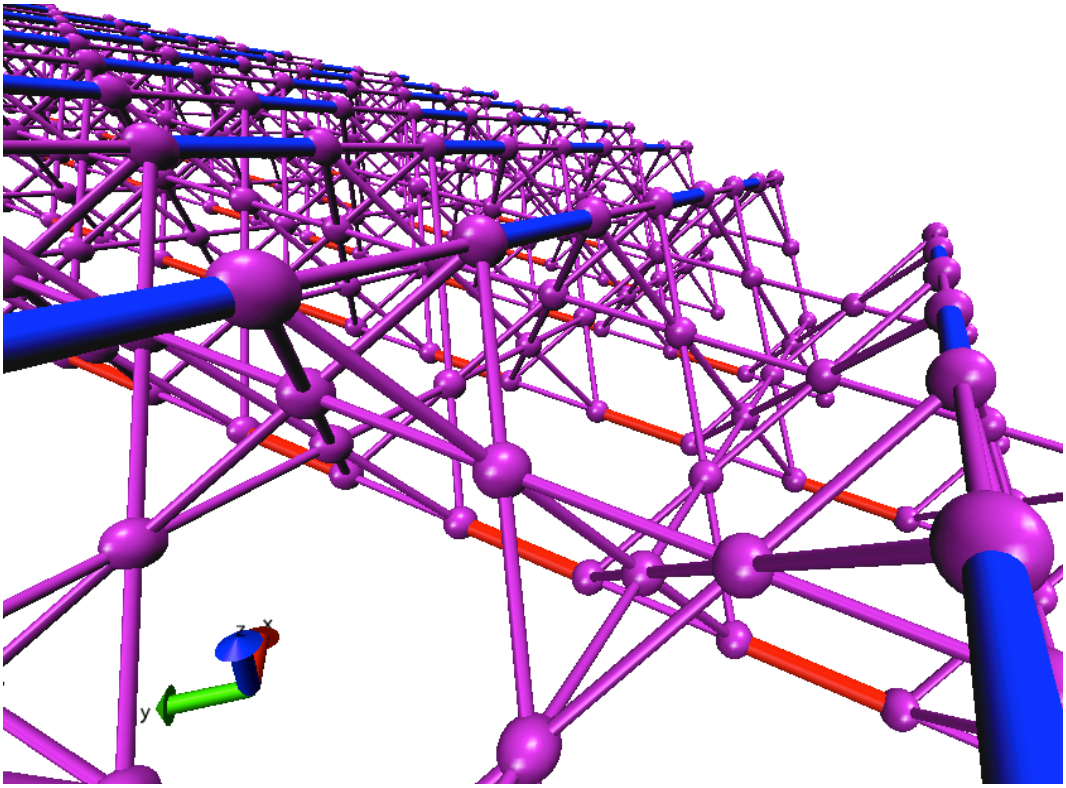

Figure 4.2: A three-dimensional perspective graph of a film of one cubic layer thick. The surface is normal to the [001] direction. Orphan bonds on the top and bottom of the film are marked in blue and red respectively.

are not connected by an orphan bond (site A and site B in Fig. 4.1), the crystal environment clearly differs from two neighbouring ions that are connected by an orphan bond (site B and site C in Fig. 4.1). Although it is not obvious how the exchange interactions are modified, we can argue that it is quite possible that the exchange interaction between site A and site B might be quite different from the exchange interaction between site B and site C, due to their different crystal environments. Of course the change of crystal field environments on the surface may even destroy the Ising nature of the surface spins. However, from the point of view of developing a first class of theories for spin ice thin films, we assume the following:

- the spins on the surface remain Ising like
- an extra exchange interaction, J_{orphan}, can be added to the exchange between the two spins connected by an orphan bond, and we take the liberty of choosing the strength and sign of the added interaction

Based on these two assumptions we develop our theory for the spin ice thin films. From a model system point of view, we will later show in this chapter that interesting physics such as surface freezing can emerge from this model, and we invite future experiments to investigate predictions made in this study.

4.1.2 Surface corrections to Pauling's entropy

Having established the model for the surface, we now investigate how the surface affects the residual entropy. We will use approximations similar to those used in Pauling's calculation of the residual entropy for water ice [4], *i.e.*, we will first assume a paramagnetic state, then apply constraints *independently* to eliminate excessive number of states. The point being approximated here, as well as in Pauling's original work, is that the reduction factors from the constraints are not independent. But as we will see in the following, such an approximation works quite accurately for the thin film systems.

Suppose we have a surface normal to [001], and the whole system is composed of stackings of the conventional cubic unit cells. For each conventional cubic unit cell, there are 16 spins in it. Let the number of unit cells in the x, y and z directions being L_x, L_y and L_z. L_z is the thickness of the film and it is considered to be finite, while L_x and L_y are to be taken to be infinity. Periodic boundary conditions are applied in the x and y directions.

The total number of spins

$$N_s = 16L_xL_yL_z \tag{4.3}$$

and the total number of tetrahedra

$$N_t = 8L_xL_yL_z - 2L_xL_y \tag{4.4}$$

where the minus sign term comes from the absence of periodic boundary along the z direction. Furthermore, the number of orphan bonds, N_b, is given by

$$N_b = 4L_xL_y \tag{4.5}$$

contributed from the two sides of the film. We can now proceed to consider several [001] surface conditions.

Connected surface

In this case we consider $J_{\text{orphan}} \neq -J_{\text{eff}}$, where J_{eff} is the effective nearest-neighbour exchange interaction. Depending on the overall sign of the combined exchange $J_{\text{orphan}} + J_{\text{eff}}$, the two spins connected by the orphan bonds energetically prefer to align along or against each other, in their respective local [111] directions. In this case we refer the surface to be a *connected surface*, since neighbouring tetrahedra on the surface are still connected by a non-zero orphan bond.

Assuming a paramagnetic phase, the total number of states would be 2^{N_s} for Ising spins. Since we need to satisfy the ice rule for every tetrahedron, and out of the 16 possible spin states for the 4 spins surrounding a tetrahedron, only 6 of them satisfy the ice rule, we have a factor of $(6/16)^{N_t}$ for the over-counting of the states. Then for the non-zero orphan bonds, since whether it is ferromagnetic or anti-ferromagnetic, out of the 4 spin configurations for the 2 spins surrounding the orphan bond, only 2 of them satisfy the bond, thus we have a factor of $(1/2)^{N_b}$ for the over-counting. Therefore, the total number of states for the connected surface reads

$$W_c = 2^{N_s} \cdot (6/16)^{N_t} \cdot (1/2)^{N_b} \tag{4.6}$$

Using Eq. 4.3, 4.4 and 4.5, we have the residual entropy per spin

$$S_c/N_s = (\frac{1}{2}) \ln(\frac{3}{2}) - \ (\frac{1}{8}) \ln(\frac{3}{2})(\frac{1}{L_z}) \tag{4.7}$$

for the connected surface.

Disconnected surface

In the case of $J_{\text{orphan}} = -J_{\text{eff}}$, the constraints from the orphan bonds are effectively dropped. Thus we do not have the $(1/2)^{N_b}$ for over-counting from satisfying the orphan bonds. Consequently the total number of states reads

$$W_d = 2^{N_s} \cdot (6/16)^{N_t} \tag{4.8}$$

Using Eq. 4.3, 4.4 and 4.5, we have the residual entropy per spin

$$S_d/N_s = (\frac{1}{2})\ln(\frac{3}{2}) - \ [(\frac{1}{8})\ln(\frac{3}{2}) - (\frac{1}{4})\ln(2)](\frac{1}{L_z}) \tag{4.9}$$

for the disconnected surface.

Checkerboard charge state

Consider the connected surface with an overall anti-ferromagnetic interaction for the orphan bonds ($J_{\text{orphan}} + J_{\text{eff}} < 0$), the two spins surrounding the orphan bond energetically prefer to align head-to-head or tail-to-tail. From the monopole dumbbell model [29], there are surplus of monopole charges from the head-to-head or tail-to-tail spin configurations at the positions of the orphan bonds (right outside of the surface). Further suppose that these charges are ordered such that neighbouring charges have opposite signs. Since the midpoints of the orphan bonds on one surface form a square lattice 45 degree to the axis of the cubic unit cell, the ordering required for the surface charges resembles a checkerboard pattern. Therefore we refer to this pattern of surface ordering as the surface checkerboard charge state.

By inspection, a pair of neighbouring spins on the surface, which are not connected by the orphan bond, align in a head-to-tail configuration, dictated by the opposition of the neighbouring charges. Thus, for any tetrahedron on the surface, one of the its two spins touching the surface points into the tetrahedron, and the other one points out of the tetrahedron. Therefore, for the other two spins of the surface tetrahedron that are not on the surface, the ice rule enforces one of them to be pointing in and the other one pointing out. But this is exactly the surface condition for the connected surface if we eliminate the spins on the surface and consider the new surface starting at the one quarter of cubic unit cell higher.

Therefore, in calculating the residual entropy we have the number of Ising degrees of freedom

$$N_s' = N_s - 8L_xL_y \tag{4.10}$$

since there are $8L_xL_y$ spins on the surface which are ordered and do not contribute to the residual entropy.

Similarly the number of tetrahedra needed to be considered for obeying the ice rule constraints becomes

$$N_t' = N_t - 4L_xL_y \tag{4.11}$$

As in the previously discussed connected surface state, the number of bonds to be satisfied on the surface is

$$N_b' = N_b \tag{4.12}$$

Note that these new bonds are not solely from the ferromagnetic interaction of the orphan bonds from the new effective surface (one quarter cubic unit cell from the surface), but they rather follow from a requirement of the ice rule for the tetrahedra that are on the surface.

As in the connected surface, the total number of states reads

$$W_{\text{checkerboard}} = 2^{N_s'} \cdot (6/16)^{N_t'} \cdot (1/2)^{N_b'} \tag{4.13}$$

Substituting in Eqs. (4.10), (4.11), (4.12) and (4.3), (4.4), (4.5), we have the residual entropy per spins

$$S_{\text{checkerboard}}/N_s = (\frac{1}{2})\ln(\frac{3}{2}) + \left[-(\frac{1}{2})\ln(2) - (\frac{3}{8})\ln(\frac{3}{8}) + (\frac{1}{4})\ln(\frac{1}{2})\right](\frac{1}{L_z}) \tag{4.14}$$

Uniform charge state

Consider the following scenario: the overall strength of the orphan bonds is anti-ferromangetic, favouring free charges on the surface. But now instead of having alternative signs for neighbouring charges, as in the case of the checkerboard charge state, we consider the case where all charges on the same surface having the same sign, and we refer such surface condition as the uniform charge state.

Requiring all charge on the surface having the same sign makes all the spins on the surface pointing in the same direction, *i.e.*, they all point into (or out of) the tetrahedra on the surface. Thus enforcing ice rules on the surface tetrahedra in turn makes all the spins a quarter cubic unit cell depth away from the surface point out of (or into) the surface tetrahedra, thus they point into (or out of) the tetrahedra they are connected in the bulk. This, in turn, makes all the spins a quarter layer above point in the same direction again.

Therefore we can see that by requiring a uniform charge state, we end up with a complete ordering throughout the film.

$$S_{\text{uniform}} = 0 \tag{4.15}$$

Furthermore, the charges on the other side of the film is enforced to be uniform and of the opposite sign.

The above result for the zero entropy for a film with uniform charges is a reminder of the emergent electrostatics in the spin ice phase. [31, 80] If we were treating ordinary electric charges with opposite signs on two sides of the film, we would effectively have a capacitor defined by the film. By Gauss's law, the electric field inside an infinite capacitor depends only on the density of the charges on the two sides but not on the separation of the two plates. Similarly, the two plates of *magnetic* charges in our film system dictate the flux of the spins inside the film. Interestingly there is genuine long-range interations from these magnetic charges. The ice rule is all we need to create such a magnetic analogue of the capacitor.

4.1.3 Summary

In summary, we have Eqs. (4.7), (4.9), (4.14), (4.15) for the surface corrections to the Pauling's residual entropy. We have, except for the uniform charge state, $1/L_z$ corrections to the Pauling's residual entropy.

$$S/N_s = \begin{cases} 0.2027 - 0.0507/L_z & \text{for connected surfaces} \\ 0.2027 + 0.1226/L_z & \text{for disconnected surfaces} \\ 0.2027 - 0.1520/L_z & \text{for checkerboard charge state} \\ 0 & \text{for uniform charge state} \end{cases} \tag{4.16}$$

4.2 Monte Carlo simulations of spin ice thin films

The main method of investigation in this chapter is the Monte Carlo method on Hamiltonians of Eq. (4.1) and Eq. (4.2), with added orphan bonds J_{orphan} at the surfaces.

The simulation box is always a cubic of size L by L by L measured in units of the conventional cubic unit cells. Periodic boundary conditions are applied in all three directions.

The film geometry is achieved by emptying the space except for a slab layer of cubic unit cells. The thickness of the slab is L_z in unit of cubic unit cells. By construction we have thin films with surface normal to [001]. We illustrate in Fig. 4.3 the construction of our simulation box.

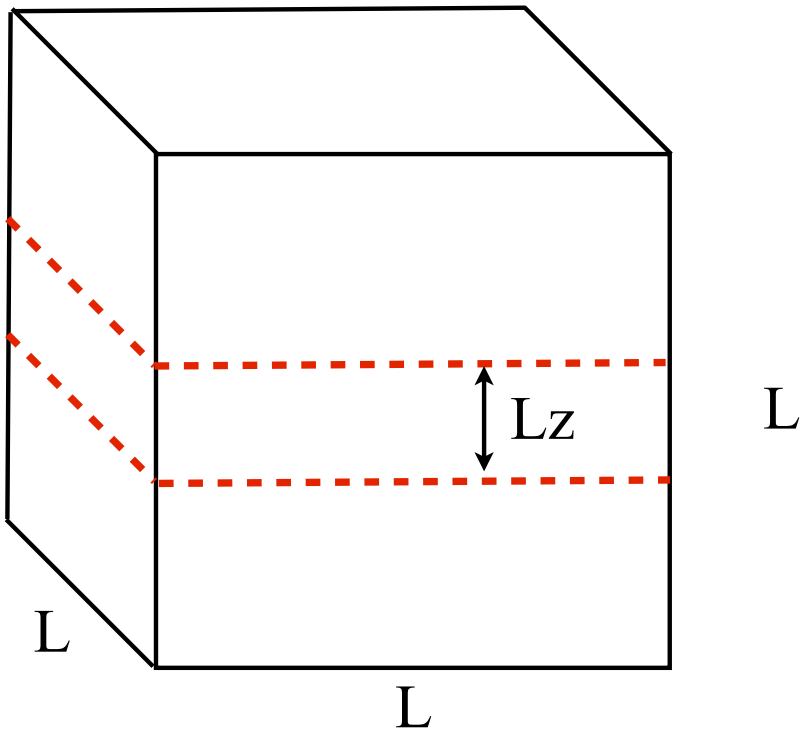

Figure 4.3: Thin film of spin ice is achieved by removing spins in a cubic simulation box of side length L. Only spins within the slab of thickness L_z are retained. Periodic boundary conditions are assumed for the cubic simulation box in all three cubic directions. The surface created is normal to the [001] direction.

For the nearest-neighbour spin ice model Eq. (4.2), there is no obvious reason for this construction. Constructions of films with surface normal to other directions are straightforward by not using the conventional cubic unit cell, but any orthorhombic units with

the desired surfaces, then periodic boundary conditions can be applied in other directions perpendicular to the surface to create the film. On the other hand for the dipolar spin ice model of Eq. (4.1), the use of a cubic simulation cell has the advantage that the ordinary Ewald summation technique can still be used.

We have used up to $L = 8$ for the simulation box, and up to three layers ($L_z = 3$) of thickness of films are studied, with single spin flip updates used in all simulations.

4.3 Residual entropies for thin films of spin ice

In this section, we present specific heat results from the Monte Carlo simulations for the dipolar spin ice and nearest-neighbour spin ice with various orphan bond strengths.

4.3.1 Dipolar spin ice thin films

First we consider the $C(T)$ results for dipolar spin ice film with one layer thick ($L_z = 1$), shown in Fig. 4.4. The specific heat results from the dipolar spin ice with $J_1 = 3.72$ K and $D = 1.41$ K are plotted for different strengths of the orphan bonds J_{orphan}. A simulation box of $L = 8$ is used for the one layer thick film. As a reference, the simulation $C(T)$ for the bulk dipolar spin ice with the same J_1 and D is also plotted on the same figure. The bulk simulation is done on a simulation box of $L = 4$ and loop updates are used.

For the J_1 and D values of our model, the effective nearest-neighbour interaction is

$$J_{\text{eff}} = -J_1/3 + 5D/3 = 1.11 \text{ K} \tag{4.17}$$

Therefore for $J_{\text{orphan}} < -1.11$ K, the overall strength of the orphan is antiferromagnetic, otherwise we have a ferromagnetic orphan bond.

The specific heat results in Fig. 4.4 show for $J_{\text{orphan}} = -2$ K and $J_{\text{orphan}} = -3$ K (both less than J_{eff}), the specific heat curves develop sharp peaks. The position of the peak increases as J_{orphan} decreases. On the other hand, for other values of J_{orphan}, the specific heat curves show broad peaks similar to the dipolar spin ice in bulk. Thus this is a strong indication that by turning the overall strength of the orphan bond being from ferromagnetic to antiferromagnetic, the low temperature physics of the film changes dramatically.

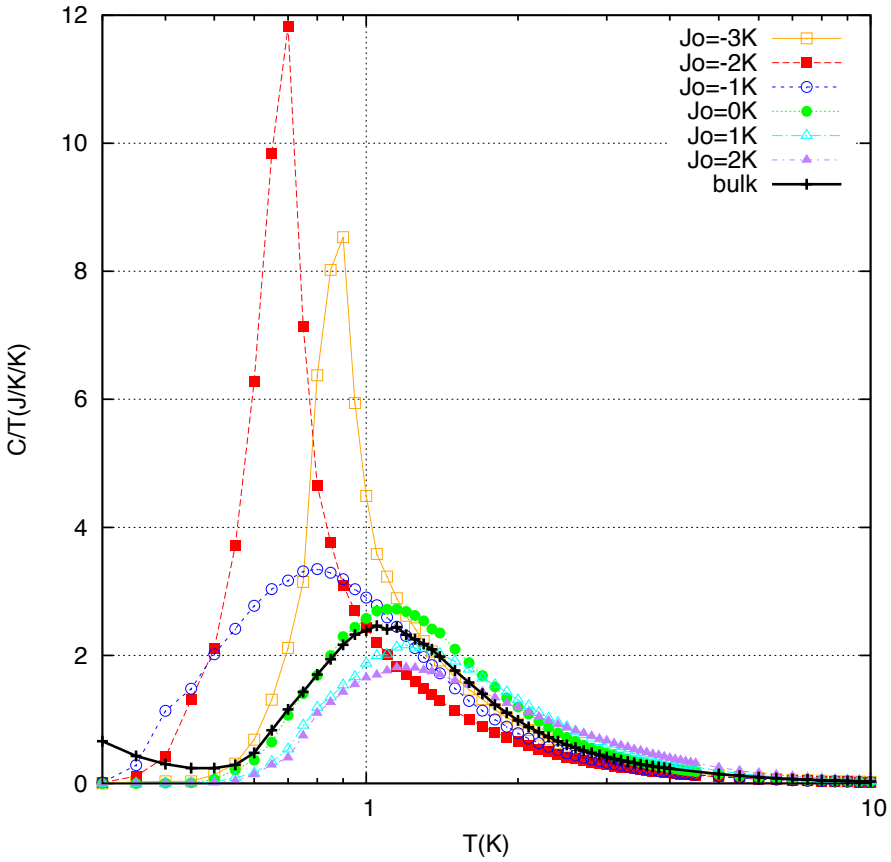

Figure 4.4: Monte Carlo simulation of the specific heat of dipolar thin film spin ice. J_1 = 3.72 K and D = 1.41 K. L = 8 for the simulation box and the thickness of the film is one cubic unit cell, *i.e.* L_z = 1.

Second, we look at the specific heat results for dipolar spin ice with more than one cubic unit cell thickness. The results for a simulation box of L = 8 are plotted in Fig. 4.5. For more than one layer of thickness and $J_{\text{orphan}} > -1.11$ K, the specific heat curves exhibit similar broad peaks as in the bulk spin ice, as in the case for one layer of thickness. For $J_{\text{orphan}} < -1.11$ K, specific heat curves for more than one layer thick film develop sharp peaks, as in the one layer films. However, the broad peak slowly re-emerges as the size (L) of the simulation box increases.

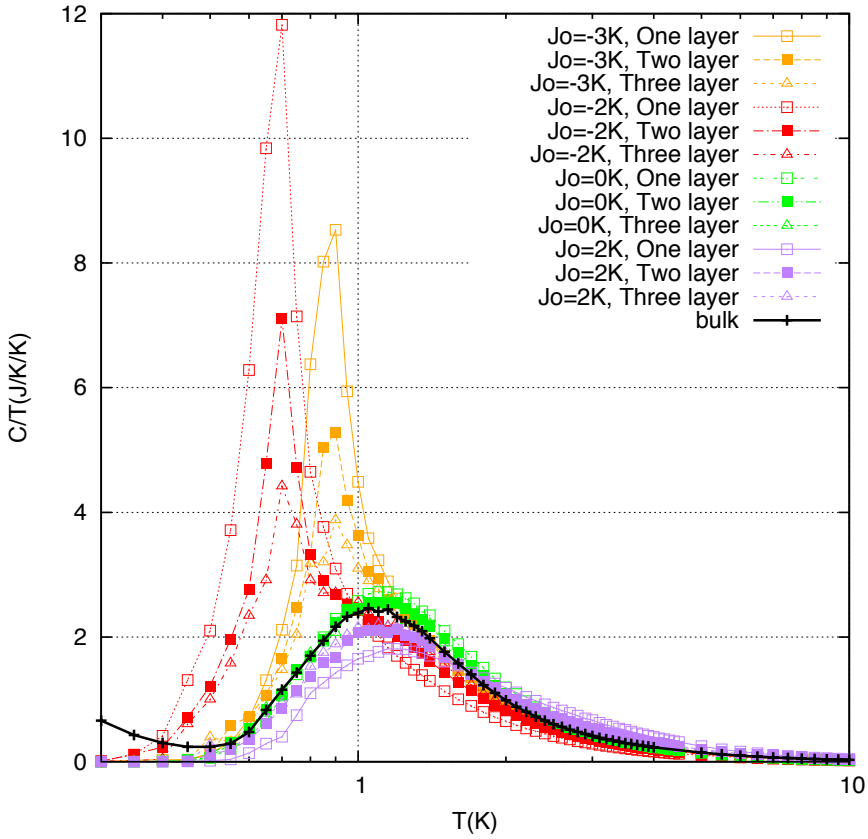

Figure 4.5: Monte Carlo simulation of the specific heat of dipolar thin film spin ice. J_1 = 3.72 K and D = 1.41 K. L = 8 for the simulation box and the thicknesses (L_z) of the film varies from one to three layers of cubic unit cells.

From the specific heat measurements, residual entropies for the films can be obtained. In Fig. 4.6, we plot the residual entropy obtained at T = 0.15 K (the lowest temperature in our simulation) as a function of the strength of the orphan bonds.

As can be seen from Fig. 4.6, the residual entropy displays a sharp decline as J_{orphan} gets below −1.11 K, *i.e.*, when the overall strength of the orphan bond becomes antiferromagnetic. The same figure also shows as the thickness of the film increases, the residual entropies march back towards the Pauling's entropy.

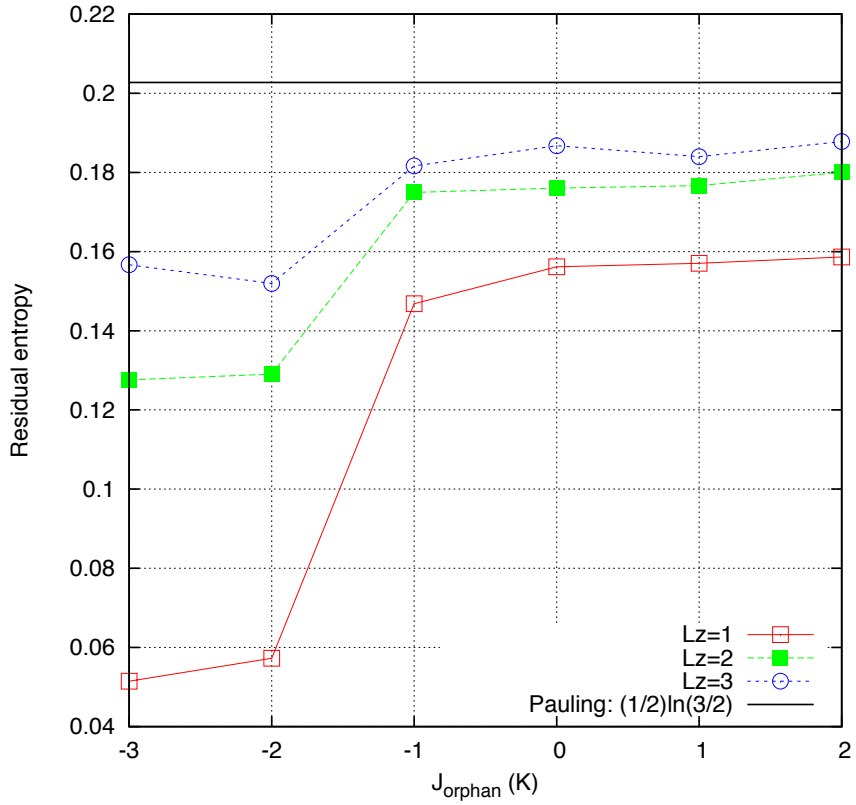

Figure 4.6: Residual entropy for various thickness of the film, as a function of the strength of the orphan bond. $J_{\text{eff}} = 1.11$ K in the dipolar Hamiltonian Eq. (4.1). A simulation box of $L = 8$ was used.

In Fig. 4.7 we investigate how the residual entropy of the films returns to the Pauling's residual entropy. As already indicted by the specific heat data, a qualitative different behaviour exists between the two sets of data of $J_{\text{orphan}} > -1.11$ K and $J_{\text{orphan}} < -1.11$ K. For $J_{\text{orphan}} > -1.11$ K where the overall strength of the orphan bond remains ferromagnetic, the $1/L_z$ corrections to the Pauling's entropy can be well described by the connected surface. For $J_{\text{orphan}} < -1.11$ K, where the overall strength of the orphan becomes antiferromagnetic, the residual entropies fall onto the slope of the checkerboard charge state corrections.

Therefore, from the residual entropy analysis, we have found indications of an antiferromagnetic orphan bond induced surface charge ordering ground state for thin films of spin ice. Interestingly, the surface charge ordering does not eliminate all the remaining entropy of the system, thus we have a situation where the surface freezes before the bulk, a point we will discuss further in later sections.

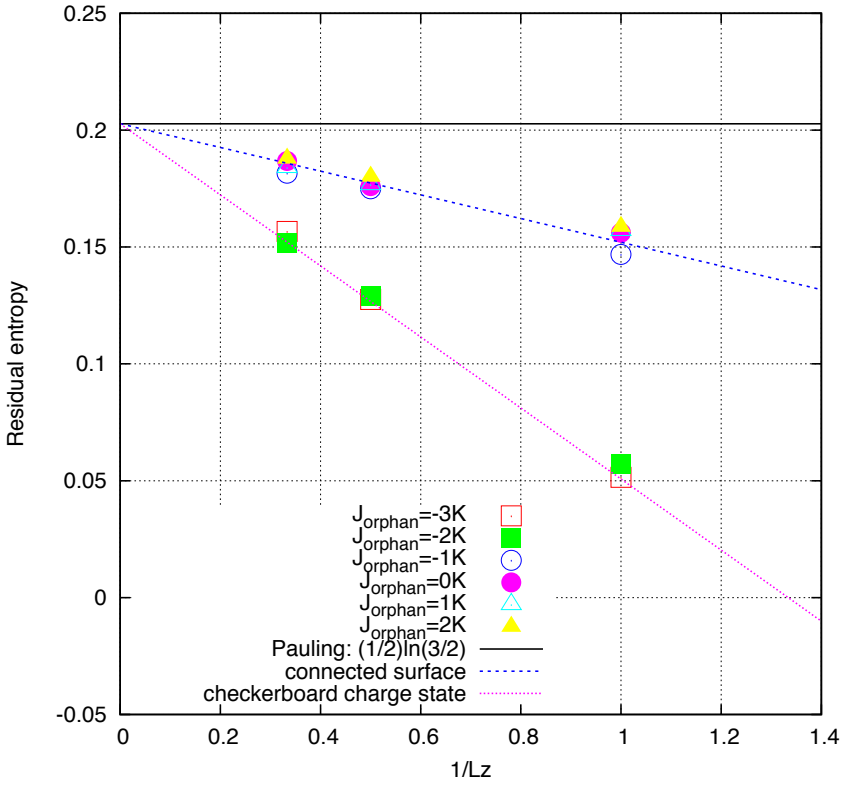

Figure 4.7: Residual entropy for various orphan bond strength of the film, as a function of the inverse thickness, $1/L_z$. J_{eff} = 1.11 K in the dipolar Hamiltonian Eq. 4.1. A simulation box of $L = 8$ was used.

4.3.2 Nearest-neighbour spin ice thin films

Monte Carlo calorimetric measurements have also been done for the nearest-neighbour spin ice thin films, described by the Hamiltonian (4.2). Here we choose $J_1 = -3$ K, making $J_{\text{eff}} = 1$ K from Eq. (4.17). In Fig. 4.8, we plot the specific heat from the simulation for a simulation box of $L = 8$, with various strength of the orphan bonds (J_{orphan}) and for one, two and three layers of film thickness.

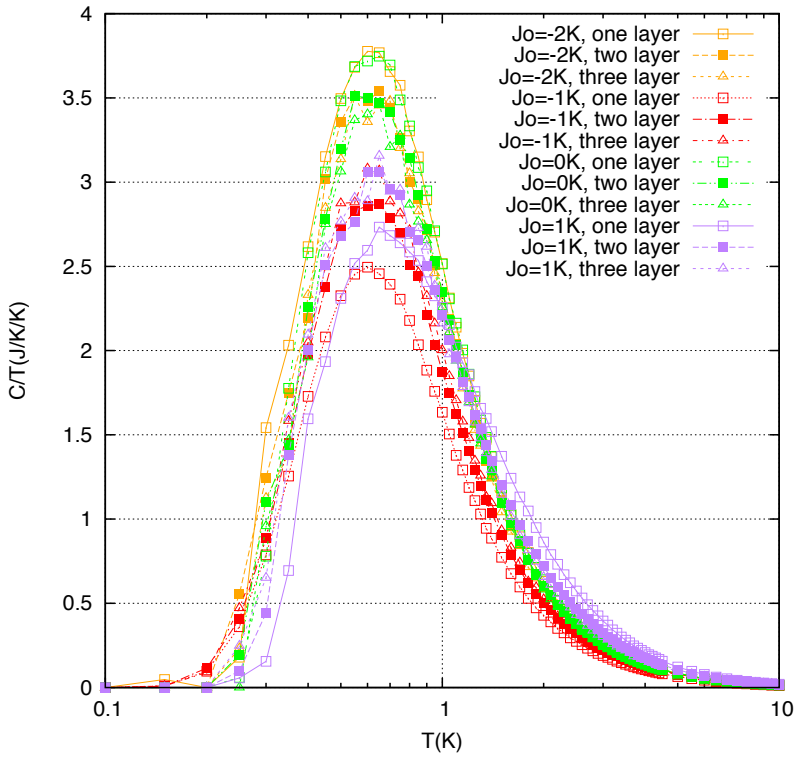

Figure 4.8: Monte Carlo specific heat results for the nearest-neighbour Hamiltonian, Eq. (4.2). The effective nearest-neighbour interaction between neighbouring spins is $J_{\text{eff}} = 1$ K. Up to three layers of cubic unit cells thickness of films were simulated. Various strengths of the orphan bonds, J_o (J_{orphan}), are used. A simulation box with size $L = 8$ was used. Only single spin flip updates are used.

As can be seen in Fig. 4.8, tuning the strength of the orphan bond does not induce a

qualitative change in the specific heat measurements. Whether the overall orphan bond strength is antiferromagnetic ($J_{\text{orphan}} < -1$ K), ferromagnetic ($J_{\text{orphan}} > -1$ K), or exactly zero ($J_{\text{orphan}} = -1$ K), only broad peaks of the specific heat appear, indicating that no transition is induced by the orphan bonds.

We further look at the residual entropy obtained at $T = 0.15$ K, (the lowest temperature in our simulations). In Fig. 4.9, we plot the residual entropy as a function of the orphan bond strength, J_{orphan}.

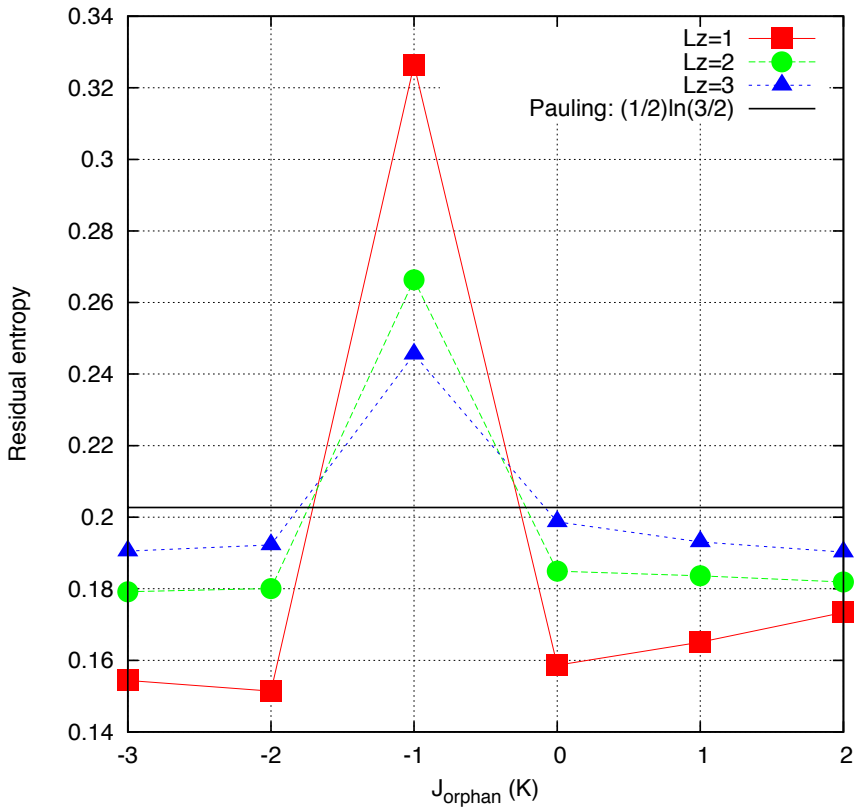

Figure 4.9: Residual entropy for various thickness of the film, as a function of the strength of the orphan bond. $J_{\text{eff}} = 1$ K in the nearest-neighbour Hamiltonian Eq. (4.2). A simulation box of $L = 8$ was used.

As can be seen in Fig. 4.9, for both overall strictly ferromagnetic or strictly antiferro-

magnetic orphan bonds, the residual entropies remains below the Pauling's entropy, while for overall zero orphan bond ($J_{\text{orphan}} = -1$ K), the residual entropies are above the Pauling's entropy. As the thickness of the film increases, all entropies approaches the Pauling's.

The feature that interests us the most is how the residual entropies scale as a function of the thickness of the film. We plot in Fig. 4.10 the residual entropies as a function of the inverse thickness. As can be seen in the figure, the residual entropies of the system fall into two categories. One is the residual entropies for the overall ferromagnetic and antiferromagnetic bonds, which can be described by the connected surface corrections to the Pauling's entropy, Eq. (4.7) The other is the residual entropies for the zero orphan bond ($J_{\text{orphan}} = -1$ K), which can be described by the disconnected surface corrections, Eq. (4.9).

Note that in the case of the antiferromagnetic orphan bonds, even though there are free charges induced by the orphan bonds, a connected surface correction to the Pauling's entropy, Eq. (4.7), instead of a checkerboard charge state correction to the Pauling's entropy, Eq. (4.14), as seen in the case for the dipolar spin ice, suggests that these charges are not ordered on the surface. In the case of nearest-neighbour spin ice model described by the Hamiltonian Eq. (4.2), there is no energetic gain in ordering the charges when they appear. It should be noted in Fig. 4.10 that at small $1/L_z$, there is a small departure of the MC integrated entropy to the connected surface correction. Such a problem is unsolved at the writing of the thesis. One possible explanation is due to the entropy interaction of the surface charges.

4.3.3 Summary

In summary, through the Monte Carlo investigations of the residual entropy of the films and the analysis of how the residual entropy scales as a function of the inverse thickness of the film, we deduce the following surface states for the film systems. For the dipolar spin ice, we have checkerboard charge state for the antiferromagnetic orphan bonds and connected surface state for the ferromagnetic orphan bonds. For the nearest-neighbour spin ice, we have connected surface state for both ferromagnetic and antiferromagnetic orphan bonds, and disconnected surface state for the zero orphan bonds.

Notice that for both Hamiltonians, the residual entropies all show inverse thickness, $1/L_z$, corrections to the Pauling's entropy. This is to be expected as $L_z \to \infty$, the film

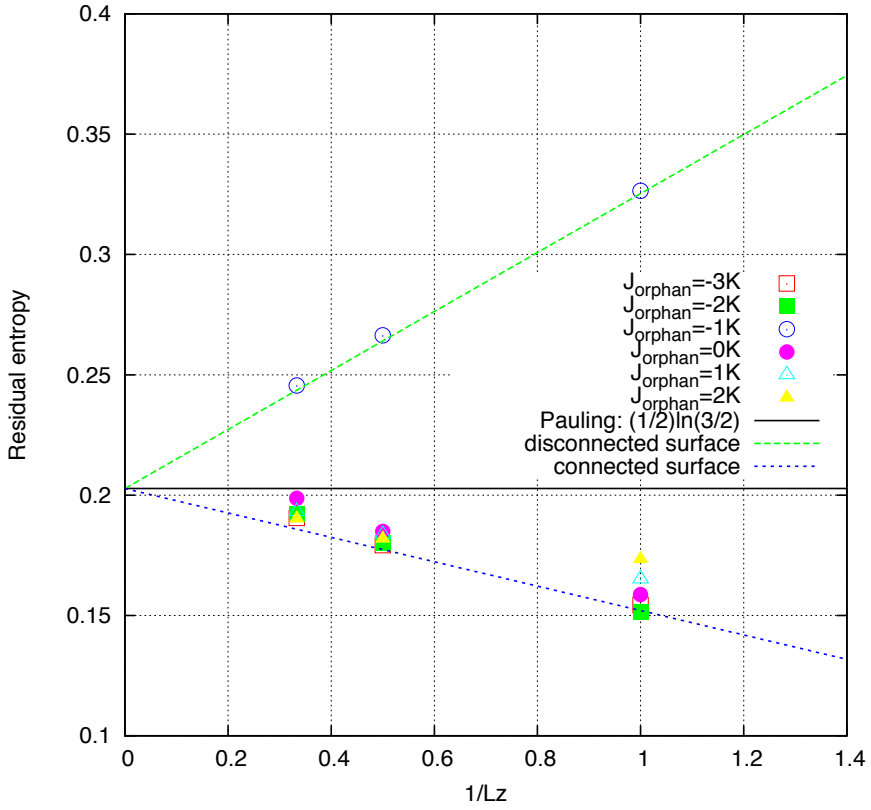

Figure 4.10: Residual entropy of the film for various strengths of the orphan bond, as a function of the inverse thickness $1/L_z$. $J_{\text{eff}} = 1$ K in the nearest-neighbour Hamiltonian of Eq. (4.2). A simulation box of $L = 8$ was used.

eventually becomes the bulk. While for the dipolar model the MC results can be better described by the surface corrections, for the nearest-neighbour model with a connected surface scenario, the description becomes less quantitative.

4.4 Continuous phase transition at the surface

In this section, we study specifically the dipolar spin ice with an overall antiferromagnetic orphan bond. In particular, we choose $J_{\text{orphan}} = -2$ K. As indicated in Section 4.3, such a film system possesses a surface ordering (checkerboard charge state, Eq. (4.14)) while the bulk remains disordered. Thus we have an unusual magnetic system capable of surface freezing. In simple arguments, surface freezing may not be uncommon if the interaction on the surface is much greater than the interactions in the bulk. However in our case, an orphan bond strength of $J_{\text{orphan}} = -2$ K is quite comparable to the exchange and dipolar interactions in the system. Thus the surface freezing in this system is a reminder of the precarious balance in our dipolar frustrated system, a point we will further discuss in the next section, Section 4.5, after we have studied in detail in this section the nature of the surface ordering phase transition.

4.4.1 Specific heat sharp peak

From Section 4.3, the clear anomalies induced by the antiferromagnetic orphan bond are the sharp peaks in the specific heat at about $T = 0.7$ K. In this section we study in detail through simulation around this temperature.

We plot in Fig. 4.11 the specific heat versus temperature for various thickness of the film in various sizes of simulation box. As seen in the figure, away from the peak of the specific heat at about $T = 0.7$ K, that there is little finite size effects from the size of the simulation box, indicating no complications from the multi-layer structure by design of the simulation box when periodic boundary condition is applied along the direction perpendicular to the film surface (z-direction). Around the peak of the specific heat, curves from larger simulation box develop higher and sharper peaks.

4.4.2 Structure factor of the surface charges

Already indicated from the analysis of the residual entropy as a function of the inverse thickness of the films, the calorimetric measurements are consistent with a checkerboard charge ordered surface state discussed in Section 4.1 of this chapter. Now in this subsection

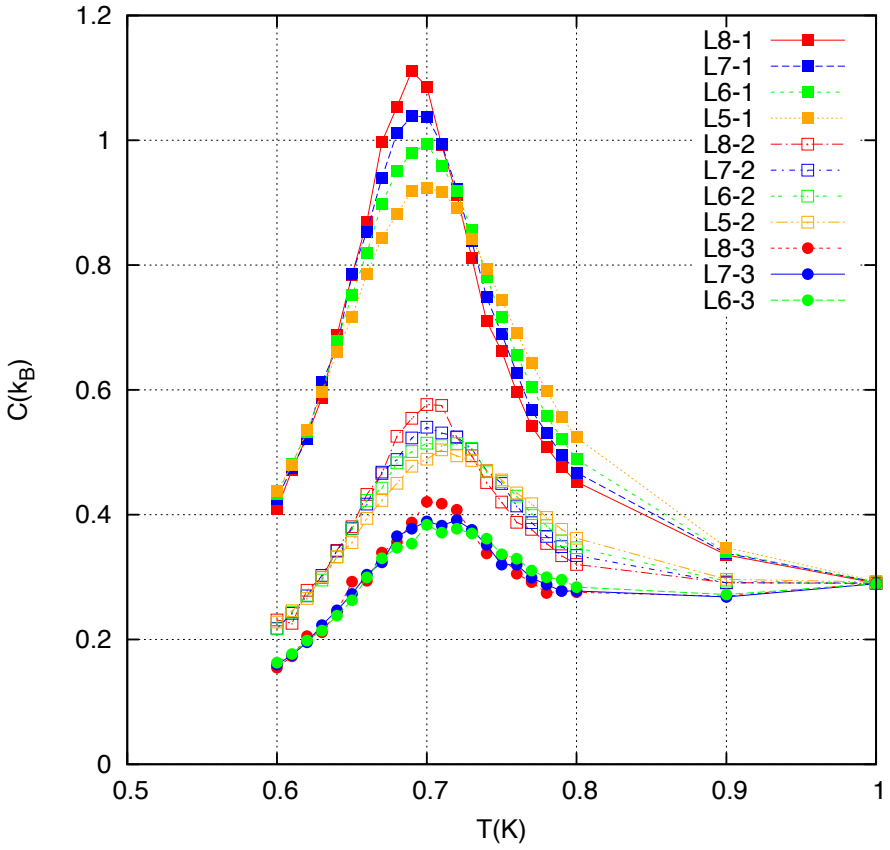

Figure 4.11: Monte Carlo specific heat for $J_{\text{orphan}} = -2$ K of the dipolar Hamiltonian 4.1 around 0.7 K. Various thicknesses and simulation box sizes are used. In the label $Lx - y$ means a simulation box of size $L = x$ and a film of thickness y cubic unit cells. There are noticeable finite size effects (dependence on the simulation box size) at the peak of the specific heat for all thicknesses.

we investigate directly through the structure factor of the charges induced on the surface to confirm the charge ordered surface.

The charges, σ, are defined at the midpoints of the orphan bonds, and their values equal to the sum of the two spin variables at the two ends of the orphan bonds. The locations of the charges on one side of the surface form a square lattice with its edge along the

[110] direction of the underlying pyrochlore lattice of the film. This distance between two neighbouring charges equals to $\sqrt{2}a/2$. The structure factor for one surface is calculated through

$$S(\vec{q}) = (1/N)\sum_{i,j}\langle\sigma(\vec{r}_i)\sigma(\vec{r}_j)\rangle e^{i\vec{q}\cdot\vec{r}_{ij}} \tag{4.18}$$

where N is the number of orphan bonds (locations of the charges) on one surface, and $\vec{r}$'s are the locations of the surface charges.

We plot in Fig. 4.12 the structure factor of the surface charges for one layer of dipolar spin ice thin film. We observe bright peaks developing at $(0, 2\pi)$ and $(2\pi, 0)$ and reciprocal lattice translated points below the sharp peak of the specific heat at around $T = 0.7$ K. Since the primitive translation vectors for the surface charges are $(1/2, 1/2)$ and $(1/2, -1/2)$, in unit of the length of the cubic cell of the pyrochlore lattice, the observed bright peaks in **q**-space indicate a change of sign for neighbouring charges. Therefore the **q**-space peaks indicate a checkerboard pattern of the charges at the orphan bonds below about 0.7 K. Thus we have a surface ordering for the dipolar spin ice thin films with antiferromagnetic orphan bonds.

A snapshot of the spin configurations at $T = 0.6$ K is plotted in Fig. 4.13. Spin configurations on the surface of the checkerboard state are indicated in Fig. 4.14

4.4.3 Order parameter of the surface checkerboard charge state

Having identified the surface charge ordering in the checkerboard pattern, we can define the order parameter, s, for the surface ordering.

$$s = (1/2)\sum_{i}\langle\sigma(\vec{r}_i)\rangle e^{i\vec{q}\cdot\vec{r}_i} \tag{4.19}$$

with the ordering wave vector $\vec{q} = (2\pi, 0)$. The 1/2 pre-factor comes from the definition that the charges, once appeared, assume values of ± 2.

We plot in Fig. 4.15 the root mean square of the order parameter [46], $s_{\text{rms}} = \sqrt{\langle s^2\rangle}$, as a function of temperature, for different sizes of the simulation box. It can be seen from the figure that once the temperature drops below about 0.7 K, the root mean square of the order parameter approaches one. Note that above about 0.7 K, s_{rms} does not approach zero as the temperature increases, but does so as the size of the system increases. This is expected

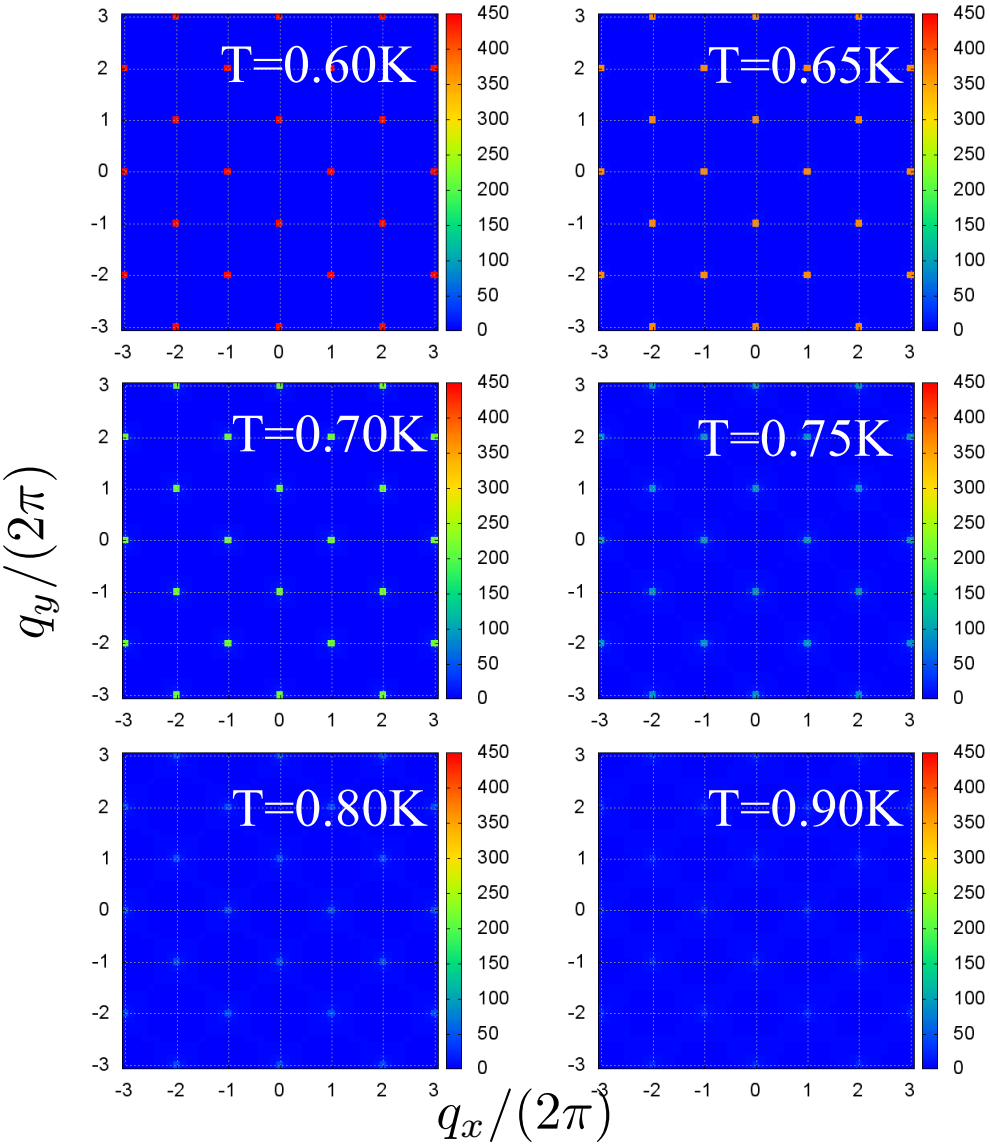

Figure 4.12: Structure factor for the surface charges at various temperatures, for film of one cubic unit cell thick. $J_{\text{orphan}} = -2$ K for the dipolar Hamiltonian, Eq. (4.1). Peaks at $(0, 2\pi)$ and $(2\pi, 0)$ are developed below about 0.7 K. A simulation box of size $L = 8$ was used.

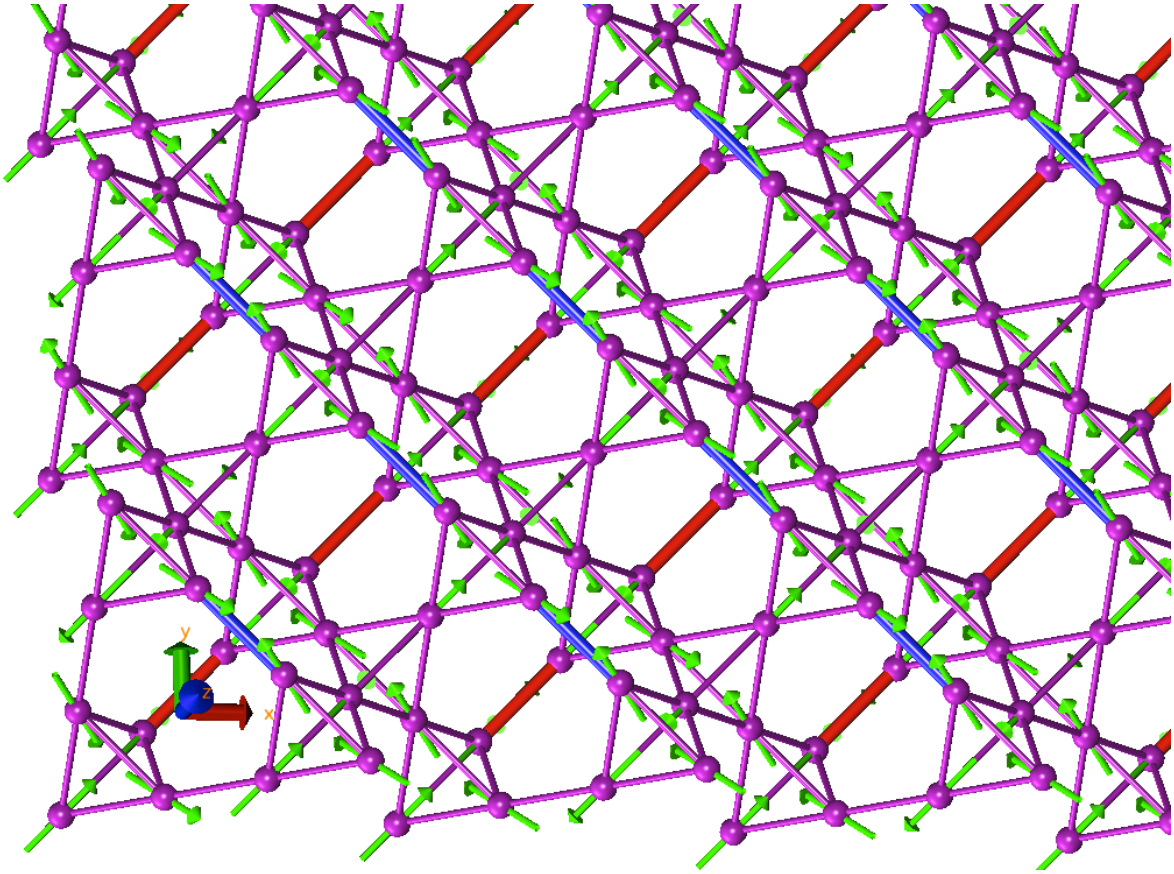

Figure 4.13: Snapshot of the spin configurations for $J_{\text{orphan}} = -2$ K, dipolar Hamiltonian Eq. (4.1), at $T = 0.6$ K. A simulation box of size $L = 8$ is used and the thickness of the film is one cubic unit cell thick, both as shown in the figure. The orphan bonds at the top ad bottom of the film are marked in blue and red, respectively. The green arrows represent the magnetic spins. This is a surface checkerboard state, indicating by the alternation of the head-to-head and tail-to-tail patterns of the two spins surrounding the orphan bonds.

for an order parameter defined this way [46]. For example, in an Ising system at infinite temperature, $\langle S_i S_j \rangle = \delta_{ij}$, which leads to the root mean square of the magnetization (order parameter for a ferromagnetic transition for the example given here) being $M_{\text{rms}} = 1/\sqrt{N}$. The same argument applies here to our order parameter, with the only difference being the charge defined by the sum of the two spin variables surrounding the orphan bond at

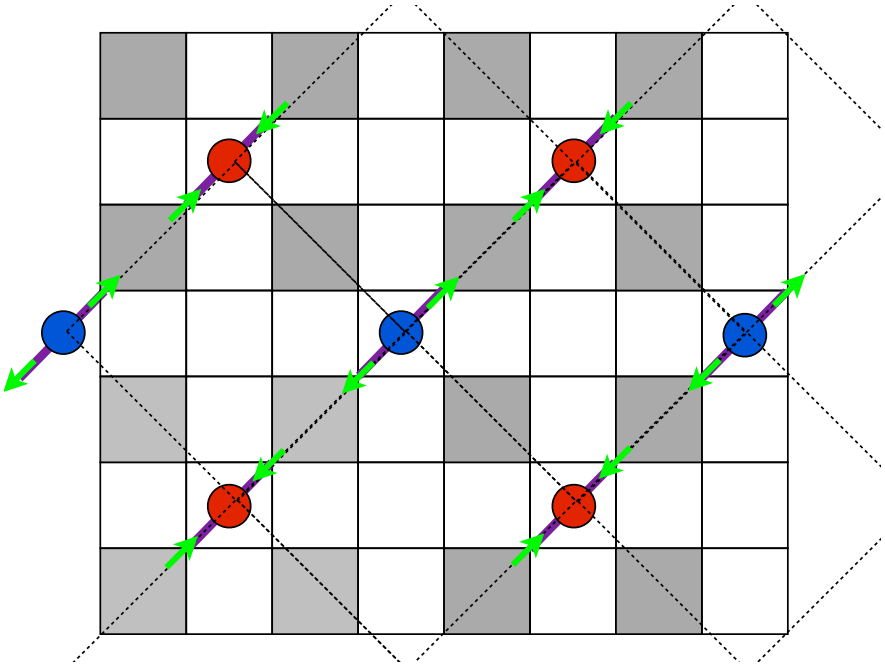

Figure 4.14: Spins on the surface of the checkerboard state.

infinite temperature will approach zero faster as the value of the charge itself may go to zero.

4.4.4 Continuous phase transition for the surface charges

To distinguish whether the transition to the checkerboard charge state on the surface is first order or continuous, we measure the 4th order energy cumulant quantity

$$V_L = 1 - \frac{\langle E^4 \rangle}{3\langle E^2 \rangle^2} \tag{4.20}$$

In Fig. 4.16, we plot the V_L quantity as a function of temperature for various system sizes. The minima of V_L approaches the value of 2/3, indicating a continuous phase transition [46].

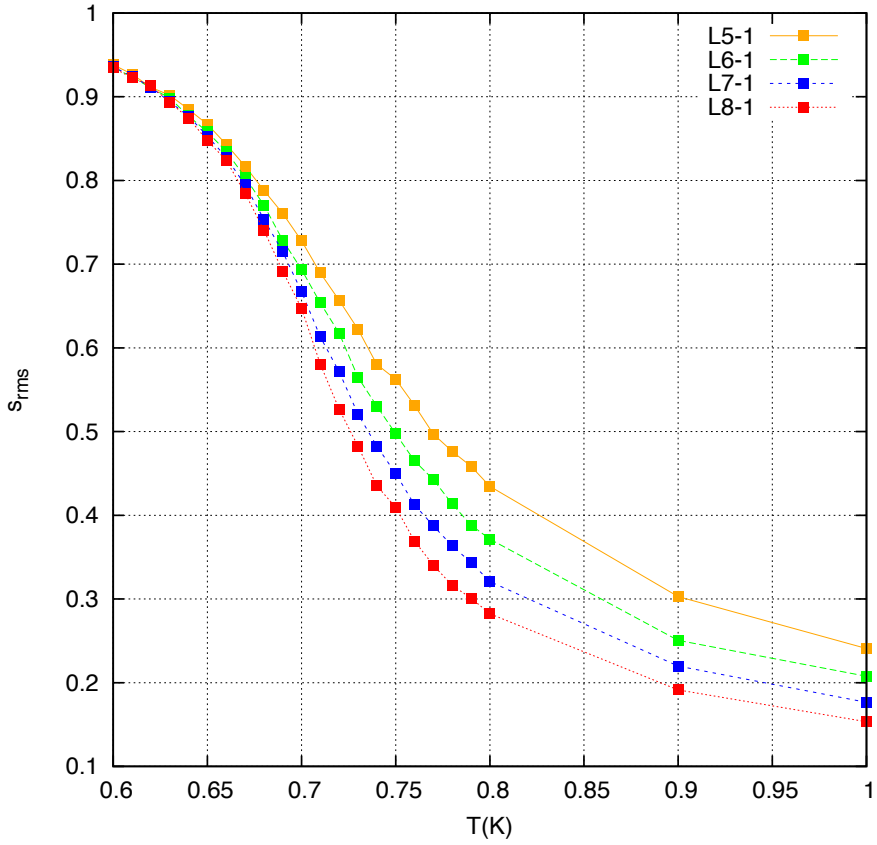

Figure 4.15: The root mean square order parameter for the surface charges. $J_{\text{orphan}} = -2$ K for a dipolar Hamiltonian, Eq. (4.1). Different curves correspond to different size of the simulation box, thus different sizes of the film. Film of one cubic unit cell thick is considered here.

Therefore we measure the 4th order cumulant of the U_L for the continuous phase transition [46].

$$U_L = 1 - \frac{\langle s^4 \rangle}{3\langle s^2 \rangle^2} \tag{4.21}$$

We plot in Fig. 4.17 U_L as a function of temperature for different system sizes. A

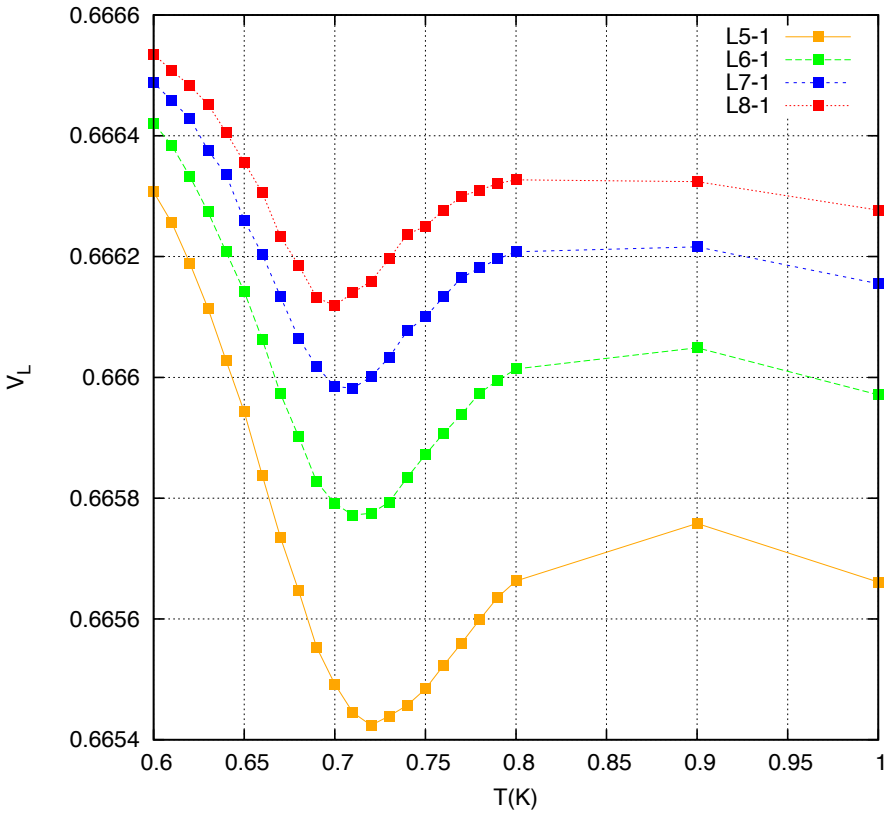

Figure 4.16: The 4th order energy cumulant, Eq. 4.20, defined in the text for one unit cell thick film. Different curves correspond to different sizes of the simulation box. The minima of the cumulant, approaches 2/3 as the size of the film increases.

crossing of the cumulant U_L's for different system sizes is found at

$$T_c = 0.675 \pm 0.005\text{K}. \tag{4.22}$$

For the continuous phase transition, near the phase transition, where the linear size of the system, L, is much smaller than the correlation length, ξ, we have the following standard finite size relations [46]:

$$\langle |s| \rangle_L = L^{-\beta/\nu} \tilde{M}(L/\xi), \tag{4.23}$$

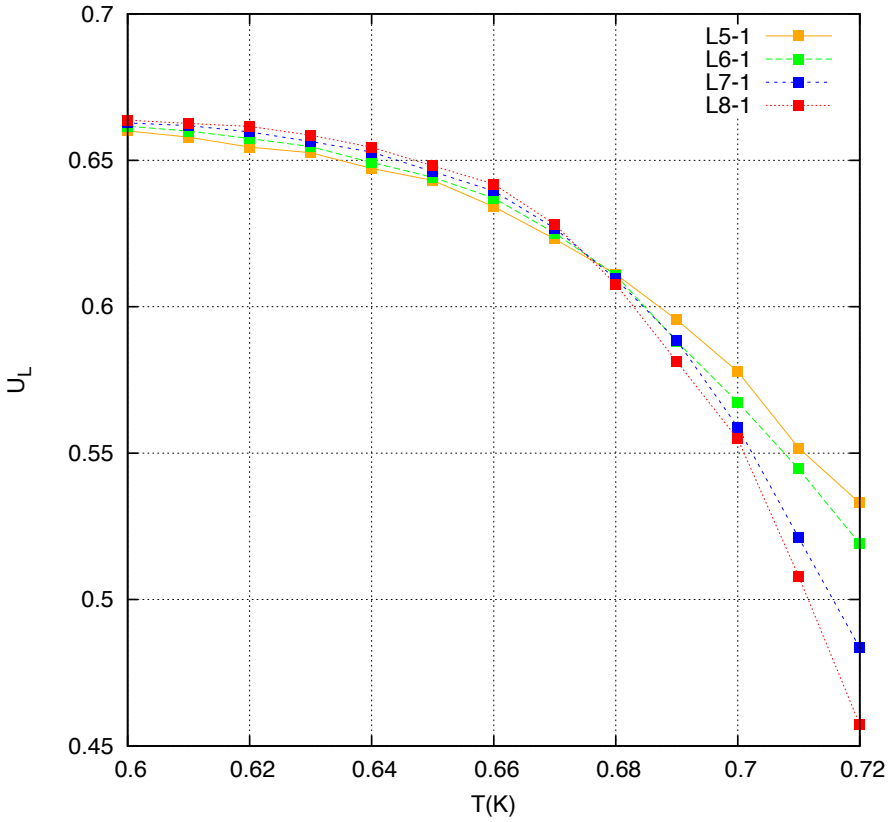

Figure 4.17: Fourth order cumulant, Eq. (4.21), for one cubic unit cell thick films with different sizes of the simulation box.

and

$$\chi'(L,T) \equiv L^d(\langle s^2\rangle_L - \langle|s|\rangle_L^2)/k_{\rm B}T = L^{\gamma/\nu}\tilde{\chi}(L/\xi). \tag{4.24}$$

Under the two-dimensional Ising universality class critical exponents, $\beta = 1/8$, $\nu = 1$, $\gamma = 7/4$, and $d = 2$, collapses of the curves are shown in Fig. 4.18 and in Fig. 4.19. Thus the continuous transition is of the two-dimensional Ising universality class.

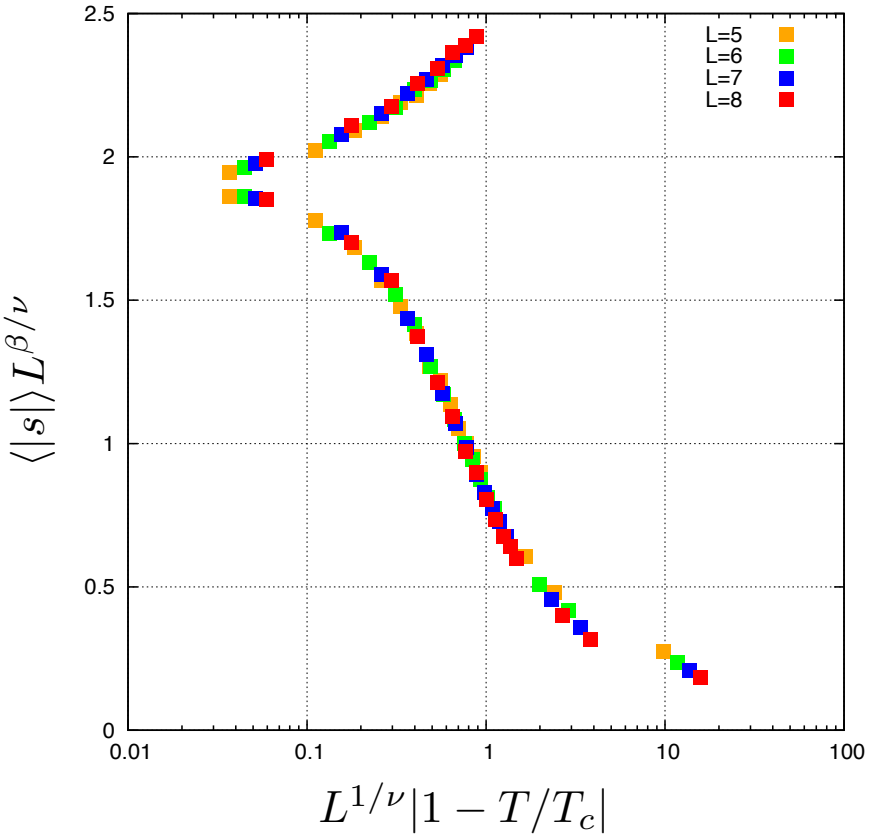

Figure 4.18: Collapse of the order parameter s.

4.4.5 Surface freezing

As analyzed above, the surface of our film system orders into checkerboard charge state for an antiferromagnetic orphan bond strength. From the entropy results we know there is still residual entropy left for the film system, thus the spins that are not part of the top or bottom surface of the film must remain disordered. To illustrate this point we investigate the structure factors of the spin variables on the surface and in the bulk of film.

The structure factor for a given layer of depth z from the surface is defined as

$$S(\vec{q}, z) = (1/N_{\text{spin}}) \sum_{i,j} \langle s_i s_j \rangle \delta(z_i - z) \delta(z_j - z) e^{i\vec{q}\cdot\vec{r}_{ij}} \tag{4.25}$$

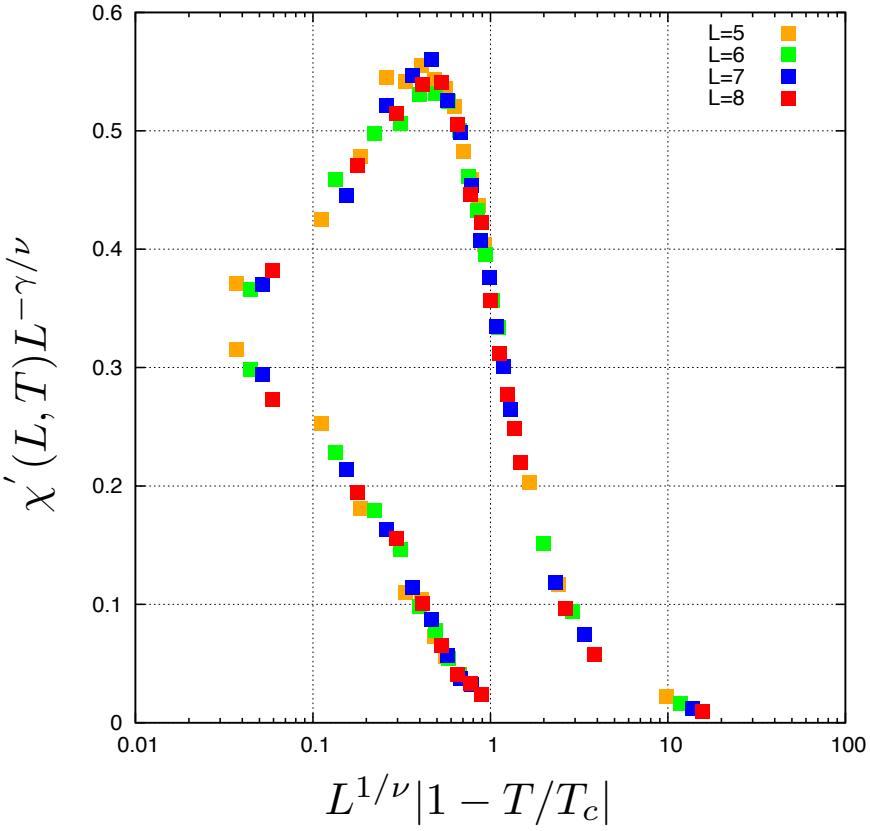

Figure 4.19: Collapse of the order parameter χ'.

In Fig. 4.20, we plot the structure factor calculated for the spins on the surface of the film. Similar to the structure factor of the surface charges, Bragg peaks are developed for the surface spin-spin correlations.

In Fig. 4.21, we plot the structure factor calculated for the spins in the bulk of the film. Diffuse intensities are found in the **q**-space. Therefore, the spins in the bulk of the film, despite surface ordering, do not form long-range order at least down to 0.6 K.

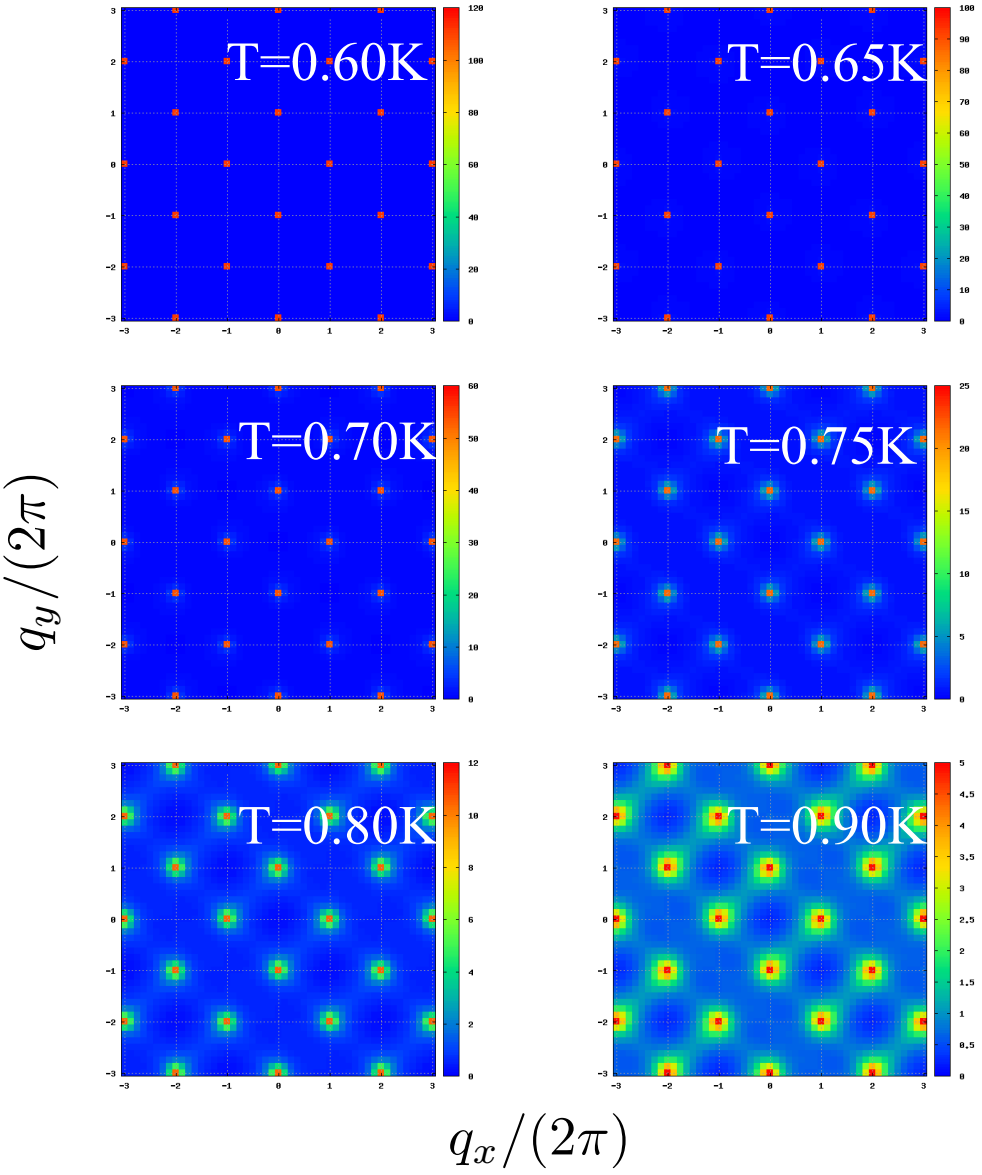

Figure 4.20: Monte Carlo results of the structure factors for the surface spins at various temperatures. $J_{\text{orphan}} = -2$ K for a dipolar Hamiltonian. A simulation box of size $L = 8$ was used. The thickness of the film is one cubic unit cell.

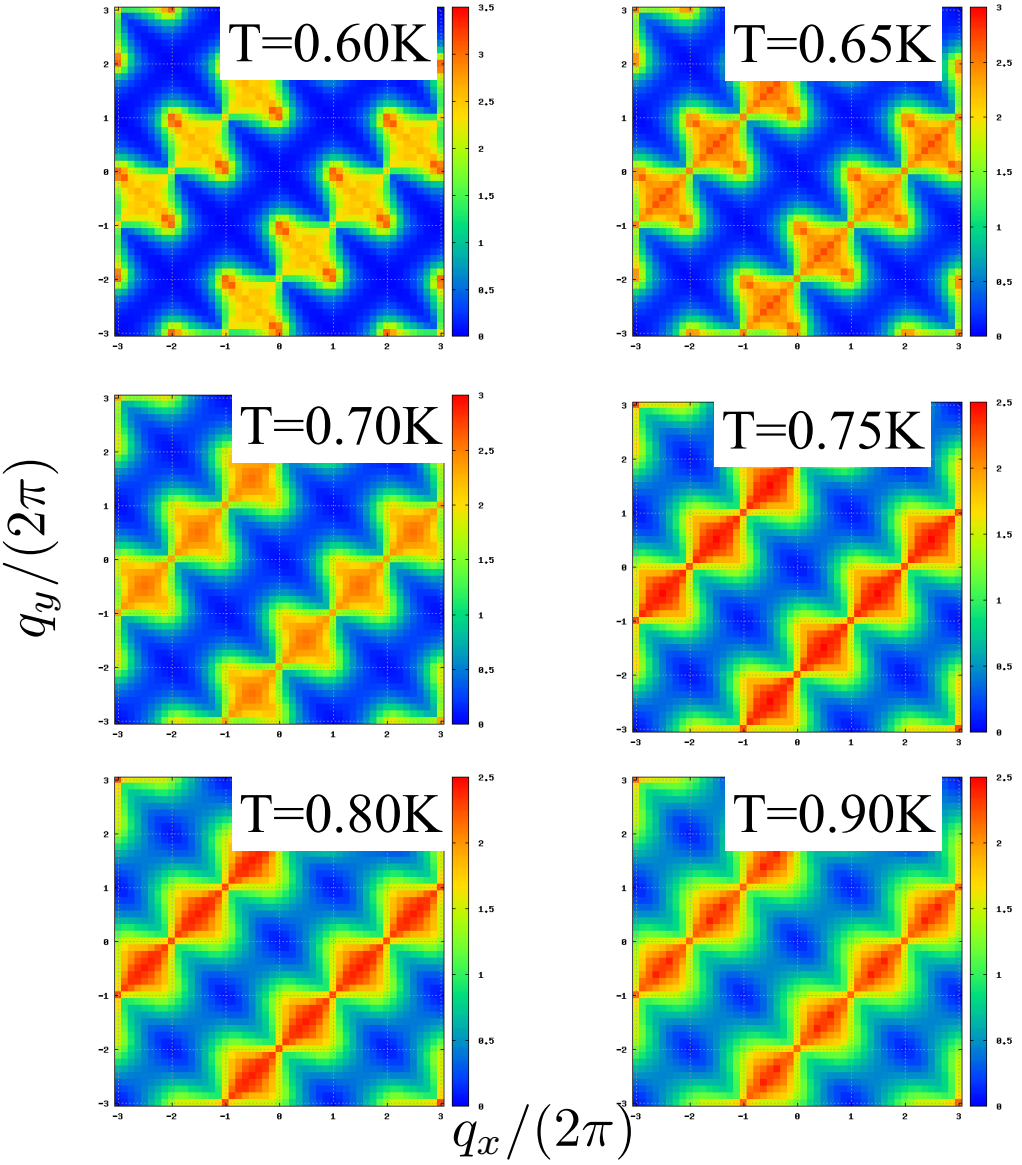

Figure 4.21: Monte Carlo results of the structure factors for the spins in the bulk (z = 0.25) of the film. J_{orphan} = −2 K for a dipolar Hamiltonian. A simulation box of size L = 8 was used. The thickness of the film is one cubic unit cell (L_z = 1).

4.5 Why surface freezing: screening of the surface charges

In this section we offer an explanation of why the surface charge ordering into checkerboard pattern does not eliminate all the residual entropy of the spins in the bulk of the film.

We show in Fig. 4.22 a snapshot of the spin configurations with the surface ordered into checkerboard charge state. For spin A, the orphan bonds adjacent to it are marked by a, b, c, and d. As shown in Fig. 4.22, of the two symmetric positions with respect to spin site A, the orphan bonds a and b possess charges of opposite signs. The same can be said for orphan bonds c and d. From the dumbbell picture of the dipolar interaction [29], these unscreened charges generate magnetic fields throughout the system. However, due to the relative positions of these charges to the spin site, and the direction of the easy axis for the spin, the net component of the magnetic fields in the direction of the spins is zero. We can see from Fig. 4.22 that all the checkerboard charges have opposite signs at the symmetric positions with respect to site A, and the same can be said to all spin sites in the bulk of the film, regardless of the thickness of the film. Therefore, even though we have unscreened charges on the surface, when these charges ordered into the checkerboard pattern as we found in the simulation, the unscreened magnetic fields have no net component along the direction of the spins in the bulk. Therefore even when the surface is ordered, we can still have disordered states for the spins in the bulk, *i.e.*, surface freezing.

Thus, in this work, we have discovered a further *self-screening* property for the pyrochlore lattice. In the original self-screening scenario [27, 28], the screening happens as we approximate the dipolar spins by two dumbbells of charges [29]: ice rule requires that the charges at the center of each tetrahedron exactly cancel each other. In this work we found that, in the film configuration we discussed, a different kind of self-screening happens even when we have unscreened charges and net magnetic fields from these charges, but now the magnetic fields created have no component along the bulk spin directions. The surface freezing results we found thus can be summarized as follows: it is the breakdown of the original self-screening (of zero charges) that causes the surface ordering at the surface orphan bond objects, and it is the screening of magnetic fields from the surface charge that shields the spins in the bulk of the film from ordering.

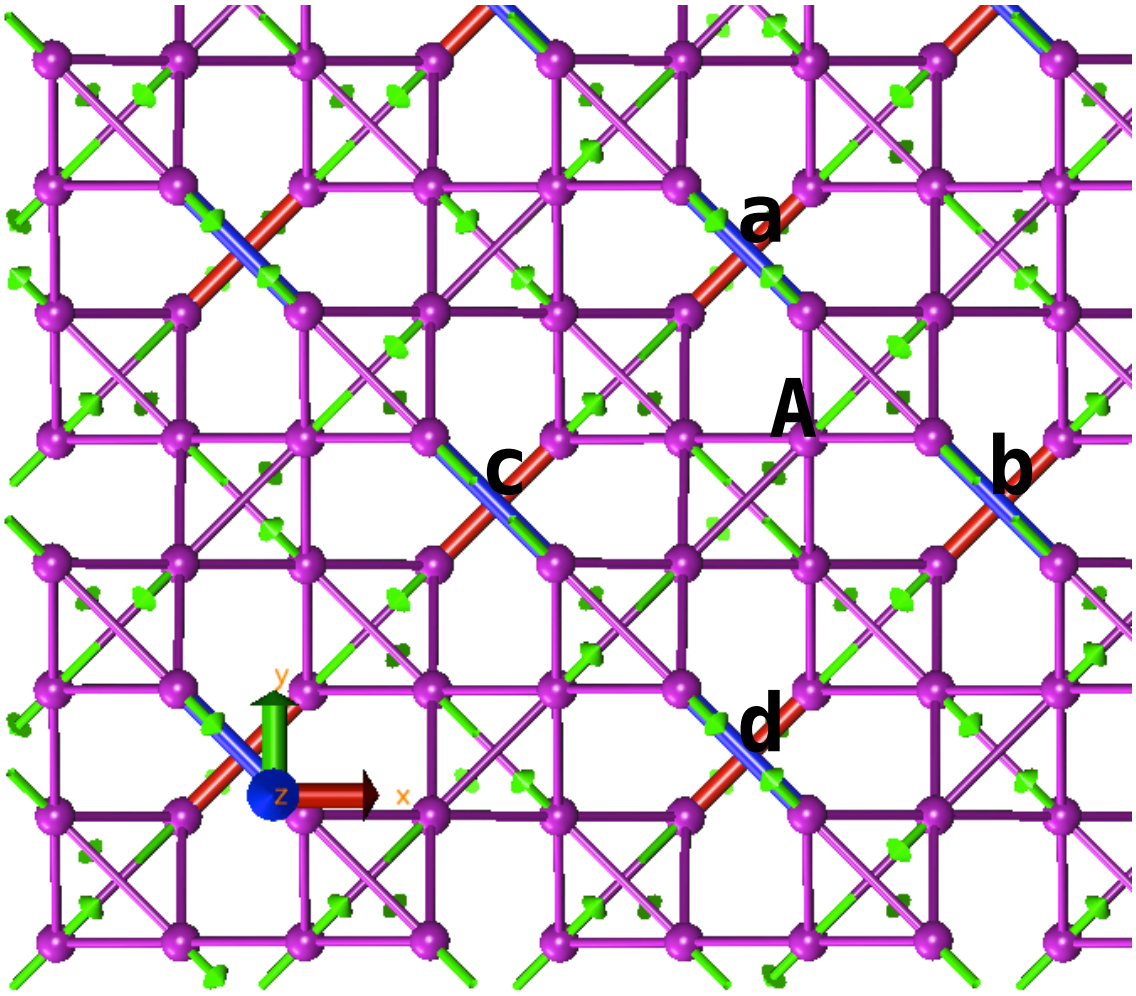

Figure 4.22: A snapshot of the state with surface checkerboard charge ordering, view along the z direction, normal to the film surface. The orphan bonds on the surface are marked by the letters a, b, c, and d. One spin in the bulk of the film is marked by the letter A.

4.6 Discussion

4.6.1 Recovery of the third law of thermodynamics?

A remaining question from this chapter is the lack of long-range order for the dipolar spin ice, even in the case of antiferromagnetic orphan bonds, surface ordering without bulk ordering is found. Should the system eventually undergo a phase transition to long-range order, thus eliminating all the remaining entropy for the bulk, if lower temperatures were reached? In principle the answer should be yes, since the details of the dipolar interaction should eventually choose one minimum energy spin configuration for the spins not on the surface. In order to see the transition, collective updates need to be used in the Monte Carlo simulations, such as the loop move algorithm, discussed in Chapter 2.

In bulk dipolar spin ice with only nearest-neighbour exchange and dipolar interaction, the transition to long-range order due to the corrections to the projective equivalence occurs at T_c = 0.18 K [48], an energy scale much lower than any energy or temperature scale discussed in this chapter. Also, the ground state found in the bulk spin ice consists of antiferromagnetic ordering of the magnetic moments for the tetrahedra, a ground state inconsistent to the surface checkerboard charge ordering (a consistent surface state would be one without free charges). Thus, if the spins inside the film were to order into the long-range order found for bulk spin ice, a phase competition would occur, pushing the transition to lower temperatures. Therefore it is unlikely that the lower temperature probable long-range order state, whatever that may be, would affect the conclusions of the surface freezing or various surface corrections to Pauling's entropy made in this study.

Furthermore, the study of the long-range order may not be experimentally relevant. First, the loop dynamics needed in Monte Carlo simulations may not be available in the experimental system. Second, for $Dy_2Ti_2O_7$ spin ice, further exchange interactions are needed to correctly describe experimental measurements as we shall discuss in Chapter 5. Studying of the long-range order in the bulk of the film without first investigating the microscopic model of $Dy_2Ti_2O_7$, which we will do so in the next chapter, Chapter 5 would appear, at least for the time being, to be solely of theoretical interest. Therefore we should postpone the study of the fully long-range order state in the film until the microscopic model of $Dy_2Ti_2O_7$ has been re-visited and suitably established.

4.6.2 Mapping to a square ice problem

Nevertheless, the long-range order transition within the bulk of the film after surface freezing remains a theoretically interesting question. In Fig. 4.23, we plot a snapshot of the spin configurations from the checkerboard surface order state for a one cubic unit cell thick film. As we discussed in Section 4.1.2, the checkerboard surface state residual entropy, the two neighbouring spins on the surface tetrahedra, which are not themselves on the surface, need to have a head-to-tail configuration. Such constraints are illustrated in Fig. 4.23 as yellow arrows. It turns out that, as indicated in the figure, the yellow arrows obeys the ice rule when they meet at the tetrahedra indicated by the circles in the figure, for one layer of cubic unit cell. (Of the four arrows presenting the head-to-tail constraint that meet at a tetrahedron, marked by the yellow circle, two of the arrows come from the bottom layer and the other two of them come from the upper layer.) Therefore the degrees of freedom for the remaining spins not on the surface can be mapped to the problem of the square ice, where the new "spins" are the ice rule constrained two-spin objects.

4.7 Conclusion

In this chapter we studied spin ice films along the [001] direction. For different surface conditions, corrections to the Pauling's entropy were derived. A geometric object, the *orphan bond*, was identified. By tuning the orphan bonds, we can achieve different surface conditions in the Monte Carlo simulations. Measured residual entropies are found to be in agreement with the analytical derived corrections to the Pauling's entropy. In particular, for overall antiferromagnetic orphan bonds in the dipolar spin ice film, we discovered a novel phenomenon of surface freezing, where the spins on the surface undergo a continuous phase transition to long-range order while the spins in the bulk remain disordered. The mechanism of the surface freezing is due to a *self-screening* of the induced magnetic charges. For one cubic unit cell thick films, the possibility of realizing a square ice problem is also discussed.

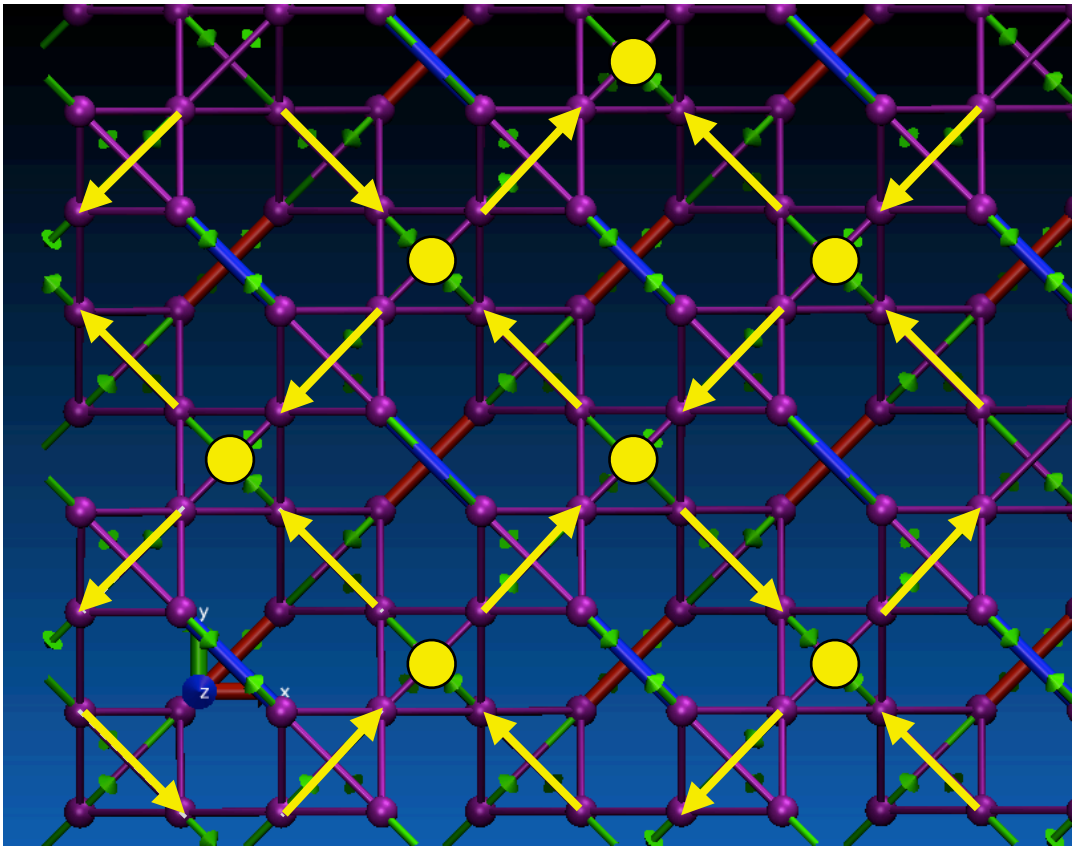

Figure 4.23: A snapshot of the spin configurations for a one cubic unit cell thick film with checkerboard charge state at the surface. The yellow arrows are the ice-rule constrained head-to-tail spin configurations for the two spins in the bulk. As these yellow arrows meet at the yellow circles, the ice rule requires two yellow arrows pointing in and the other arrows pointing out. Thus for the yellow arrows, the problem maps to that of the square ice.

Chapter 5

Magnetic Ground States and Low Temperature Properties of Spin Ice $Dy_2Ti_2O_7$

In the previous two chapters, we have studied the site dilution behaviour and thin film properties of spin ice. One important common question for these two sets of systems is the deviation from the projective equivalence due to geometrical defects. For the dilution problem, the defects are scattered randomly in the bulk, whereas for the film problem, the defects, corresponding to the orphan bonds, are periodically located on the surfaces. The temperature range for the study of the above question, is the temperature range where the projective equivalence would still work for the otherwise defect-less systems. In other words, in the previous two chapters we departed from the projective equivalence not because of the corrections in the projective equivalence but due to defect-induced charges.

However, some remaining questions motivated by the last two chapters require us to investigate the lower temperature regimes. It remains unknown in the last two chapters what the zero temperature magnetic ground state for spin ices is, diluted or in the form of thin films. To answer the ground state questions, we need to answer a more fundamental question: what is the magnetic ground state for spin ices in the pure and bulk samples.

For the spin ice model with only nearest neighbour and dipolar interactions, this question was solved numerically by Melko *et al.* [48]. A zero magnetization ground state is found with antiferromagnetic alignment of the tetrahedron magnetization. The ground

state is solely induced by the dipolar interaction, specifically its corrections to the projective equivalence. But it remains unknown whether this is the true ground state of any real spin ice compounds due to the lack of experimental evidence. At the time of writing this thesis, we remain unaware of any experiment successfully finding the ground state for any spin ice compounds. The lack of experimental information is due to the slow relaxation time in equilibrating the sample and the glassiness of the compound at low temperatures [1]. Furthermore, there are clearly indications in earlier works [24] that further neighbour interactions are needed to correctly describe the low temperature correlations seen in neutron scattering for $Dy_2Ti_2O_7$[3]. With further neighbouring interactions, the answer to the magnetic ground state problem may seem even more elusive.

Another motivation for revisiting the microscopic models of spin ice is from a recent experimental measurement of $Dy_2Ti_2O_7$[1]. In the work by Pomaranski *et. al.* [1], it was found that the magnetic specific heat of $Dy_2Ti_2O_7$ rises below about 0.6K, once the flow of heat into and out of the material is tracked carefully. Surprisingly, from this new measurement, there is no Pauling's residual entropy observed as a clear plateau at the lowest temperature. Thus such measurement is in qualitative contradiction with all all previous specific heat measurements on $Dy_2Ti_2O_7$ [2, 34, 35, 59, 81, 82, 83, 84, 85], and thus in contradiction with either the simplest model with nearest neighbour and dipolar interaction, with which the ground state has been found and which has a clear Pauling's entropy plateau at low temperatures, or the model with further neighbouring interaction, with which the ground state is unknown yet but simulation results nevertheless show plateaus of the Pauling's entropy at low temperatures [24]. Thus a problem in the consistency of the various experimental measurements arises. One way to solve or even fully expose the problem is through theoretical investigation of the microscopic models of spin ice. By fitting model Hamiltonians, we can assess not only the consistency of the various specific heat measurements, but also other experimental observations such as the neutron scattering.

Thus for spin ice, the study for its magnetic ground state and its low temperature properties consists of finding the microscopic model that accounts for the low temperature experiments. The problem of ground state and low temperature properties is a consequence of investigations of the *correct* microscopic Hamiltonian. This chapter is devoted to the study of these problems, and we focus our attention to the compound $Dy_2Ti_2O_7$.

Previous attempts in the search of a microscopic model for spin ice have converged into

the so-called dipolar spin ice model for $Dy_2Ti_2O_7$ [23, 24, 26], which reads:

$$\mathcal{H}_{\text{DSIM}} = \sum_{i>j} \sigma_i \sigma_j \{ J_{i,j} \hat{z}_i \cdot \hat{z}_j + D(r_{nn}/r_{ij})^3 [\hat{z}_i \cdot \hat{z}_j - 3(\hat{z}_i \cdot \hat{r}_{ij})(\hat{z}_j \cdot \hat{r}_{ij})] \} \tag{5.1}$$

as already discussed in Chapter 1, $J_{i,j}$'s are the neighbouring exchange interactions and D is the dipolar coupling. Currently the most comprehensive work is by Yavors'kii *et al.* [24], where the parameters read $J_1 = 3.41$ K, $J_2 = -0.14$ K, $J_3 = 0.025$ K, and $D = 1.3224$ K, the same model we used in our study of the diluted dipolar spin ice $Dy_2Ti_2O_7$ in Chapter 3.

Clearly in the presence of the new specific heat experiment [1], the validity of the above dipolar model is doubted. Without resorting to more exotic explanations, such as stuffing impurities reported by a previous work [86] (even if it turned out that the new specific heat measurement was due to impurities, one still has to content the question of what the ground state of the material should be, for an impurity-free sample), we approach the problem by re-visiting the dipolar spin ice model with a systematic fitting method. In this chapter we study up to fourth nearest neighbour interaction in Hamiltonian 5.1, and the scope of this chapter is to infer the microscopic couplings of the above Hamiltonian through a series of magnetic field, neutron scattering, and specific heat experimental measurements.

In considering the microscopic models for $Dy_2Ti_2O_7$ we might be confronted with the task of exploring on as high as a six-dimensional parameter phase space. Thus we must identify settings in which these parameters are clearly exposed and easily quantified. One important setting we have found is the magnetic measurement of $Dy_2Ti_2O_7$ in a saturating magnetic field along the [112] direction. We study in Section 5.1 of this chapter the constraints on the parameters that we can extract from the magnetic measurement. Only with these constraints, we are in a better shape in accessing the magnetic ground state problems.

In Section 5.2, we use the sets of constraints identified in Section 5.1 to fit the new specific heat measurement by Pomaranski *et. al.* Two distinct magnetic ground states are observed in the best fits to the new specific heat measurement, with one of them corresponding to the ground state previously reported by Melko *et. al.* [48].

In Section 5.3, we study the neutron scattering in the parameter space. It is found that the neutron scattering a contradiction between the neutron scattering measurements and the new specific heat measurement. While other specific heat measurements are consistent

with the neutron, we encounter a puzzle in the newly found absence of Pauling's entropy in $Dy_2Ti_2O_7$.

In Section 5.4, we discuss the inconsistency between the calorimetric and neutron scattering measurements exposed by our analysis.

Section 5.5 concludes the chapter.

5.1 Parametric constraints for spin ice $Dy_2Ti_2O_7$ in magnetic fields near 112

In the first two subsecitons, we revisit the numerical work of Yavors'kii *et al.* [24] and the experimental work by Sato *et al.* [7] for the spin ice compound $Dy_2Ti_2O_7$, both of which are important for the study in this chapter.

5.1.1 The work by Yavors'kii *et al.* revisited

We begin the chapter by first revisiting the current status of spin ice models. The most recent (and comprehensive) work on the spin ice model for $Dy_2Ti_2O_7$ was by Yavors'kii *et. al.* [24]. In this work, up to third neighbour nearest neighbour exchanges are considered, thus in Eq. (5.1) we have

$$J_{i,j} \equiv \begin{cases} J_1, & \text{if } i,j \text{ are nearest neighbours} \\ J_2, & \text{if } i,j \text{ are 2nd nearest neighbours} \\ J_{3a}, & \text{if } i,j \text{ are 3rd nearest neighbours of type a} \\ J_{3b}, & \text{if } i,j \text{ are 3rd nearest neighbours of type b} \\ 0, & \text{otherwise.} \end{cases} \tag{5.2}$$

Note that in the current notation, we differentiate the two types of third nearest neighbours, referred to as type a and type b. For type a, the pair share a common nearest neighbour, while it does not for type b. For any given spin, the numbers of type a and type b 3rd neighbours are both 6.

In the work by Yavors'kii *et al.* [24], the parameters for $Dy_2Ti_2O_7$ were determined to be: $J_1 \simeq 3.41$ K, $J_2 \simeq -0.14$ K, $J_{3a} \equiv J_{3b} \simeq 0.025$ K, $D = 1.3224$ K, with the magnetic moment $g\langle J_z\rangle = 9.87$. Here is a summary of how these numbers were obtained.

The magnetic moment $g\langle J_z\rangle = 9.87$ was calculated based on the crystal field Hamiltonian of $Dy_2Ti_2O_7$. The values $J_{3a} = J_{3b} = J_3$ was assumed in the work, and the value was estimated by the Monte Carlo critical temperature, obtained from the location of the maximum of the specific heat, of the ferromagnetic ordering of $Dy_2Ti_2O_7$ in a magnetic field near [112] direction. Experimentally, the specific heat [59], susceptibility [87], and magnetization [7] measurements give a critical temperature of 0.34, 0.28 and 0.26 K, respectively. From these values, Yavors'kii *et. al.* concluded that 0.019 K $\lesssim J_3 \lesssim$ 0.026 K. Constraints on J_1 and J_2 was determined from the root mean square deviation from the Monte Carlo $C_m(T)$ to the specific heat measurement [83], based on the observation that the above range for J_3 only weakly affects the $C_m(T)$. In addition, the $J_1 - J_2$ constraint was also examined through comparing the Monte Carlo critical field H_c for $Dy_2Ti_2O_7$ in the [111] field at $T < 0.36$K, to the empirical line $H_c = 0.90 + 0.08\ T$ in experiments [88, 89] Combining the two constraints, it was concluded that 3.26 K$\lesssim J_1 \lesssim 3.53$ K, and -0.20 K$\leq J_2 < 0$ K. Further restrictions on J_2 came from comparing the Monte Carlo neutron intensity to measurement [3], at $T = 300$ mK. The concluded range for J_2 becomes: -0.16 K$\lesssim J_2 \lesssim -0.10$ K. Finally the result $J_1 = 3.41$ K, $J_2 = -0.14$ K, $J_{3a} = J_{3b} = 0.025$ K, $D = 1.3224$ K falls into the ranges determined above.

In essence, the Yavors'kii *et al.* [24] fitting procedure is the following: (a) J_3 was determined from the critical temperature T_c of the ferromagnetic ordering of $Dy_2Ti_2O_7$ in the [112] field setting, and was found to be small compared to the first and second neighbour exchange interactions. (b) Then J_1, J_2, and J_3 are basically treated as independent variables in fitting the zero field $C_m(T)$, H_c in [111] field, and neutron scattering. (J_3 was not necessary in most of the fittings since it was found to be small in (a) compared with other interactions.)

The problem with the above fitting procedure is that (a) as we will show in this work, the [112] field experiment of Sato *et al.* [7] does not dictate J_3 being small, if we consider the situation of $J_{3a} \neq J_{3b}$. Also in (b), in finding the optimal values of J_1, J_2, J_{3a}, and J_{3b}, it is neither efficient nor even correct in assuming them to be independent valuables. It turns out, as we will show in this work, that the [112] field experiment can be further exploited in providing constraints on these exchange interactions.

5.1.2 Spin ice near 112 field, the work by Sato *et al.* revisited

In the work of Sato *et al.* [7], the spin ice compound $Dy_2Ti_2O_7$ was subject to the following experimental conditions.

An approximate 2 T magnetic field was applied to a single crystal of $Dy_2Ti_2O_7$ along the [112] direction. Since the magnetic moment of the rare-earth ion is about $10\mu_B$ (from the crystal field calculation [24], and from this experiment itself, as we discuss soon), the 2 T field corresponds to about 13.4 K in energy scale and is therefore much larger than the exchange and dipolar interactions in $Dy_2Ti_2O_7$. From the geometry of the pyrochlore, the [112] direction is perpendicular to the local [111] direction of only one sublattice of the pyrochlore lattice. Therefore in the presence of a large 2 T field, all spins but the ones on that particular sublattice are saturated by the applied field. The spins on that particular sublattice form the *triangular layers* (an FCC lattice) of the pyrochlore, and the spins frozen by the [112] field from the *kagome layers* of the pyrochlore, both specific layer being apparent when the pyrochlore lattice is viewed along a local [111] direction.

Although the spins on the triangular plane do not experience the external 2 T magnetic field, they nevertheless are influenced by the internal fields from the spins on the kagome layer, while they interact with each other. In the work by Sato *et al.* [7], a weak field was then applied along the local [111] direction of the triangular plane spins, so as to cancel the internal field from the spins on the kagome planes. Thus at the exact cancellation by the weak field, we have a dipolar Ising Hamiltonian on an FCC lattice. The direction of the weak field is referred to as the *transverse* direction.

Measurements of the magnetization along the transverse direction, M_t, as a function of the weak field along that direction, H_t, as well as the associated susceptibility, were performed in the work. Such data are vital to our following analysis.

5.1.3 Parametric constraints from the 112 field experiment

Magnetic moment from the offset in magnetization

In measuring the magnetization along the transverse direction, M_t, it was found in the work by Sato *et al.* [7] that M_t possessed an offset from zero by a constant of 0.82 μ_B. As noted in their paper, the offset comes from the transverse component of the kagome plane

magnetization. The local [111] direction of the Dy^{3+} Ising spins makes an angle of

$$\hat{z}_{kagome} \cdot \hat{t} = -1/3 \tag{5.3}$$

with respect to the transverse direction $\hat{t}$. In the presence of the large saturation field along the [112] direction, of the three sublattices of spins on the kagome plane, two of the sublattices are along the transverse field, and one of them is against the transverse field. Thus on average the magnetic moments of the Dy^{3+} ions contribute a quarter to the offset of the transverse magnetization. Therefore we have

$$\left(\frac{1}{3}\right)\left(\frac{1}{4}\right) g\langle J^z\rangle = 0.82$$

which gives

$$\boxed{g\langle J^z\rangle = 9.84} \tag{5.4}$$

This is in excellent agreement with the calculated value in Yavors'kii *et al.* [24], $g\langle J^z\rangle = 9.87$.

$J_1 - J_2$ constraint from the cancellation field

Sato *et al.* [7] found that the *critical* or cancellation field applied perpendicular to the saturation field is -0.28 ± 0.02T. Since the cancellation field measures the internal fields on the triangular plane spins from the influence of the frozen spins on the kagome plane, we can extract a constraint on the exchange interaction from the cancellation field.

Under the definition of Eq. (5.1) for the $Dy_2Ti_2O_7$ Hamiltonian, the internal field is given by

$$h_{\text{int}} = \left(\frac{2}{3}\right) J_1 + \left(\frac{4}{3}\right) J_2 + \left(\frac{4}{3}\right) J_4 + \left(\frac{8}{3}\right) J_5 + 2J_7 + \left(\frac{4}{3}\right) J_8 - 2.972D \tag{5.5}$$

up to eighth nearest neighbour exchange interactions. The last term is from numerical calculations using Ewald summation for the dipolar interaction for a simulation box of size $L = 8$. Note the absence of J_3 and J_6 in this equation, as they connect spins on the same FCC sublattice and therefore do not contribute to the internal field originated from the kagome layers.

Using the above determined magnetic moment, and considering only up to second nearest neighbour, we obtain, for a cancellation field of 0.28 T,

$$\boxed{\left(\frac{2}{3}\right) J_1 + \left(\frac{4}{3}\right) J_2 = 2.073K} \tag{5.6}$$

$J_{3a} - J_{3b}$ constraint from the susceptibility

The constraints on $J_{3a} - J_{3b}$ can be extracted from the transverse magnetic susceptibility measured in Sato *et al.* [7]. In the experiment, the transverse susceptibilities as a function of the transverse field were measured at four temperatures, 0.29, 0.41, 0.70, and 1.08 K. Since the susceptibility under such setting is determined by the third neighbour (and to the next order, sixth neighbour, which we ignore) exchange and dipolar interactions, we can fit the third neighbour exchanges through comparing Monte Carlo simulations and experimental measurements.

When the transverse weak field is exactly at the value of the cancellation field, the spins on the triangular layer undergo a transition to long range order at $T_c \simeq 0.26$ K. In our fitting to the measured susceptibility, we need to be sufficiently away from the critical temperature, since the finite size effect of our simulation introduces unwanted complications. However, the higher the temperature, the less "structure" the susceptibility has, due to decreased correlation lengths, and the fitting consequently becomes harder. Based on these two concerns, we choose our fitting temperature to be 0.70 K.

We perform our Monte Carlo simulations for spins on the triangular planes with exchange interactions J_{3a} and J_{3b} and dipolar interactions. Simulation boxes of $L = 4$ are used for the fitting. The goodness of the fit, σ, is calculated through

$$\sigma = \sum_i \left(\chi^{\mathrm{MC}}(H_i) - \chi^{\mathrm{EXP}}(H_i)\right)^2 \tag{5.7}$$

where $\chi^{\mathrm{MC}}(H_i)$ and $\chi^{\mathrm{EXP}}(H_i)$ are the Monte Carlo and experimental susceptibility at transverse field strength H_i, respectively.

We plot in Fig. 5.1 the goodness of fit as a function of J_{3a} and J_{3b}.

In Fig. 5.2, we plot the difference between the Monte Carlo susceptibility and experimental susceptibility at cancellation field strength

$$\Delta = \chi^{\mathrm{MC}}(H = 0) - \chi^{\mathrm{EXP}}(H = 0) \tag{5.8}$$

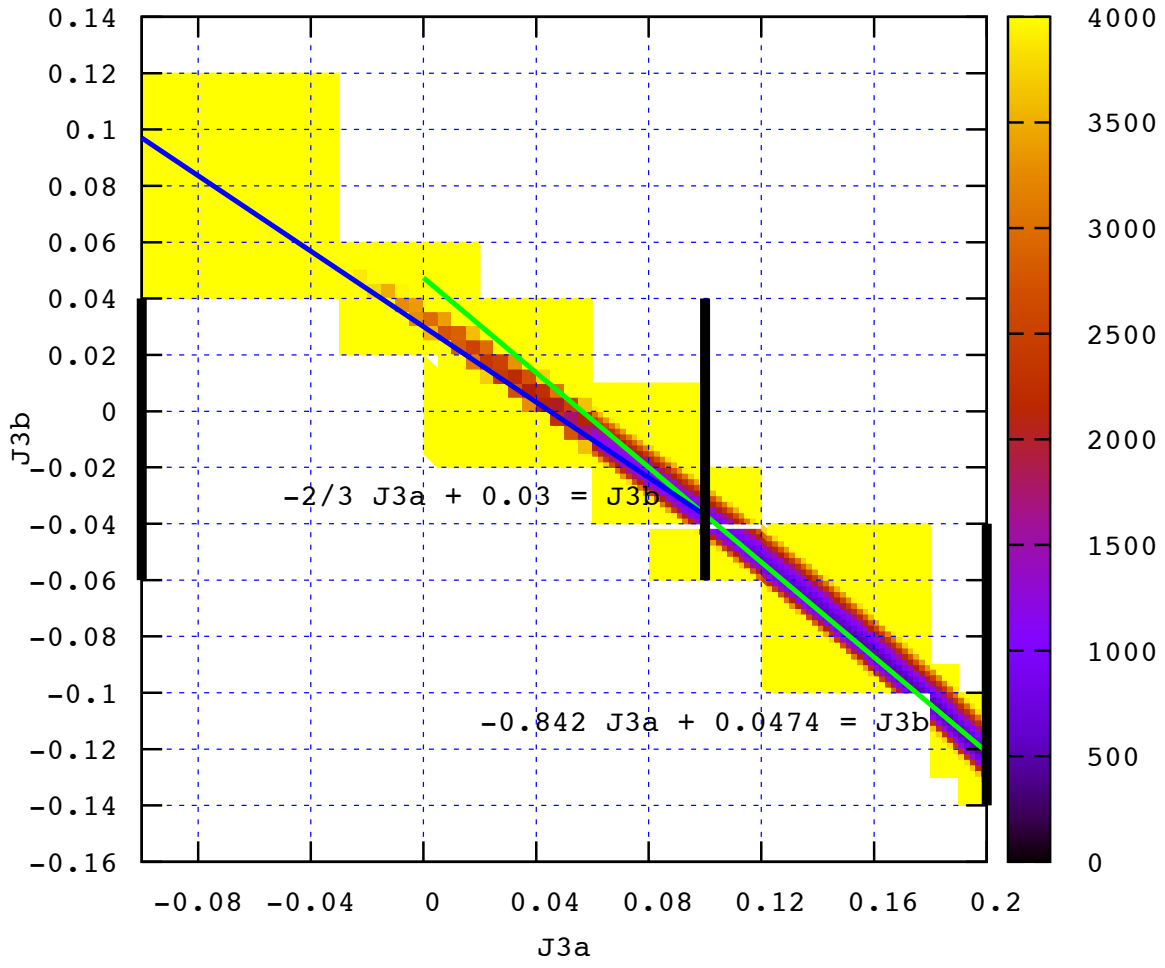

Figure 5.1: The goodness of fit for the susceptibility in the plane of J_{3a} and J_{3b} from Eq. (5.7) for $T = 0.7$ K.

where both susceptibility are at their maxima.

As can be seen from the fittings, the optimal region of the fitting falls onto a slightly bent line. A simple argument can be offered to the appearance of such a line: from the mean-field perspective, the susceptibility is determined by a weighted summation of the interactions. Thus on a line with negative slope, the loss of value for J_{3a} is compensated

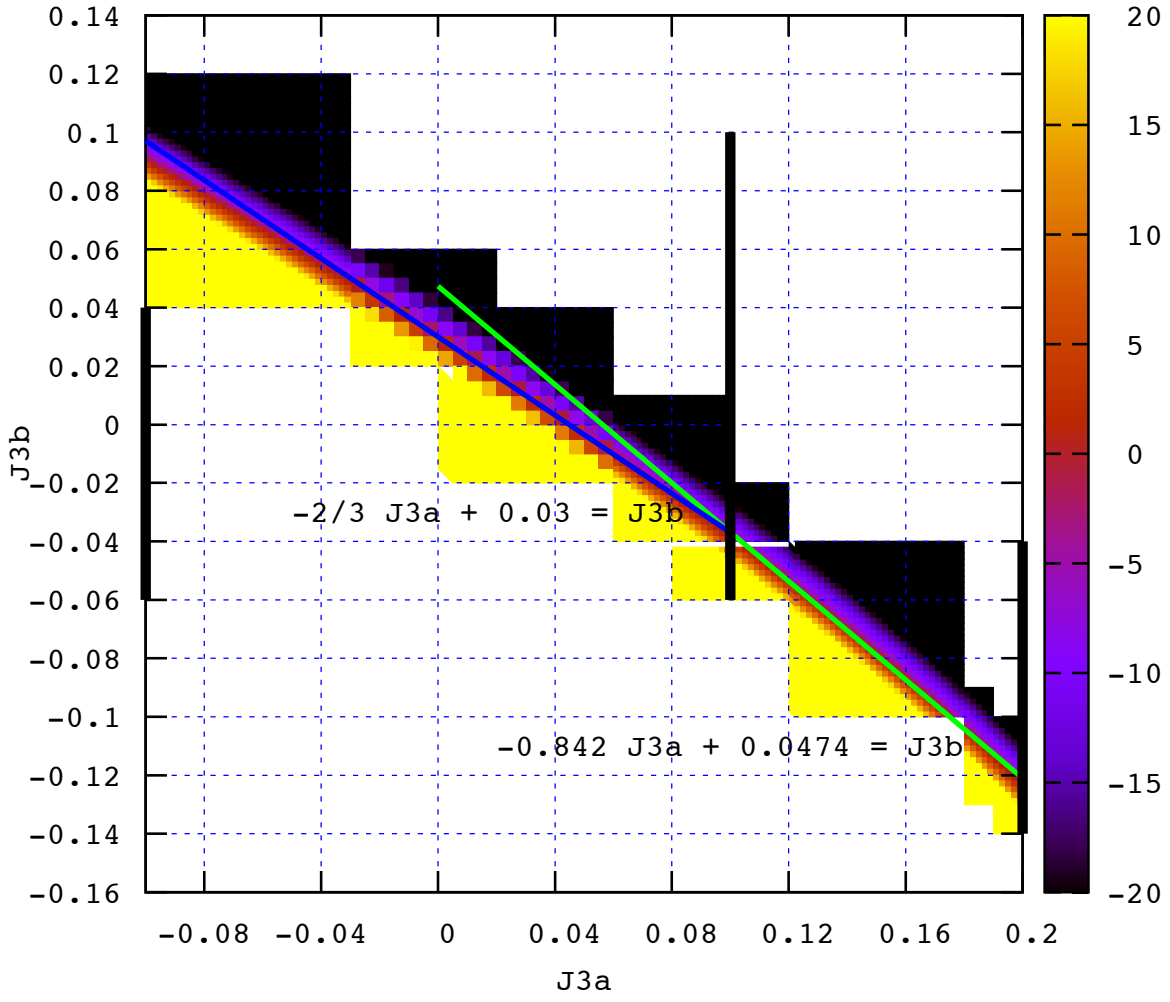

Figure 5.2: The height difference for the susceptibility, Eq. (5.8), in the plane of J_{3a} and J_{3b} at $T = 0.7$ K.

by the increase of value for J_{3b}, therefore in the mean-field level keeping the susceptibility the same.

We plot in Fig. 5.3 some of the susceptibility curves on the J_{3a} and J_{3b} to give a visual notion of what the color represents in Fig. 5.1 and in Fig. 5.2. Note that in the Monte

Carlo simulation of the susceptibility, there is no overall fitting parameter applied, and as plotted for J_{3a} and J_{3b} close to the optimal fitting lines, a very good fit to the experimental data was found.

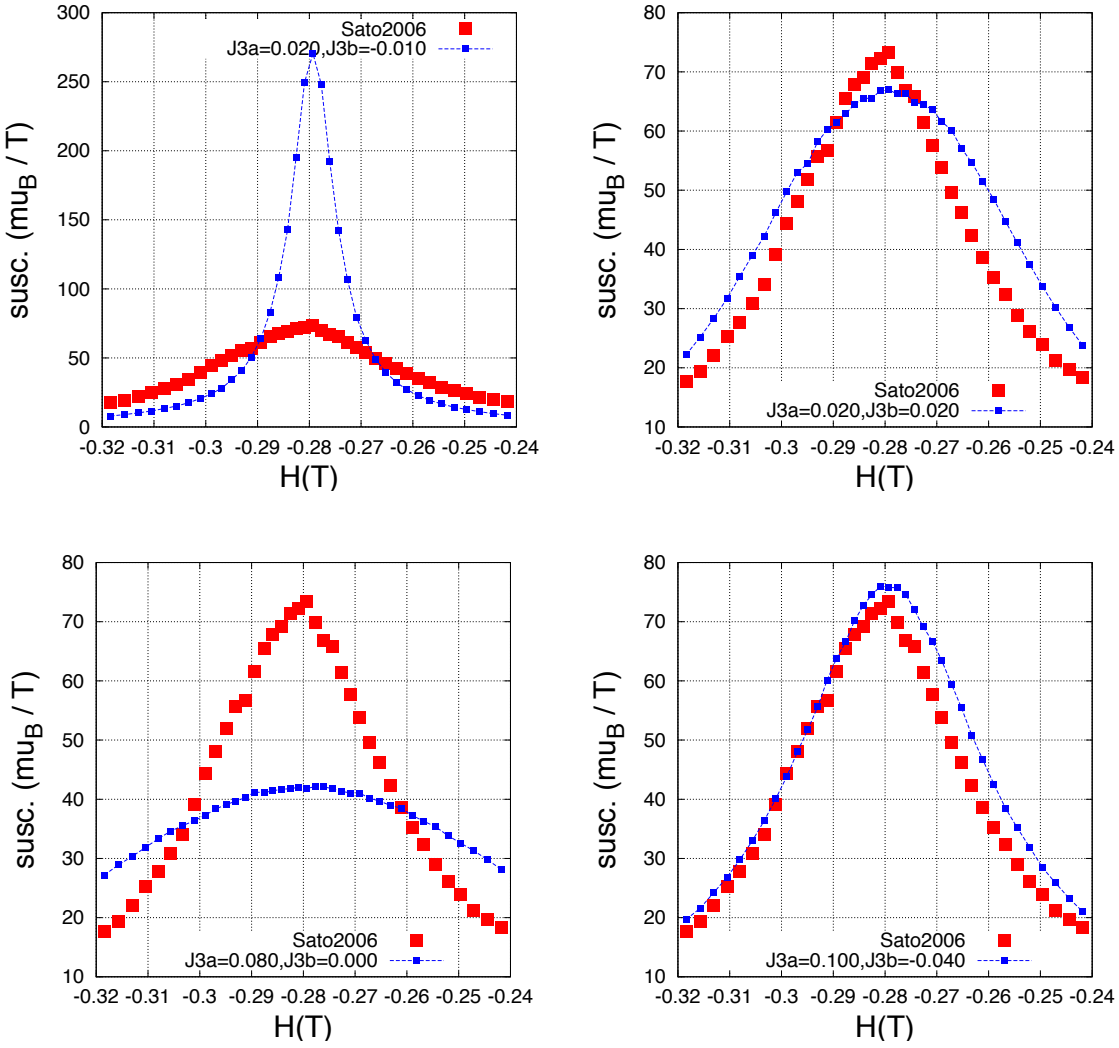

Figure 5.3: Some examples in the $J_{3a} - J_{3b}$ plane for the Monte Carlo susceptibility curve, compared with the experimental measurements of Sato *et al.* [7].

From Fig. 5.1 and Fig. 5.2, we have the constraint for $J_{3a} - J3_{3b}$

$$\boxed{\begin{cases} -(2/3)\, J_{3a} + 0.03 = J_{3b} & \text{for } J_{3a} < 0.1 \text{ K} \\ -0.842 J_{3a} + 0.0474 = J_{3b} & \text{for } J_{3a} > 0.1 \text{ K} \end{cases}} \tag{5.9}$$

5.1.4 Summary

In summary from the [112] field experiment, the parametric constraints we extracted are given by Eqs. (5.4), (5.6) and (5.9). In later sections, we shall try to fit the specific heat measurements and neutron scattering results under these constraints.

5.2 Fitting the specific heat measurements

5.2.1 Specific heat curves fitting

Using the parametric equations, Eqs. (5.4), (5.6), and (5.9), out of the five parameters of J_1, J_2, J_{3a}, J_{3b}, and D, we are left with only two. Therefore we can examine the zero magnetic field specific heat curves in the parameter plane of J_1-J_{3a}, with the rest of the parameters obeying the constraints.

We plot in Fig. 5.4 two sets of experimental data for the specific heat for $Dy_2Ti_2O_7$ in zero field. One is from the work by Pomaranski *et al.* [1], which shows a rise in the specific heat curve below about 0.7 K. The other is from the work of Ke *et al.* [2], which is consistent with most other specific heat measurements [34, 35, 81, 82, 83, 84, 85].

Three temperature ranges, R_1, R_2 and R_3, are considered

- R_1: [0.45, 1] K
- R_2: [1, 4.5] K
- R_3: [0.45, 4.5] K

R_1 is chosen such that it includes the departure from the new experiment to the previous ones. R_2 corresponds to the high temperature range where almost all experiments

agree, yet not too high so that the experimental uncertainty associated with the lattice phonon contribution to the total specific heat sets in (see Section 3.1.3). Finally R_3 is the combination of the two ranges R_1 and R_2.

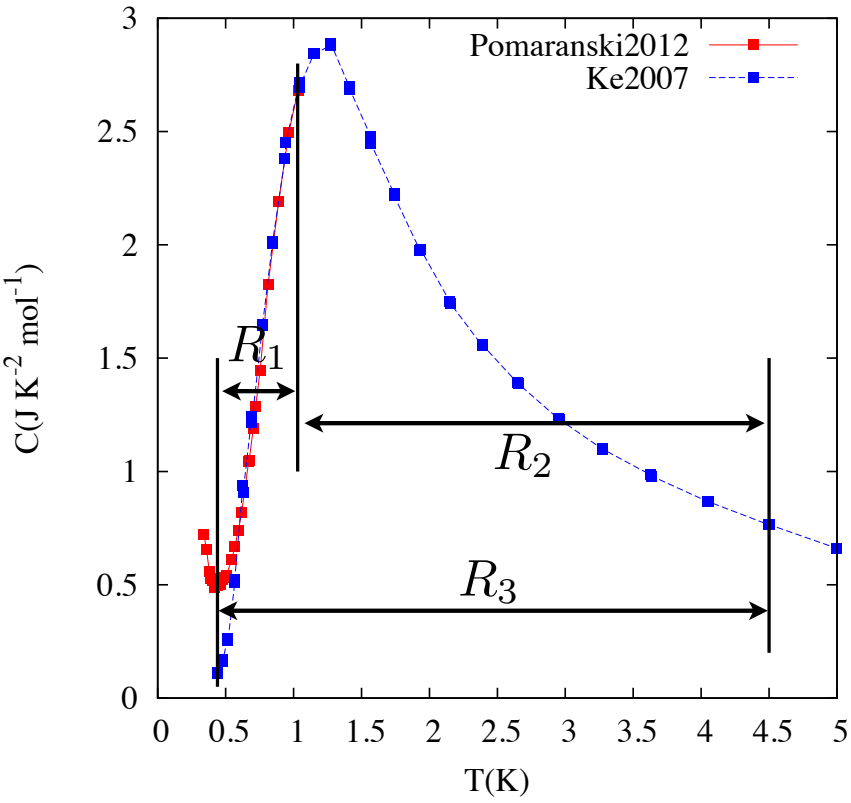

Figure 5.4: Specific heat data from the work by Pomaranski *et al.* [1] (red) and from the work by Ke *et al.* [2] (blue). The two temperature ranges: R_1, from 0.45 K to 1 K and R_2, from 0.45 K to 4.5 K, are used to in the fitting of the specific heat (see text).

The goodness of the fit, σ_R, for a temperature range R, is calculated through the following equation

$$\sigma_R = \frac{\sum_{i\epsilon R}(C_i^{\mathrm{MC}} - C_i^{\mathrm{EXP}})^2}{\sum_{i\epsilon R} 1} \tag{5.10}$$

where the summation is over the temperature range R. C^{MC} and C^{EXP} refer to the Monte Carlo and experimental specific heat values respectively.

First, we evaluate the goodness of the Monte Carlo specific heat results as a function of J_1 and J_{3a}, for

- the Pomaranski data in the range R_1
- the Ke data in the range R_1
- the Ke data in the range R_2
- the Ke data in the range R_3

We plot in Fig. 5.5, Fig. 5.6, Fig. 5.7, and in Fig. 5.8 the goodness of fit, for the above four ranges, respectively, for the two sets of experimental data.

First, we compare the goodness of fits for the Pomaranski *et. al.* data and Ke *et. al.* data in the range R_1, Fig. 5.5 and Fig. 5.6. For regions with the goodness below 0.05, the two sets of fits barely overlap. For the Pomaranski data, the best fits are separated in two distinct regions with $J_{3a} > 0$ and $J_{3a} < 0$, which we call the "upper" basin and the "lower" basin. For the Ke *et. al.* data, the best fits are concentrated in the region with smaller values of J_{3a} and larger values of J_1. The difference between the two regions, reflects the difference in the specific heat data, namely that the Pomoranski data rises below about 0.7 K, as shown in Fig. 5.4.

Next, we look at the goodness of fits for the Ke *et. al.* data in the R_2 range. This is the temperature range where most experimental data agree (Fig. 5.7). In this range, the restriction for low values of goodness is weak. This is anticipated, since at high temperature where the ice-rule correlations are absent, the thermodynamic properties of the paramagnetic state is largely determined by the strength of the exchanges and the coordination number. This can be seen as the most optimal region of the fit is roughly on a line with a negative slope, where increase in J_1 is compensated by the decrease in J_{3a}. Overall with J_{3a} only varies with a few percent compared with J_1, and J_1 varies slightly, the whole region has a low value of the goodness of the fit.

Therefore, as we turn to Fig. 5.8, for the fit for the R_3 temperature range of the Ke *et. al.* data, we see that the dominant features are almost the same as in Fig. 5.6. Therefore the convenience of the argument, we can focus on the fitting in temperature range R_1.

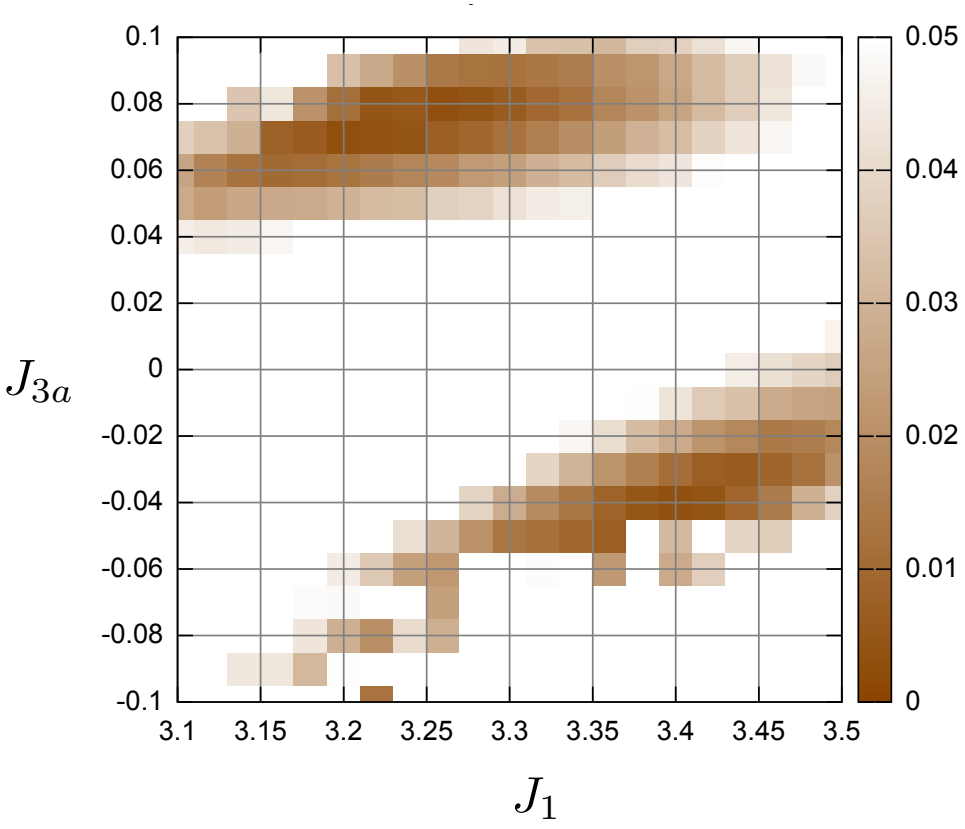

Figure 5.5: Goodness of the Monte Carlo fit in the $J_1 - J_{3a}$ plane in the R_1 temperature range for the Pomaranski *et. al.* data [1].

In summary, in this subsection we have found

- The temperature range needed to expose the experimental difference is R_1 (0.45 ~ 1 K).
- The optimal fitting to the Pomaranski data is separated into two regions: the "upper" basin and the "lower" basin (see Fig. 5.5).
- The optimal fitting to the Ke *et. al.* data is concentrated in the region between the two basins (see Fig. 5.6).

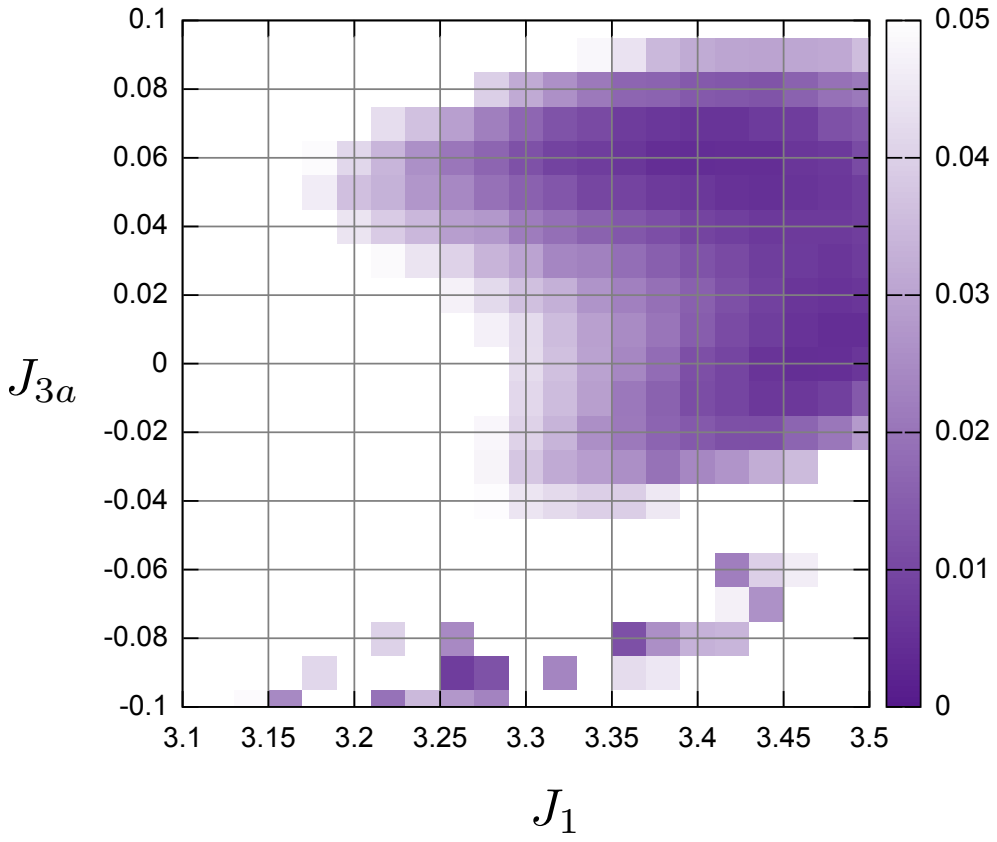

Figure 5.6: Goodness of the Monte Carlo fit in the $J_1 - J_{3a}$ plane in the R_1 temperature range for the Ke *et. al.* data [2].

5.2.2 Two possible magnetic ground states for $Dy_2Ti_2O_7$

To shed light to the fittings of the specific heat in the last subsection, we investigate the ground states in different regions of the $J_1 - J_{3a}$ plane. We have identified two distinct magnetic ground states for the "upper" and "lower" basin of the $J_1 - J_{3a}$ map, a "single-chain" and "double-chain" state, respectively. The following is a description of these two different ground states.

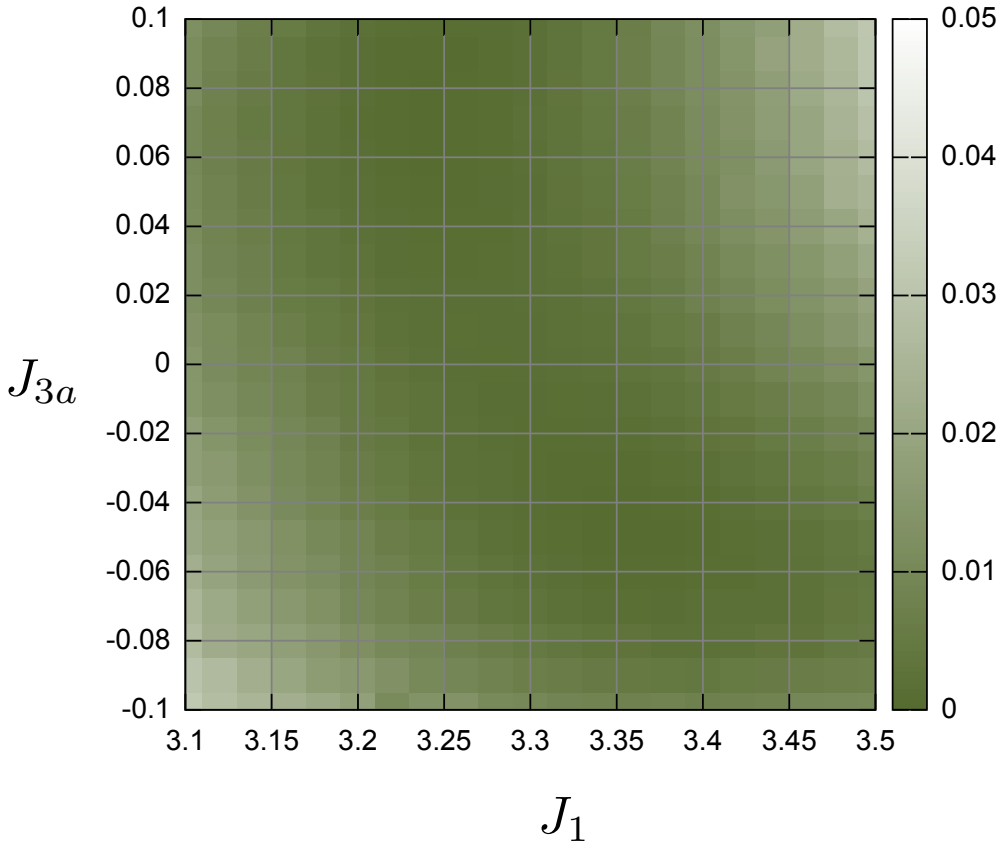

Figure 5.7: Goodness of the Monte Carlo fit in the $J_1 - J_{3a}$ plane in the R_2 temperature range for the Ke *et. al.* data [2].

"Single-chain" magnetic ground state

Deep inside the upper basin, the magnetic ground state is found to be a "single-chain" state. This is the same state found in the work by Melko *et al.* [48]. We plot in Fig. 5.9 and in Fig. 5.10 a single layers of cubic unit cell of the "single-chain" state. The cubic symmetry of the lattice is broken and in the figures one ordering direction, $\hat{z}$, is selected. One set of parallel neighbouring spin chains perpendicular to the $\hat{z}$ axis are marked by α, β, γ, δ, and ϵ. The characteristic of such a state is that the spins on the same chain

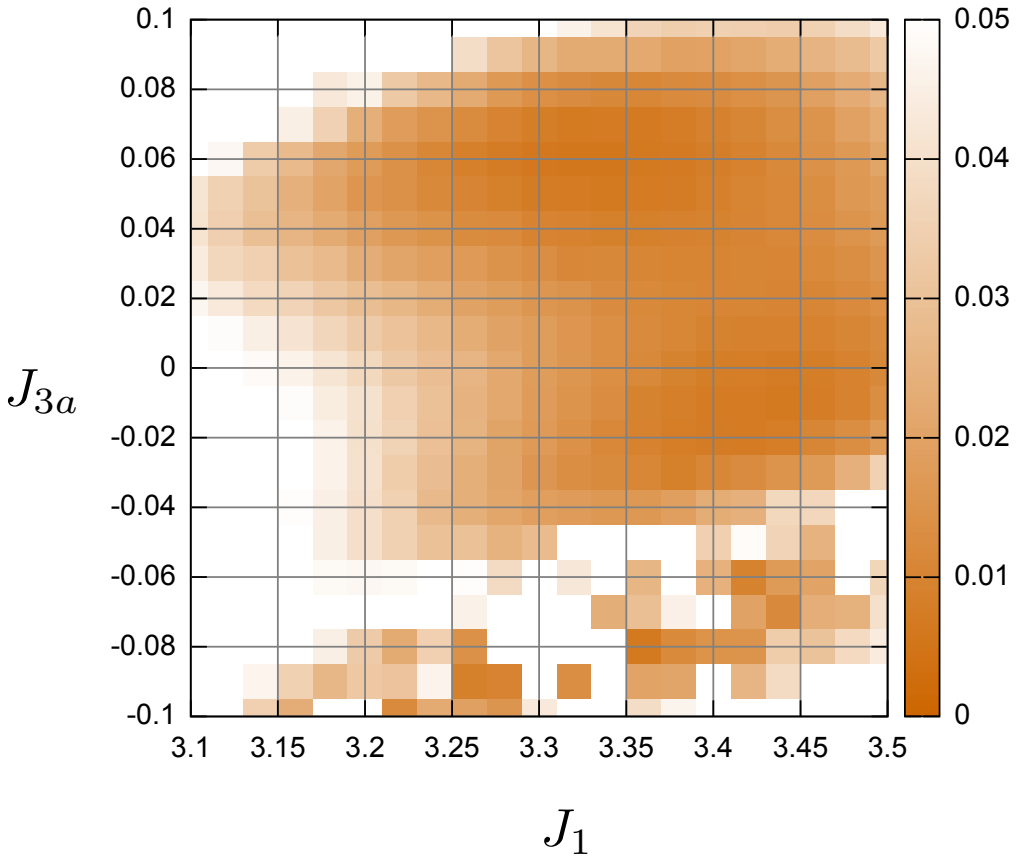

Figure 5.8: Goodness of the Monte Carlo fit in the $J_1 - J_{3a}$ plane in the R_3 temperature range for the Ke *et. al.* data [2].

of the set are aligned in the same direction, and the neighbouring chains of the set alter their directions, thus the name "single-chain" state. As can be seen from Fig. 5.9 and Fig. 5.10, the same spin-chain configuration holds for the other set of parallel spin chains perpendicular to the set just discussed.

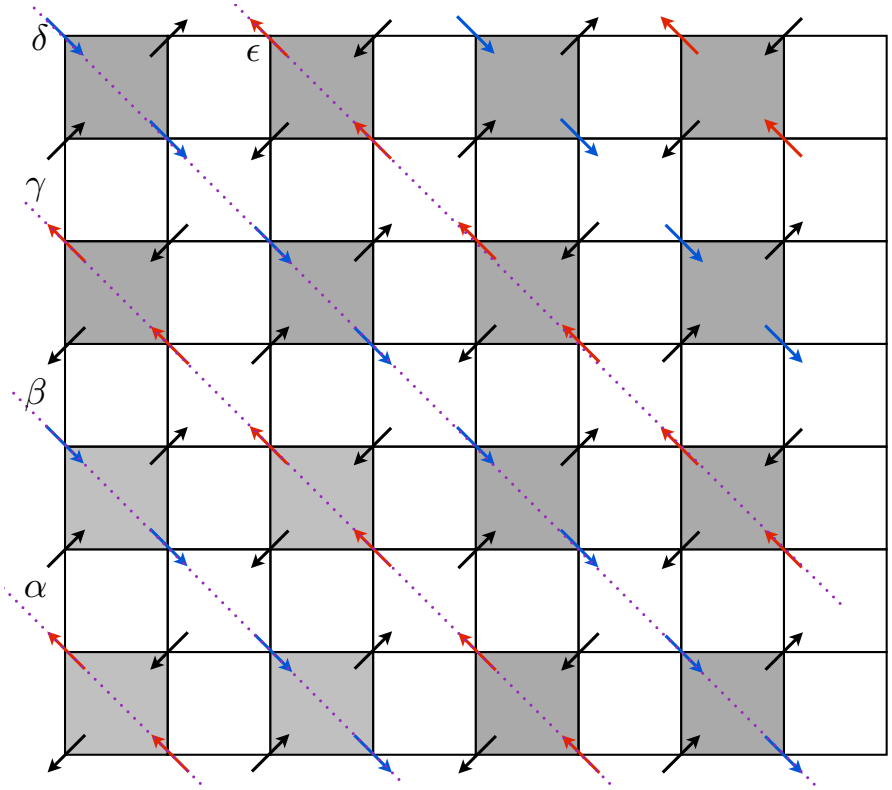

Figure 5.9: Single-chain state viewed along one of the cubic direction, the neighbouring chains are marked by α, β, γ, δ, and ϵ. Note that the spins on neighbouring chains point in the opposite directions. A corresponding 3D figure of the state is shown in Fig. 5.10.

"Double-chain" magnetic ground state

Deep inside the "lower" basin, the magnetic ground state is found to be the "double-chain" state. We plot in Fig. 5.11 and Fig. 5.12 one layer of cubic unit cell spins with the double-chain state. As in the single-chain state, the cubic symmetry is broken and one ordering direction, $\hat{z}$, is picked as shown in the figures. One set of parallel neighbouring chains perpendicular to the $\hat{z}$ axis are marked by α, β, γ, δ, ϵ and ζ in the figures. The characteristics of the double-chain state is that spins on the above marked chains align in the same direction, and for every two chains the direction of the spin chain alternates, thus the name "double-chain" state. For the spins on the other set of parallel chains

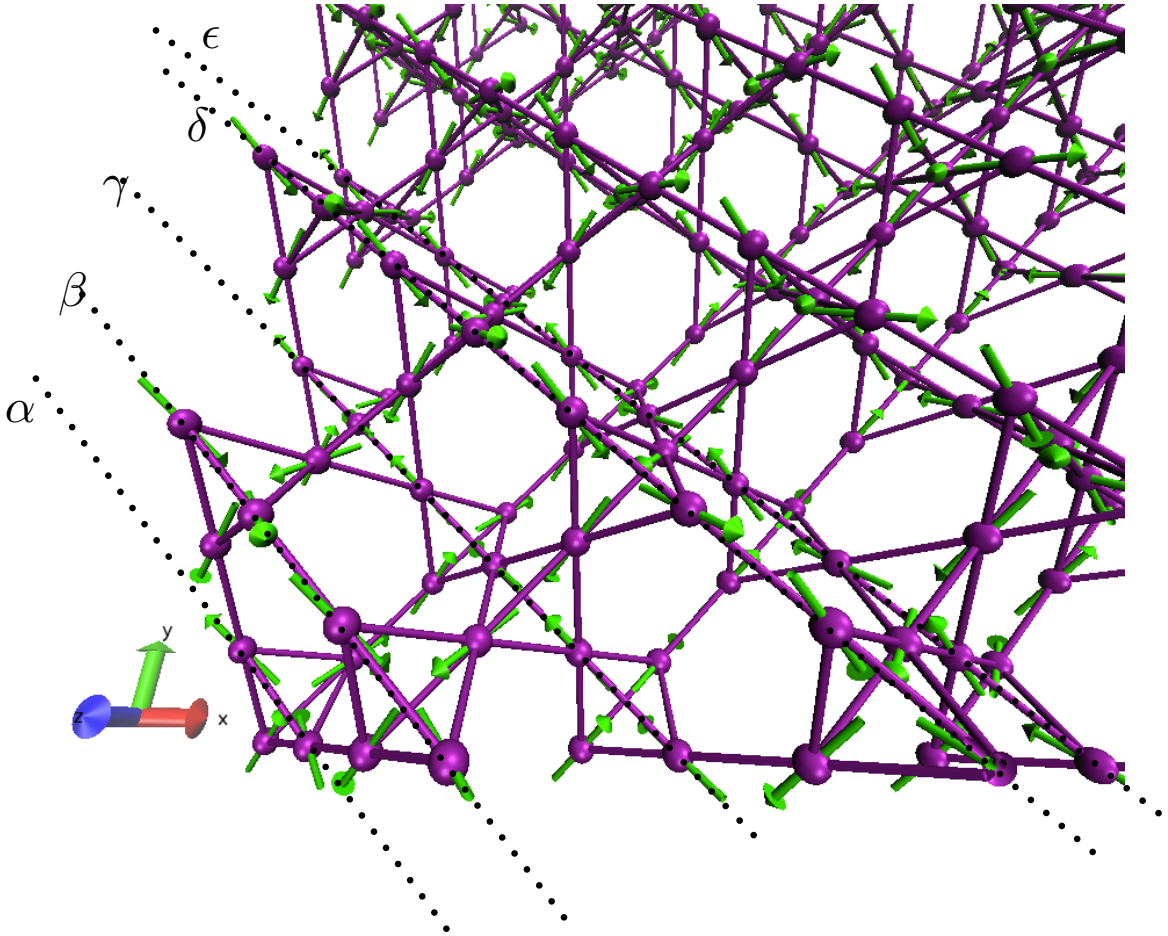

Figure 5.10: Single-chain state with neighbouring chains marked by α, β, γ, δ, and ϵ. A corresponding 2D figure of the state is illustrated in Fig. 5.9

perpendicular to the z axis, the same spin chain configuration is found.

Note that for the double-chain state, the minimum conventional cell dimension to contain the state is 2 by 2 in units of cubic unit cell perpendicular to the ordering direction, $\hat{z}$. This is different from the case of the single-chain state where the whole state can be constructed by repeating the same cubic unit cell. In the ordering $\hat{z}$ direction, the double-chain state can be stacked uniformly or with the layer above or below flipped completely

for every spin. It turns out that the energy difference is quite small as we discuss in the following.

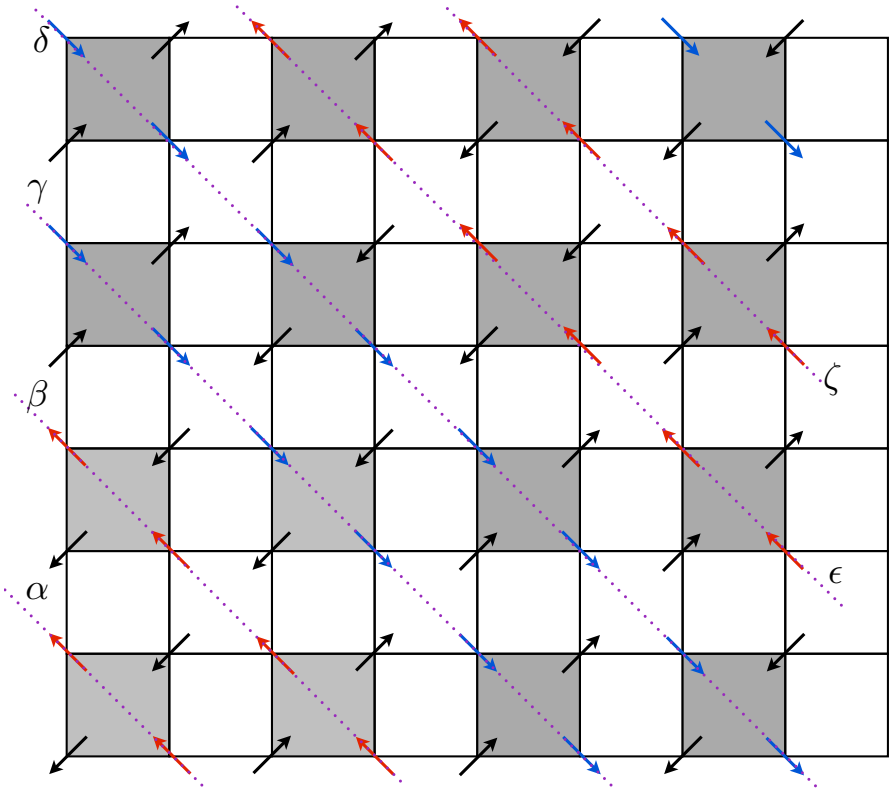

Figure 5.11: Double-chain state viewed along the z direction of the cubic unit cell, the neighbouring chains are marked by α, β, γ, δ, ϵ and ζ. Note that the spin chain changes direction for every two chains. A corresponding 3D figure of the state is plotted in Fig. 5.12.

Phase boundary between the two states

The ground state energies of the two proposed magnetic ground states can be expressed in terms of the exchange and dipolar couplings, up to 4th order nearest neighbour, we have for the single-chain state

$$E_{\text{s-c}} = (1/3)J_1 - (2/3)J_2 - J_{3a} - J_{3b} + (2/3)J_4 - 1.95D \tag{5.11}$$

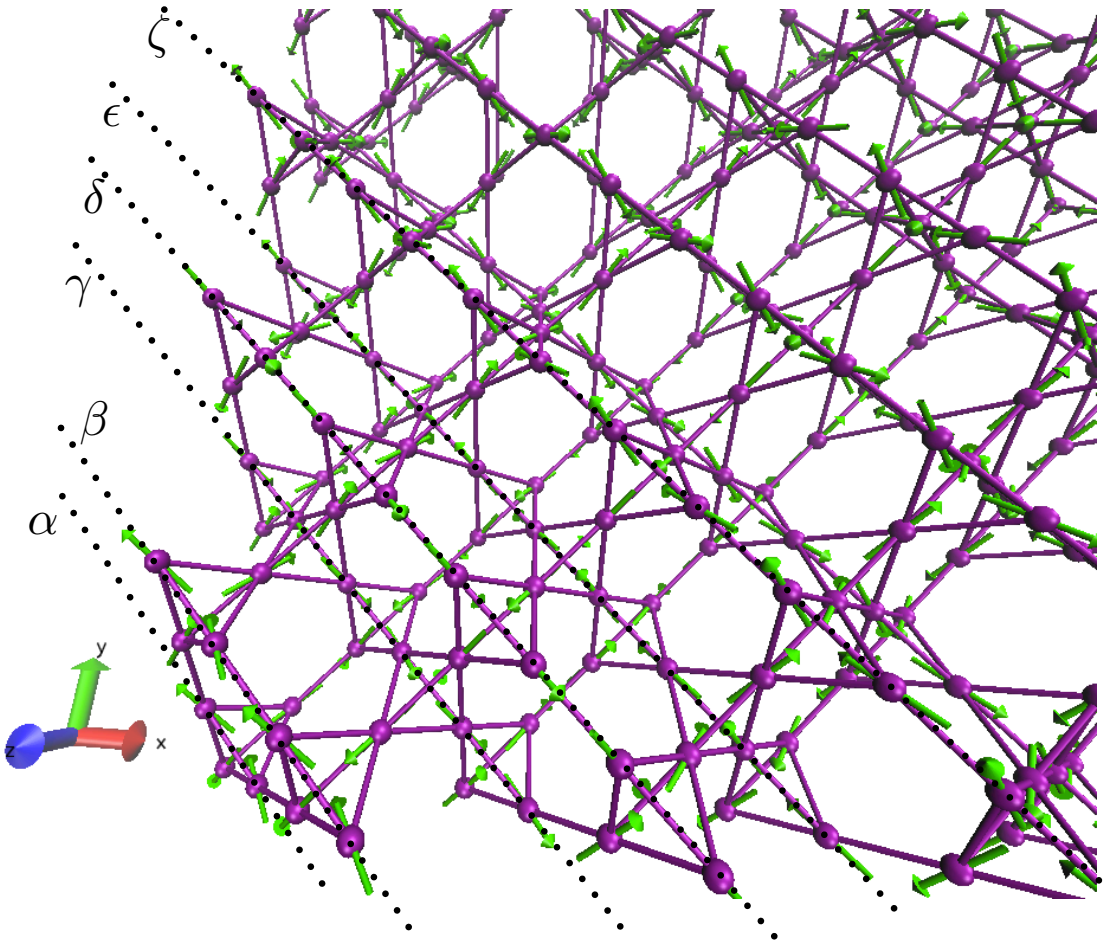

Figure 5.12: Double-chain state for one cubic unit cell thick layer, with the neighbouring chains are marked by α, β, γ, δ, ϵ and ζ. A corresponding 2D figure of the state is plotted in Fig. 5.11.

and for the double-chain state

$$E_{\mathrm{d-c}} = (1/3)J_1 + J_{3a} - J_{3b} - (2/3)J_4 - 1.91D \tag{5.12}$$

For both equations the dipolar interaction contributed energy is calculated through an Ewald summation for a simulation box of size $L = 8$. And for the double-chain state, the

difference between different stacking along the order direction is smaller than the presented digit in Eq. 5.12.

Using the constraints of Eq. (5.4), Eq. (5.6) and Eq. (5.9), the phase boundary between these two states in the $J_1 - J_{3a}$ plane can be determined to be

$$(1/3)J_1 - 2J_{3a} = 1.093\text{K} \tag{5.13}$$

5.2.3 Summary

In summary, in this section we attempted to fit both the Pomaranski *et. al.* [1] and the Ke *et. al.* [2] specific heat data using the Hamiltonian (5.1). Constraints extracted from the [112] field experiment [7], Eq. (5.4), Eq. (5.6), Eq. (5.9), are applied to reduce the fitting to be in the plane of two parameters, J_1 and J_{3a}. Optimal regions for both experiment in the fitting of their data were found. In particular, in the fitting of the Pomaranski *et. al.* data, two regions, the "upper basin" and the "lower basin" of optimal fitting were found. In the "upper basin" the magnetic ground state was identified to be a single-chain state while in the "lower basin" the magnetic ground state was identified to be a double-chain state. We plot in Fig. 5.13 the main results of this section. As can be seen in Fig. 5.13, the two regions of optimal fits to the Pomaranski data are away from the boundary of the two proposed magnetic ground states (panel (a) of Fig. 5.13). This is in contrast with the optimal fit region to the Ke *et. al.* data, where the best regions are around the boundary of the two magnetic ground states (panel (b) of Fig. 5.13).

5.3 Fitting the neutron scattering measurement

In this section we turn to the study of neutron scattering experiment by Fennell *et al.* [3]. The neutron data provides us with an independent experiment other than the specific heat measurements for fitting the Hamiltonian parameters for $Dy_2Ti_2O_7$. In Fig. 5.14, we reproduce the figure published by Fennell *et al.* [3], which we aim to fit with our model, Eq. 5.1, within the J_1-J_{3a} plane.

We now examine some of the features in the experimental neutron scattering data. First are the scattering intensities at the boundaries of the Brillouin zone, referred to as

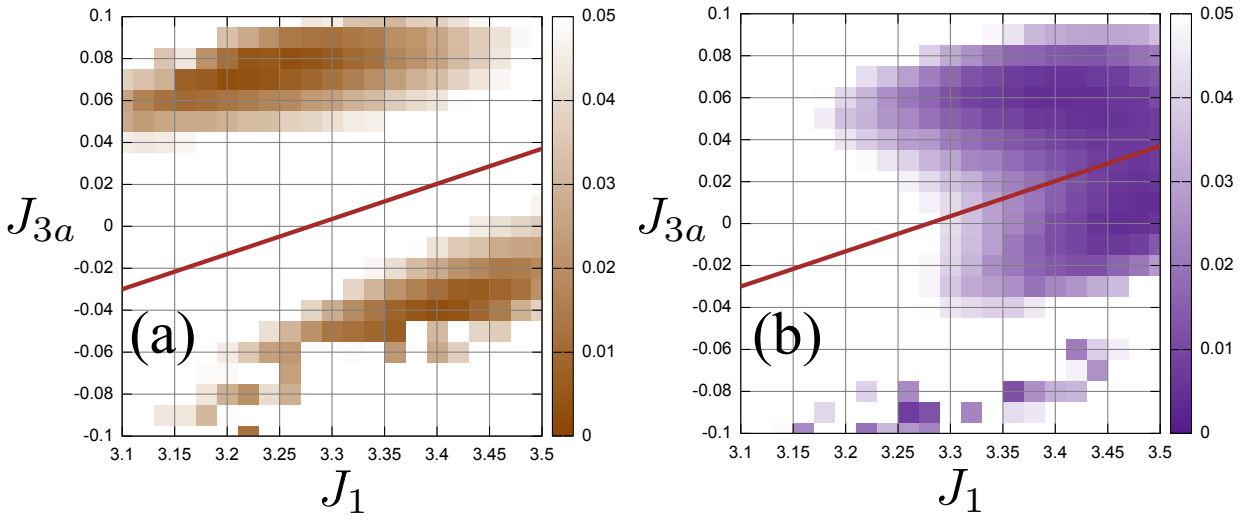

Figure 5.13: (a) Optimal fitting regions in the J_1-J_{3a} plane for the Pomaranski *et. al.* data [1]. (b) Optimal fitting regions for the Ke *et. al.* data [2]. The lines in both panels are the ground state energy boundary between the two proposed magnetic ground states discussed in the text.

"zone boundary scattering" (ZBS) in Ref [3]. The appearance of the ZBS might indicate the emergence of hexagonal excitations in the system [90], an idea not without controversy [24]. The interpretation of the hexagonal excitations is following: scatterings in the zone boundary (large q value) corresponds to short range real space correlations, and for the pyrochlore the smallest collective excitations are the hexagonal loops (Section 2.4). However, in subsequent work by Yavors'kii *et. al.* [24], the hexagonal excitation interpretation was questioned of being void of a real nature. Nevertheless, for the purpose of this work, we are only interested in the experimental ZBS feature itself, and whether our microscopic model can be fitted to produce numerically such feature. The debated origin of the ZBS feature is avoided in this work.

In the process of fitting the ZBS feature in our $J_1 - J_{3a}$ plane, we introduce a criterion of the flatness, σ_{flatness}, along the line segments indicated in the left panel of Fig. 5.15 to assess the existence of ZBS in the Monte Carlo neutron scattering data. The flatness is

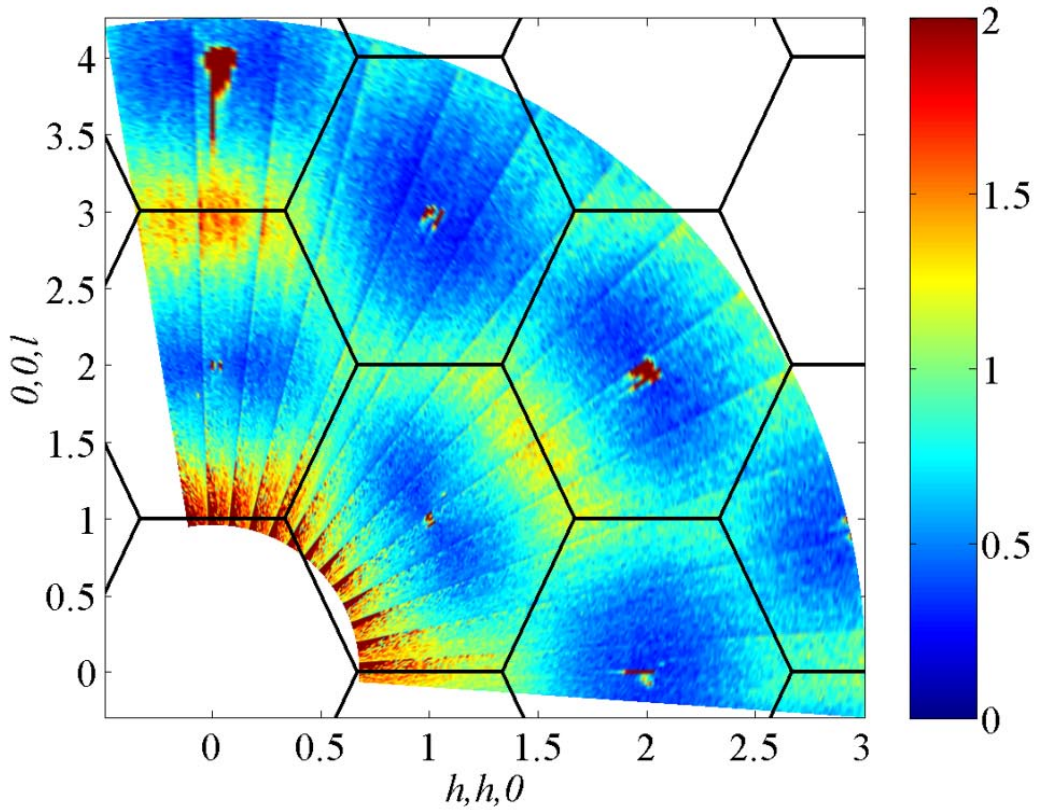

Figure 5.14: Neutron scattering at $T = 0.3$ K in the (hhl) plane of the reciprocal space. Figure reproduced from the work of Fennell *et al.* [3]. Permission to reproduce this figure has been granted by the American Physical Society.

defined as

$$\sigma_{\text{flatness}} = \sum_i (I_{\text{MC}}(\mathbf{Q}_i) - \overline{I_{\text{MC}}})^2 \tag{5.14}$$

where the summation is over the **q**-points on the line segments shown in Fig. 5.15, and $\overline{I_{MC}}$ is the average of the scattering intensity of the summation. The premise of choosing such a flatness quantity in accessing the ZBS feature is that, an even intensity along the L-shaped line segment in the left of panel of Fig. 5.15 creates the image perception of the

ZBS. Thus under this simple criterion, the closer the number σ_{flatness} to zero, the more certain we can say a neutron pattern has the ZBS.

Details of the Monte Carlo simulation can be found in Chapter 6, with the magnetic form factor for Dy^{3+} ion presented in Appendix B.

We plot in the right panel of Fig. 5.15 the flatness criterion, σ_{flatness}, in the $J_1 - J_{3a}$ plane. As can be seen from the figure, the ZBS feature requires the J_1 and J_{3a} relation to be near the phase boundary line. Note that in $J_1 - J_{3a}$ plane, there are some scattered points away from the phase boundary line. This is due to the development of intensity Bragg peaks in the neutron scattering, which make the scattering elsewhere (on the zone boundary) zero. Clearly this is not the desired feature. In summary, the requirement of having the ZBS feature in the neutron scattering, simplified by our "flatness" quantity, σ_{flatness}, constraints J_1 and J_{3a} being close to the boundary line between the two possible magnetic phases.

Next we investigate the neutron scattering intensity along the line cut of $l = 2.375$, for h from 0 to 3. The Monte Carlo data with different J_1 and J_{3a}, multiplied by the magnetic form factor, are compared with the neutron scattering data from the work by Fennell *et al.* [3]. The goodness of fit, is evaluated as

$$\sigma = \sum_i (I_{\text{MC}} - I_{\text{EXP}})^2 \tag{5.15}$$

We plot in Fig. 5.16 the goodness of fit as a function of J_1 and J_{3a}. As can be seen from Fig. 5.16, the optimal areas of the fitting is also near the phase boundary, similar to what is found in the ZBS feature fitting.

A more qualitative feature from the line cut along $l = 2.375$ is revealed from some of the MC results shown in Fig. 5.17, where for a fixed $J_1 = 3.32$ K, different values of J_{3a} shows qualitatively different oscillations of the intensity as a function of h. The relative heights for different **q**-points changes for different parameter values, and as seen clearly in the experimental neutron scattering, we should have intensities that have peaks at about half values and valleys at about integer values. Thus in Fig. 5.17 we plot whether the criterion for having peaks at half values and valleys at integer values of h is satisfied, as a function of J_1 and J_{3a}. As can be seen from the figure, most of the "upper basin" is eliminated when considering such a criterion.

Lastly, a more subtle feature of the neutron scattering is considered. For the experimental intensity peak near $(0, 0, 3)$, the intensity is spread along the zone boundary across

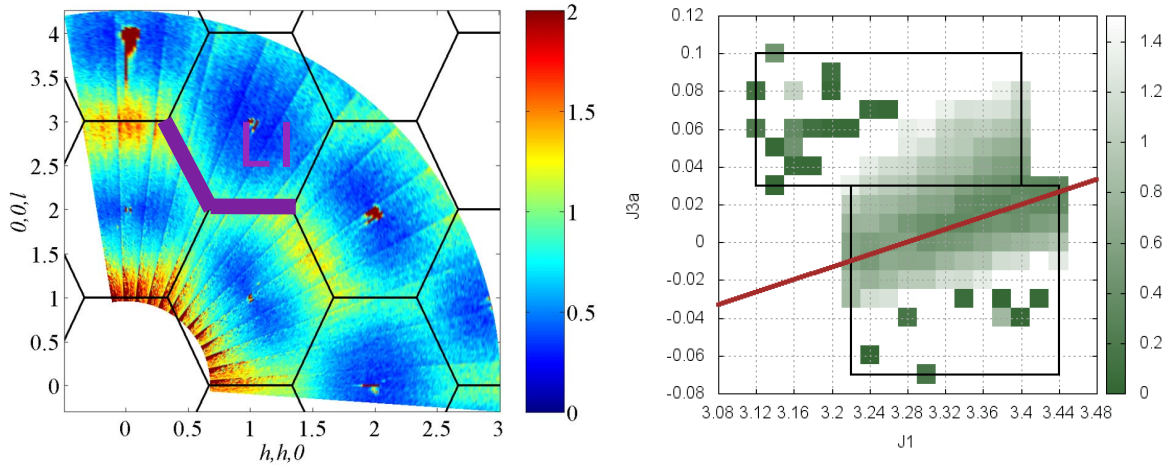

Figure 5.15: Left panel: Reproduction of the Fennell *et al.* [3] neutron scattering data at $T = 0.3$ K. The presence of ZBS is exposed by the flatness of the data along the line indicated by the purple shaped line segments L_1 in the left panel. Right panel: the flatness along the line segments as a function of J_1 and J_{3a} from the Monte Carlo simulated neutron data in the $J_1 - J_{3a}$ plane, at $T = 0.3$ K. The phase boundary line between the double-chain state and the single-chain state is drawn as the brown line in the right panel.

that point, and it is clear that the intensity is higher in the middle of that segment of the zone boundary, than it is on the two ends. This provides us with another criterion to consider in the $J_1 - J_{3a}$ plane. In Fig. 5.18, we plot whether the criterion is satisfied as a function of J_1 and J_{3a}. As can be seen from the figure, the criterion from the experimental neutron data eliminates most of the "lower basin"

In summary, the optimal region of the parameters for the experimental neutron data, as an overlap of Fig. 5.15, Fig. 5.16, Fig. 5.17, and Fig. 5.18, lies in the region close to the phase boundary. Therefore, through fitting of the microscopic Hamiltonian 5.1 to various experimental quantities, we find that the new specific heat measurement by Pomaranski *et al.* [1] is inconsistent with the experimental neutron data by Fennell *et al.* [3].

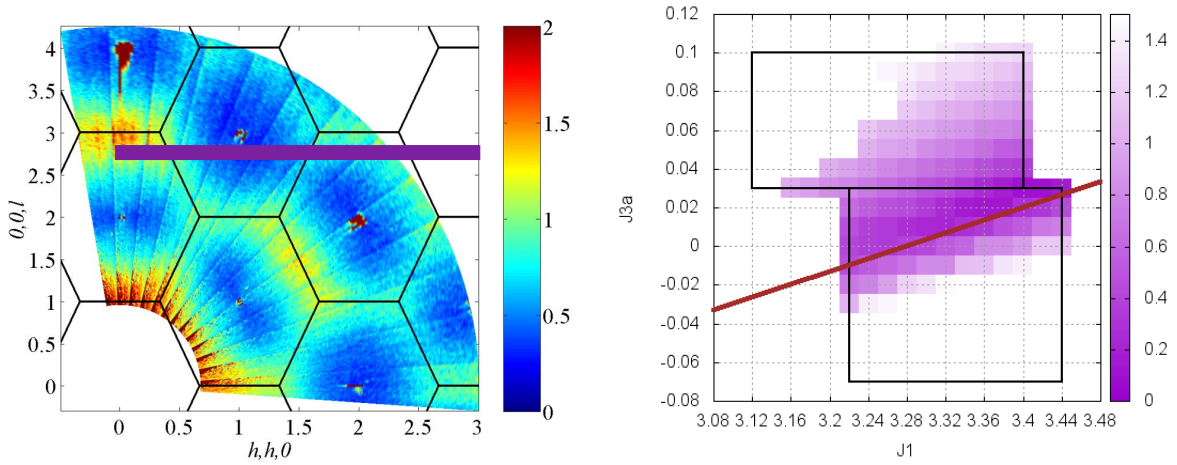

Figure 5.16: Left panel: Reproduction of the Fennell *et al.* [3] neutron scattering data at $T = 0.3$ K. The line cut, $l = 2.375$, is marked by the purple line in the left panel. Right panel: Goodness of fit for the line cut as a function of J_1 and J_{3a} from the Monte Carlo simulated neutron data in the $J_1 - J_{3a}$ plane, at $T = 0.3$ K. The phase boundary line between the double-chain state and the single-chain state is drawn as a brown line in the right panel.

5.4 Issue of inconsistencies in measurements for $Dy_2Ti_2O_7$

In attempts to discover the microscopic model for $Dy_2Ti_2O_7$ based on a classical dipolar spin ice Hamiltonian with further exchange interactions, we have exposed several levels of inconsistencies between the new measurement by Pomaranski *et. al.* [1] in specific heat and older measurements by Ke *et. al.* [2] in specific heat and Fennell *et. al.* [3] in neutron scattering. We summarize in the following.

Out attempt was to fit the experimental data through a dipolar spin ice Hamiltonian with at least five parameters: up to third neighbour interactions, J_1, J_2, J_{3a}, and J_{3b}, where we differentiate two types of third neighbours, and the dipolar coupling, D, between the spins.

By studying the work by Sato *et al.*, we extracted constraints on the relations of $J_1 - J_2$, $J_{3a} - J_{3b}$ and value of D (by the size of the magnetic moment) in terms of Eq. (5.6), Eq. (5.9)

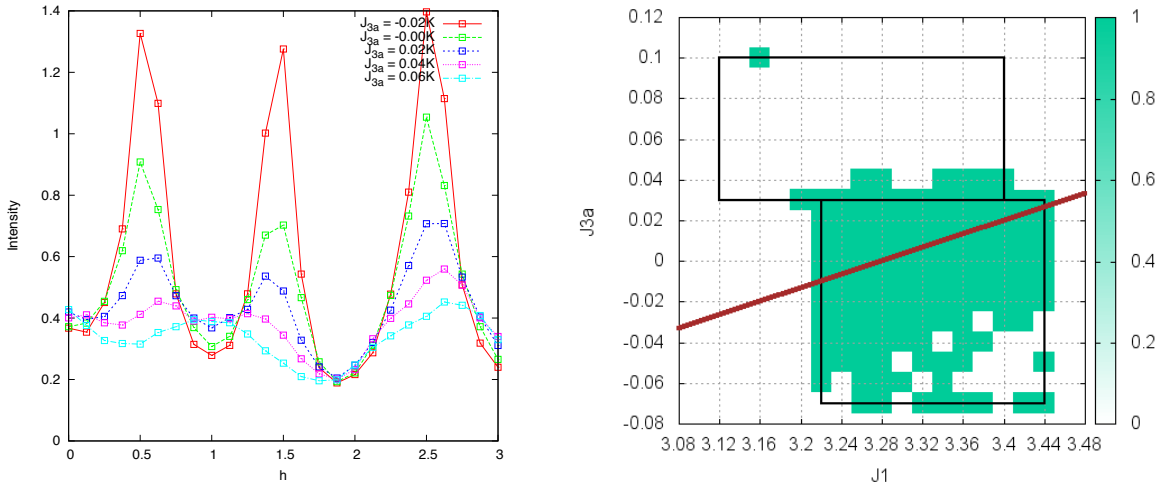

Figure 5.17: Left panel: Some intensity example along the line cut l = 2.375, for a fixed J_1 = 3.32 K and various values of J_{3a}. Right panel: Whether or not the intensities satisfy the criterion that the intensities have maxima at h = 0.5, h = 1.5 and have minima at h = 1.0, and h = 2.0, along the line cut of l = 2.375. The color map value 1 indicates the criterion is satisfied and the color map value 0 indicates the criterion is not satisfied.

and Eq. (5.4). From this, we were left with only two "free parameters", J_1 and J_{3a}.

In the plane of J_1 and J_{3a}, we identified a phase boundary line, where the energy difference between the single-chain and double-chain state is zero. In fact, for discussions in this section, the origin of the line is irrelevant.

Globally, here is what we have found through the fitting of the specific heat by Pomaranski *et al.* [1], the specific heat by Ke *et al.* [2], and the neutron scattering by Fennell *et al.* [3]:

- The Pomaranski *et al.* data requires the (J_1, J_{3a}) to be *away* from the phase boundary line, and be described by a model with (J_1, J_{3a}) parameters in either one of the two separate regions we termed the "upper" and "lower" basin.
- The Ke *et al.* data requires the (J_1, J_{3a}) to be near the phase boundary line. (The Ke *et al.* data quantitatively resembles the majority of the experimental data up-to-day [1].)

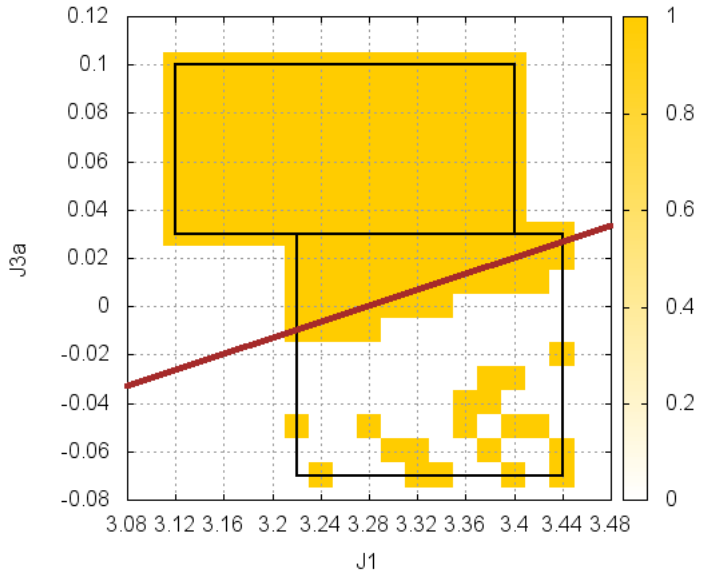

Figure 5.18: Whether or not the intensities at the zone boundary across $(0, 0, 3)$, *i.e.* the line segment from $(-0.5, -0.5, 3)$ to $(0.5, 0.5, 3)$, have more intensities at $h = 0.0$ than at $h = 0.5$. The color map value of 1 indicates the criterion is satisfied while the color map value of 0 indicates the criterion is not satisfied.

- The Fennell *et al.* data requires the (J_1, J_{3a}) to be near the phase boundary line.

Here is an extra comment added to the parameter fitting: In fact, if we try to fit the Ke *et al.* data and the Fennell *et al.* data, we would get parameters very close to what is found in the work by Yavors'kii *et al.* ($J_1 = 3.41$ K , $J_2 = -0.14$ K, $J_{3a} = J_{3b} = 0.025$, and $D = 1.3224$ K). Even though in Yavors'kii *et al.* there is no explicit requirement to satisfy the constraints we identify from the [112] field experiment, the final fitted parameter does lie in range of the constraints.

Thus, the present work shows that the Pomaranski *et al.* data is not only inconsistent with the majority of the specific heat data for $Dy_2Ti_2O_7$, which have a Pauling's residual entropy plateau, and represented by the Ke *et al.* data, but also inconsistent with the Fennell *et al.* data through the microscopic dipolar spin ice model.

One possibility is that the Fennell *et al.* data is also somewhat "faulted" due to the same problem as in the majority of the specific heat measurements, namely, that it was not fully equilibrated as well due to the long relaxation time [1], since the measurement took place at $T = 0.3$ K. If this is the case, then what left is the puzzle why in thermally "quenched" spin ice, the neutron experiment and the calorimetric measurements can be described by the *same* Hamiltonian. Maybe there is an "effective" Hamiltonian for spin ice out of thermal equilibrium? The best way to resolve this puzzle would be to have more neutron experiment data obtained by taking into account the slow relaxation time noted in Pomaranski *et al.* [1].

5.5 Conclusion

In conclusion, in this chapter we investigated the microscopic model for spin ice $Dy_2Ti_2O_7$. Parametric constraints on the model parameters were extracted from the [112] field experiment. With these constraints, we tried to fit three set of the experiments: the specific heat from Pomaranski *et al.* [1] and from Ke *et al.* [2] and the neutron scattering from Fennell *et al.* [5]. We found the Pomaranski *et al.* data is inconsistent with the Fennell *et al.* data, through the microscopic model we use, while the Ke *et al.* data and the Fennell *et al.* data can be reconciled through our model. The inconsistency exposed in this work may encourage interest in future experimental measurements in resolving the issue.

Chapter 6

Pinch point singularities and correlations in spin ice

In this chapter we turn to the discussion of spin-spin correlations in spin ices. As we discussed previously, spin ice, as a highly frustrated magnet, possesses a macroscopic quasi-ground state degeneracy, manifested in the Pauling's residual entropy[4]. Such massive degeneracy is due to the ice-rule constraints on an otherwise paramagnetic spin state, *i.e.*, a *liquid* phase of matter where degrees of freedom are strongly correlated but remain disordered.

An interesting question to ask is what are the long distance consequences for the spins in spin ice, given the local ice-rule constraint. From a coarse-grained point of view, we denote $\mathbf{M}(\mathbf{r})$ as the averaged magnetization from the spins in a macroscopically small but microscopically large volume. The ice-rule constraint on each tetrahedron requires that the divergence of $\mathbf{M}(\mathbf{r})$ be zero:

$$\nabla \cdot \mathbf{M}(\mathbf{r}) = 0. \tag{6.1}$$

Thus in the Fourier space, we have

$$\mathbf{k} \cdot \mathbf{M}(\mathbf{k}) = 0, \tag{6.2}$$

meaning there is no longitudinal component of $\mathbf{M}(\mathbf{k})$.

By projecting out this component in the equipartition result for a paramagnet [32], we

have

$$\langle M_\mu(-\mathbf{k})M_\nu(\mathbf{k})\rangle \propto (\delta_{\mu\nu} - \frac{k_\mu k_\nu}{|\mathbf{k}|^2}) \tag{6.3}$$

which gives the so-called pinch point at $k = 0$. Experimentally, in neutron scattering, the locations of the pinch points are moved to non-zero $\mathbf{q}$-points [31]. Fourier transforming back to the real space, we have

$$\langle M_\mu(0)M_\nu(\mathbf{r})\rangle \propto \frac{\delta_{\mu\nu} - 3\hat{r}_\mu \cdot \hat{r}_\nu}{r^3}, \tag{6.4}$$

meaning the spins are correlated in the form of a dipole-dipole interaction. Therefore the ice-rule state in spin ice is also refer to the *Coulomb phase* [32].

From an experimental point of view, the observation of the pinch points may seem as a signature for the Coulomb phase [5]. However, as noted in previous works [27, 69], pinch points exist beyond the ice-rule manifold, where the temperature dependence of the pinch points are analyzed using the large-N approximation [69].

In this chapter, we investigate the existence of pinch points through Monte Carlo simulations. Both dipolar and nearest-neighbour spin ice models are studied, where the fate of the pinch points are demonstrated through a comparative study of the two models. We study specifically the spin-flip and non-spin-flip channels of the neutron scattering, thus comparing results with the neutron scattering experiment.

For the nearest-neighbour model, ice-rule correlation lengths are extracted by studying the thermal broadening of the pinch point singularities. The correlation length as a function of temperature is compared with the average distance between thermal defects.

The chapter is organized as follows. In Section 6.1 we present Monte Carlo results for the neutron scatterings at different temperatures for two types of spin ice models, *i.e.*, models with and without dipolar interactions. Also we comment on the persistence of the pinch point singularities in the dipolar spin ice model through a simple high temperature expansion argument.

In Section 6.2 we analyze the nearest-neighbour spin ice model and study the evolution of the ice rule correlation lengths extracted from the widths of the Lorentz peaks as a function of temperature.

6.1 A comparative study of the neutron scatterings between dipolar spin ice and nearest neighbour spin ice

6.1.1 Models of spin ice

The two models we study in this chapter for spin ices, as discussed in Chapter 1, are the dipolar spin ice model and the nearest-neighbour spin ice model. Here are their Hamiltonians.

The dipolar spin ice Hamiltonian

$$\mathcal{H}_{\text{dip}} = \sum_{i>j} \sigma_i \sigma_j \{ J_1 \delta_{r_{ij}, r_{nn}} \hat{z}_i \cdot \hat{z}_j + D(r_{nn}/r_{ij})^3 [\hat{z}_i \cdot \hat{z}_j - 3(\hat{z}_i \cdot \hat{r}_{ij})(\hat{z}_j \cdot \hat{r}_{ij})] \} \tag{6.5}$$

where $J_1 = 1.56$ K is the exchange interaction when i and j are nearest neighbours, and $D = 1.41$ K is the dipolar coupling strength. These particular numbers are for $Ho_2Ti_2O_7$, the material we focus on in this chapter in comparison with its neutron scattering measurments [5]. The Hamiltonian parameters were determined from a previous study [25]. The σ's are the Ising variables and the $\hat{z}$'s are the local [111] directions of the Ising spins. r_{nn} is the nearest-neighbour distance in the pyrochlore lattice. The effective nearest-neighbour interaction between the Ising variables is $J_{\text{eff}} = 1.8$ K from this model for $Ho_2Ti_2O_7$.

The nearest-neighbour spin ice Hamiltonian reads

$$H_{\text{nn}} = J_{\text{nn}} \sum_{\langle i,j \rangle} \sigma_i \sigma_j \tag{6.6}$$

where the sum is over all neighbour neighbours. In this study we choose $J_{\text{nn}} = 1.8$ K, a value corresponding to the effective nearest neighbour interaction, J_{eff}, in $Ho_2Ti_2O_7$.

6.1.2 Pinch point singularity for the dipolar model at high temperatures

We show, through a simple argument based on high temperature expansion that, for the dipolar spin ice model, the spin-spin correlation function has a dipole-dipole form as a function of distance between them and thus pinch points in **q**-space, even at high temperature, well above the formation of the spin ice manifold.

Consider the spin-spin correlation function

$$C(\sigma_k, \sigma_l) \equiv \langle \sigma_k \sigma_l \rangle - \langle \sigma_k \rangle \langle \sigma_l \rangle \tag{6.7}$$

for the Ising variables σ_k and σ_l. In the paramagnetic phase,

$$\langle \sigma \rangle = 0. \tag{6.8}$$

Thus in the canonical ensemble, we have for the correlation function

$$\langle \sigma_k \sigma_l \rangle = \frac{\sum_{\{\sigma\}} \sigma_k \sigma_l e^{-H/k_B T}}{Z} \tag{6.9}$$

where the summation is over all the possible spin configurations $\{\sigma\}$, and Z is the partition function.

In general the energy H of the system can be written as

$$H = \sum_{i,j} \sigma_i \sigma_j J_{i,j}. \tag{6.10}$$

Therefore, if we expand the exponential in powers of inverse temperature, T, we have

$$\langle \sigma_k \sigma_l \rangle \simeq \sum_{\{\sigma\}} \sigma_k \sigma_l [1 + (-\sum_{i,j} \sigma_i \sigma_j J_{i,j})/k_B T] \tag{6.11}$$

Consider the first term in the numerator $\sum_{\{\sigma\}} \sigma_k \sigma_l$, since when summed over all the possible configurations, the term $\sigma_k \sigma_l$ occurs the same number of times of being positive as being negative, we have

$$\sum_{\{\sigma\}} \sigma_k \sigma_l = 0 \tag{6.12}$$

Consider the second term in the numerator $\sum_{\{\sigma\}} \sigma_k \sigma_l (-\sum_{i,j} \sigma_i \sigma_j J_{i,j})/k_B T$. The summation over the spin configurations is not zero only when $k = i$ and $l = j$ (assuming $k < l$ and $i < j$).

Therefore we have for the correlation

$$\langle \sigma_k \sigma_l \rangle = -\sum_{i,j} \delta_{k,i} \delta_{l,j} J_{i,j}/k_B T \tag{6.13}$$

or

$$\langle \sigma_k \sigma_l \rangle = -J_{k,l}/k_B T \tag{6.14}$$

Therefore at high temperatures, the spin-spin correlation function *is* the interaction. For the dipolar spin ice Hamiltonian, the interaction is of the dipole-dipole form, thus, at high temperature, the spin-spin correlation is of the dipole-dipole form, and we have pinch points for the dipolar spin ice model at high temperatures [5].

6.1.3 Spin flip and non spin flip channels in polarized neutron scattering

Fennell *et al.* [5] performed polarized neutron scatterings for $Ho_2Ti_2O_7$. Two channels of the neutron scattering were measured separately, the spin-flip (SF) channel and the non-spin-flip (NSF) channel.

For the neutron scattering plane (h, h, l), we re-summarize the definition of the SF and NSF neutron scattering from Fennell *et al.* as follows. Define direction $\mathbf{z}_1 = [1\bar{1}0]$, which is perpendicular to the scattering plane. Define direction $\mathbf{x}_1$, which is parallel to the scattering wave vector $\mathbf{Q}$. Then, the direction $\mathbf{y}_1$ is defined as the cross product of $\mathbf{z}_1$ and $\mathbf{x}_1$. The SF and NSF cross sections are then defined as the Fourier transform of the spin-spin correlation function with only components along the $\mathbf{y}_1$ and $\mathbf{z}_1$ directions, respectively, for SF and NSF.

For the SF channel,

$$S^{\mathrm{SF}}(\mathbf{Q}) = (1/N)\left|\sum_{i,j} \sigma_i \sigma_j (\hat{z}_i \cdot \hat{y}_1)(\hat{z}_j \cdot \hat{y}_1) e^{i\mathbf{Q}\cdot\mathbf{r}_{ij}}\right|^2, \tag{6.15}$$

while for the NSF channel,

$$S^{\mathrm{NSF}}(\mathbf{Q}) = (1/N)\left|\sum_{i,j} \sigma_i \sigma_j (\hat{z}_i \cdot \hat{z}_1)(\hat{z}_j \cdot \hat{z}_1) e^{i\mathbf{Q}\cdot\mathbf{r}_{ij}}\right|^2, \tag{6.16}$$

where in both equations, the $\hat{z}_i$ and $\hat{z}_j$ are the easy-axis directions of the Ising spins.

Note that the four easy axes for the Ising spins on different sublattices are along $(1,1,1)/\sqrt{3}$, $(-1,-1,1)/\sqrt{3}$, $(-1,1,-1)/\sqrt{3}$, and $(1,-1,-1)/\sqrt{3}$. Therefore, two of the sublattices have no spin component along the NSF direction, $\mathbf{z}_1 = [1\bar{1}0]$, *i.e.* the NSF neutron scattering only probes half of the spins.

The total neutron scattering equals to the sum of the SF and NSF channels.

6.1.4 Monte Carlo neutron scatterings for spin ices

We perform Monte Carlo simulations for the spin ice Hamiltonians of Eq. (6.5) and Eq. (6.6) with parameters suitable for $Ho_2Ti_2O_7$ [25]. SF and NSF channels are calculated. The simulation box is of the size $L = 8$. We plot in Fig. 6.1 and Fig. 6.2 the SF neutron scatterings for the dipolar model and the nearest-neighbour model at various temperatures. The scattering wavevectors are in the (h, h, l) plane.

As can be seen from these figures, for the dipolar spin ice model, the pinch points appear at the $(0, 0, 2)$, $(1, 1, 1)$ positions. At higher temperatures, the contrast between different directions crossing the pinch points gets lowered, nevertheless, the pinch points appear for all temperatures. As the temperature drops below 1.7 K, intensity develops at $(0, 0, 1)$ and $(0, 0, 3)$, foretelling the long range order developed at lower temperatures [48].

For the nearest-neighbour spin ice model, at low temperatures the pinch points appear at the same locations as in the dipolar spin ice model. At higher temperatures, not only the contrast between high intensity region and low intensity region gets lowered, but the pinch points are also broadened. Eventually the pinch points become "rods" of scatterings.

The NSF neutron scattering for the dipolar spin ice is plotted in Fig. 6.3. As can be seen in the figure, scattering intensity develops as a checkerboard pattern in the (h, h, l) map. The contrast of the intensities gets lowered at higher temperatures, but at 5 K and even barely at 10 K, the contrast can still be perceived on the scale of the contour plots. No pinch point is seen for the NSF neutron scattering.

For the nearest-neighbour model, the NSF neutron scattering is completely flat at all temperatures.

Thus our results show that pinch points are *not* a signature of the Coulomb phase for dipolar spin ice. In a system with dipolar interactions, pinch point is merely a reflection of the dipolar interaction itself, as we have seen from the high-temperature expansion argument in Subsection 6.1.2.

6.2 Correlations for the nearest neighbour model

In this section we study the thermal broadening of the pinch points for nearest-neighbour spin ice. In the vicinity of the pinch point at non-zero temperature, the SF signal acquires

the form [5, 31, 91]

$$S^{\mathrm{SF}}(q_h, q_k, q_l) \propto \frac{q_{l-2}^2 + \xi_{\mathrm{ice}}^2}{q_{l-2}^2 + q_h^2 + q_k^2 + \xi_{\mathrm{ice}}^2} \tag{6.17}$$

where the ice-rule correlation, ξ_{ice}, is a function of temperature, and broadens the pinch point singularities.

In this chapter, we perform Monte Carlo simulation to study the thermal broadening of the pinch point through Eq. (6.17). Simulation boxes of up to size of $L = 32$ are used. We plot in Fig. 6.4 the SF neutron scattering along the horizontal line cut across the pinch point, where the symbols are for the simulation data points and the line are from the fitting through Eq. (6.17).

The ice-rule correlation [5], ξ_{ice}, extracted from the above Lorentz fit, as a function of temperature, is plotted in Fig. 6.5. On the same figure, we also plotted the averaged distance between thermal defects, defined as $(1/\rho)^{1/3}$. It turns out that the correlation lengths from the Lorentzian fits and the defect densities can be described by the $\exp(J/T)$ and the $\exp(2J/3T)$ functions, respectively.

From the Debye-Huckel theory in the work by Castelnovo *et al.* [71], we have

$$\xi_{\mathrm{Debye}} \propto \sqrt{\frac{T}{\rho}} \tag{6.18}$$

This indicates the correlation length, ξ_{ice}, extracted from the Lorentzian fit to the broandening of the pinch point presented above, is the Debye screening length.

6.3 Conclusion

In this chapter, we have shown through Monte Carlo simulation that for a dipolar spin ice, the pinch points exist at high temperatures where local ice-rule constraints do not apply. This is in agreement with the high temperature expansion argument for a dipolar system. For a nearest-neighbour spin ice model, we have shown that the correlation lengths extracted from the thermal broadening of the pinch points agree with the Debye-Huckle correlation length.

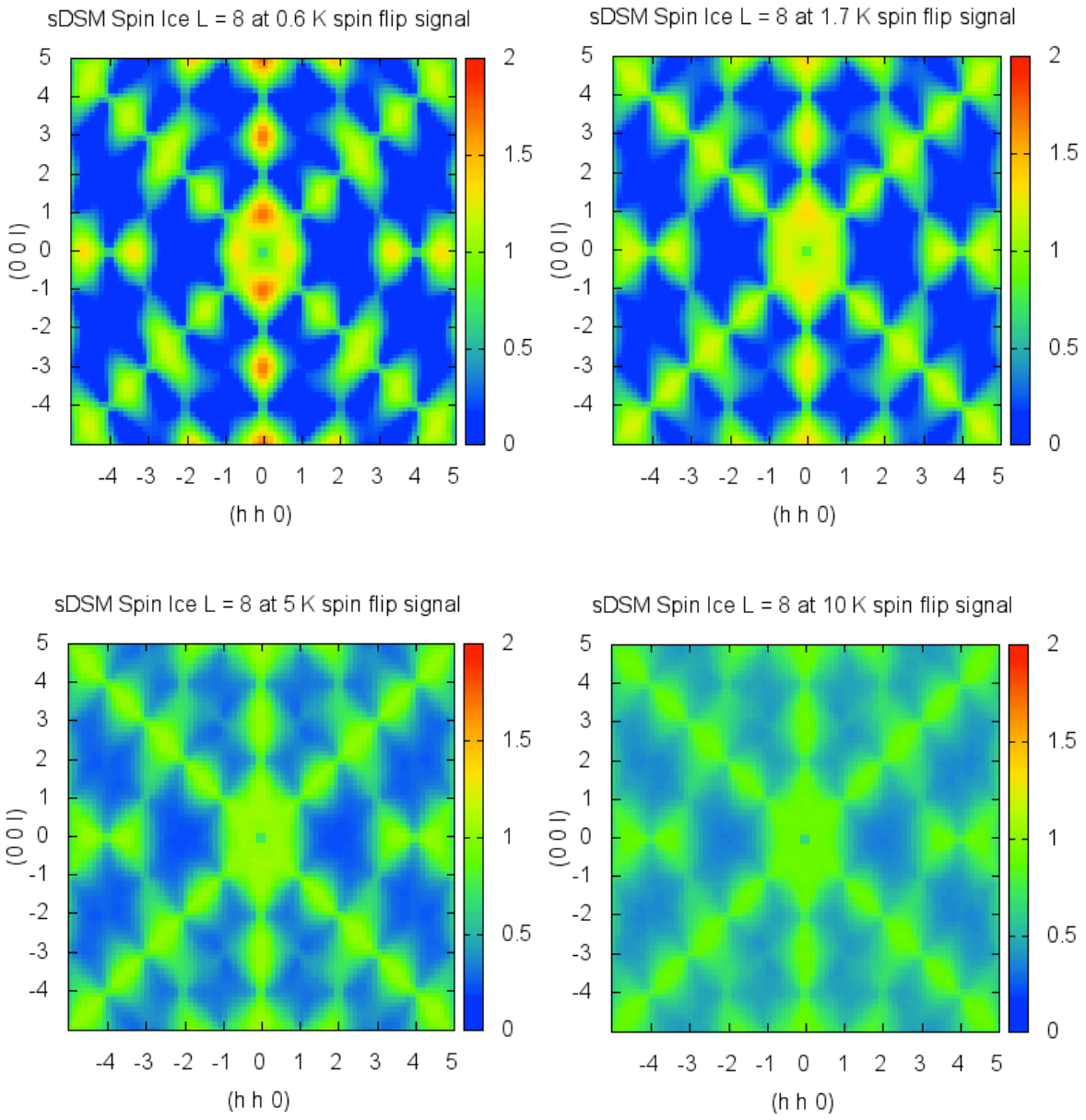

Figure 6.1: Spin-flip channel of the neutron scattering in the (h, h, l) plane for the dipolar Hamiltonian (6.5) at various temperatures. Monte Carlo method is used with a simulation box of size $L = 8$. From top left, top right, to bottom right, bottom left, the temperatures are $T = 0.6$ K, $T = 1.7$ K, $T = 5$ K, and $T = 10$ K. The pinch points persist up to the highest temperature.

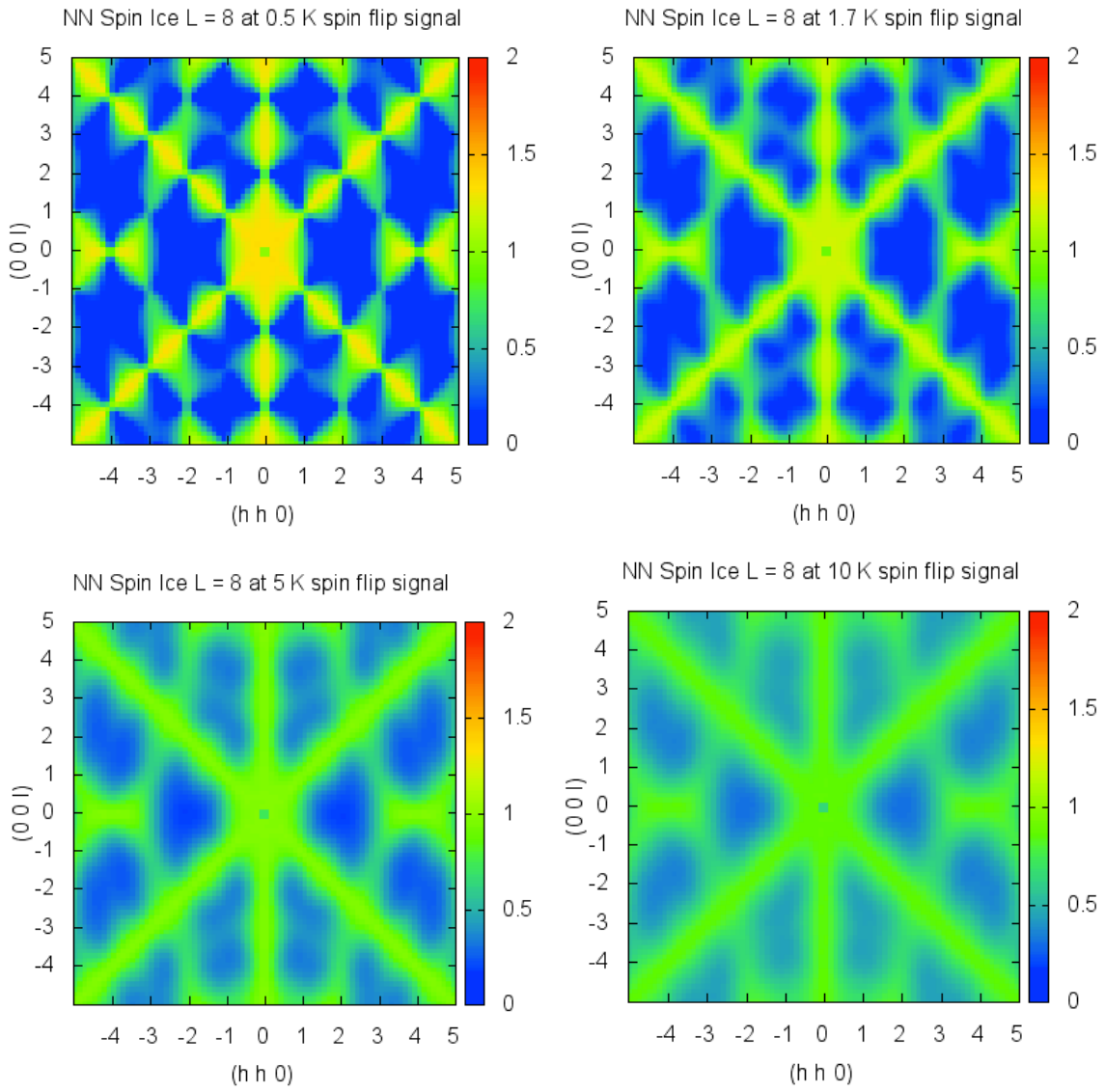

Figure 6.2: Spin-flip channel of the neutron scattering, in the (h, h, l) plane for the nearest neighbour Hamiltonian (6.6) at various temperatures. Monte Carlo method is used with a simulation box of size $L = 8$. From top left, top right, to bottom right, bottom left, the temperatures are $T = 0.5$ K, $T = 1.7$ K, $T = 5$ K, and $T = 10$ K. As temperature rises, the pinch points broaden and disappear.

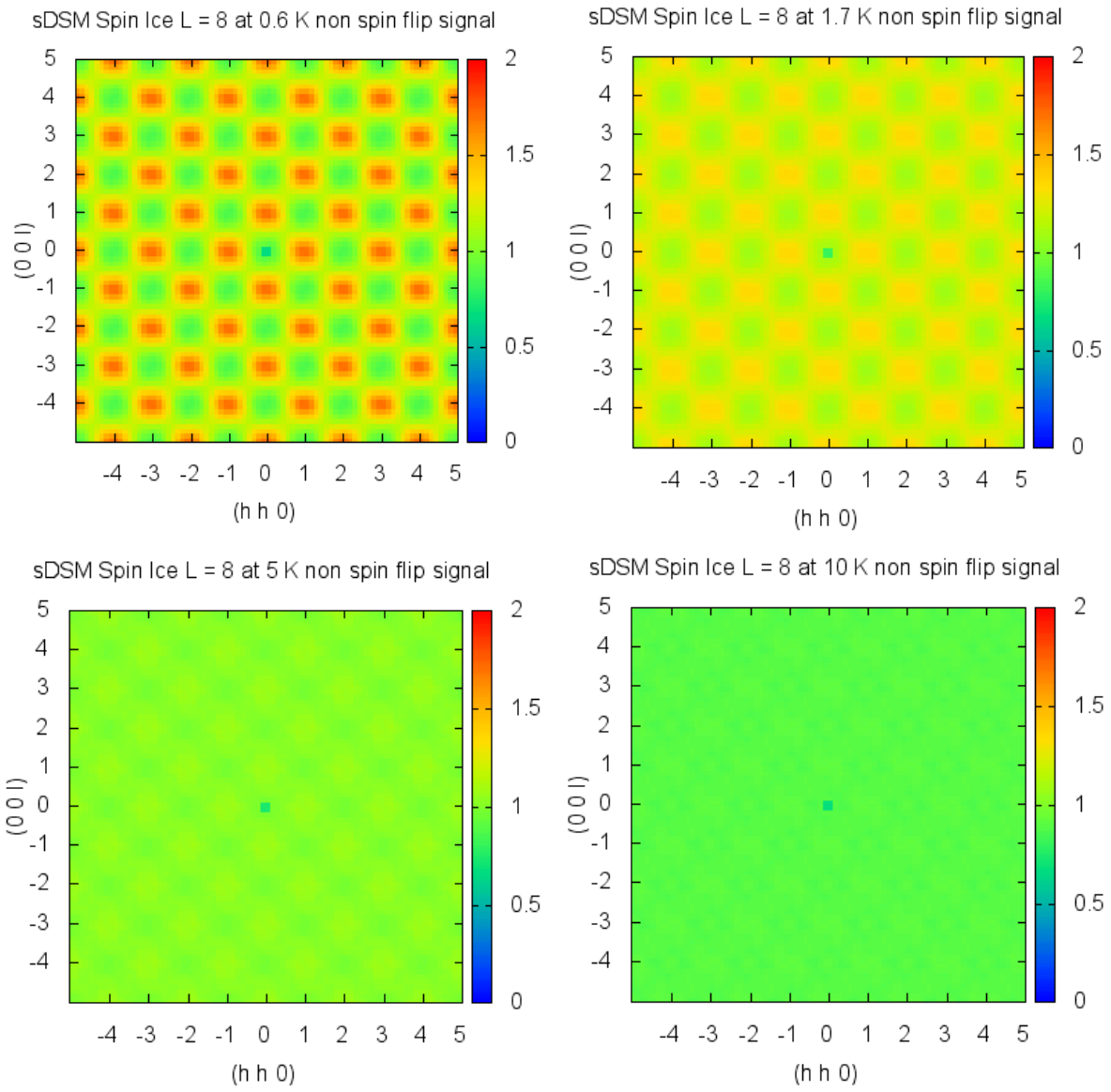

Figure 6.3: Non-spin-flip channel of the neutron scattering in the (h, h, l) plane for the dipolar Hamiltonian (6.5) at various temperatures. Monte Carlo method is used with a simulation box of size $L = 8$. From top left, top right, to bottom right, bottom left, the temperatures are $T = 0.6$ K, $T = 1.7$ K, $T = 5$ K, and $T = 10$ K. There is no pinch point in this channel of the neutron scattering, instead checkerboard patterns are seen with intensity peaks at locations of $(1, 1, 0)$, $(0, 0, 1)$ and so on.

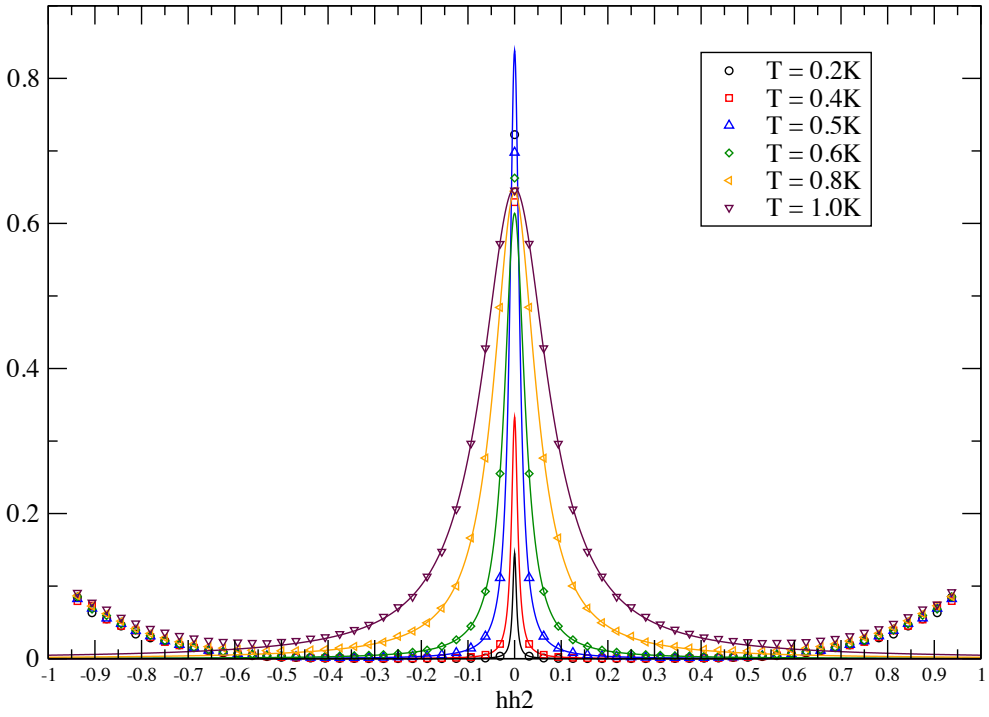

Figure 6.4: Intensities along the $l = 2$ line across the pinch point for the nearest-neighbour spin ice, Eq. (6.6), at various temperatures. Monte Carlo simulation is used with a simulation box of size $L = 32$. $J_{\rm nn} = 1.8$ K in Eq. (6.6). The symbols are the Monte Carlo data, the lines are the fit to Eq. (6.17).

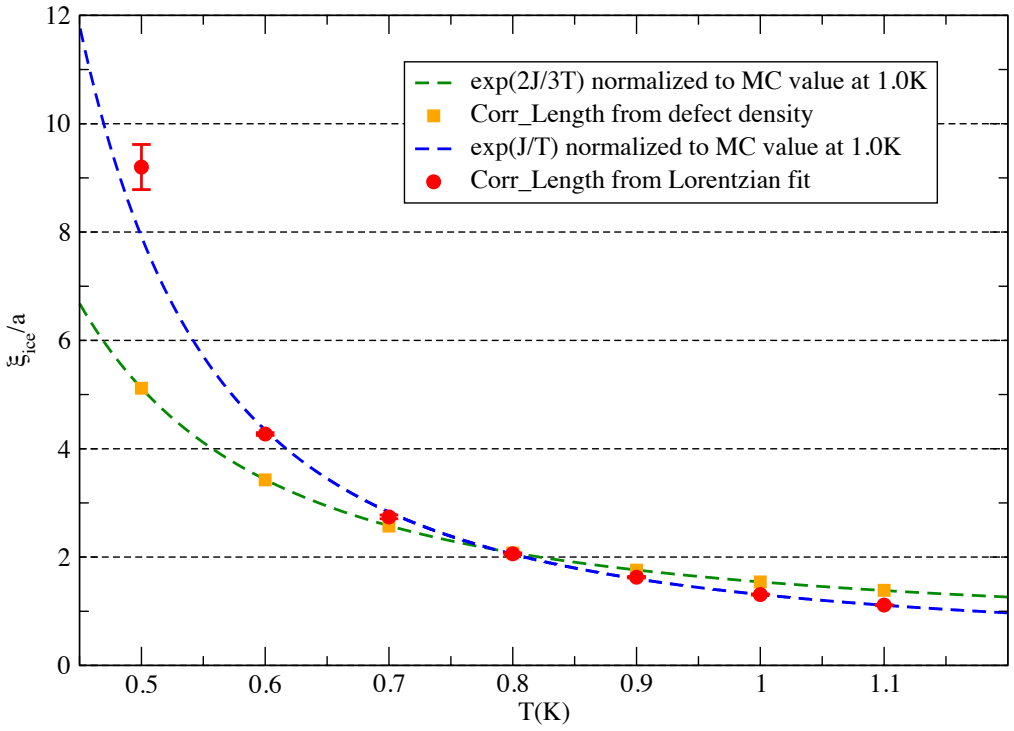

Figure 6.5: Length scales extracted from the Lorentz fit of the pinch points through Eq. (6.17) (circle) and extracted from the average distance between thermal defects.

Chapter 7

Numerical linked cluster study of polarized neutron scattering for quantum spin ice $Yb_2Ti_2O_7$

As noted in the Introduction, quantum spin ice $Yb_2Ti_2O_7$ may be a candidate for a quantum spin liquid with a known Hamiltonian [6]. The question that interests us is then, with this Hamiltonian, whether experimental observables can be calculated and compared with measurements quantitatively. The numerical linked cluster expansion (NLC) method [52, 53, 54], which has been used in calculating the specific heat and magnetization for $Yb_2Ti_2O_7$ in previous works [44, 45], is found to be quite successful and gives results with controllable errors. The goal of this chapter, is to demonstrate the capability of the method in calculating polarized neutron scattering signals for a quantum spin ice Hamiltonian.

7.1 Quantum spin ice model for $Yb_2Ti_2O_7$

For the rare-earth pyrochlore $Yb_2Ti_2O_7$, the magnetic ions Yb^{3+} reside on the pyrochlore lattice and have anisotropic along their local $\langle 111 \rangle$ directions, as dictated by their crystal field environments. Its microscopic Hamiltonian may be described by an effective quantum pseudospin-1/2 model [40, 41].

In a previous work by Ross *et al.* [6], the model was fitted with high-field inelastic neutron scattering and the parameters were found to be quantitatively accurate in previous NLC works by Applegate *et al.* [44] and Hayre *et al.* [45] for specific heat and magnetization, respectively. In this chapter, we adopt the same model for our NLC investigation for the neutron scatterings.

The spin-1/2 model Hamiltonian from Ross *et al.* [6] reads

$$\begin{aligned} H_{\mathrm{QSI}} = \sum_{\langle i,j \rangle} \{ & J_{zz} S_i^z S_j^z - J_{\pm}(S_i^+ S_j^- + S_i^- S_j^+) + J_{\pm\pm}[\gamma_{ij} S_i^+ S_j^+ + \gamma_{ij}^* S_i^- S_j^+] \\ & + J_{z\pm}[S_i^z(\zeta_{ij} S_j^+ + \zeta_{ij}^* S_j^- + i \leftrightarrow j]\} - \sum_i \vec{h} \cdot \mathrm{g} \cdot \mathrm{S_i}, \end{aligned} \tag{7.1}$$

where S_i^z, S_j^z are for the local spin coordinates, and the summation is over all nearest neighbours. $\zeta = -\gamma^*$ is the 4×4 complex unimodular matrix, whose values can be found in Appendix C. The couplings for $Yb_2Ti_2O_7$ were determined to be [6, 44, 45] $J_{zz} = 0.17$, $J_{\pm} = 0.05$, $J_{\pm\pm} = 0.05$, and $J_{z\pm} = -0.14$ all in meV, and $g_{zz} = 1.80$ and $g_{xy} = 4.32$ for the g-tensor.

7.2 Numerical linked cluster expansion calculation

7.2.1 Linked cluster expansion for quantum spin ice

For spin ices, as noted in Chapter 1, the most important physics is incompassed in the two-in-two-out ice-rule constraint on each tetrahedron. Therefore, in developing the cluster expansions for a ice model, it is wise to build orders of the clusters by the whole tetrahedron instead of by spins to avoid the problem of rapid oscillation in the presence of incomplete tetrahedra.

Consider the general case with the possible presence of non-zero magnetic fields, the cluster expansion consists of the following terms.

The zeroth order cluster, depicted in Fig. 7.1, consists of only one site. Since we are focusing on the spin-spin correlation functions in this chapter, and the cluster with only one site does not contribute to the two-point correlation functions for non-zero reciprocal space vectors, we therefore ignore this term in the calculations presented here. (It was pointed out during the submission stage of this thesis by my supervisor, Dr. Gingras, that

for zero reciprocal space vector, the zeroth order cluster can not be omitted.) Note that for the calculations of the magnetization or specific heat in a magnetic field, this 1-site cluster cannot be ignored.

Figure 7.1: Linked cluster for the pyrochlore lattice, 0th order, which consists of a single (isolated) site.

The first order cluster, depicted in Fig. 7.2, consists of a single tetrahedron. There is only one such type of cluster, as the permutation of the sublattices on the four different sites basically refers to the same tetrahedron. The corresponding lattice constant, as defined in Chapter 2, is

$$L_1 = 1/2, \tag{7.2}$$

since the number of such cluster is the number of the tetrahedron $(N/2)$ in the lattice.

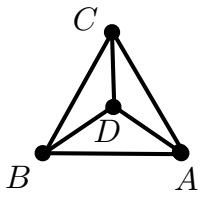

Figure 7.2: Linked cluster for the pyrochlore lattice, 1st order

The second order cluster, depicted in Fig. 7.3, consists of two tetrahedra connected by a common site A. There are four types of second order cluster, depending on which sublattice site A corresponds to. The lattice constant for each type is

$$L_2 = 1/4, \tag{7.3}$$

since the number of such cluster can be counted by the number of site A on the lattice, which is the number of one sublattice sites.

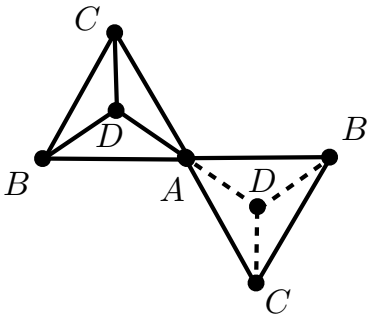

Figure 7.3: Linked cluster for the pyrochlore lattice, 2nd order. There are four distinct clusters of this order based on the choice of the sublattice for site A.

The third order cluster, depicted in Fig. 7.4, consists of three tetrahedra connected by two common sites A and B. The number of different third order cluster is 6, counted from the choices of the sublattices for the common sites A and B. The lattice constant for each type of third order cluster is

$$L_3 = 1/4, \tag{7.4}$$

as the cluster can be specified by its central tetrahedron.

For the fourth order cluster, three different topologies are possible for the connections of the tetrahedra.

The first type, referred to as ABA type in previous works [44, 45], is depicted in Fig. 7.5. Within this type, there are 12 distinct clusters, counted by the choices of sublattices for site A and site B. Then, for each distinct cluster, the lattice constant is

$$L_{4,\mathrm{ABA}} = 1/4, \tag{7.5}$$

as the cluster can be specified by the choice of the site A in the lattice.

The second type of fourth order cluster, referred to as the ABC type in previous works [44, 45], is depicted in Fig. 7.6. Within this type, there are 24 distinct clusters, counted

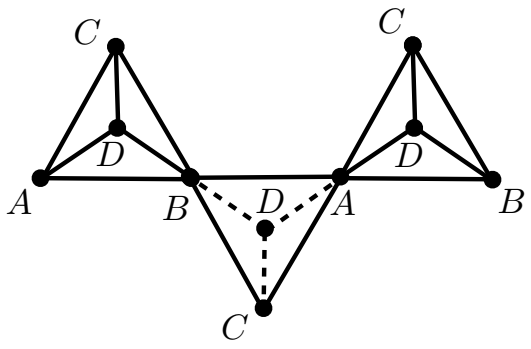

Figure 7.4: Linked cluster for the pyrochlore lattice, 3rd order. There are six distinct clusters of this order based on the choice of the sublattice for sites A and B.

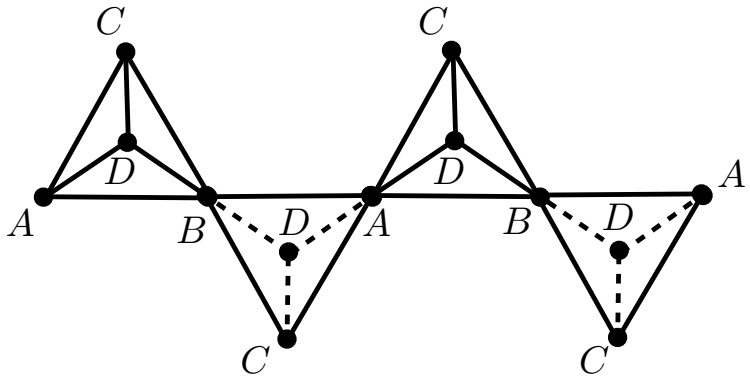

Figure 7.5: Linked cluster for the pyrochlore lattice, 4th order, type ABA. There are twelve distinct clusters of this type based on the choice of the sublattices for sites A and B.

by the choices of the sublattices for sites A, B, and C. Then for each distinct cluster, the lattice constant is

$$L_{4,\mathrm{ABC}} = 1/4, \tag{7.6}$$

as the cluster can be specified by the choice of site A in the lattice.

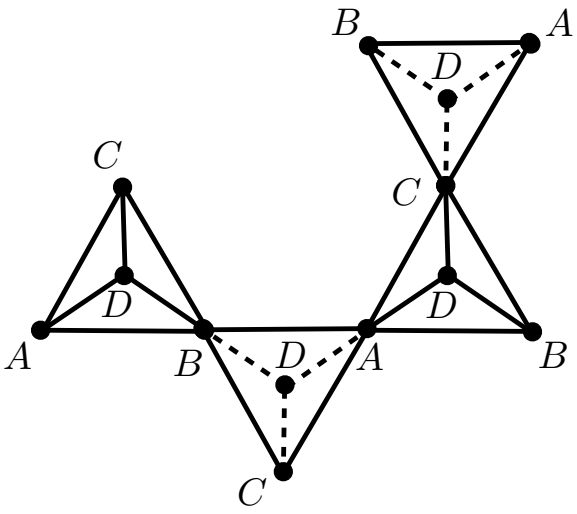

Figure 7.6: Linked cluster for the pyrochlore lattice, 4th order, type ABC. There are twenty-four distinct clusters of this type based on the choice of the sublattices for sites A, B, and C.

Finally, the third type of fourth order cluster, referred to as the Y type in previous works [44, 45], is depicted in Fig. 7.7. For this type, there are 4 distinct clusters, counted by the choices of the sublattices for site A. Then for each distinct cluster, the lattice constant is

$$L_{4,\mathrm{Y}} = 1/2, \tag{7.7}$$

as the cluster can be specified by the choice of the central tetrahedron in the lattice.

With all these clusters and their lattice constants, the numerical linked cluster program can be carried out as described in Chapter 2. For the final results, it is often easier to write out the contribution from different orders expressed in the form of the averaged properties of each type of clusters. Denote C_1, $C_{\mathrm{avg},2}$, $C_{\mathrm{avg},3}$, $C_{\mathrm{avg},4,\mathrm{ABA}}$, $C_{\mathrm{avg},4,\mathrm{ABC}}$, and $C_{\mathrm{avg},4,\mathrm{Y}}$ as the averaged cluster properties from each of the above discussed clusters, respectively. We have for the numerical linked cluster expansion

$$P_{\mathrm{NLC1}} = (1/2)C_1, \tag{7.8}$$

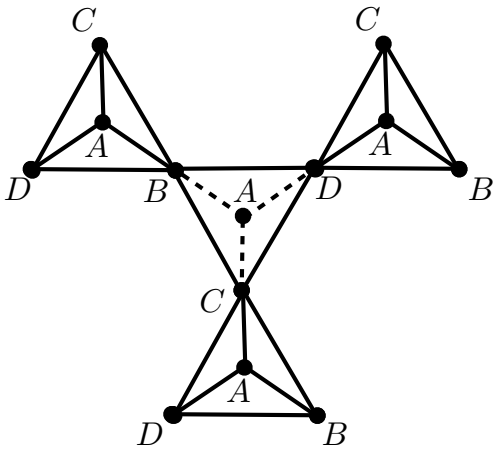

Figure 7.7: Linked cluster for the pyrochlore lattice, 4th order, type Y. There are 4 distinct clusters of this type based on the choice of the sublattice for site A.

$$P_{\mathrm{NLC2}} - P_{\mathrm{NLC1}} = C_{\mathrm{avg},2} - 2C_1, \tag{7.9}$$

$$P_{\mathrm{NLC3}} - P_{\mathrm{NLC2}} = 3C_{\mathrm{avg},3} - 6C_{\mathrm{avg},2} + 3C_1, \tag{7.10}$$

and the contribution from the ABA cluster to the 4th order is

$$\{P_{\mathrm{NLC4}} - P_{\mathrm{NLC3}}\}_{\mathrm{ABA}} = 3C_{\mathrm{avg},4,\mathrm{ABA}} - 6C_{\mathrm{avg},3} + 3C_{\mathrm{avg},2}, \tag{7.11}$$

and the contribution from the ABC cluster to the 4th order is

$$\{P_{\mathrm{NLC4}} - P_{\mathrm{NLC3}}\}_{\mathrm{ABC}} = 6C_{\mathrm{avg},4,\mathrm{ABC}} - 12C_{\mathrm{avg},3} + 6C_{\mathrm{avg},2}, \tag{7.12}$$

and the contribution from the Y cluster to the 4th order is

$$\{P_{\mathrm{NLC4}} - P_{\mathrm{NLC3}}\}_{\mathrm{Y}} = 2C_{\mathrm{avg},4,\mathrm{Y}} - 6C_{\mathrm{avg},3} + 6C_{\mathrm{avg},2} - 2C_1, \tag{7.13}$$

Combining the above three contributions, the total contribution from the 4th order linked cluster expansion is

$$P_{\mathrm{NLC4}} - P_{\mathrm{NLC3}} = 3C_{\mathrm{avg,4,ABA}} + 6C_{\mathrm{avg,4,ABC}} + 2C_{\mathrm{avg,4,Y}} - 24C_{\mathrm{avg,3}} + 15C_{\mathrm{avg,2}} - 2C_1. \quad (7.14)$$

7.2.2 Calculation of the observables

The quantities that we calculate in this chapter, are the spin-flip and non-spin-flip signals of the neutron scattering, as defined in Chapter 6. The total scattering is equal to the sum of the two channels.

For a polarized neutron intensity for spin components selected along a particular direction, $\hat{Y}$, the intensity is calculated by

$$\hat{I}_{\hat{Y}}(\mathbf{Q}) = \sum_{i,j} e^{-i\mathbf{Q}\cdot\vec{R}_{i,j}} (\hat{Y}\cdot g\cdot\vec{S}_i)(\hat{Y}\cdot g\cdot\vec{S}_j), \quad (7.15)$$

where $\vec{S} = S^x\hat{x} + S^y\hat{y} + S^z\hat{z}$ is the spin-1/2 quantum operator, and g is the g-tensor for the magnetic moment.

For a given cluster and a given temperature, the property of the cluster is given by

$$I_{\hat{Y}}(\mathbf{Q}) = \sum_n \frac{\langle\Psi_n|\hat{I}_{\hat{Y}}|\Psi_n\rangle e^{-\beta E_n}}{Z} \quad (7.16)$$

where $|\Psi_n\rangle$ are the eigenstates for the cluster the given cluster.

The procedure for performing the numerical linked cluster expansion goes as follows:

- Construct the Hamiltonian for each of the cluster ;
- Diagonalize the Hamiltonians and calculate the properties of each cluster using Eq. (7.16) ;
- Use Eqs. (7.8), (7.9), (7.10) and (7.14) to calculate the numerical linked cluster expansion quantities up to 4th order.

After this procedure, only properties that are converged as the order of the clusters gets higher are physically relevant.

In our study, the diagonalization is performed through the CLAPACK library. Note that the matrices for the Hamiltonians and observables are large sparse matrices, therefore in order to facilitate calculations for large clusters, compressed sparse row representation is used in this work as the data structure for the matrices.

7.3 Neutron scattering results and discussions

7.3.1 Total neutron scattering

With the NLC method discussed above, we compute the polarized neutron scattering for the quantum spin ice model. In Fig. 7.8, we plot the total neutron scattering signals for the model at $T = 1.4$ K up to the fourth order in the (h, h, l) scattering plane. Also, in order to check convergence between different orders, we plot in Fig. 7.9 the intensities along different directions.

From Fig. 7.8, a clear rod of scattering feature can be seen in the neutron map. Such a feature has been linked to the two-dimensional correlations in the $Yb_2Ti_2O_7$ material [43, 92]. As shown in Fig. 7.9, the convergence of the NLC method is quite good at $T = 1.4$ K for clusters bigger than two tetrahedra, except for $\mathbf{q}$ values near the intensity peak at $(2, 2, 2)$.

We also calculated the neutron scattering at $T = 0.8$ K, where the thermodynamic calculation indicates a failure of the convergence in the NLC [44, 45] for the specific heat and the magnetization. We plot in Fig. 7.10 the neutron scattering maps at $T = 0.8$ K. As shown in the figure, the peaks in the (h, h, l) map become more pronounced, while the rod scattering feature remains.

We plot in Fig. 7.11 the intensities along different line cuts for the $T = 0.8$ K neutron scattering. As can be seen from the figure, away from the intensity peaks, the NLC converges very well. Thus we find that the usefulness of the NLC method in the spin-spin correlation functions extends below the temperatures where for specific heat or magnetization measurements the method fails to converge, at wavevectors away from the Bragg peaks. Therefore we are allowed to look into some of the non-critical features of the correlation in the lower-temperature correlated regime of the system. For example, as seen in Fig. 7.9 and Fig. 7.11, the rod scattering evolves as a function of temperature only slightly from $T = 1.4$ to $T = 0.8$, with its intensity slightly increasing.

7.3.2 Spin-flip and non-spin-flip channels of the neutron scattering

The polarized neutron spin-flip and non-spin-flip [5] scatterings can be separately calculated.

We plot in Fig. 7.12 the spin-flip channel for the neutron scattering at $T = 1.4$ K. Also as a check for the convergence, we plot the intensities along various line cuts as shown in Fig. 7.13 From Fig. 7.12 we see that the rod feature from $(0, 0, 0)$ to $(2, 2, 2)$ is twisted in the SF channel. Also the rod feature from $(0, 0, 4)$ to $(2, 2, 2)$ is gone all together.

Next we turn to the non-spin-flip channel for the neutron scattering at $T = 1.4$ K, plotted in Fig. 7.14. Its linecuts are plotted in Fig. 7.15. It turns out that the NSF channel is also highly structured. Comparing the scattering with the SF channel, it can be seen that the rod feature from $(0, 0, 4)$ to $(2, 2, 2)$ in the total neutron scattering is contributed entirely from the NSF channel.

7.4 Conclusion

In this chapter we reported calculations of the polarized neutron scattering through the numerical linked cluster expansion for quantum spin ice $Yb_2Ti_2O_7$. Down to at least 0.8 K, the NLC convergence is good except for $\mathbf{q}$ points near the intensity Bragg peaks.

The rod scattering in $Yb_2Ti_2O_7$ [43, 92], the most salient feature in the neutron experiment for the material, can be reproduced in our NLC calculation, thus showing the robustness of the method.

Future progress in the quantum spin ice research could benefit from the NLC method discussed in this chapter.

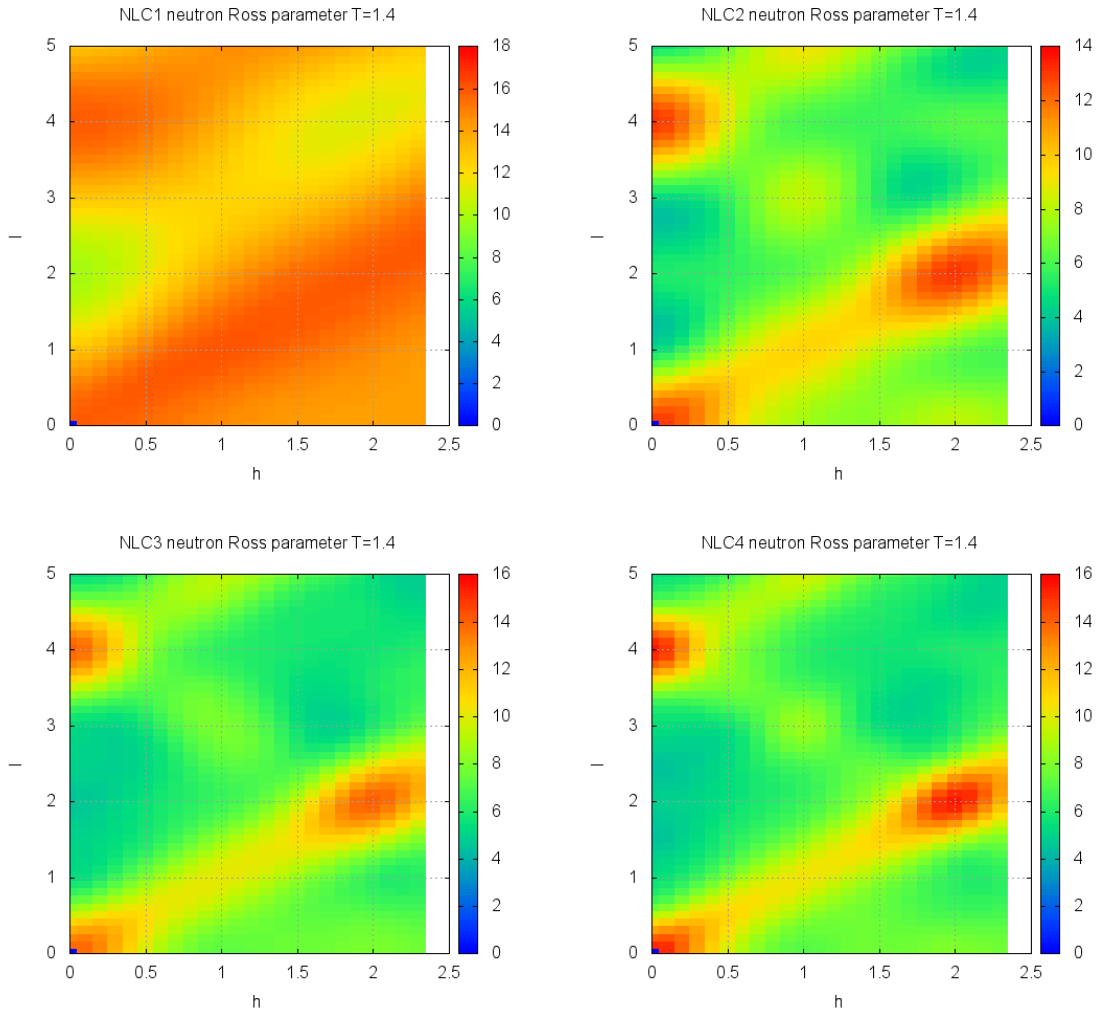

Figure 7.8: Neutron scattering in the (h, h, l) map for Hamiltonian (7.1) at $T = 1.4$ K in zero field. Top left, NLC 1st order; top right: 2nd order bottom left: 3rd order; bottom right: 4th order.

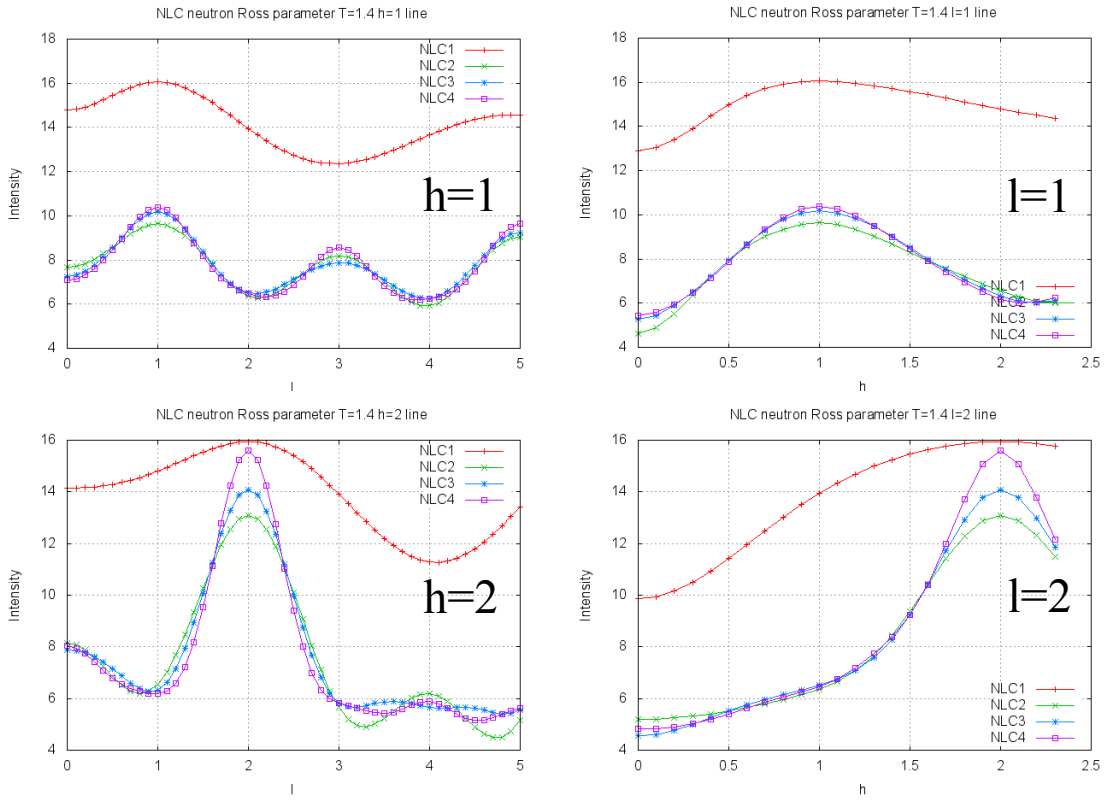

Figure 7.9: Line cuts in the neutron scattering in the (h, h, l) map for Hamiltonian (7.1) at $T = 1.4$ K in zero field, for up to 4th order of NLC. Top left: Intensities along the line $h = 1$; top right : intensities along the line $l = 1$; bottom left: intensities along the line $h = 2$; bottom right: intensities along the line $l = 2$.

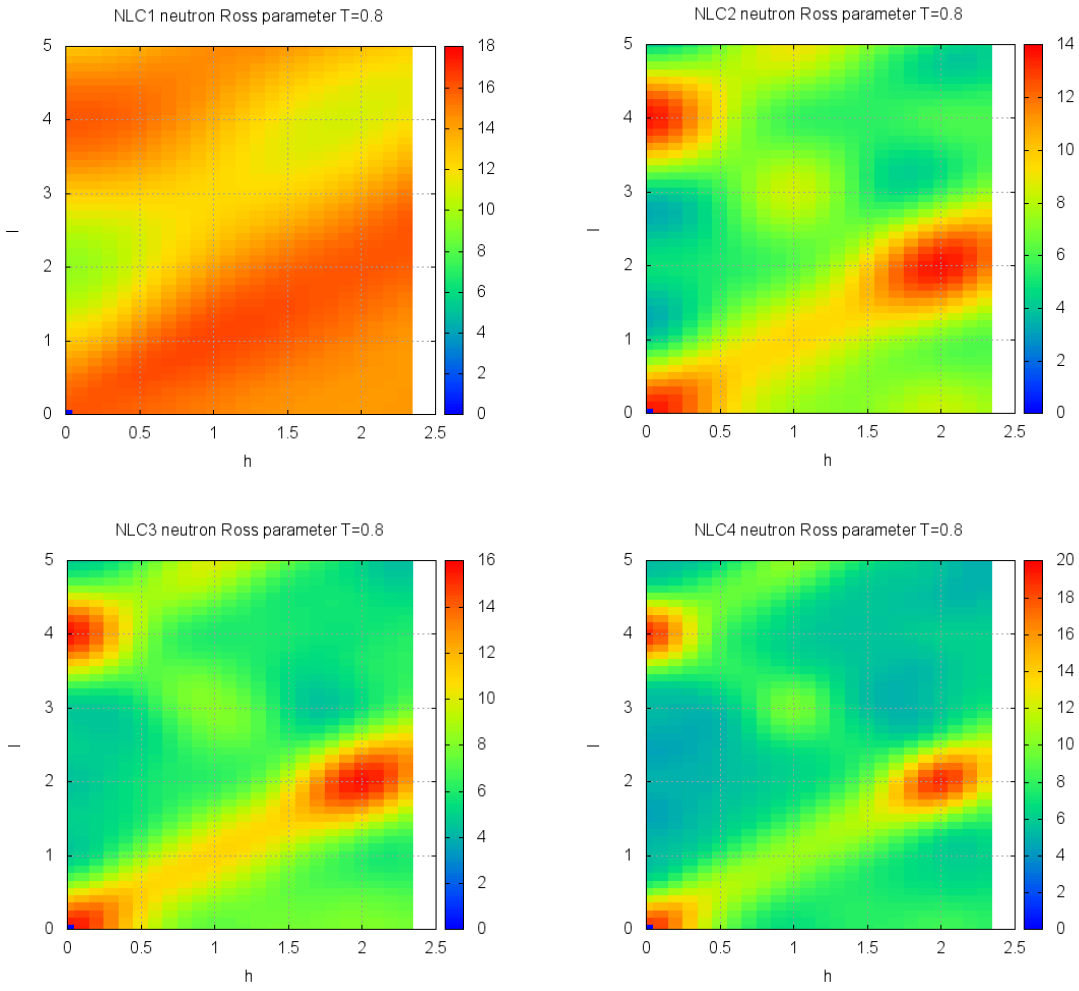

Figure 7.10: Neutron scattering in the (h, h, l) map for Hamiltonian (7.1) at $T = 0.8$ K in zero field. Top left, NLC 1st order; top right: 2nd order bottom left: 3rd order; bottom right: 4th order.

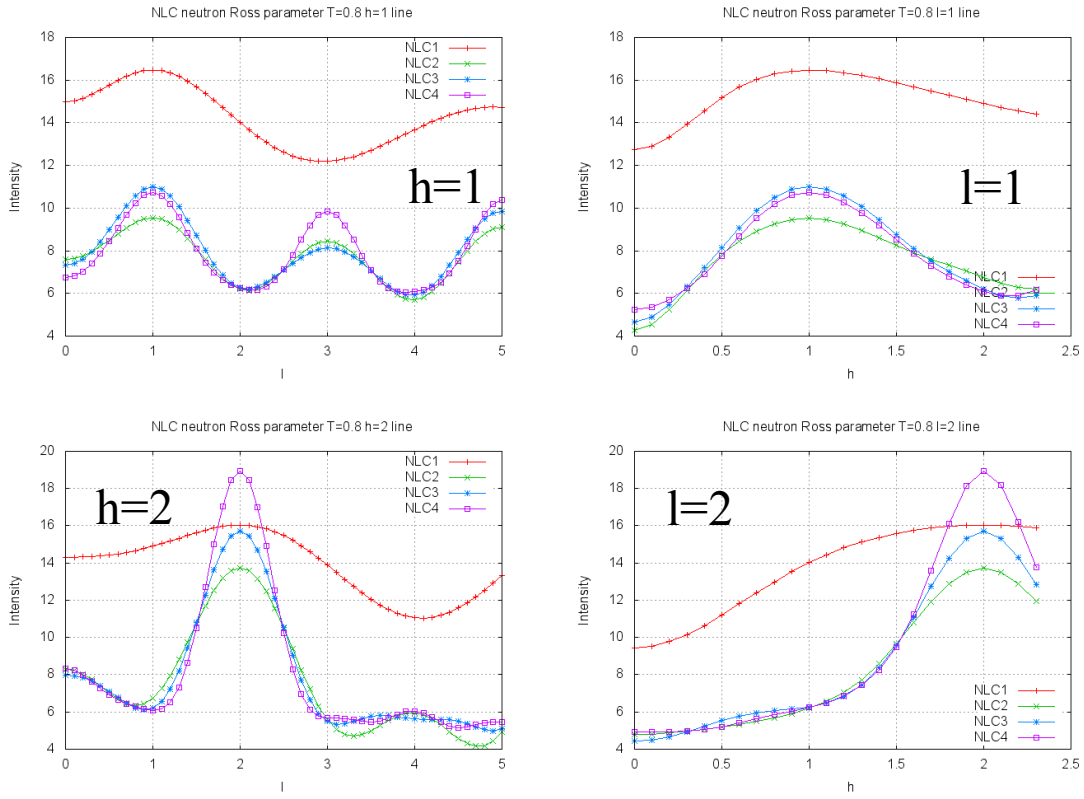

Figure 7.11: Line cuts in the neutron scattering in the (h, h, l) map for Hamiltonian (7.1) at $T = 0.8$ K in zero field, for up to 4th order of NLC. Top left: Intensities along the line $h = 1$; top right : intensities along the line $l = 1$; bottom left: intensities along the line $h = 2$; bottom right: intensities along the line $l = 2$.

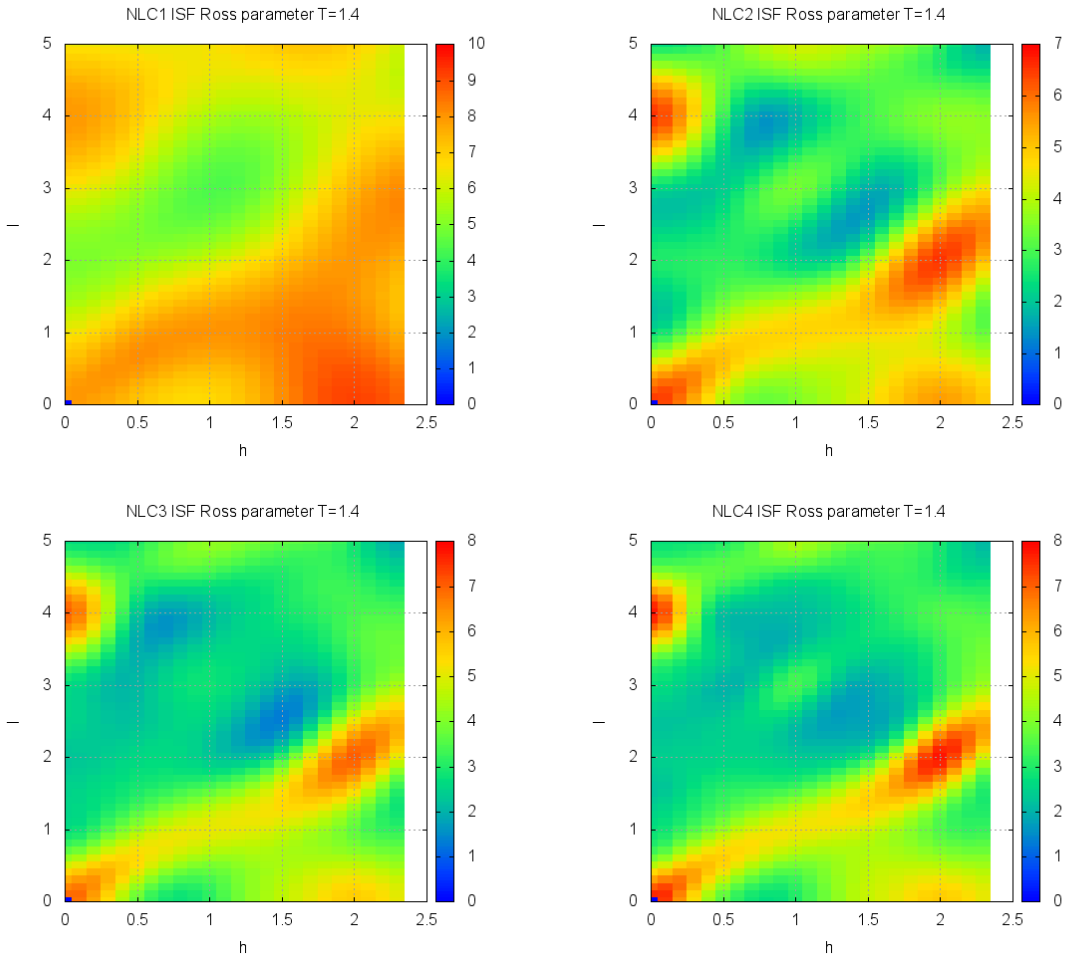

Figure 7.12: Spin-flip channel of the neutron scattering in the (h, h, l) map for Hamiltonian (7.1) at $T = 1.4$ K in zero field. Top left, NLC 1st order; top right: 2nd order bottom left: 3rd order; bottom right: 4th order.

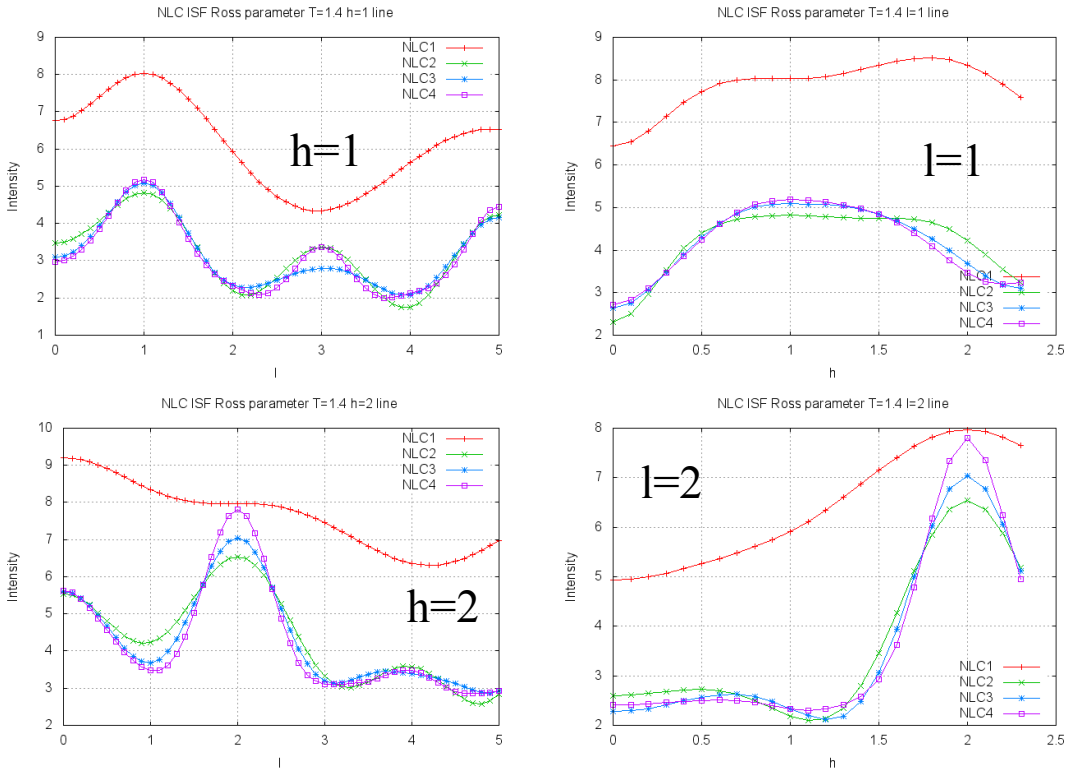

Figure 7.13: Line cuts in the spin-flip channel of the neutron scattering in the (h, h, l) map for Hamiltonian (7.1) at $T = 1.4$ K in zero field, for up to 4th order of NLC. Top left: Intensities along the line $h = 1$; top right : intensities along the line $l = 1$; bottom left: intensities along the line $h = 2$; bottom right: intensities along the line $l = 2$.

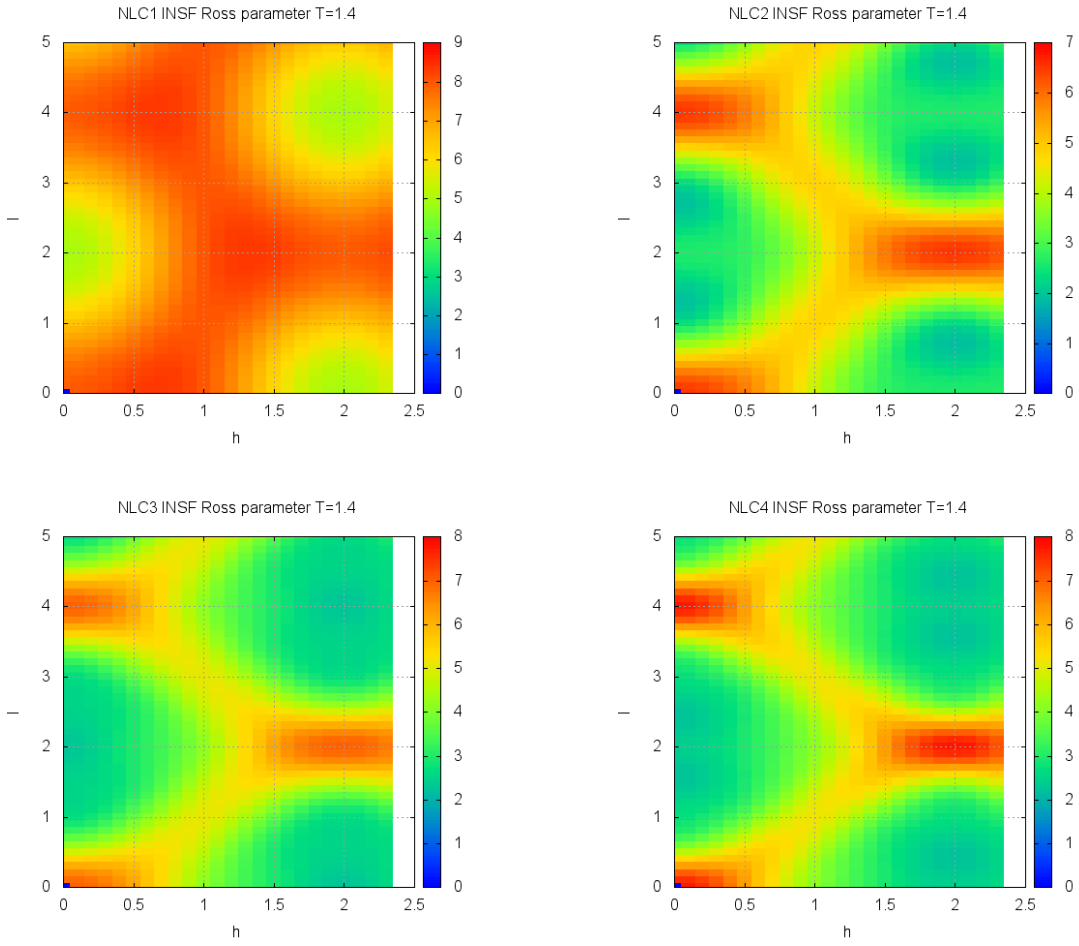

Figure 7.14: Non-spin-flip channel of the neutron scattering in the (h, h, l) map for Hamiltonian (7.1) at $T = 1.4$ K in zero field. Top left, NLC 1st order; top right: 2nd order bottom left: 3rd order; bottom right: 4th order.

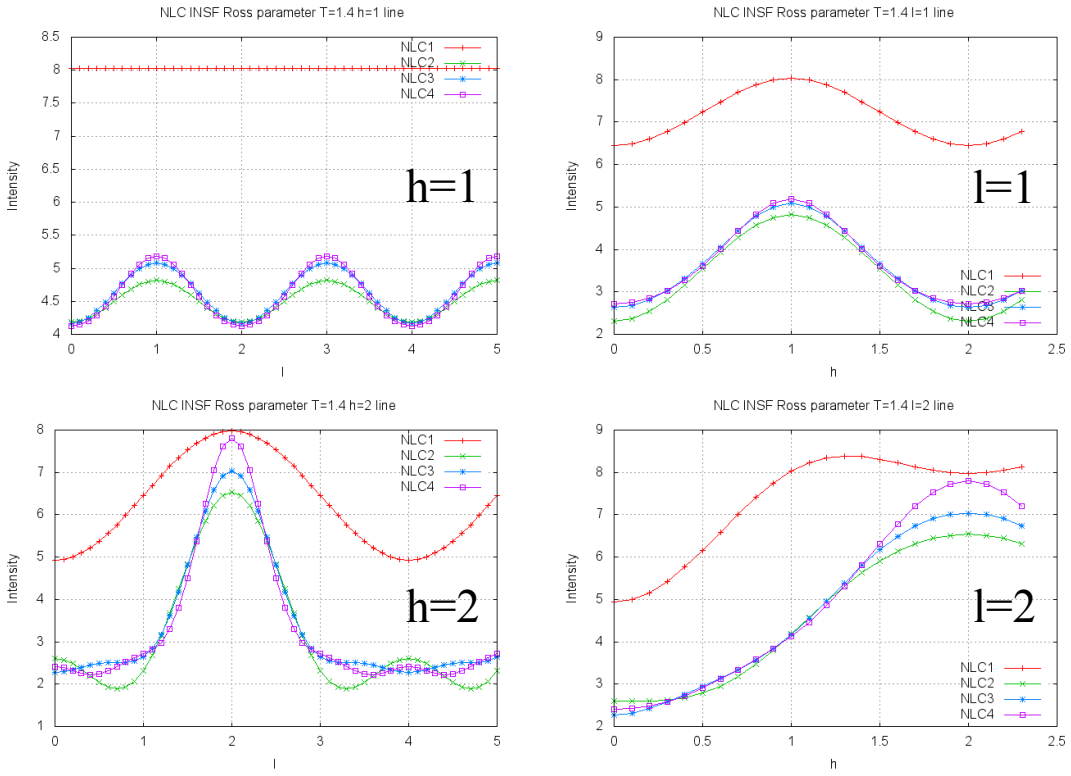

Figure 7.15: Line cuts in the non-spin-flip channel of the neutron scattering in the (h, h, l) map for Hamiltonian (7.1) at $T = 1.4$ K in zero field, for up to 4th order of NLC. Top left: Intensities along the line $h = 1$; top right : intensities along the line $l = 1$; bottom left: intensities along the line $h = 2$; bottom right: intensities along the line $l = 2$.

Chapter 8

Conclusion and Future Works

In this thesis we studied a range of properties of spin ices when subject to different types of perturbations to the system. These include random site dilution, finite-size surface effects, weak exchange interactions, and quantum dynamics. The topic of pinch points in neutron scattering in dipolar spin ice was also briefly discussed. All these problems are motivated by recent experiments in the field of study.

In Chapter 3, we studied the dilution problem in spin ice. For $Dy_{2-x}Y_xTi_2O_7$ and $Ho_{2-x}Y_xTi_2O_7$, we found that the Monte Carlo simulations of the site-diluted dipolar spin ice models have a close match to the experiments in the temperature range of 0.5 K $\lesssim T \lesssim$ 5 K and with up to $x = 1.7$ levels of dilution. The good agreement between simulations and experiments validated the dipolar spin ice models for the two compounds. On top of the close match between simulations and experiments over a large temperature range, the simulation results were void of the high temperature phonon noises and were better equilibrated at low temperatures. This enables for a more accurate determination of the residual entropy. Non-monotonicity of the residual entropy, as well as the rare-earth ion dependence of the residual entropy [2], were confirmed in the simulations. The rare-earth ion dependence was determined to originate from the material-specific spin-spin interactions, particularly the relative strength of the dipolar interaction with respect to the nearest neighbour exchange coupling. The importance of specifying the base temperature, T_0, in the determination of the residual entropy was also emphasized in the chapter.

Having established the model Hamiltonians for the diluted compounds $Dy_{2-x}Y_xTi_2O_7$ and $Ho_{2-x}Y_xTi_2O_7$, in Chapter 3 Section 3.2 we embarked on the study of the physics due

to random dilution on the spin ice Hamiltonian. We started by asking what is the physical meaning of the broad peak of specific heat observed in spin ice. For the minimal model, the nearest-neighbour spin ice model, we found the single tetrahedron approximation to be quite accurate in describing Monte Carlo simulations of specific heat. Through the approximation, we interpret the meaning of the specific heat broad peak in spin ice in terms of the populations of the thermal defects. As an application of the single tetrahedron approximation, we used it in explaining the non-monotonicity seen in the specific heat curves. For the problem of possible long-range order or glass order phase transition induced by the random site dilution [37], we performed a Bethe-Peierls calculation for the site diluted Husimi tree structure, and found that the paramagnetic solution is stable for all finite temperatures and at all dilution levels. The lost of projective equivalence was commented as the site dilution sites permits the appearance of unscreened monopole charges.

A future work following this project would be to investigate the interactions between the unscreened monopole charges. Note that for every spin site diluted in the pyrochlore lattice, two connecting tetrahedra are defected, which permit the appearance of the unscreened monopole charges at their centers. It is most likely that the neighbouring monopole charges form dipoles and it is interesting to ask whether such dipole objects undergo a glass transition as seen in a similar dilute spin system $LiHo_xY_{1-x}F_4$ [64, 73, 74].

In Chapter 4 we study the problem of spin ice in a thin film geometry. Confining ourselves to the film surface normal to the [001] direction, we discovered some interesting surface effects due to the dipolar interaction. For the [001] surface, we identified the orphan bonds objects as the lingering nearest-neighbour bonds on the surface that are no longer part of any tetrahedron. By tuning the strength of the orphan bond, we can achieve several surface conditions through Monte Carlo simulations, with residual entropy well described by analytically derived surface corrections to the Pauling's entropy. With dipolar interaction, we discovered a novel phenomenon of surface freezing at AFM orphan bond strength. The mechanism of surface freezing is due to the self-screening of the dipolar interactions, even in the presence of monopole charges in the system.

Future directions on the "film problem" are very broad. Properties of the film normal to other directions of the surface would be of great interest, and their calculation requires a genuine redesign of the Ewald summation technique for the given geometry. Also, the experimental puzzle of the recovery of the third law of the thermodynamics in film systems is still an open question [75].

In Chapter 5, we re-investigated the microscopic model for the spin ice material $Dy_2Ti_2O_7$. By turning to the [112] field experiment, parametric constraints were extracted for the exchange interactions in microscopic model. Using these constraints we exposed an inconsistency between the neutron scattering measurements by Fennell *et al.* [3], and the specific heat measurements by Pomaranski *et al.* [1].

In Chapter 6, we turned to the pinch point neutron scattering in spin ice. For dipolar spin ice, we showed through Monte Carlo simulations that the pinch points exist at high temperatures where local ice-rule constraints no longer apply. For nearest-neighbour spin ice, we extracted the correlation lengths from the thermal broadenings of pinch points and compared its temperature dependence on the Debye-Huckel theory.

In Chapter 7, we demonstrated the numerical linked cluster method as an effective tool in studying of the quantum spin ice. In particular, in this work we examined its capability in the calculations of the neutron scattering.

We hope the work presented in this thesis will be able to stimulate further experimental surveys into the spin ice systems. Two particular directions appear particularly promising. Experimentally, as we exposed in Chapter 5, regarding the inconsistencies with existing experiments, new neutron measurements on $Dy_2Ti_2O_7$ at low temperatures should be very interesting. For the thin film spin ice problem, it would be most interesting to detect in an experimental system the phenomena of surface freezing that we exposed in our theoretical model in Chapter 4.

APPENDICES

Appendix A

Pauling's entropy through the strings in spin ice

One of the fundamental problems in frustrated magnets is to label and navigate the highly degenerate states within the constrained manifold [32]. For spin ice, the phase space of interest is the macroscopically degenerate states with the ice rules fulfilled for every tetrahedron. Therefore, one may ask if there is an alternative way enumerate all the ice-rule fulfilling states, making possible to further categorize these states. One such idea was introduced in the work of by Jaubert *et al.* [49], where string objects are introduced to categorize ice-rule states into different topological sectors. In this subsection we summarize the definition of such string objects and further explore the usefulness of such a concept. By introducing further constraints on the strings, we can achieve in this work a one-to-one mapping between the string configurations and the ice-rule spin configurations. Residual entropy through approximation similar to Pauling's can also be derived through the string objects.

String objects in spin ice

Let us consider a cubic sample of spin ice of dimension L by L by L, which consists of a stacking of the conventional cubic unit cells. As defined in Jaubert *et al.* [49], a string is an oriented path starting from one end of the boundary (x, y, or $z = 0$) and ending at the other end of the boundary (x, y, or $z = L$). The string lies on the diamond lattice bonds

and goes *monotonically* in the x, y, or z direction, in such a way that spins along the path of the string all point in the same direction.

With this definition, it is argued in Jaubert *et al.* [49] that it is always possible to find a string in the ice-rule manifold. This is because the direction of the string propagation is defined along the cubic axis and, as seen in Fig. A.1, of the two neighbouring spins in the possible propagation direction of the string, at least one of them points in the "right" direction to form a string, due to the two-in-two-out spin configurations for each tetrahedron. In other words for any spin in the lattice, it is alway possible to grow the string in the two opposite cubic directions. Therefore, we can always have a boundary-to-boundary string. One subtle point here is if we are dealing with string propagating in a particular direction, say along z, then for the other two directions, x and y, periodic boundary condition is applied, meaning the string may go outside the side of the cubic sample and immediately rejoin it in the opposite position corresponding to the same z value.

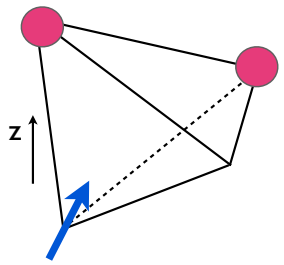

Figure A.1: A spin (blue arrow) along the direction of the string in the z direction and its two neighbours (red circles) the string may propagate.

The total number of spins on a string equals to $4L$. This is because for each layer of cubic unit cell the string propagates, it travels through 4 spin, a fact derived from the construction of the conventional cubic unit cells.

The total number of distinct strings (they may overlap) of a particular propagation direction equals to $4L^2$. This is because there are $4L^2$ spins on the boundary and as we have proven for every such spin it is possible to grow a string out of it.

In fact the total number of strings, N_s, in the system may become larger than $4L^2$. For example, in Fig. A.2, where the strings enter through spins a and c, and leave through ei-

ther or both spins b and d. Thus there can be four different string configurations associated with the spin configuration shown.

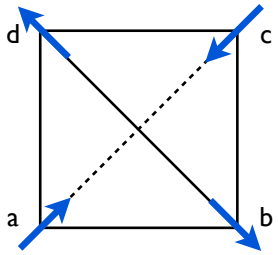

Figure A.2: A string enters through spins a and c and leaves through either or both of spins b and d.

One-to-one mapping between the spins and the strings

To find the one-to-one mapping between the spin configuration and the string configuration, we first ask whether given any ice-rule spin configuration, $4L^2$ strings can always be drawn to visit all the spins, *i.e.*, is there always (at least) a string configuration corresponding to any ice-rule spin configuration.

To see this, we plot in the Fig A.3 the pyrochlore lattice viewed along the z direction, and consider the strings growing from the bottom ($z = 0$) going up in the z direction.

At the boundary all the $z = 0$ spins (blue solid) are visited.

Then, as the strings climb up one step in the z direction we investigate whether all $z = 0.25$ spins (blue open) can be visited. The $z = 0.25$ spins are connected to the $z = 0$ spins through tetrahedra marked in yellow. There are only three different possible configurations the entry ($z = 0$) spins can take, *i.e.*, two-in, two-out, or one-in-one-out. By inspection, we see for the three cases we can always visit both the two exit ($z = 0.25$) spins when drawing the strings. (For the two-in or two-out cases, there is more than one way of choosing.) Therefore all the $z = 0.25$ spins can be visited.

Next we consider the $z = 0.50$ spins as the strings climb up one further step. The $z = 0.50$ spins are connected to the $z = 0.25$ spins through the green tetrahedra. Following the same argument as for the yellow tetrahedra, all the $z = 0.50$ spins can be visited.

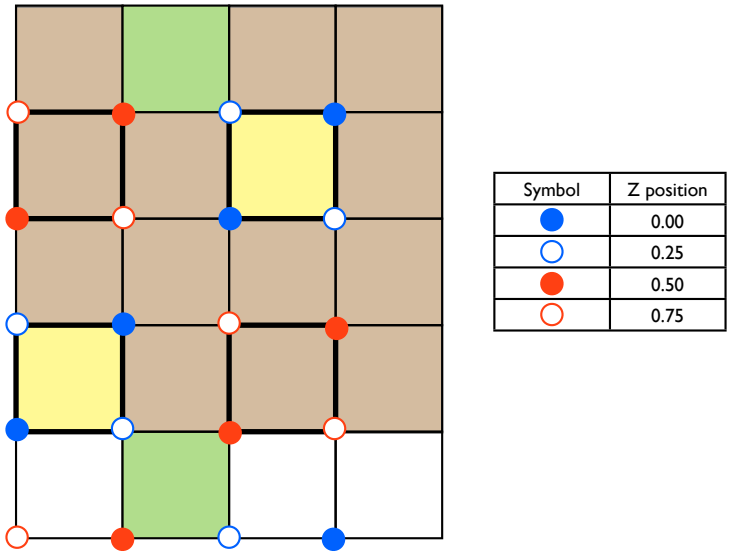

Figure A.3: Pyrochlore lattice viewed along the z direction.

Therefore as we go one step at a time in the z direction, all the spins can be visted.

Clearly there is still ambiguity in arriving at a string configuration from a spin configuration (one to more mapping). The ambiguity comes from the tetrahedra where the two entry spins are both in or out, as shown in Fig. A.4. Both the x and y configurations for the strings are valid and visit every spin once given the spin configuration. The simple way to eliminate such ambiguity is to *always* choose one configuration over the other when such situation arrives. With this additional constraint, we have a unique string configuration corresponding to any given ice-rule spin configuration.

On the other hand, given a string configuration we trivially have a unique spin configuration. Therefore, in this sub-subsection we demonstrate that a one-to-one mapping between the spin and string configuration can be achieved through the introduction of the above additional constraint.

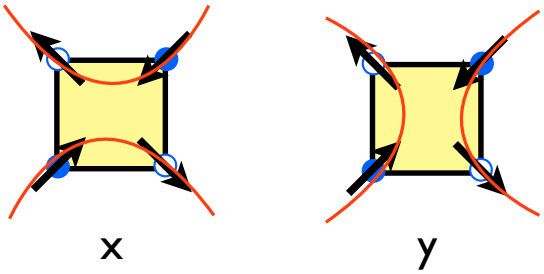

Figure A.4: Two preferences of the string configurations.

Pauling's residual entropy through the counting of the strings

In this sub-subsection, we count the number of string configurations using the x preference discussed in the last sub-section and show that we can recover the Pauling's approximation for the entropy of the ice manifold.

Before counting, let us consider Fig. A.5, which shows how the six ice-rule fulfilling spin configurations can be mapped to the string configurations, if we prefer the x strings. Note that for the y-directed strings we can not have the one-string-up-one-string-down configuration, since it will double count the same spin configuration for the one-string-left-one-string-right configuration in the x-directed strings. So we have four x directed strings and two y-directed strings.

Now we count the number of string configurations, W.

First, let us consider *undirected* strings. For every pair of undirected strings coming into a tetrahedron, there are two ways of them choosing the exits. Since there are $8L^3$ tetrahedra in the system, we have

$$W = (2)^{8L^3} \tag{A.1}$$

Then, for each undirected string, there are two ways of choosing the direction of the string. As the number of strings in the system is $N = 4L^2$, the total number of configurations becomes

$$W = (2)^{8L^3}(2)^{4L^2} \tag{A.2}$$

However, of the eight possible string configurations, only six of them are acceptable as in Fig. A.5. Similar to the original Pauling's approximation, we assume the probability of

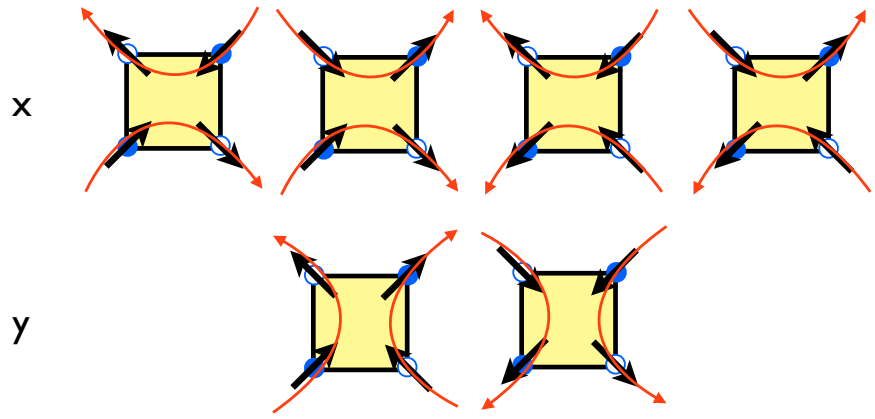

Figure A.5: Strings corresponding to the spin configurations using the x preference.

getting the right string configuration is six out of eight. Therefore the final total number becomes

$$W = (2)^{8L^3}(2)^{4L^2}(6/8)^{8L^3} \tag{A.3}$$

which gives the entropy per spin

$$S/k_B = (1/2)\ln(3/2) + (1/4L)\ln(2) \tag{A.4}$$

And as L approaches thermodynamic limit, we recover the Pauling's residual entropy by dropping the second term.

This counting gives us a further insight into the Pauling's residual entropy, *i.e.* it is the configurational redistribution of the strings that contributes to the residual entropy in the thermodynamic limit and the orientations of the strings are insignificant. Or, in terms of the spin variables, it is how the spins are linked and form paths of strings in the system that matters but not the orientation of each path.

Appendix B

Magnetic Form Factors

The calculation for the magnetic form factors is adopted from Ref. [93].

The magnetic form factor is written as

$$f(s) = \langle j_0(s) \rangle + (1 - 2/g)\langle j_2(s) \rangle \tag{B.1}$$

where s is the value of $\sin(\theta)/\lambda$ in Å^{-1}, and it relates to the scattering vector $\mathbf{q}$ as

$$|\mathbf{q}| = 4\pi \sin(\theta)/\lambda = 4\pi s \tag{B.2}$$

g is the Lande factor. For Dy^{3+}, $g = 4/3$.

$\langle j_0(s) \rangle$ is given by

$$\langle j_0(s) \rangle = A_0 \exp(-a_0 s^2) + B_0 \exp(-b_0 s^2) + C_0 \exp(-c_0 s^2) + D_0 \tag{B.3}$$

For Dy^{3+}, we have $A_0 = 0.1157,\ a_0 = 15.073,\ B_0 = 0.3270,\ b_0 = 6.799,\ C_0 = 0.5821,\ c_0 = 3.020,\ D_0 = -0.0249$.

$\langle j_2(s) \rangle$ is given by

$$\langle j_2(s) \rangle = A_2 s^2 \exp(-a_2 s^2) + B_2 s^2 \exp(-b_2 s^2) + C_2 s^2 \exp(-c_2 s^2) + D_2 s^2 \tag{B.4}$$

For Dy^{3+}, we have $A_2 = 0.2523,\ a_2 = 18.517,\ B_2 = 1.0914,\ b_2 = 6.736,\ C_2 = 0.9345,\ c_2 = 2.208,\ D_2 = 0.0250$.

Appendix C

Quantum spin ice model

As defined in Chapter 7, the spin-1/2 model Hamiltonian reads [6]:

$$H_{\mathrm{QSI}} = \sum_{\langle i,j \rangle} \{ J_{zz} S_i^z S_j^z - J_{\pm}(S_i^+ S_j^- + S_i^- S_j^+) + J_{\pm\pm}[\gamma_{ij} S_i^+ S_j^+ + \gamma_{ij}^* S_i^- S_j^+] + J_{z\pm}[S_i^z(\zeta_{ij} S_j^+ + \zeta_{ij}^* S_j^- + i \leftrightarrow j]\} - \sum_i \vec{h} \cdot \mathbf{g} \cdot \vec{S}_i, \tag{C.1}$$

where S_i^z, S_j^z are for the local spin coordinates, and the summation is over all nearest neighbours.

For the four sublattices of the pyrochlore lattice, we have the $(\hat{\boldsymbol{a}}_i, \hat{\boldsymbol{b}}_i, \hat{\boldsymbol{e}}_i)$ basis.

$$\begin{aligned}
\hat{\boldsymbol{e}}_0 &= \frac{1}{\sqrt{3}}(1,1,1), & \hat{\boldsymbol{a}}_0 &= \frac{1}{\sqrt{6}}(-2,1,1), \\
\hat{\boldsymbol{e}}_1 &= \frac{1}{\sqrt{3}}(1,-1,-1), & \hat{\boldsymbol{a}}_1 &= \frac{1}{\sqrt{6}}(-2,-1,-1), \\
\hat{\boldsymbol{e}}_2 &= \frac{1}{\sqrt{3}}(-1,1,-1), & \hat{\boldsymbol{a}}_2 &= \frac{1}{\sqrt{6}}(2,1,-1), \\
\hat{\boldsymbol{e}}_3 &= \frac{1}{\sqrt{3}}(-1,-1,1), & \hat{\boldsymbol{a}}_3 &= \frac{1}{\sqrt{6}}(2,-1,1),
\end{aligned}$$

where $\hat{\boldsymbol{e}}$ is along the local $\langle 111 \rangle$ direction of the rare-earth ions and $\hat{\boldsymbol{b}}_i = \hat{\boldsymbol{e}}_i \times \hat{\boldsymbol{a}}_i$.

The ζ and γ are the 4×4 complex unimodular matrix given by

$$\zeta = \begin{pmatrix} 0 & -1 & e^{i\pi/3} & e^{-i\pi/3} \\ -1 & 0 & e^{-i\pi/3} & e^{i\pi/3} \\ e^{i\pi/3} & e^{-i\pi/3} & 0 & -1 \\ e^{-i\pi/3} & e^{i\pi/3} & -1 & 0 \end{pmatrix}, \qquad \gamma = -\zeta^*,$$

References

[1] D. Pomaranski, L. R. Yaraskavitch, S. Meng, K. A. Ross, H. M. L. Noad, H. A. Dabkowska, B. D. Gaulin, and J. B. Kycia. Absence of Pauling's residual entropy in thermally equilibrated $Dy_2Ti_2O_7$. *Nat Phys*, 9(6):353–356, April 2013.

[2] X. Ke, R. S. Freitas, B. G. Ueland, G. C. Lau, M. L. Dahlberg, R. J. Cava, R. Moessner, and P. Schiffer. Nonmonotonic Zero-Point Entropy in Diluted Spin Ice. *Physical Review Letters*, 99:137203, September 2007.

[3] T. Fennell, O. A. Petrenko, B. Fåk, S. T. Bramwell, M. Enjalran, T. Yavors'kii, M. J. P. Gingras, R. G. Melko, and G. Balakrishnan. Neutron scattering investigation of the spin ice state in $Dy_2Ti_2O_7$. *Physical Review B*, 70:134408, October 2004.

[4] L. Pauling. The structure and entropy of ice and of other crystals with some randomness of atomic arrangement. *Journal of the American Chemical Society*, 57:2680–2684, 1935.

[5] T. Fennell, P. P. Deen, A. R. Wildes, K. Schmalzl, D. Prabhakaran, A. T. Boothroyd, R. J. Aldus, D. F. McMorrow, and S. T. Bramwell. Magnetic Coulomb Phase in the Spin Ice $Ho_2Ti_2O_7$ — Supporting Online Material. *Science*, 326(5951):415–417, October 2009.

[6] K. A. Ross, L. Savary, B. D. Gaulin, and L. Balents. Quantum Excitations in Quantum Spin Ice. *Phys. Rev. X*, 1:021002, October 2011.

[7] H. Sato, K. Matsuhira, T. Tayama, Z. Hiroi, S. Takagi, and T. Sakakibara. Ferromagnetic ordering on the triangular lattice in the pyrochlore spin-ice compound $Dy_2Ti_2O_7$. *Journal of Physics: Condensed Matter*, 18(22):L297, 2006.

[8] J. S. Gardner, M. J. P. Gingras, and J. E. Greedan. Magnetic pyrochlore oxides. *Rev. Mod. Phys.*, 82(1):53–107, January 2010.

[9] A. P. Ramirez. Strongly geometrically frustrated magnets. *Annual Review of Materials Science*, 24(1):453–480, 1994.

[10] K. W. H. Stevens. Matrix elements and operator equivalents connected with the magnetic properties of rare earth ions. *Proceedings of the Physical Society. Section A*, 65(3):209, 1952.

[11] J. E. Greedan. *Magnetic Properties of Nonmetallic Compounds Based on Transition Elements*. Springer Verlag, 1992.

[12] Y. M. Jana, A. Sengupta, and D. Ghosh. Estimation of single ion anisotropy in pyrochlore $Dy_2Ti_2O_7$, a geometrically frustrated system, using crystal field theory. *Journal of Magnetism and Magnetic Materials*, 248(1):7–18, July 2002.

[13] S. Rosenkranz, A. P. Ramirez, A. Hayashi, R. J. Cava, R. Siddharthan, and B. S. Shastry. Crystal-field interaction in the pyrochlore magnet $Ho_2Ti_2O_7$. *Journal of Applied Physics*, 87(9):5914–5916, 2000.

[14] M. J. Harris, S. T. Bramwell, P. C. W. Holdsworth, and J. D. M. Champion. Liquid-gas critical behavior in a frustrated pyrochlore ferromagnet. *Physical Review Letters*, 81(20):4496–4499, 1998.

[15] S. T. Bramwell and M. J. P. Gingras. Spin Ice State in Frustrated Magnetic Pyrochlore Materials. *Science*, 294(5546):1495–1501, November 2001.

[16] X. Ke, B. Ueland, D. V. West, M. L. Dahlberg, R. J. Cava, and P. Schiffer. Spin-ice behavior in $Dy_2Sn_{2x}Sb_xO_{7+x2}$ and Dy_2NbScO_7. *Physical Review B*, 76(21):214413, December 2007.

[17] H. Kadowaki, Y. Ishii, K. Matsuhira, and Y. Hinatsu. Neutron scattering study of dipolar spin ice $Ho_2Sn_2O_7$:Frustrated pyrochlore magnet. *Physical Review B*, 65(14):144421, March 2002.

[18] H. D. Zhou, S. T. Bramwell, J. G. Cheng, C. R. Wiebe, G. Li, L. Balicas, J. A. Bloxsom, H. J. Silverstein, J. S. Zhou, and J. S. Goodenough, J. B .and Gardner.

High pressure route to generate magnetic monopole dimers in spin ice. *Nat Commun*, 2, September 2011.

[19] H. D. Zhou, J. G. Cheng, A. M. Hallas, C. R. Wiebe, G. Li, L. Balicas, J. S. Zhou, J. B. Goodenough, J. S. Gardner, and E. S. Choi. Chemical Pressure Effects on Pyrochlore Spin Ice. *Physical Review Letters*, 108:207206, May 2012.

[20] X. Ke, M. L. Dahlberg, E. Morosan, J. A. Fleitman, R. J. Cava, and P. Schiffer. Magnetothermodynamics of the Ising antiferromagnet $Dy_2Ge_2O_7$. *Physical Review B*, 78:104411, September 2008.

[21] E. Morosan, J. A. Fleitman, Q. Huang, J. W. Lynn, Y. Chen, X. Ke, M. L. Dahlberg, P. Schiffer, C. R. Craley, and R. J. Cava. Structure and magnetic properties of the $Ho_2Ge_2O_7$ pyrogermanate. *Physical Review B*, 77:224423, June 2008.

[22] M. J. Harris, S. T. Bramwell, D. F. McMorrow, T. Zeiske, and K. W. Godfrey. Geometrical Frustration in the Ferromagnetic Pyrochlore $Ho_2Ti_2O_7$. *Physical Review Letters*, 79:2554–2557, September 1997.

[23] B. C. den Hertog and M. J. P. Gingras. Dipolar Interactions and Origin of Spin Ice in Ising Pyrochlore Magnets. *Physical Review Letters*, 84:3430–3433, April 2000.

[24] T. Yavors'kii, T. Fennell, M. J. P. Gingras, and S. T. Bramwell. $Dy_2Ti_2O_7$ Spin Ice: A Test Case for Emergent Clusters in a Frustrated Magnet. *Physical Review Letters*, 101:037204, July 2008.

[25] S. T. Bramwell, M. J. Harris, B. C. den Hertog, M. J. P. Gingras, J. S. Gardner, D. F. McMorrow, A. R. Wildes, A. L. Cornelius, J. D. M. Champion, R. G. Melko, and T. Fennell. Spin correlations in $Ho_2Ti_2O_7$: A dipolar spin ice system. *Physical Review Letters*, 87(4), 2001.

[26] Y. Tabata, H. Kadowaki, K. Matsuhira, Z. Hiroi, N. Aso, E. Ressouche, and B. Fåk. Kagome Ice State in the Dipolar Spin Ice $Dy_2Ti_2O_7$. *Physical Review Letters*, 97:257205, December 2006.

[27] S. V. Isakov, R. Moessner, and S. L. Sondhi. Why Spin Ice Obeys the Ice Rules. *Physical Review Letters*, 95:217201, November 2005.

[28] M. J. P. Gingras and B. C. den Hertog. Origin of spin-ice behavior in Ising pyrochlore magnets with long-range dipole interactions: an insight from mean-field theory. *Canadian Journal of Physics*, 79(11-12):1339–1351, 2001.

[29] C. Castelnovo, R. Moessner, and S. L. Sondhi. Magnetic monopoles in spin ice. *Nature*, 451(7174):42–45, 2008.

[30] G.-W. Chern, P. Mellado, and O. Tchernyshyov. Two-Stage Ordering of Spins in Dipolar Spin Ice on the Kagome Lattice. *Physical Review Letters*, 106(20), 2011.

[31] C. L. Henley. Power-law spin correlations in pyrochlore antiferromagnets. *Physical Review B*, 71:014424, January 2005.

[32] C. L. Henley. The "Coulomb Phase" in Frustrated Systems. *Annual Review of Condensed Matter Physics, Vol 1*, 1:179–210, 2010.

[33] L. D. C. Jaubert and P. C. W. Holdsworth. Signature of magnetic monopole and Dirac string dynamics in spin ice. *Nat Phys*, 5(4):258–261, April 2009.

[34] D. J. P. Morris, D. A. Tennant, S. A. Grigera, B. Klemke, C. Castelnovo, R. Moessner, C. Czternasty, M. Meissner, K. C. Rule, J. U. Hoffmann, K. Kiefer, S. Gerischer, D. Slobinsky, and R. S. Perry. Dirac Strings and Magnetic Monopoles in the Spin Ice $Dy_2Ti_2O_7$. *Science*, 326(5951):411–414, October 2009.

[35] H. Kadowaki, N. Doi, Y. Aoki, Y. Tabata, T. J. Sato, J. W. Lynn, K. Matsuhira, and Z. Hiroi. Observation of Magnetic Monopoles in Spin Ice. *Journal of the Physical Society of Japan*, cond-mat.dis-nn(10):103706, October 2009.

[36] L. Balents. Spin liquids in frustrated magnets. *Nature*, 464(7286):199–208, March 2010.

[37] J. Villain. Insulating Spin-Glasses. *Zeitschrift Fur Physik B-Condensed Matter*, 33(1):31–42, 1979.

[38] M. Hermele, M. P. A. Fisher, and L. Balents. Pyrochlore photons: The $U(1)$ spin liquid in a S=1/2 three-dimensional frustrated magnet. *Physical Review B*, 69:064404, February 2004.

[39] A. Castro Neto, P. Pujol, and E. Fradkin. Ice: A strongly correlated proton system. *Physical Review B*, 74(2):024302, July 2006.

[40] S. Lee, S. Onoda, and L. Balents. Generic quantum spin ice. *Physical Review B*, 86:104412, September 2012.

[41] S. Onoda and Y. Tanaka. Quantum fluctuations in the effective pseudospin-1/2 model for magnetic pyrochlore oxides. *Physical Review B*, 83(9):094411, March 2011.

[42] A. Yaouanc, P. Dalmas de R 'eotier, C. Marin, and V. Glazkov. Single-crystal versus polycrystalline samples of magnetically frustrated $Yb_2Ti_2O_7$: Specific heat results. *Physical Review B*, 84:172408, November 2011.

[43] K. A. Ross, L. R. Yaraskavitch, M. Laver, J. S. Gardner, J. A. Quilliam, S. Meng, J. B. Kycia, D. K. Singh, Th. Proffen, H. A. Dabkowska, and B. D. Gaulin. Dimensional evolution of spin correlations in the magnetic pyrochlore $Yb_2Ti_2O_7$. *Physical Review B*, 84(17):174442, November 2011.

[44] R. Applegate, N. R. Hayre, R. R. P. Singh, T. Lin, A. G. R. Day, and M. J. P. Gingras. Vindication of $Yb_2Ti_2O_7$ as a Model Exchange Quantum Spin Ice. *Physical Review Letters*, 109:097205, August 2012.

[45] N. R. Hayre, K. A. Ross, R. Applegate, T. Lin, R. R. P. Singh, B. D. Gaulin, and M. J. P. Gingras. Thermodynamic properties of $Yb_2Ti_2O_7$ pyrochlore as a function of temperature and magnetic field: Validation of a quantum spin ice exchange Hamiltonian. *Physical Review B*, 87(18):184423, May 2013.

[46] K. Binder and D. W. Heermann. *Monte Carlo simulation in statistical physics: an introduction*. Springer, 2010.

[47] M. E. J. Newman and G. T. Barkema. *Monte Carlo Methods in Statistical Physics*. Oxford, 1999.

[48] R. G. Melko, B. den Hertog, and M. J. P. Gingras. Long-Range Order at Low Temperatures in Dipolar Spin Ice. *Physical Review Letters*, 87(6):067203, July 2001.

[49] L. D. C. Jaubert, M. J. Harris, T. Fennell, R. G. Melko, S. T. Bramwell, and P. C. W. Holdsworth. Topological-sector fluctuations and Curie-law crossover in spin ice. *Physical Review X*, 3(1):011014, 2013.

[50] N. Shannon, O. Sikora, F. Pollmann, K. Penc, and P. Fulde. Quantum Ice: A Quantum Monte Carlo Study. *Physical Review Letters*, 108:067204, February 2012.

[51] R. J. Baxter. *Exactly Solved Models in Statistical Mechanics*. Academic Press, 1982.

[52] M. Rigol, T. Bryant, and R. R. P. Singh. Numerical linked-cluster algorithms. I. Spin systems on square, triangular, and kagome lattices. *Physical Review E*, 75(6), June 2007.

[53] M. Rigol, T. Bryant, and R. R. P. Singh. Numerical linked-cluster algorithms. II. t-J models on the square lattice. *Physical Review E*, 75(6), June 2007.

[54] M. Rigol, T. Bryant, and R. R. P. Singh. Numerical linked-cluster approach to quantum lattice models. *Physical Review Letters*, 97(18), 2006.

[55] J. Oitmaa, C. Hamer, and W. Zheng. *Series Expansion Methods for Strongly Interacting Lattice Models*. Cambridge University Press, April 2006.

[56] Y. Tajima, T. Matsuo, and H. Suga. Phase transition in KOH-doped hexagonal ice. *Nature*, 299(5886):810–812, October 1982.

[57] S. J. Singer. Hydrogen-Bond Topology and Proton Ordering in Ice and Water Clusters. In *Advances in Chemical Physics, Volume 147*. John Wiley & Sons, Inc, 2011.

[58] L. J. Chang, Y. Su, Y.-J. Kao, Y. Z. Chou, R. Mittal, H. Schneider, Th. Brueckel, G. Balakrishan, and M. R. Lees. Magnetic correlations in the spin ice $Ho_{2-x}Y_xTi_2O_7$ as revealed by neutron polarization analysis. *Physical Review B*, 82(17), 2010.

[59] A. P. Ramirez, A. Hayashi, R. J. Cava, R. Siddharthan, and B. S. Shastry. Zero-point entropy in 'spin ice'. *Nature*, 399(6734):333–335, May 1999.

[60] Ruff, J. P. C., R. G. Melko, and M. J. P. Gingras. Finite-Temperature Transitions in Dipolar Spin Ice in a Large Magnetic Field. *Physical Review Letters*, 95:097202, August 2005.

[61] A. Biltmo and P. Henelius. Phase diagram of the dilute magnet $LiHo_xY_{1-x}F_4$. *Physical Review B*, 76:054423, August 2007.

[62] A. Biltmo and P. Henelius. Low-temperature properties of the dilute dipolar magnet $LiHo_xY_{1-x}F_4$. *Physical Review B*, 78:054437, August 2008.

[63] K.-M. Tam, S. Geraedts, S. Inglis, M. J. P. Gingras, and R. G. Melko. Superglass Phase of Interacting Bosons. *Physical Review Letters*, 104:215301, May 2010.

[64] J. A. Quilliam, S. Meng, and J. B. Kycia. Experimental phase diagram and dynamics of a dilute dipolar-coupled Ising system. *Physical Review B*, 85:184415, May 2012.

[65] Z. Wang and C. Holm. Estimate of the cutoff errors in the Ewald summation for dipolar systems. *The Journal of Chemical Physics*, 115(14):6351–6359, 2001.

[66] E. Marinari and G. Parisi. Simulated Tempering - a New Monte-Carlo Scheme. *Europhysics Letters*, 19(6):451–458, 1992.

[67] R. G. Melko and M. J. P. Gingras. Monte Carlo studies of the dipolar spin ice model. *Journal of Physics: Condensed Matter*, 16(43):R1277, 2004.

[68] H. Fukazawa, R. G. Melko, R. Higashinaka, Y. Maeno, and M. J. P. Gingras. Magnetic anisotropy of the spin-ice compound $Dy_2Ti_2O_7$. *Physical Review B*, 65:054410, January 2002.

[69] A. Sen, R. Moessner, and S. L. Sondhi. Coulomb Phase Diagnostics as a Function of Temperature, Interaction Range, and Disorder. *Physical Review Letters*, 110(10):107202, March 2013.

[70] A. Andreanov, J. T. Chalker, T. E. Saunders, and D. Sherrington. Spin-glass transition in geometrically frustrated antiferromagnets with weak disorder. *Physical Review B*, 81:014406, January 2010.

[71] C. Castelnovo, R. Moessner, and S. L. Sondhi. Debye-Hückel theory for spin ice at low temperature. *Physical Review B*, 84:144435, October 2011.

[72] R. Melin and S. Peysson. Spin glass behavior upon diluting frustrated magnets and spin liquids: a bethe-peierls treatment. *The European Physical Journal B - Condensed Matter and Complex Systems*, 14:169, 2000.

[73] A. Biltmo and P. Henelius. Unreachable glass transition in dilute dipolar magnet. *Nat Commun*, 3:857, May 2012.

[74] K.-M. Tam and M. J. P. Gingras. Spin-Glass Transition at Nonzero Temperature in a Disordered Dipolar Ising System: The Case of $LiHo_xY_{1-x}F_4$. *Physical Review Letters*, 103(8):087202, August 2009.

[75] L. Bovo, X. Moya, D. Prabhakaran, Y.-A. Soh, A. T. Boothroyd, N. D. Mathur, G. Aeppli, and S. T. Bramwell. Restoration of the third law in spin ice thin films. *Nature Communications*, 5:3439, March 2014.

[76] S. T. Bramwell, S. R. Giblin, S. Calder, R. Aldus, D. Prabhakaran, and T. Fennell. Measurement of the charge and current of magnetic monopoles in spin ice. *Nature*, 461(7266):956–959, October 2009.

[77] D. I. Khomskii. Electric dipoles on magnetic monopoles in spin ice. *Nature Communications*, 3, June 2012.

[78] B. M. Ocko, X. Z. Wu, E. B. Sirota, S. K. Sinha, O. Gang, and M. Deutsch. Surface freezing in chain molecules: Normal alkanes. *Phys. Rev. E*, 55(3):3164–3182, March 1997.

[79] D. P. Leusink, F. Coneri, M. Hoek, S. Turner, H. Idrissi, G. Van Tendeloo, and H. Hilgenkamp. Thin films of the spin ice compound $Ho_2Ti_2O_7$. *arXiv.org*, September 2013.

[80] S. Isakov, K. Gregor, R. Moessner, and S. L. Sondhi. Dipolar Spin Correlations in Classical Pyrochlore Magnets. *Physical Review Letters*, 93(16):167204, October 2004.

[81] B. Klemke, M. Meissner, P. Strehlow, K. Kiefer, S. A. Grigera, and D. A. Tennant. Thermal Relaxation and Heat Transport in the Spin Ice Material $Dy_2Ti_2O_7$. *Journal of Low Temperature Physics*, 163(5-6):345–369, June 2011.

[82] R. Higashinaka, H. Fukazawa, D. Yanagishima, and Y. Maeno. Specific heat of $Dy_2Ti_2O_7$ in magnetic fields: comparison between single-crystalline and polycrystalline data. *Journal of Physics and Chemistry of Solids*, 63(6â“8):1043–1046, 2002.

[83] R. Higashinaka, H. Fukazawa, and Y. Maeno. Anisotropic release of the residual zero-point entropy in the spin ice compound $Dy_2Ti_2O_7$: Kagome ice behavior. *Physical Review B*, 68:014415, July 2003.

[84] R. Higashinaka, H. Fukazawa, K. Deguchi, and Y. Maeno. Low temperature specific heat of Dy2Ti2O7 in the kagome ice state. *Journal of the Physical Society of Japan*, 73(cond-mat/0406307):2845–2850, October 2004.

[85] H. W. J. Blot, R. F. Wielinga, and W. J. Huiskamp. Heat-Capacity Measurements on Rare-Earth Double Oxides $R_2M_2O_7$. *Physica*, 43(4):549–&, 1969.

[86] H. M. Revell, L. R. Yaraskavitch, J. D. Mason, K. A. Ross, H. M. L. Noad, H. A. Dabkowska, B. D. Gaulin, P. Henelius, and J. B. Kycia. Evidence of impurity and boundary effects on magnetic monopole dynamics in spin ice. *Nature Physics*, 9(1):34–37, January 2013.

[87] R. Higashinaka and Y. Maeno. Field-Induced Transition on a Triangular Plane in the Spin-Ice Compound $Dy_2Ti_2O_7$. *Physical Review Letters*, 95:237208, November 2005.

[88] T. Sakakibara, T. Tayama, Z. Hiroi, K. Matsuhira, and S. Takagi. Observation of a Liquid-Gas-Type Transition in the Pyrochlore Spin Ice Compound $Dy_2Ti_2O_7$ in a Magnetic Field. *Physical Review Letters*, 90:207205, May 2003.

[89] H. Aoki, T. Sakakibara, K. Matsuhira, and Z. Hiroi. Magnetocaloric Effect Study on the Pyrochlore Spin Ice Compound $Dy_2Ti_2O_7$ in a [111] Magnetic Field. *Journal of the Physical Society of Japan*, 73(10):2851–2856, October 2004.

[90] S. H. Lee, C. Broholm, W. Ratcliff, G. Gasparovic, Q. Huang, T. H. Kim, and S. W. Cheong. Emergent excitations in a geometrically frustrated magnet. *Nature*, 418(6900):856–858, August 2002.

[91] R. Youngblood and J. Axe. Polarization fluctuations in ferroelectric models. *Physical Review B*, 23(1):232–238, January 1981.

[92] J. D. Thompson, P. A. McClarty, H. M. Rønnow, L. P. Regnault, A. Sorge, and M. J. P. Gingras. Rods of Neutron Scattering Intensity in $Yb_2Ti_2O_7$: Compelling Evidence for Significant Anisotropic Exchange in a Magnetic Pyrochlore Oxide. *Physical Review Letters*, 106(18):187202, May 2011.

[93] E. Prince, editor. *International Tables for Crystallography*. John Wiley & Sons, Inc, 2012.

[94] Z. Hiroi, K. Matsuhira, and M. Ogata. Ferromagnetic Ising spin chains emerging from the spin ice under magnetic field. *Journal of the Physical Society of Japan*, 72(12):3045–3048, December 2003.

[95] P. W. Anderson. More Is Different. *Science*, 177(4047):393–396, 1972.

[96] D. A. Huse, W. Krauth, R. Moessner, and S. L. Sondhi. Coulomb and Liquid Dimer Models in Three Dimensions. *Physical Review Letters*, 91:167004, October 2003.

[97] R. R. P. Singh and J. Oitmaa. Corrections to Pauling residual entropy and single tetrahedron based approximations for the pyrochlore lattice Ising antiferromagnet. *Physical Review B*, 85:144414, 2012.

[98] J. C. Shelley and G. N. Patey. Boundary condition effects in simulations of water confined between planar walls. *Molecular Physics*, 88(2):385–398, 1996.